Synthesis, Characterisation and Catalytic Applications of Novel Iron *N*-Heterocyclic Carbenes immobilised on Renewable Resources

Suleiman Ahmed

Doctor of Philosophy

University of York

Chemistry

January 2018

Abstract

The synthesis, characterisation, and catalytic applications of a range of novel iron-*N*-heterocyclic carbenes (Fe-NHCs) immobilised on renewable resources (expanded high amylose corn starch **4a**, Starbon™ 350 **4b**, Starbon™ 400 **4c**, mango peel cellulose **4d** and orange peel cellulose **4e**) are reported. The efficacy of the resultant heterogeneous catalysts was measured for their ability to convert: fructose to 5-(hydroxymethyl) furfural (HMF); glucose to HMF and glucose to 5-(chloromethyl)furfural (CMF).

The immobilised catalysts were prepared using a convergent strategy starting from the appropriate renewable resource, e.g., (**4a-e**) and 1-(3-aminopropyl) imidazole (**7**) to afford the precursor nitrogen heterocyclic carbene, e.g., (**13a-e**), which was treated with $FeCl_3$ to furnish the desired Fe-NHC, e.g., (**1a-e**). Iron-loadings of 0.68 mmol g^{-1} for (**1a**), 0.31 mmol g^{-1} for (**1b**), 0.32 mmol g^{-1} for (**1c**), 0.30 mmol g^{-1} for (**1d**) and 0.52 mmol g^{-1} for (**1e**) were achieved. At 100^{o}C and varying reaction time (10 min, 20 min, 0.5 h, 1 h, 3 h and 6 h), all catalyst types showed good performance for the dehydration of fructose to HMF: Fe-NHC expanded HACS (**1a**), HMF yield 86 % (t=0.5 h), TOF=206 h^{-1}; Fe-NHC Starbon™ 350 (**1b**), HMF yield 81.7 % (t=0.5 h), TOF=169 h^{-1}; Fe-NHC Starbon™ 400 (**1c**), HMF yield 81.0 % (t=0.35 h), TOF= 241 h^{-1}; Fe-NHC MPC (**1d**), HMF yield 70.0 % (t=1 h), TOF= 79.2 h^{-1}; Fe-NHC OPC (**1e**), HMF yield 71.7 % (t=0.5 h), TOF= 146 h^{-1}. The catalysts showed very good recycling stabilities up to 5 catalytic cycles.

The fabricated catalysts were also employed in other catalytic application in important reactions including glucose dehydration to HMF, and gluose/fructose dehydration to CMF. The supported catalysts slightly effect CMF production from glucose and fructose but were ineffective towards amidation reactions of carboxylic acids and amines (as higlighted in future work).

Table of Contents

Abstract 3

List of Tables 9

List of Figures 11

List of Schemes 21

Declaration 23

Acknowledgements 25

Abbreviations 27

CHAPTER 1 INTRODUCTION and AIMS 29

1.1 Introduction 31

1.1.1 Green chemistry and sustainable development 33

1.2 Aims, Overview of NHCs and Objectives 35

1.2.1. Aims 35

1.2.2. Overview of NHCs 38

1.2.2.1. Carbenes 38

1.2.2.2. Nitrogen-heterocyclic carbenes (NHCs) 38

1.2.2.3. Fe-Nitrogen Heterocyclic Carbenes (Fe-NHCs) 47

1.2.3. Objectives 52

CHAPTER 2. EXPERIMENTAL 59

2.1. REAGENTS and MATERIALS 60

2.2. CHARACTERISATION TECHNIQUES 60

2.2.1. ATR-FTIR 60

2.2.2. Solid-state ^{13}C CPMAS 60

2.2.3. X-ray photoelectron spectroscopy (XPS) 60

2.2.4. Thermogravimetric Analysis (TGA) 61

2.2.5. Scanning & Transmission Electron Microscopy (SEM & TEM) 61

2.2.6. N_2 Porosimetry 62

2.2.7. CHN and ICP-MS elemental analysis 63

2.2.8. High Performance liquid chromatography (HPLC) 64

2.3. PROCEDURES 64

2.3.1. Microwave assisted hydrothermal extraction of cellulose from Orange and Mango peels 64

2.3.2. Convergent synthesis of immobilized Fe-NHCs (Scheme 1.21) 65

2.3.2.1. Synthesis of 1-[(*N*-*tert*-butoxycarbonyl)aminopropyl]-imidazole (9)……65

2.3.2.2. Synthesis of 1-[(*N*-*tert*-butoxycarbonyl)aminopropyl]-3- (2,4,6-trimethylbenzyl)imidazolium chloride (11) 65

2.3.2.3 Synthesis of 1-[aminopropyl]-3-(2,4,6-trimethylbenzyl)-imidazolium chloride (12)..... 66

2.3.2.4. Synthesis of succinimidyl carbonate (DSC) activated mesoporous solid support (6a-e) 66

2.3.2.5. Synthesis of NHC ligand grafted mesoporous solid support (13a-e) ……...67

2.3.2.6. Synthesis of Fe-NHCs (1a-e) 67

2.4. Fructose dehydration reaction in DMSO with fabricated Fe-NHC catalysts. ……..68

2.5. Glucose dehydration reaction in DMSO with fabricated Fe-NHC catalysts. ……..69

2.6. Fructose and glucose conversion to CMF with fabricated Fe-NHC catalysts and 1M HCl 69

2.7. Attempted amide synthesis using the fabricated supported Fe-NHC catalyst (1b)……..70

CHAPTER 3. RESULTS and DISCUSSION 71

3.1 Introduction 72

3.2. Part 1: Synthesis and characterisation of Fe-NHCs (1a-e) 74

3.2.1. Fe-NHCS immobilised on expanded HACS (1a) 74

3.2.1.1. Solvent selection study for the DSC (5) activation of expanded HACS (4a), i.e., preparation of (6a) 74

3.2.1.2. DSC (5) concentration study for activation of expanded HACS (4a), i.e., preparation of (6a)..... 77

3.2.1.3. Reaction temperature optimisation study for DSC activation . 79

3.2.1.4. Reaction time optimisation study for DSC activation 80

3.2.1.5. Summary of DSC optimisation study 82

3.2.1.6. Ligand grafted HACS (13a) and Fe-NHC immobilised on HACS (1a)……..82

3.2.1.7. Solid-state ^{13}C NMR spectroscopy investigation for the formation of (1a) from (4a) via intermediates (6a) and (13a)..... 84

3.2.1.8. CHN and ICP-MS elemental analysis of succinimidyl carbonate activated HACS 6a, ligand binded HACS 13a and Fe-NHC HACS 1a..... 85

3.2.1.9. Thermogravimetric analysis of conversion of 4a to 1a via intermediates 6a and 13a 85

3.2.1.10. X-Ray Photoelectron Spectroscopy of (13a) and (1a) 87
3.2.1.11. Mössbauer Spectroscopy of (1a)..... 90
3.2.1.12. Scanning Electron Microscopy (SEM) of (1a) 91
3.2.1.13. Transmission Electron Microscopy (TEM) of (1a) 92
3.2.1.14. N_2 Porosimetry of (4a) and (1a) 92
3.2.2. Fe-NHCS immobilised on Starbon 350 (1b) and 400 (1c) 95
3.2.2.1 ATR FT-IR Spectroscopy 95
3.2.2.2. Solid-state ^{13}C NMR spectroscopy investigation for the formation of 1b and 1c from 4b and 4c via intermediates 6b and 6c and 13b and 13c ... 97
3.2.2.3. CHN and ICP-MS elemental analysis of Fe-NHC immobilised on Starbon-350 (1b) and Fe-NHC immobilised on Starbon-400 (1c) 98
3.1.2.4. Thermogravimetric analysis of Fe-NHC immobilised on Starbon-350 (1b) and Fe-NHC immobilised on Starbon-400 (1c) 99
3.2.2.5. Mössbauer Spectroscopy of (1b) and (1c) 102
3.2.2.6. X-ray photoelectron spectroscopy of 1b, 1c and 4b and 4c..... 103
3.2.2.7. Scanning Electron Microscopy (SEM) 106
3.2.2.8. Transmission Electron Microscopy (TEM) 107
3.2.2.9. N_2 Adsorption Porosimetry..... 108
3.2.3. Fe-NHCS immobilised on mango peel (1d) and orange peel cellulose (1e)……109
3.2.3.1. ATR-FTIR spectroscopy..... 109
3.2.3.2. ^{13}C CPMAS Spectroscopy 112
3.2.3.3. CHN and ICP-MS elemental analysis. 114
3.2.3.4. Thermogravimetric Analysis (TGA)..... 115
3.2.3.5. X-Ray photo electron spectroscopy 117
3.2.3.6. Scanning Electron Microscopy 120
3.2.3.7. Transmission Electron Microscopy (TEM) 122
3.2.3.8. N_2 adsorption porosimetry 122
3.3. Part 2: Catalytic study: Fructose (2) to HMF (3) conversion 133
3.3.1. ^{1}H and ^{13}C NMR spectroscopy study of catalytic conversion of fructose (2) to HMF (3) with respect to time..... 133
3.3.2. HPLC analysis of fructose to HMF..... 141
3.3.3. Comparative study of Fe-NHCs immobilised on renewable supports (1a-e) with other heterogeneous catalysts (Amberlyst-15, Montmorillonite K10 and ZSM-5) for fructose (2) to HMF (3) dehydration 146
3.3.4. Catalyst recycling study 149

3.3.5. Catalysts leaching test 152
3.3.6. Temperature and reaction time study for the catalytic conversion of fructose (2) to HMF (3) with Fe-NHC immobilised on Starbon 350 (1b)..... 152
3.3.7. Kinetic studies 155
3.3.8. Summary 158
3.4. Part 3: Glucose and fructose dehydration to CMF 160
3.4.1. Application of the fabricated catalyst towards fructose dehydration to 5-(chloromethyl)furfural (CMF) 160
3.4.1.1. ^{1}H NMR spectroscopy results on the fructose conversions to CMF……...160
3.4.1.2. HPLC results for the fructose conversion to CMF using the fabricated supported Fe-NHC catalyst. 164
3.4.2. Application of the fabricated catalyst towards glucose dehydration to 5-(chloromethyl)furfural (CMF) 165
3.4.2.1. ^{1}H NMR spectroscopy results on the glucose conversions to CMF ……165
3.4.2.2. HPLC results for the glucose conversion to CMF using the fabricated supported Fe-NHC catalyst. 168
3.4.3. Application of the fabricated catalyst towards glucose dehydration to 5-(hydroxymethyl)furfural. 169
3.4.3.1. ^{1}H NMR spectroscopy study on the glucose dehydration to HMF. 169
3.4.3.2. HPLC results of the glucose dehydration to HMF using the fabricated Fe-NHC catalyst. 172
3.4.3.3. Plausible mechanism for glucose isomerisation to fructose 174
CHAPTER 4. Summary, Conclusions and Future Work 175
4.1. Summary of Research Findings 176
4.2. Conclusion 177
4.3. Future work 178
Appendix A Preliminary Amidation reaction 179
Appendix B Fe loading calculations 181
Appendix C HPLC standard calculation 184
Appendix D XPS deconvolution of S350 and S400 185
Appendix E XPS deconvolution of MPC and OPC 188
Appendix F ^{1}HNMR and ^{13}C NMR of ligand synthesis 191
Appendix G S350 thermogravimetry in air 194
References 195

List of Tables

Table 2.1. Amounts of the catalysts **1a-e** in mg equivalent to 0.01 mmol Fe……68

Table 3.1. Succinimidyl carbonate loading (mmol g^{-1}) and degree of substitution in (**6a**) with respect to reaction solvent at 80°C and 24 h reaction time…….75

Table 3.2. Succinimidyl carbonate loadings (mmol g^{-1}) and degree of substitution based on varying DSC loadings (mmol g^{-1} HACS)……78

Table 3.3. Succinimidyl carbonate loading (mmol g^{-1}) and degree of substitution at fixed concentration (40 mmol g^{-1}) with respect to temperature (°C) at 24 h reaction time…….80

Table 3.4. Results of starch DSC activation at different temperatures……...82

Table 3.5. Summary of the TG data for expanded HACS **(4a**), succinimidyl carbonate derivative (**6a**), ligand grafted HACS (**13a**), and Fe coordinated HACS (**1a**)……87

Table 3.6. Summary of the porosity data for expanded HACS and modified forms...94

Table 3.7. Loading levels (mmol g^{-1}) of succinimidyl carbonate, NHC ligand and Fe on Starbon 350 and Starbon 400…….98

Table 3.8. Porosity data for the Starbon™ and modified Starbons……108

Table 3.9. Summary of the surface and porosity properties of the samples analysed…….123

Table 4.1. Summary of measured parameters of the fabricated Fe-NHC catalysts…176

Table A1. Result of the ICP-MS analysis…….181

Table A2. Result of the ICP-MS analysis…….181

Table A3. Result of the ICP-MS analysis…….182

Table A4. Result of the ICP-MS analysis…….182

Table A5. Result of the ICP-MS analysis…….183

List of Figures

Figure 1.1 Society, economy and environmental importance in sustainable development……31

Figure 1.2 UK five principle approach to sustainability……..32

Figure 1.3 Sustainable Development Goals…….32

Figure 1.4 Example of some important chemicals obtained from HMF and CMF….37

Figure 1.5. π - electron-donating and σ – electron withdrawing illustrations of NHCs……..39

Figure 1.6. General structures of NHCs used in organo-catalysis……..39

Figure 1.7. Cancer inhibiting NHC-Ru^{II} complex…….……41

Figure 1.8. Ag^{I}, Au^{I} and Ru^{II} NHC complexes having antitumor activity……..…….41

Figure 1.9. Position of immobilization of NHCs……....43

Figure 1.10. Immobilized NHC complex at the surface of π-extended nanostructured electrodes……45

Figure 1.11 Strong-field $Fe^{II}L_6$ complexes with significantly extended ^{3}MLCT……51

Figure 1.12. Production of Starbon™ through controllable pyrolysis of expanded starch……...54

Figure 1.13. D-glucopyranose units linked by β (1 → 4) glycosidic bonds……55

Figure 3.1. ATR-IR spectroscopy of expanded HACS after DSC activation in various solvents……..…….....74

Figure 3.2. FT-IR spectra for succinimidyl carbonate derivative of HACS **6a** with respect to DSC concentration (mmol g^{-1} starch)……..77

Figure 3.3. FT-IR results of the optimisation of DSC activation temperature on Expanded HACS……79

Figure 3.4. FT-IR spectra for optimisation of DSC activation of HACS (**4a**) with respect to reaction time……81

Figure 3.5 FT-IR spectra of expanded HACS (**4a**), DSC activated HACS (**6a**), Ligand grafted HACS (**13a**) and Fe coordinated HACS (**1a**)……..83

Figure 3.6 ^{13}C CPMAS spectra of expanded HACS (**4a**), succinimidyl carbonate derivative (**6a**), ligand grafted derivative (**13a**) and Fe-NHC immobilised on HACS (**1a**)……..85

Figure 3.7. Thermograms for expanded HACS (**4a**) and modified expanded HACS, i.e., (**6a**), (**13a**), (**1a**) in N_2……..…85

Figure 3.8. Differential thermograph (dTG) curves for expanded HACS (**4a**) and modified expanded HACS, i.e., (**6a**), (**13a**), (**1a**) in N_2……...86

Figure 3.9. Fitted carbon 1s peaks for the expanded HACS and Fe-NHC expanded HACS……..87

Figure 3.10. Fitted carbon 1s peaks for the expanded HACS (**4a**) and Fe-NHC immobilised HACS (**1a**)……..88

Figure 3.11. Fitted oxygen 1s peaks for the expanded HACS and Fe-NHC expanded HACS……..88

Figure 3.12. Fitted nitrogen 1s and iron 2p peaks for the Fe-NHC expanded HACS.87

Figure 3.13. Mössbauer spectrum of Fe-NHC immobilised on HACS (**1a**)……...90

Figure 3.14. SEM micrographs of (A) expanded HACS (**4a**) (B) Succinimidyl carbonate activated HACS (**6a**) (C) Ligand grafted HACS (**13a**) and (D) Fe-NHC HACS (**1a**).....91

Figure 3.15. TEM micrographs of Fe-NHC HACS (**1a**), at 200 nm (a) and 100 nm (b).....92

Figure 3.16. Adsorption/desorption isotherms for expanded HACS (**4a**) and Fe-NHC HACS (**1a**).....93

Figure 3.17 FT-IR spectra of Starbon™-350 (**4b**), DSC activated Starbon™-350 (**6b**), ligand grafted Starbon™-350 (**13b**) and Fe-NHC immobilised on Starbon™-350 (**1b**)……..95

Figure 3.18. FT-IR spectra of Starbon™-400 (**4c**), DSC activated Starbon™-400 (**6c**), ligand grafted Starbon™-400 (**13c**) and Fe-NHC immobilised on Starbon™-400 (**1c**)……..96

Figure 3.19 FT-IR spectra of Starbon™-350 (blue line), DSC activated Starbon™-350 (red line), ligand grafted Starbon™-350 (green line) and Fe coordinated NHC Starbon™-350 (purple line)……97

Figure 3.20. FT-IR spectra of Starbon™-400 (blue line), DSC activated Starbon™-400 (red line), ligand grafted Starbon™-400 (green line) and Fe coordinated NHC Starbon™-400 (purple line)……98

Figure 3.21. Thermal analysis data (TG) of Starbon™ 350 (Top) and Starbon™ 400 (Bottom)……100

Figure 3.22. Thermal analysis data (dTG) of Starbon™ 350 (Top) and Starbon™ 400 (Bottom)……....101

Figure 3.23. Mössbauer trace for the fabricated Starbon™-Fe catalyst……103

Figure 3.24. XPS survey scan for Starbon™-350 and Fe-NHC Starbon™-350…...105

Figure 3.25. XPS survey scan for Starbon™-400 and Fe-NHC Starbon™-400…...104

Figure 3.26. SEM micrographs of (A) Starbon™-350 (**4b**) (B) Succinimidyl carbonate activated Starbon™-350 (**6b**) (C) Ligand grafted Starbon™-350 (**13b**) and (D) Fe-NHC Starbon™-350 (**1b**).....106

Figure 3.27. SEM micrographs of (A) Starbon™-400 (**4c**) (B) Succinimidyl carbonate activated Starbon™-400 (**6c**) (C) Ligand grafted Starbon™-400 (**13c**) and (D) Fe-NHC Starbon™-400 (**1c**).....107

Figure 3.28. TEM microimages of (A) Fe-NHC Starbon™-350 (**1b**) and (B) Fe-NHC Starbon™-400 (**1c**).....107

Figure 3.29 FT-IR spectra of microcrystalline cellulose (black line), mango peel cellulose (**4d**) and orange peel cellulose (**4e**)……109

Figure 3.30 FT-IR spectra of mango peel cellulose (**4d**), DSC activated mango peel cellulose (**6d**), ligand grafted mango peel cellulose (**13d**) and Fe-NHC immobilised on mango peel cellulose (**1d**)……110

Figure 3.31 FT-IR spectra of orange peel cellulose (**4e**), DSC activated orange cellulose (**6e**), ligand grafted orange peel cellulose (**13e**) and Fe-NHC immobilised on orange peel cellulose (**1e**)……..111

Figure 3.32 ^{13}C CP-MAS NMR spectra of microcrystalline cellulose (blue line), mango peel cellulose (**4d**) and orange peel cellulose (**4e**)……112

Figure 3.33 ^{13}C CP-MAS NMR stacked spectra of mango peel cellulose (**4d**), DSC activated mango peel cellulose (**6d**), ligand grafted mango peel cellulose (**13d**) and Fe-NHC immobilised on mango peel cellulose (**1d**)……..113

Figure 3.34 ^{13}C CP-MAS NMR spectra of orange peel cellulose (**4e**), DSC activated orange peel cellulose (**6e**), ligand grafted orange peel cellulose (**13e**) and Fe-NHC immobilised on orange peel cellulose (**1e**)……113

Figure 3.35. Thermograms for mango peel cellulose (**4d**) and its derivatives (**6d**) and (**13d**) leading to Fe-NHC immobilised on mango peel cellulose (**1d**)……..115

Figure 3.36. Thermograms for orange peel cellulose (**4e**) and its derivatives (**6e**) and (**13e**) leading to Fe-NHC immobilised on orange peel cellulose (**1e**)……115

Figure 3.37. Differential thermograms for mango peel cellulose (**4d**) and its derivatives (**6d**) and (**13d**) leading to Fe-NHC immobilised on mango peel cellulose (**1d**)…….116

Figure 3.38. Differential thermograms for mango peel cellulose (**4e**) and its derivatives (**6e**) and (**13e**) leading to Fe-NHC immobilised on mango peel cellulose (**1e**)…….117

Figure 3.39. XPS survey scan for the mango peel cellulose (**4d**) and orange peel cellulose (**4e**)……118

Figure 3.40. XPS survey scan for the Fe-NHC mango peel cellulose (**1d**) and Fe-NHC orange peel cellulose (**1e**)……..118

Figure 3.41. SEM images of commercial microcrystalline cellulose (a) mango peel cellulose (b) and orange peel cellulose (c)……120

Figure 3.42. SEM images of (A) mango peel cellulose, (B) DSC activated mango peel cellulose, (C) IL grafted mango peel cellulose, and (D) Fe-NHC mango peel cellulose……121

Figure 3.43. SEM images of (E) orange peel cellulose, (F) DSC activated orange peel cellulose, (G) IL grafted orange peel cellulose, and (H) Fe-NHC orange peel cellulose……121

Figure 3.44. TEM images of (a) Fe-NHC mango peel cellulose, (b) Fe-NHC orange peel cellulose……122

Figure 3.45: Nitrogen adsorption/desorption isotherm of mango cellulose (**4d**), DSC activated mango cellulose (**6d**), IL grafted mango cellulose (**13d**) and Fe-NHC mango cellulose (**1d**)……125

Figure 3.46. BJH adsorption dV/dlog(D) pore volume distribution for mango cellulose (**4d**), activated mango cellulose (**6d**), ligand grafted mango cellulose (**13d**) and Fe-NHC mango cellulose (**1d**)……..126

Figure 3.47. BJH adsorption dV/dD pore volume distribution of mango cellulose (**4d**), activated mango cellulose (**6d**), ligand grafted mango cellulose (**13d**) and Fe-NHC mango cellulose (**1d**)……127

Figure 3.48. Nitrogen adsorption/desorption isotherms of orange peel cellulose (**4e**), DSC activated orange peel cellulose (**6e**), ligand grafted orange peel cellulose (**13e**) and Fe-NHC orange peel cellulose (**1e**)……129

Figure 3.49. BJH adsorption dV/dD pore volume distribution of orange cellulose (**4e**), activated orange cellulose (**6e**), ligand grafted orange cellulose (**13e**) and Fe-NHC orange cellulose (**1e**)……130

Figure 3.50. BJH desorption dV/dlog(D) pore volume distribution of orange cellulose (**4e**), activated orange cellulose (**6e**), ligand grafted orange cellulose (**13e**) and Fe-NHC orange cellulose (**1e**)……131

Figure 3.51 Colour change as fructose is converted to HMF with time……133

Figure 3.52. Stacked ^{1}H NMR spectra for fructose (**2**) conversion to HMF (**3**) with Fe-NHC HACS catalyst (**1a**)……..134

Figure 3.53 (A and B). Stacked ^{1}H NMR spectra for fructose (**2**) conversion to HMF (**3**) with Fe-NHC Starbon™ 350 catalyst (1**b,** Figure A) and Starbon™ 400 catalyst (**1c,** Figure B), respectively……...……135

Figure 3.54 (C and D). Stacked ^{1}H NMR spectra for fructose (**2**) conversion to HMF (**3**) with Fe-NHC mango peel cellulose catalyst (**1d,** Figure C) and orange peel cellulose catalyst (**1e,** Figure C) respectively……137

Figure 3.55. Stacked ^{13}C NMR spectra for fructose (**2**) conversion to HMF (**3**) with Fe-NHC HACS catalyst (**1a**)……138

Figure 3.56. (A and B) Stacked ^{13}C NMR spectra for fructose (**2**) conversion to HMF (**3**) with Fe-NHC Starbon™ 350 catalyst (1**b**, A) and Starbon™ 400 catalyst (**1c**, B) respectively……...139

Figure 3.57. (C and D). Stacked ^{13}C NMR spectra for fructose (**2**) conversion to HMF (**3**) with Fe-NHC mango peel cellulose catalyst (1**d**) and orange peel cellulose catalyst (**1e**), respectively……..141

Figure 3.58. HPLC results of Fructose conversion to HMF with Fe-NHC HACS catalyst (**1a**)……..142

Figure 3.59. (A and B) Consolidated HPLC results for fructose (**2**) conversion to HMF (**3**) with Fe-NHC Starbon™ 350 catalyst (1**b**, A) and Starbon™ 400 catalyst (**1c**, B), respectively……...143

Figure 3.60. (C and D) Consolidated HPLC results for fructose (**2**) conversion to HMF (**3**) with Fe-NHC mango peel cellulose catalyst (**1d**, C) and orange peel cellulose catalyst (**1e**, D) respectively……..145

Figure 3.61A-C. HPLC results for fructose conversion (A), HMF yield (B) and HMF selectivity (C) for **1a**-**e** and selected commercially available catalysts…….148

Figure 3.62. (A-E) Catalytic (re)use data for fructose conversion, HMF yield and selectivity over (A) Fe-NHC expanded HACS (**1a**), (B) Fe-NHC Starbon™ 350 (**1b**),

(C) Fe-NHC Starbon™ 400 (**1c**), (D) Fe-NHC MPC (**1d**) and (E) Fe-NHC OPC (**1e**)……151

Figure 3.63. A, B and C. Comparative study of the fructose to HMF conversion with other catalysts……154

Figure 3.64. Reaction kinetic curve (yield vs time) for Fe-NHC HACS (**1a**) and Fe-NHC-Starbon^{TM}-350 (**1b**), Fe-NHC Starbon^{TM} 400 (**1c**), Fe-NHC mango peel cellulose (**1d**) and Fe-NHC orange peel cellulose (**1e**)……..155

Figure 3.65. Kinetic parameters for fructose (**2**) to HMF (**3**) conversion at 80 ^{o}C and 100 ^{o}C based on first-order assumption for Starbon 350 (**1b**)……...157

Figure 3.66 ^{1}H NMR of fructose to CMF conversion using aqueous HCl……161

Figure 3.67 ^{1}H NMR of fructose to CMF conversion using aqueous HCl and Fe-NHC Starbon 350 catalyst (**1b**)……..161

Figure 3.68 ^{13}C NMR of fructose to CMF conversion using aqueous HCl……...162

Figure 3.69 ^{13}C NMR of fructose to CMF conversion using aqueous HCl and Fe-NHC Starbon 350 catalyst (**1b**)……...163

Figure 3.70. HPLC data on fructose conversion to CMF using aqueous HCl……..164

Figure 3.71 ^{1}H NMR of glucose to CMF conversion using aqueous HCl……165

Figure 3.72 ^{1}H NMR of glucose to CMF conversion using aqueous HCl and Fe-NHC Starbon 350 catalyst (**1b**)……...166

Figure 3.73 ^{13}C NMR of glucose to CMF conversion using aqueous HCl……167

Figure 3.74 ^{13}C NMR of glucose to CMF conversion using aqueous HCl and Fe-NHC Starbon 350 catalyst (**1b**)……..167

Figure 3.75. HPLC glucose conversion to CMF study using aqueous HCl……..168

Figure 3.76 ^{1}H NMR results of glucose dehydration to HMF using Fe-NHC catalyst (**1a**)……169

Figure 3.77 ^{1}H NMR results of glucose dehydration to HMF using Fe-NHC catalyst (**1b**)……170

Figure 3.78 ^{13}C NMR results of glucose dehydration to HMF using Fe-NHC catalyst (**1a**)……171

Figure 3.79 ^{13}C NMR results of glucose dehydration to HMF using Fe-NHC catalyst (**1b**)……171

Figure 3.80. HPLC results of glucose dehydration to HMF using Fe-NHC HACS catalyst (**1a**)……...172

Figure 3.81 HPLC results of glucose dehydration to HMF using Fe-NHC Starbon 350 catalyst (**1b**)……..173

Figure D1. Deconvoluted C 1s peaks for Starbon 350 (**4b**) and Fe-NHC Starbon-350 (**1b**)……185

Figure D2. Deconvoluted O 1s peaks for Starbon 350 (**4b**) and Fe-NHC Starbon-350 (**1b**)……185

Figure D3. Deconvoluted N 1s and Fe 2 p peaks for Fe-NHC Starbon-350 (**1b**)….186

Figure D4. Deconvoluted C 1s peaks for Starbon 400 (**4c**) and Fe-NHC Starbon-400 (**1c**)……186

Figure D5. Deconvoluted O 1s peaks for Starbon 400 (**4c**) and Fe-NHC Starbon-400 (**1c**)……187

Figure D6. Deconvoluted N 1s and Fe 2 p peaks for Fe-NHC Starbon-400 (**1c**)….187

Figure E1. Deconvoluted C 1s peaks for mango peel cellulose (**4d**) and Fe-NHC orange peel cellulose (**1d**)……188

Figure E2. Deconvoluted O 1s peaks for mango peel cellulose (**4d**) and Fe-NHC orange peel cellulose (**1d**)……188

Figure E3. Deconvoluted N 1s and Fe 2 p peaks for Fe-NHC mango peel cellulose (**1d**)……189

Figure E4. Deconvoluted C 1s peaks for orange peel cellulose (**4e**) and Fe-NHC orange peel cellulose (**1e**)……..189

Figure E5. Deconvoluted O 1s peaks for orange peel cellulose (**4e**) and Fe-NHC orange peel cellulose (**1e**)……..190

Figure E6. Deconvoluted N 1s and Fe 2 p peaks for Fe-NHC orange peel cellulose (**1e**)……190

Figure F1. ^{1}H NMR spectrum of the synthesised NHC ligand **12**. Methanol d4…..191

Figure F2. ^{13}C NMR spectrum of the synthesised NHC ligand **12**. Methanol d4…..191

Figure F3. ^{1}H NMR spectrum of the synthesised BOC protected mesityl imidazole **11**. $CDCl_3$……...192

Figure F4. ^{13}C NMR spectrum of the synthesised BOC protected mesityl imidazole **11**. $CDCl_3$……192

Figure F5. ^{1}H NMR spectrum of the synthesised BOC protected imidazole **9**. $CDCl_3$……....193

Figure F6. ^{13}C NMR spectrum of the synthesised BOC protected imidazole **9**. $CDCl_3$……193

Figure G1. Thermal analysis data (TG) of Starbon 350 in air……..194

Figure G2. Thermal analysis data (dTG) of Starbon 350 in air……..194

List of Schemes

Scheme 1.1. Synthesis of 1,3-di-l-adamantylimidazol-2-ylidene……...38

Scheme 1.2. NHCs as stabilizing ligands for Pd oxidation reactions…..……40

Scheme 1.3. Rapid fixation of O_2 and CO_2 from air by NHC……40

Scheme 1.4. Synthesis of imidazolium salts by direct quaternization of *N*-substituted imidazoles or imidazolines with alkyl or aryl halides…….42

Scheme 1.5. Synthesis of NHCs by symmetrical *N*-substitution…….42

Scheme 1.6. Symmetrical synthesis of imidazolium chloride……..43

Scheme 1.7. Unsymmetrical synthesis of NHCs……...……..43

Scheme 1.8. Immobilization of NHC via the formation of ether bond……44

Scheme 1.9. Immobilization of NHC via the formation of ester bond…….44

Scheme 1.10. Immobilized NHC on silica via direct quaternization of benzyl chloride modified materials with N-substituted imidazoles……..44

Scheme 1.11. Immobilization of NHC through ATRP…….…….....45

Scheme 1.1.2 Polymer-supported N-heterocyclic carbene prepared from chloromethyl polystyrene (CM PS) resin……..46

Scheme 1.13. Synthesis of Fe(NHC)(CO) from iron carbonyl complex…..……..47

Scheme 1.14. Synthesis of $Fe(NHC)(CO)_4$ from iron carbonyl complex…..……..48

Scheme 1.15. Synthetic route to polystyrene supported NHC-metal complex. …..…48

Scheme 1.16. Hydroxylation of arenes an iron(II) bis(NHC) complex…..……..49

Scheme 1.17. Homogeneous Fe-NHC for Kumada type cross-coupling…..……49

Scheme 1.18. Hydrosilylation of benzaldehyde and its derivatives catalysed by $Fe(IMes)(CO)_4$. ……..50

Scheme 1.19. Fe-NHC catalysed atom radical transfer polymerization (ATRP) of olefins……..50

Scheme 1.20. Fe-NHC catalysed ring-opening polymerisation reaction of ε -caprolactone……50

Scheme 1.21. Convergent synthesis of Fe-NHCs (**1a-e**) immobilised on renewable supports (**4a-e**)……53

Scheme 1.22. Fructose dehydration to 5-(hydroxymethyl)furfural using Fe-NHC…57

Scheme 1.23. Glucose and fructose dehydration to 5-(chloromethyl)furfural using Fe-NHC……58

Scheme 3.1. Plausible mechanism for DSC activation in the presence of DMAP……76

Scheme 3.2. HMF rehydration to levulinic acid and formic acid……..……133

Scheme 3.3. Proposed fructose dehydration mechanism to HMF by Fe-NHC catalyst……..159

Scheme 3.4. Fructose and glucose dehydration to HMF and its subsequent conversion to CMF……..160

Scheme 3.5. Plausible mechanism for glucose isomerisation to fructose…….174

Scheme A1. Amide synthesis from amines and carboxylic acids……..179

Declaration

I declare that this thesis is a presentation of an original work for which I am the sole author. This work has not previously been presented for an award at this, or any other, University. Some of the results presented in this thesis were obtained in collaboration with other workers. All sources are acknowledged as References.

Suleiman Ahmed.

February 2018.

Acknowledgements

All thanks and praise are due to my creator for making this research successful and for His guidance and protection throughout the work.

I first acknowledge my first supervisor Dr Avtar S. Matharu to whom my most sincere appreciation goes to. Indeed, Dr Avtar's continuous and unrelenting guidance, support and encouragement has helped in making this research successful. I would also like to acknowledge and appreciate the support, supervision and guidance I received from my second supervisor Dr Duncan Macquarrie, whose efforts are very significant to the success of this research. My appreciation also goes to Professor James Clark and Dr Thomas Farmer for their advice and encouragement.

My deep love and appreciation goes to my wife Hafsat Ibrahim Maifada and my daughters Aisha Suleiman and Amina Suleiman.

I would also like to express my appreciation to the present and previous members of the laboratory technical team at Green Chemistry Centre of Excellence in persons of; Paul Elliot, Dr Hannah Briers, Charlotte Brannigan, Jennifer Dyer, and Maria Garcia for their prompt and professional technical support. My appreciation goes to Dr Meg Stark of the biology department for her assistance with SEM and TEM, Dr Pedro Aguiar and Dr Julia Walton for training and assistance on working with solid ^{13}C NMR machine. I appreciate the assistance from Dr Andrew Pratt, Dr Jason Zhang and Dr Balati Kuerbanjiang of physics department, University of York and Dr Benjamin Johnson, School of Physics and Astronomy University of Leeds for their assistance with XPS analysis. Moreover, I appreciate the assistance I received from Dr Brian A. Schaefer of Princeton University, USA. for Mössbauer spectroscopy.

For financial assistance, I would like to acknowledge and thank the Tertiary Education Trust Fund (TETFUND) Nigeria and WILD FUND department of chemistry, University of York. Also, Isa Kaita College of Education Dutsin-ma.

Special thanks and appreciation to my colleagues and friends previously at the Green Chemistry Centre of Excellence University of York, including Dr Yohan Kim, Badriya Almonthery, Abdulrahman Alweihaibi, Dr Kaana Asemave, Dr Joseph Ogunjobi, Dr Cheng Ding, and Dr Zhangrong Zhang.

Importantly, I would like to express my profound gratitude to my parents; Ahmed Bala Ibrahim and Zulaihat Muhammad Daku and my uncles General Ahmad Muhammad Daku and Dr Labaran Ibrahim Doro for their moral and financial support. May they live long to enjoy the fruit of their labour.

Finally, my appreciation goes to my brothers; Umaru Bala, Hayatuddeen Macido, Usman Ahmed, Bishir Ahmed, Abubakar Ahmed, Ibrahim Ahmed, Aliyu Ahmed and Nuhu Ibrahim Maifada, and my Sisters; Kahdijah Ahmed and Aisha Ahmed; my friend Kamaladdeen Abdullahi and my uncle Commander Isa Musa Danjuma for their support.

Abbreviations

CHN	Carbon, hydrogen and nitrogen
CMF	5-(Chloromethyl)furfural
CPME	Cyclopentyl methyl ether
DCM	Dichloromethane
DMF	Dimethylformamide
DMAP	4-(Dimethylamino)pyridine
DMSO	Dimethyl sulfoxide
DSC	Disuccinimidyl carbonate
DS	Degree of substitution
Fe-NHC	iron- *N*-heterocyclic carbene
HACS	High amylose corn starch
HMF	5-(Hydroxymethyl)furfural
HPLC	High pressure liquid chromatography
ICP-MS	Inductively coupled plasma mass spectrometry
IL	Imidazolium ligand
MPC	Mango peel cellulose
NHC	*N*-heterocyclic carbene
NOx	Nitrogen oxides
OPC	Orange peel cellulose
S350	Starbon™ 350
S400	Starbon™ 400
SEM	Scanning electron microscopy

STA	Simultaneous thermal analysis
TEA	Triethylamine
TEM	Transmission electron microscopy
TFA	Trifluoroacetic acid
TOF	Turnover frequency
TG	Thermogravimetry
dTG	Differential thermogravimetry
THF	Tetrahydrofuran
XPS	X-ray photoelectron spectroscopy
^{13}C CPMAS	^{13}C cross-polarisation magic angle spinning

CHAPTER 1 INTRODUCTION and AIMS

Prelude

This chapter highlights the aims, objectives and justification of the research within the general context of global drivers, sustainability and the 12 Principles of Green Chemistry. An overview of NHC's and Fe-NHC's is given within the context of recent literature with focus on structural properties, synthetic routes and applications. Mesoporous materials to be used in this research are discussed, namely: expanded starch, Starbon™, orange peel cellulose and mango peel cellulose residue.

Parts of the work in this chapter has been published:

"Novel Starbon™/HACS-supported *N*-heterocyclic carbene-iron(III) catalyst for efficient conversion of fructose to HMF."

Avtar S. Matharu, Suleiman Ahmed, Badriya Almonthery, Duncan J. Macquarrie, Yoon-Sik Lee and Yohan Kim, *ChemSusChem*, 2017.

DOI: 10.1002/cssc.201702207

(impact factor 2016, 7.226)

1.1 Introduction

Global warming and inter-related climatic in-balances/rapid changes are predominantly due to the actions of humans.[1,2,3] It has become evident that we humans, as species, need to change our lifestyle to ensure future sustainable development, i.e., the fulfilment of contemporary needs of the present without compromising the ability of the future generations to fulfil their needs.[4] To ensure sustainable development (Figure 1.1) a subtle balance of three inter-related factors: social, economic, and; environmental, is needed.

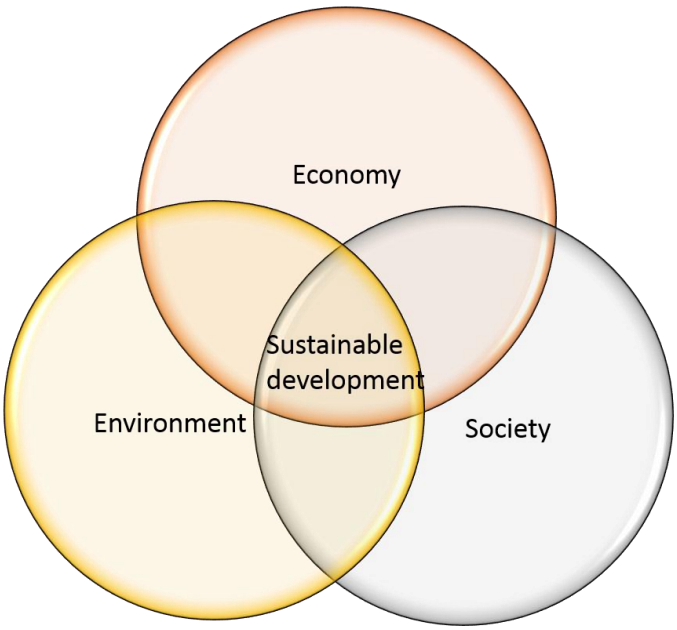

Figure 1.1 Society, economy and environmental importance in sustainable development.

However, the UK government reframed the above to a five principles approach to incorporate "promoting good governance" and "using sound science responsibly," [5] which form a set of shared UK principles to achieve sustainable development (Figure 1.2).

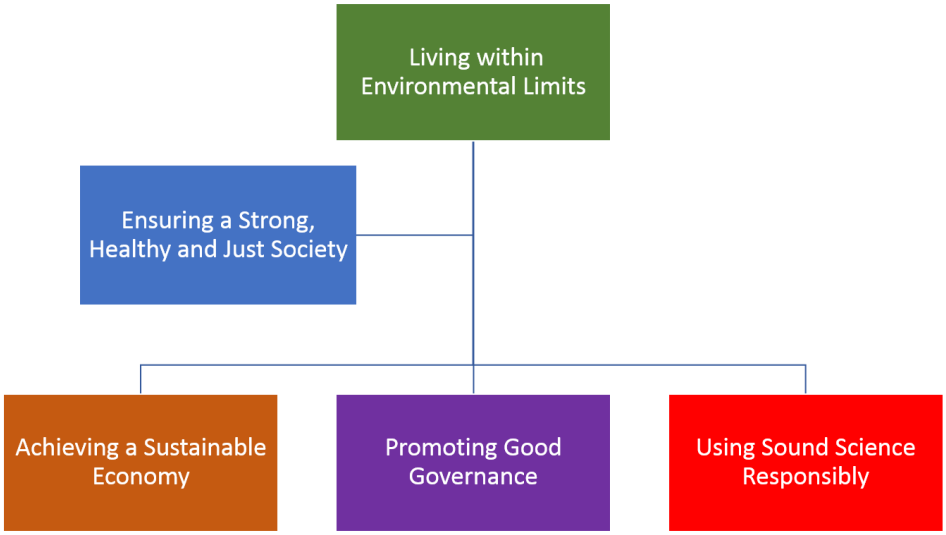

Figure 1.2 UK five principle approach to sustainability.

In September 2015, the 193 member countries of the United Nations met and agreed upon 17 Sustainable Development Goals (SDGs, Figure 1.3),[6] which are targets and indicators member states are expected to follow as guiding principles. The SDGs are essentially a follow-up and expansion on the millennium development goals (MDGs), which expired in 2015.

Figure 1.3 Sustainable Development Goals.

SDG 12 seeks to control the environmental impact of wastes and the depletion of natural resources, through responsible consumption and production. SDG 12 promotes doing more with less and circular- rather than linear-thinking. To this end, the principles and practice of green chemistry has become an essential tool to achieving responsible consumption and production.

1.1.1 Green chemistry and sustainable development

Increased concerns over declining fossil oil reserves and negative environmental impact associated with their continued use as a feedstock for chemicals, materials and energy, has ignited tremendous interest in developing new processes that both reduce energy consumption and minimize pollution.[7, 8] The transition from petroleum to bio-based or bio-renewable feedstocks and the development of circular, bio-based economies is a key driver towards a sustainable 21st century.[9] The need for materials and processes compatible with the environment has motivated the increasingly intense study of materials obtained from renewable sources (biomass), and the development of recyclable or biodegradable products.[10-12]

Green Chemistry, as defined by Anastas and Warner,[13] is the design of chemical products and processes that reduce or eliminate the use and generation of hazardous substances, and is governed by 12 Principles as listed:

1. **Prevention:** It is better to prevent waste than to treat or clean up waste after it has been created.

2. **Atom Economy:** Synthetic methods should be designed to maximise the incorporation of all materials used into final products.

3. **Less Hazardous Chemical Syntheses:** Wherever practicable, synthetic methods should be designed to use and generate substances that possess little or no toxicity to human health and the environment.

4. **Designing Safer Chemicals:** Chemical products should be designed to affect their desired function while minimizing their toxicity.

5. **Safer Solvents and Auxiliaries:** The use of auxiliary substances (e.g., solvents, separation agents, etc.) should be made unnecessary wherever possible and innocuous when used.

6. **Design for Energy Efficiency:** Energy requirements of chemical processes should be recognized for their environmental and economic impacts and should be minimized. If possible, synthetic methods should be conducted at ambient temperature and pressure.

7. **Use of Renewable Feedstocks:** A raw material or feedstock should be renewable rather than depleting whenever technically and economically practicable.

8. **Reduce Derivatives:** Unnecessary derivatization (use of blocking groups, protection/deprotection, and temporary modification of physical/chemical processes) should be minimized or avoided if possible, because such steps require additional reagents and can generate waste.

9. **Catalysis:** Catalytic reagents (as selective as possible) are superior to stoichiometric reagents.

10. **Design for Degradation:** Chemical products should be designed so that at the end of their function they break down into innocuous degradation products and do not persist in the environment.

11. **Real-time analysis for Pollution Prevention:** Analytical methodologies need to be further developed to allow for real-time, in-process monitoring and control prior to the formation of hazardous substances.

12. **Inherently Safer Chemistry for Accident Prevention:** Substances and the form of a substance used in a chemical process should be chosen to minimize the potential for chemical accidents, including releases, explosions, and fires.

Within the context of Principle 7 (Use of Renewable Feedstocks) agricultural wastes and industrial wastes have gained tremendous interest due to their high volume, availability and low cost.[14-18] For example, cellulose is one of the most abundant biopolymers on earth which maintains the structural integrity of plants occurring in wood, cotton, hemp and food residues.[17-21] According to the Pike Report, adoption of green chemistry practices and principles through utilisation of renewable feedstocks can save the chemical industry $65 billion by 2020.[22]

Within the context of Principle 9 (Catalysis) heterogeneous catalysis which benefits from the ease of separation and recycling of catalysts, plays a crucial role in a future bio-based chemical economy. Thus, the search for novel green catalysts that enable efficient conversion of naturally abundant carbohydrates in to platform molecules, such as the conversion of fructose into 5-(hydroxymethyl)furfural (HMF) attracts considerable interest. [23-31] The growing concern over elemental sustainability and critical elements has seen the emergence of base-metal catalysis over traditional precious metal catalysis because of the relatively abundance and lower cost of the former.[31] In this context, iron salts and molecular defined iron complexes have emerged as interesting and powerful synthetic tools in the chemist's armory.[32-33]

1.2 Aims, Overview of NHCs and Objectives

1.2.1. Aims

The overall aim of this research is to synthesise and characterise novel iron-nitrogen heterocyclic carbenes (Fe-NHCs) (Scheme 1, **1a**-**e**), immobilized on a variety of renewable mesoporous supports (**4a-e**), in order to investigate their efficacy as potential heterogeneous catalysts for dehydration of fructose to 5-(hydroxymethyl) furfural (HMF); glucose to HMF, and; glucose to 5-(chloromethyl)furfural (CMF).

The dehydration of carbohydrates to HMF has attracted increasing attention due to its possible application as a substitute for petroleum derived building blocks.[34, 35, 36] HMF (**3**) is a versatile and top value-added chemical that has received significant attention as a platform chemical essential for the production of broad range of chemicals and liquid transportation fuel (Figure 1.4).[37] HMF is a key intermediate for the production of a wide variety of bio-based chemicals.[38-39] It is essential to find new fuels to replace existing ones, which can simultaneously meet the energy needs of the population and protect the environment.[40] Since the identification of HMF as valuable molecule by the US Department of Energy, several attempts have been made to produce HMF from fructose and biomass using homogeneous or heterogeneous Brønsted acid and Lewis acid catalysts in various reaction media. Qi *et al.* reported conversion of sugars including glucose and fructose into HMF (72 %) in ɤ-valerolactone using H_2SO_4.[41] Qi *et al.* reported the conversion of fructose to HMF in DMSO/acetone co-solvent using ion exchange resins.[42] Upare *et a.l* reported the conversion of fructose in butanol to HMF (93 %) and subsequently to 2,5-dimethyl

furan using double catalyst systems of Amberlyst-15 and Ru-Sn/ZnO catalyst.[43] High HMF yields (60% to 90%) were also reported in ionic liquids systems. [44-47]

Kim *et al.* reported good yield (73%) HMF from fructose using an Fe-NHC supported on polystyrene beads using DMSO as reaction solvent at 100 ^{o}C for 3 hours reaction time.[48] HMF can be obtained from biomass by hydrolysis followed by dehydration (eg. cellulosic biomass),[40] or isomerization and dehydration of mono and disaccharides,[49] or polysaccahrides,[50-51] using acid catalyst or base catalyst at lower reaction temperatures of 100 to 150 ^{o}C. Although the conversion of fructose to HMF is autocatalytic,[52-53] it is important to note that only low conversions were obtained in most solvents in up to six hours reaction times. Hao *et al.* were able to achieve 73 % HMF yield in methyl isobutyl ketone/water biphasic solvent system without any added catalyst.[54]

However, HMF does have thermal and chemical instability, high solubility in water, and low melting point, which in recent years has paved the way for CMF as an alternative (Figure 1.3). The advantages of CMF over HMF as an intermediate building block include better thermal and chemical stability, lower polarity (immiscible in water), and it can be more readily produced from glucose and cellulose biomass due to its lipophilicity.[55-56] As reported by Mascal *et al.* CMF serves as a precursor to the new generation bio-fuels and high value chemicals.[57] Breeden *et al.* reported conversions of fructose and inulin to CMF with yields >70 %.[60] Brasholz *et al.* reported a highly efficient dehydration of carbohydrates to CMF, HMF and levulinic acid by biphasic continuous flow processing with yields of up to 76 % at shorter reaction times of 5 minutes to 80 minutes depending on substrate and system.[58] Gao *et al.* reported an efficient one-pot synthesis of CMF from carbohydrates in mild biphasic systems with yields up to 47 %.[59] and can be converted to numerous valuable furan moieties by means of oxidation, reduction and aldol additions.[60]

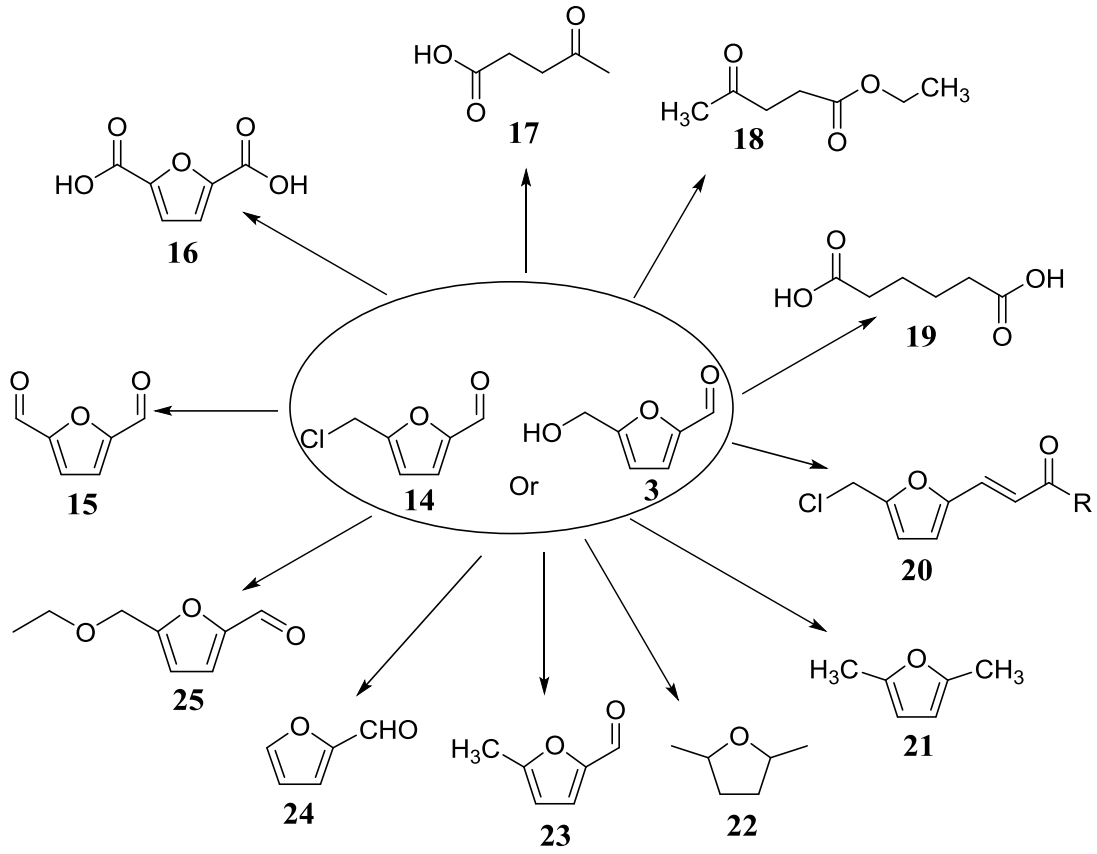

Figure 1.4 Example of some important chemicals obtained from HMF and CMF.

CMF (**14**) can efficiently be converted into HMF (**3)** by hydrolysis in water at 100 ^{o}C. Other top-value added products like levulinic acid (**17)** and ethyl levulinate (**18)** can then be obtained by reaction with water or alcohols at elevated temperatures.[61] (**14)** and **(3)** can also be converted to 5-methylfurfural (**23)** by reaction with hydrogen. (**3)** and **(14)** can also be reduced to 2,5-dimethylfuran (**21)** or 2,5-dimethyltetrahydrofuran (**22)**, both high energy liquids which have been proposed as fuel additives. HMF **3** is also a precursor to the polyester monomer furan-2,5-dicarboxylic acid (**16).**[57] Both (**3**) and (**14**) can also be oxidised to 2,5-diformylfuran (**15**) with higher yields obtained from (**3**) >70 % while up to 54 % yields were obtained from (**14**) under microwave irradiation.[56] (**18**) has used in the manufacture of various intermediates of pharmaceuticals, antifungal agents, organic conductors, cross-linking agents and polymeric materials.[62-64]

1.2.2. Overview of NHCs

1.2.2.1. Carbenes

Carbenes are species containing a neutral carbon atom with two unshared valence electrons having a general formula R=C: or R-(C:)-R'. Most carbenes are very short-lived. Depending upon their electronic structure (electron spin), carbenes are classified as either singlets or triplets. Up until 1960, there were few reports on nitrogen heterocyclic carbenes, perhaps due to the general assumption at the time that carbenes were too reactive to be isolated.[65]

Wanzlick was first to investigate the reactivity and stability of carbenes in 1960s and in 1968 he reported the first application of NHCs as ligands for metal complexes, with a report on the direct synthesis of mercury salt carbene complex.[66-67] Thereafter, surprisingly there wasn't much research reported on nitrogen heterocyclic carbenes until 1991 when Arduengo *et al*. reported the first example of a crystalline nitrogen heterocyclic carbene. The carbene 1,3-di-l-adamantylimidazol-2-ylidene (Figure 1.4), forms colourless crystals with sufficient kinetic and thermodynamic stability to be easily isolated and characterized.[68] The deprotonation of 1,3-di-1-adamantylimidazolium chloride in THF at room temperature in the presence of 1 equivalent of sodium hydride produces the crystalline carbene 1,3-di-l-adamantylimidazol-2-ylidene. The same deprotonation can also be achieved with potassium *tert*-butoxide in THF (Figure 1.4).

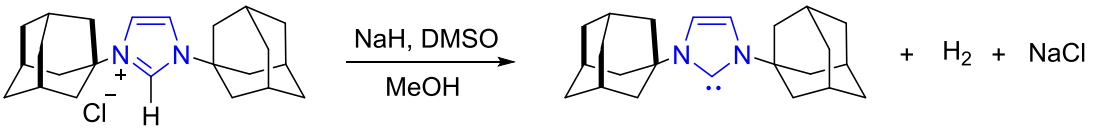

1,3-di-1-adamantylimidazolium chloride 1,3-di-l-adamantylimidazol-2-ylidene

Scheme 1.1 Synthesis of 1,3-di-l-adamantylimidazol-2-ylidene.

1.2.2.2. Nitrogen-heterocyclic carbenes (NHCs)

Nitrogen-heterocyclic carbenes (NHCs) are firmly established as one of the most versatile ligands in a synthetic chemist's toolkit. [69-71] They are electronically and sterically tunable and isolable.[48,72] NHCs are nucleophilic due the lone pair situated in the plane of the heterocyclic ring (Figure 1.5). NHCs are strong σ-donors and weak π-acceptors,[73-75] which in turn increases the electron density around the metal center

and thus improve its catalytic ability.[76-79] The ring size, nitrogen heteroatoms, the ring backbone and nitrogen-substituents affects the stability and reactivity of the NHC. The σ-withdrawing and π-donating effects of the nitrogen heteroatoms help to stabilize the singlet carbene structure (Figure 1.5).[80-83]

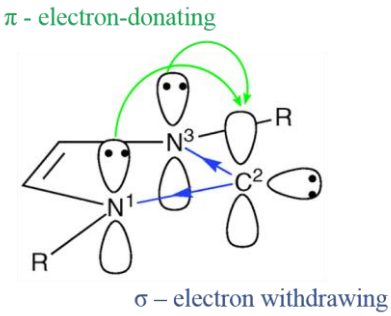

Figure 1.5. π - electron-donating and σ – electron withdrawing illustrations of NHCs.

NHCs have also been extensively used in transition metal catalysis.[66-67] Reactions including but not limited to cross-coupling reactions, olefin metathesis, hydrosilylation, cyanosilylation and hydrogenation have been extensively reported to be catalysed by transition metal NHC complexes.[48, 66] The use of Pd-NHC complexes have been widely reported, example include a recent direct Suzuki–Miyaura cross-coupling of wide range of amides with arylboronic acids in very good yields using commercially available, air- and moisture-stable (NHC)Pd(R-allyl)Cl complexes.[84]

NHCs have been used as organo-catalysts. Organo-catalysed reactions represent an attractive alternative to metal-catalysed (e.g., Pd, Ru and Ni) processes notably because of their lower cost and benign environmental impact in comparison to organometallic catalysis.[85] Grasa *et al.* in 2004, reported efficient protocols for nucleophilic NHC-catalysed transesterification and acylation reactions.[86] In 2007, Marion *et al.* studied the numerous applications of imidazolylidene, imidazolinylidene, triazolylidene, and thiazolylidene in organo-catalysis (Figure 1.6).[87] Their use in condensation, transesterification and acylation reaction has been widely reported. [87]

Figure 1.6. General structures of NHCs used in organo-catalysis.

NHCs have been used as stabilizing ligands. Studies show that some NHC ligands play a key role as stabilising ligands in palladium oxidation reactions (Scheme 1.2).[82]

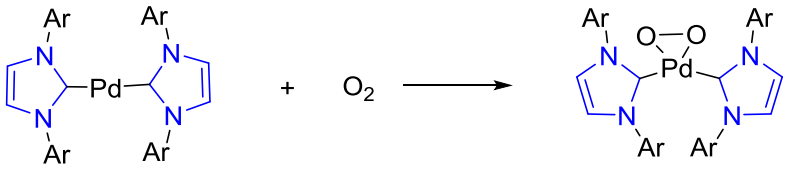

Scheme 1.2 NHCs as stabilizing ligands for Pd oxidation reactions.

An example of this stabilisation effect is seen in the rapid fixation reaction of both O_2 and CO_2 from air to the palladium (0) complex bearing a novel N-heterocyclic carbene [1,3-bis(2,2″,6,6″-tetramethyl-m-terphenyl-5′-yl)imidazol-2-ylidene] abbreviated as ITmt.[88] (Scheme 1.3).

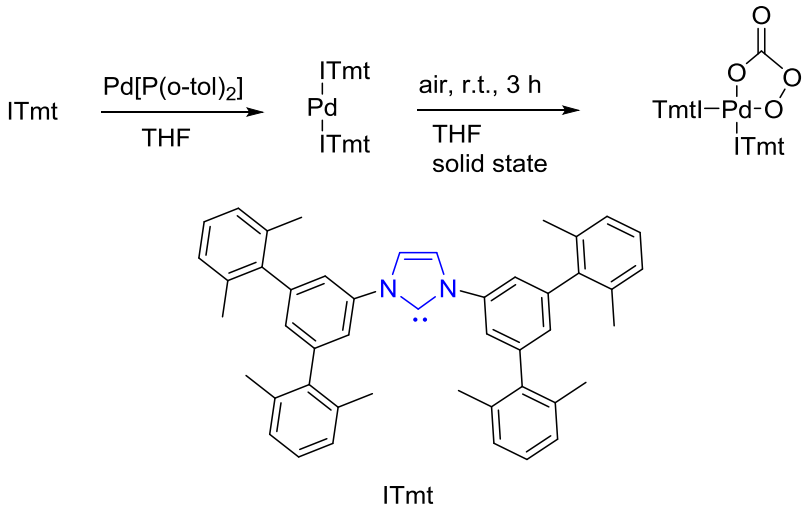

Scheme 1.3 Rapid fixation of O_2 and CO_2 from air by NHC.

NHCs have also been used in biological applications. A recent study conducted by Chen *et al.* on the synthesis, structure, biological evaluation, and catalysis of two pyrazole-functionalized NHC–Ru^{II} complexes, shows that the first complex [RuCl(L1)(*p*-cymene)](PF_6) (where L1 = 1-ethyl-3-(*N*-mesitylimidazolylidenylmethyl)-5-methylpyrazole]), could efficiently inhibit the proliferation of and destroy cancer cells (Figure 1.7).[89]

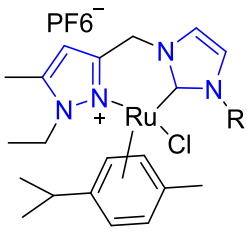

Figure 1.7 Cancer inhibiting NHC-Ru^{II} complex.

Recently, Monticelli *et al.* reported the synthesis, structure and antitumoural activity of triazole-functionalised NHC–metal complexes (Figure 1.8). Ag^{I}, Au^{I} and Ru^{II} complexes with an NHC ligand functionalised in the backbone of the imidazole by a triazole ring were synthesised and their in-vitro antitumor activities were evaluated towards three different human cancer cell lines (prostate, breast and colon cancer). The results confirmed their inhibitory action towards the cancer cells.[90]

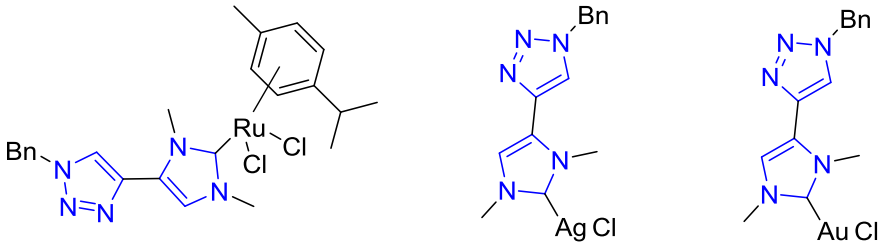

Figure 1.8 Ag^{I}, Au^{I} and Ru^{II} NHC complexes having antitumor activity.

Rieb *et al.* reported on the influence of wing-tip substituents and reaction conditions on the structure, properties and cytotoxicity of Ag(I)– and Au(I)–bis(NHC) complexes, also reported potential of certain NHC complexes towards cancer treatments.[91]

1.2.2.2.1. NHC Ligand synthesis

NHC ligands can be synthesised by *N*-alkylation of existing imidazoles with appropriate ligands.[92] The easiest and most straight forward method to prepare imidazole or imidazolium salts is by direct quaternization of *N*-substituted imidazoles or imidazolines with alkyl or aryl halides.[93-94] Two different approaches can be followed for this type of NHC ligand synthesis; either functionalized alkyl halides are reacted with *N*-substituted imidazoles, or *N*-functionalized imidazoles react with alkyl halides as shown in Scheme 1.4.

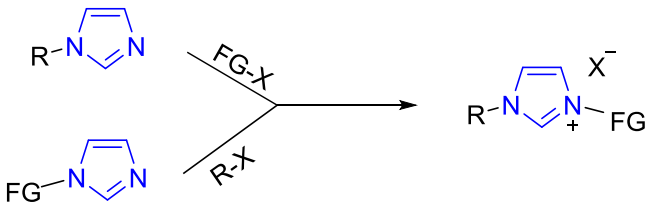

Scheme 1.4. Synthesis of imidazolium salts by direct quaternization of *N*-substituted imidazoles or imidazolines with alkyl or aryl halides.

This method is considered efficient since alkyl halides, can effectively react with various *N*-substituted imidazoles or imidazolines under mild conditions to afford the quaternized products in good to excellent yields. Secondly the isolation of the products from the reaction mixture is relatively easy as the synthesized imidazolium salts usually precipitate from the reaction mixture and can be collected by filtration.

Alternatively, NHC ligands can also be synthesised by building the appropriate NHC ring, using either symmetrical or unsymmetrical *N*-substitution.[82]

Synthesis by symmetrical N-substitution: This can be achieved by the condensation of symmetrical anilines with glyoxal to produce diimines which are then cyclised by chloromethylethyl ether (Scheme 1.5).

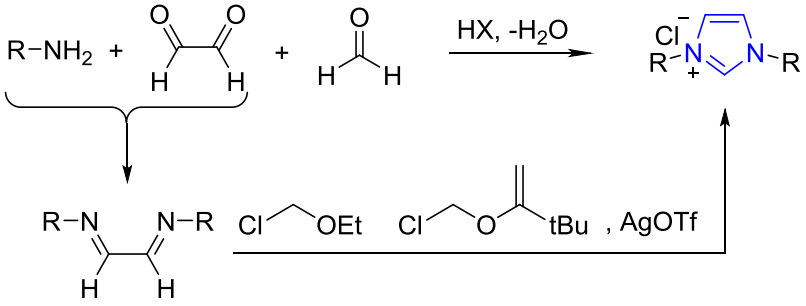

Scheme 1.5. Synthesis of NHCs by symmetrical *N*-substitution.

An example of this symmetrical synthesis of NHC ligands is the acid-catalysed condensation of chiral anilines with glyoxal to produce diimines followed by subsequent cyclization of the diimines with chloromethylethylether producing the corresponding imidazolium chloride (Scheme 1.6).[95]

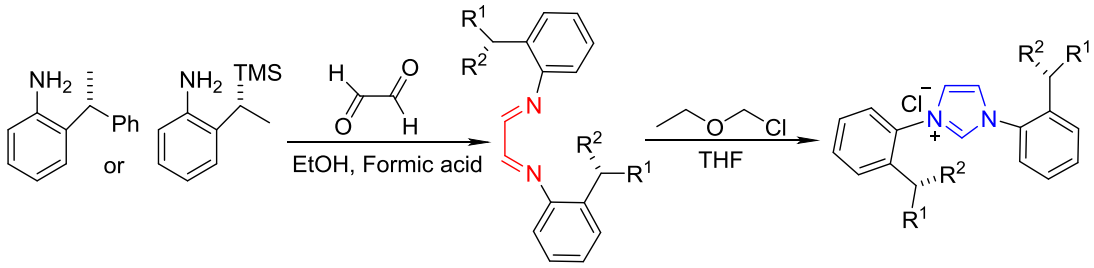

Scheme 1.6. Symmetrical synthesis of imidazolium chloride.

Synthesis by unsymmetrical N-substitution: Unsymmetrical synthesis of NHC ligands can be performed by the halo acid-catalysed condensation of an aniline with glyoxal and formic acid to produce the corresponding imidazolium halide (Scheme 1.7).

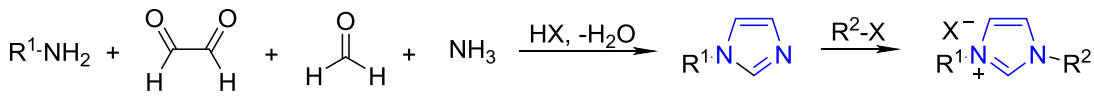

Scheme 1.7 Unsymmetrical synthesis of NHCs.

1.2.2.2.2. NHC Ligand Immobilisation

To immobilize NHCs, three important aspects need to be considered: i. immobilization position; ii. immobilization method, and; iii. the support material.[96]

Immobilisation position: The functionalities introduced during the formation of the NHC moiety usually predetermined the immobilization position. As shown in Figure 1.9 immobilisation may occur via the carbene centre (position c), the C-C bond (position b) or the *N*-centre (position a).

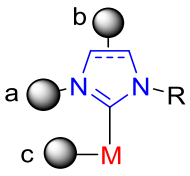

where: a = N-immobilized; b = Backbone immobilized, and; c = Metal immobilized

Figure 1.9 Position of immobilization of NHCs.

Immobilisation methods: Immobilisation can occur via several methods, for example, covalent grafting, non-covalent grafting and 'self-supporting.

Covalent grafting is the most commonly employed method of immobilization of homogeneous NHC catalysts on a support material. It involves the grafting of ligand precursors or metal complexes to a solid support via a covalent bond. The strongest binding between support and NHC species is achieved through this method. The surface of the support material is usually modified with functionality known to react with the functional group on the NHC ligand forming an ether, ester etc. bonds. [96-99] (see Scheme 1.8 to 1.11).

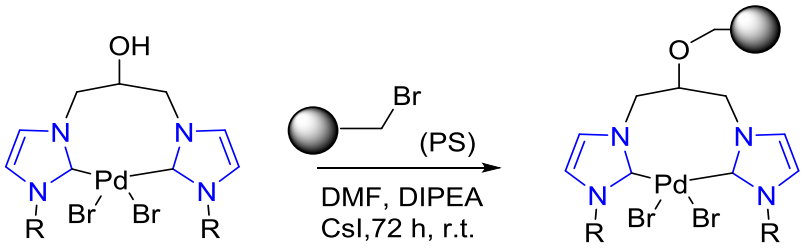

Scheme 1.8 Immobilization of NHC via the formation of ether bond.

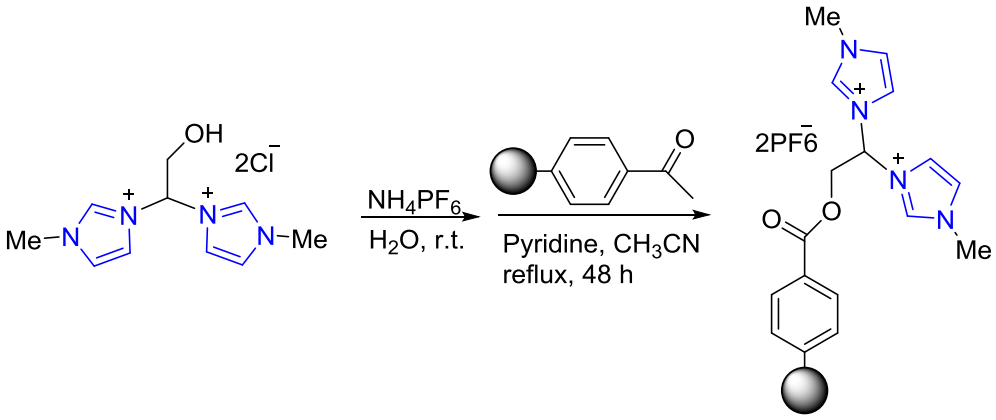

Scheme 1.9 Immobilization of NHC precursor via the formation of ester bond.

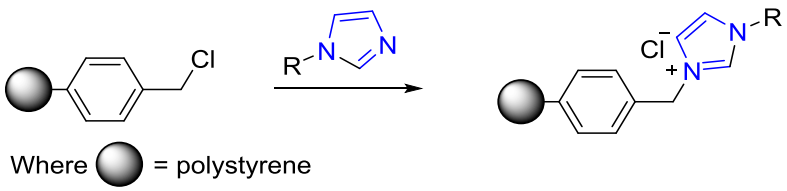

Scheme 1.10 Immobilized NHC precursor on silica via direct quaternization of benzyl chloride modified materials with *N*-substituted imidazoles.

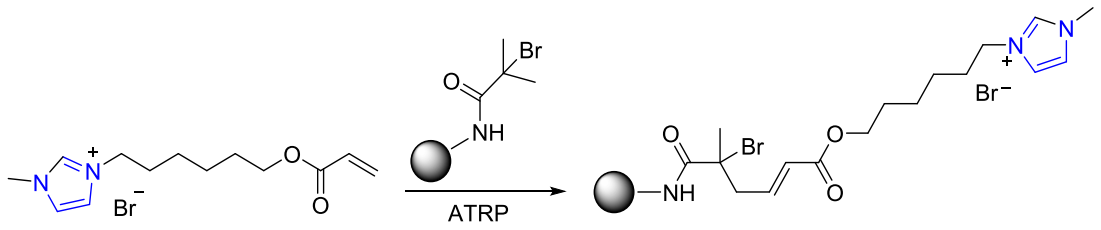

Scheme 1.11 Immobilization of NHC precursor through atom transfer radical polymerisation (ATRP).

Non-covalent grafting involves the immobilization of species including NHC ligands via weaker interactions between the species and the support material. These weaker interactions include; electrostatic interaction, π–π stacking, physical adsorption and entrapment as reported in literature. [100-103] An example of π–π stacking (Figure 1.10) was reported by Lalaoui *et al.* who showed non-covalent immobilization of Os^{II}-NHC-based metallopolymers on carbon-nanotube (CNT) electrodes through the interaction between the Os^{II}-NHC-based metallopolymers and CNTs' sidewalls through π–π interactions.

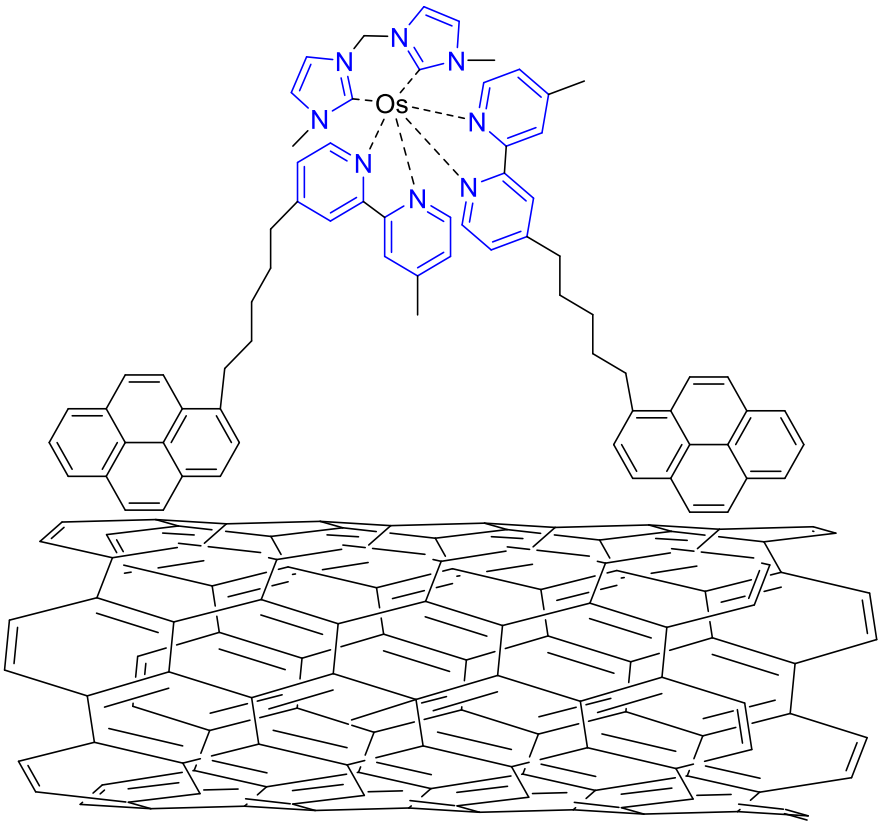

Figure 1.10 Immobilized NHC complex at the surface of π-extended nanostructured electrodes.

"Self-supporting" involves the immobilization of NHC complexes, ligands, and precursors, concomitantly in the construction of the supporting material. "Self-supporting method" is a general term that refers to a process of coordination and self-assembly yielding polymeric functional metal−organic assemblies, where metal atoms are typically coordinated by ditopic or polytopic ligands.[96] As such it is considered that the formation of metal−organic assemblies, organic polymerization,[104] and sol−gel processes are self-supporting methods. With self-supporting method, the density of the catalytically active centres on the support can be tuned easily, and a homogeneous distribution of the reactive centres is ensured.

Support material: Taking into consideration the type of support material used for NHCs immobilization, silica-based materials and organic polymers are the two most widely employed solid supports for NHC compounds.[105-111] However, carbon-based materials (i.e. carbon nanotubes, graphene oxide), as well as coordination polymers and metal-organic frame works are also used as supports in a certain number of examples.[96, 112] An example is the polymer-supported NHC prepared from chloromethyl polystyrene resin (CM PS, Scheme 1.12) resin used as the ligand for palladium (Pd) catalyzed Suzuki cross-coupling of aryl halides and phenylboronic acid in good yields and excellent purities under aqueous conditions.[113]

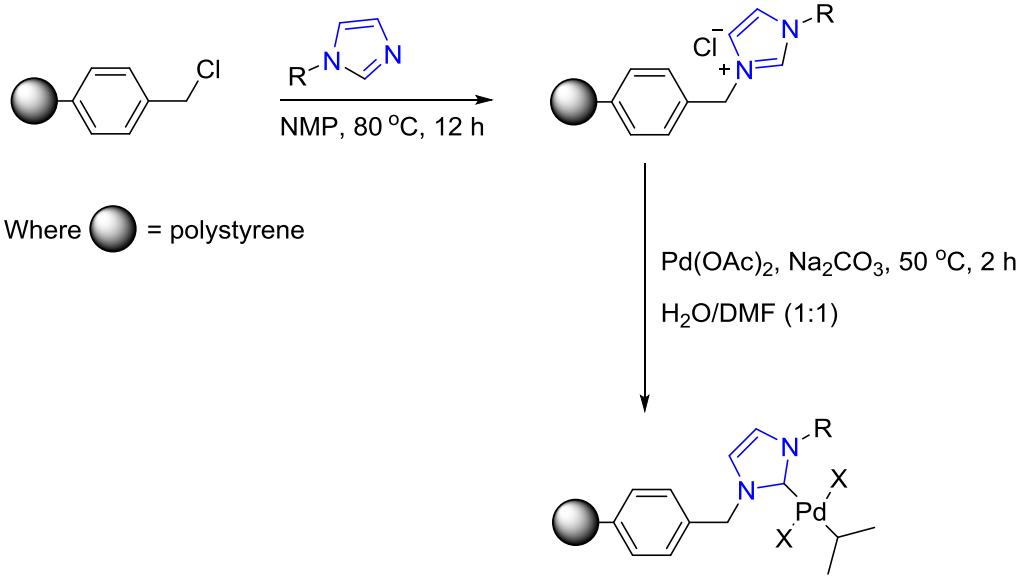

Scheme 1.12 Polymer-supported N-heterocyclic carbene prepared from chloromethyl polystyrene (CM PS) resin.

1.2.2.3. Fe-Nitrogen Heterocyclic Carbenes (Fe-NHCs)

Fe-NHCs are highly resistant towards decomposition, as a result of the NHCs strong σ-electron-donating ability which makes them form strong bonds with metal centers.[114] Significant studies have been conducted on Fe-NHCs as homogeneous catalysts.[115, 69, 77] However, the catalyst post reaction makes it difficult to isolate for reuse. The immobilization of Fe-NHCs onto heterogeneous supports represent an exciting approach for sustained catalytic use. While most of the NHCs systems use ruthenium[116] or palladium as metal centers,[74, 75, 117-120] our approach prefers the more abundant, cheap and environmentally benign Fe as metal center. Recent research shows that, using a bulky *N*-alkyl substituted group on the heterocyclic carbene enhances the catalytic activity of the NHCs.[121-125] As such *N*-mesityl substituted imidazolium was synthesized for the fabrication of the Fe-NHC catalyst. Recently however, apart from catalysis, the use of Fe-NHCs as promising photosensitizers has also been reported.[126]

The early approach to the synthesis of Fe-NHCs involved reacting an Fe-carbonyl complex with an imidazolium salt to produce the respective Fe-NHC. In 1969, Öfele reported the first Fe-NHC complex synthesized from $K[FeH(CO)_4]$ and 1,3-dimethylimidazolium iodide.[127]

Cardoso *et al*. reported a direct synthesis of bidentate cyclopentadienyl-functionalised NHC–iron(II) complexes by using imidazolium salts and commercially available $Fe_3(CO)_{12}$ (Scheme 1.13).[128]

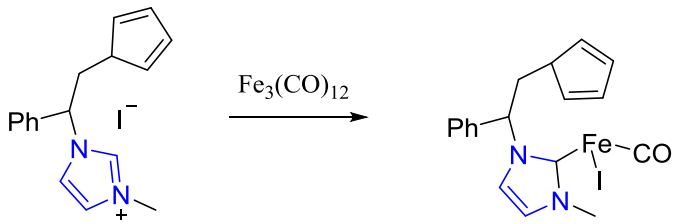

Scheme 1.13 Synthesis of $Fe(NHC)(CO)_4$ from iron carbonyl complex.

Recently, Warratz *et al*. reported $Fe(NHC)(CO)_4$ complexes formed by direct reaction of $Fe_3(CO)_{12}$ with equimolecular amounts of NHC imidazolium halide precursors (Scheme 1.14).[129]

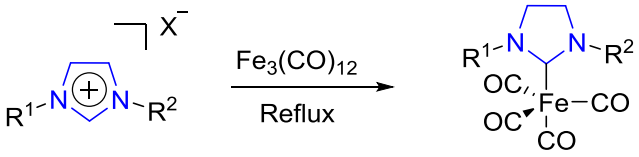

Scheme 1.14 Synthesis of $Fe(NHC)(CO)_4$ from iron carbonyl complex.

The addition of an iron halide to a free carbene marked a breakthrough in Fe-NHC synthesis initially adopted by Fehlhammer *et al*. which involves the deprotonation of the respective imidazolium salt by an external base prior to the addition of an Fe-halide.[130] However, this route is used for synthesis of a homogeneous Fe-NHC complex. To synthesise a heterogeneous Fe-NHC complex, as in our own case, we use a technique that involves the immobilisation of the imidazolium ligand onto a solid mesoporous support. The immobilised imidazolium was then deprotonated by a base prior to the addition of $FeCl_3$ giving the desired immobilised Fe-NHC complex (see Scheme 1.21).

A similar approach was employed by Kim *et al*.[48] to synthesise a polystyrene supported Fe-NHC prepared from chloromethyl polystyrene resin via two-step reaction (Scheme 1.15). Metals were loaded into 1.6 – 16 mol % of total imidazolium with the remaining imidazolium chloride salt providing ionic liquid moiety. The catalyst was used for dehydration of fructose to HMF with yields up to 70% in 3 hours reaction time.[48]

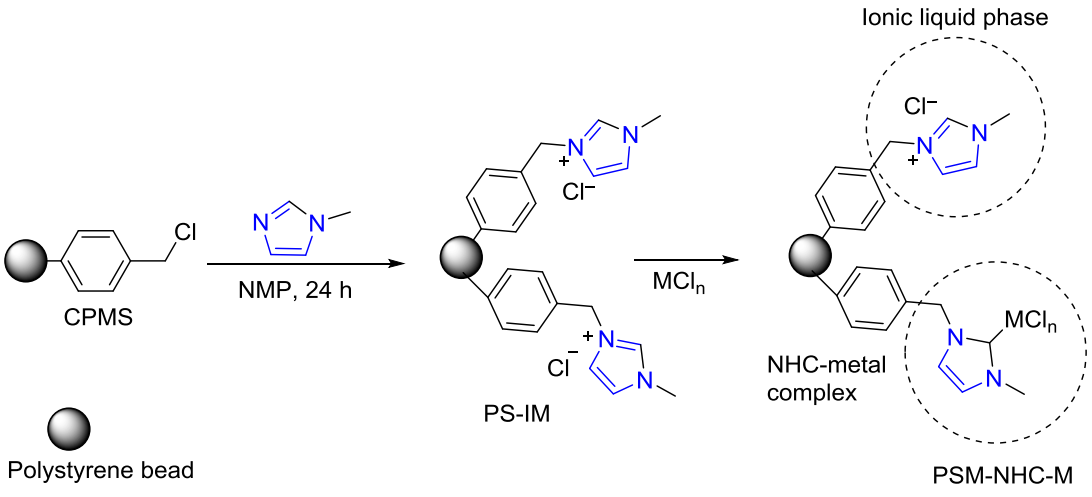

Scheme 1.15 Synthetic route to polystyrene supported NHC-metal complex.

1.2.2.3.1. Applications of Fe-NHCs

Dehydration reactions: Fe-NHCs have recently been utilized as catalysts for the catalytic dehydration of fructose to HMF.[131-132] Kim *et al.* recently reported the dehydration of fructose to HMF using an Fe-NHC supported on polystyrene beads. in which a 73 % HMF yield was obtained.[48]

Hydroxylation of arenes: Recently the mechanism of the hydroxylation of benzene by an iron(II) bis(NHC) complex, $[Fe^{II}(NCCN)(CH_3CN)_2]$ $(PF_6)_2$ (1; NCCN = bis(o-imidazol-2-ylidenepyridine) methane), in the presence of hydrogen peroxide was investigated. The aromatic hydroxylation reaction was proposed to proceed via an iron-arene σ-complex as intermediate species (Scheme 1.16).[133]

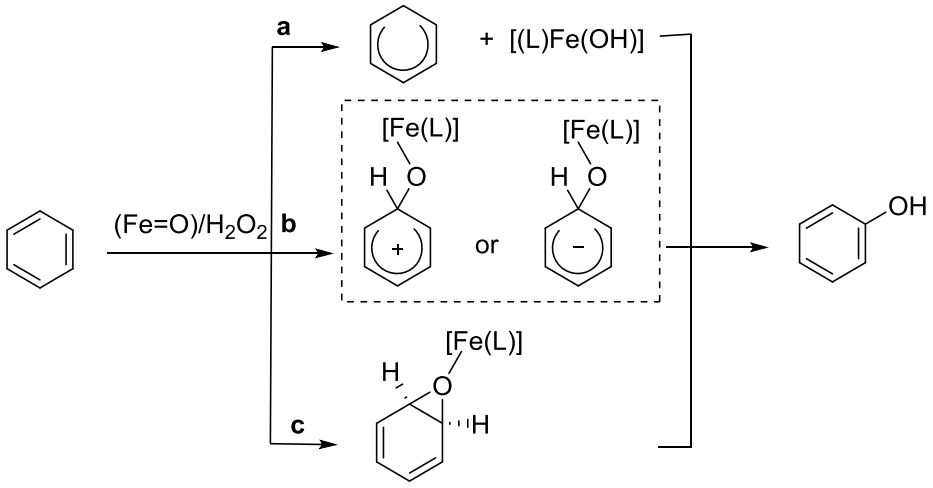

Scheme 1.16 Hydroxylation of arenes an iron(II) bis(NHC) complex.

C-C bond formation reactions: Diverse types of carbon-carbon bond formation using Fe-NHC as catalytic systems has been studied. Fe-NHCs were found to be effective in various type of C-C bond formation including the Kumada, Suzuki and Negishi type cross coupling reaction.[134-135, 127] An example is a novel Fe-NHC catalytic system that allows for the Kumada type alkyl–alkyl cross-coupling reaction of alkyl halides and alkylmagnesium reagents (Scheme 1.17).[136]

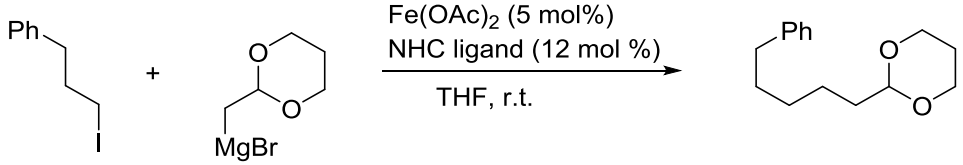

Scheme 1.17 Homogeneous Fe-NHC for Kumada type cross-coupling.

Reduction reactions: Selective reduction is one of the major challenges in synthetic chemistry. Fe-NHCs were found to be effective in certain selective reduction reactions. Several application of Fe-NHCs were found in hydrosilylation of ketones, imines and sulfoxides, transfer hydrogenation, and hydrogenation reactions.[127] An example of this is the work reported by Warratz *et al.* on the hydrosilylation of benzaldehyde and its derivatives catalysed by $Fe(IMes)(CO)_4$ (Scheme 1.18).[129]

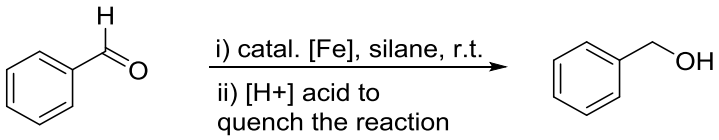

Scheme 1.18. Hydrosilylation of benzaldehyde and derivatives catalysed by $Fe(IMes)(CO)_4$.

Polymerisation reactions: Diverse types of Fe-NHCs were found to effectively catalyse polymerisation reaction. Applications were found in both atom radical transfer polymerisation (ARTP) and ring opening polymerisation.[65, 137] in 2000, Grubbs *et al.* reported an Fe-NHC catalysed Atom Radical Transfer Polymerization (ATRP) of olefins (Scheme 1.19).[138]

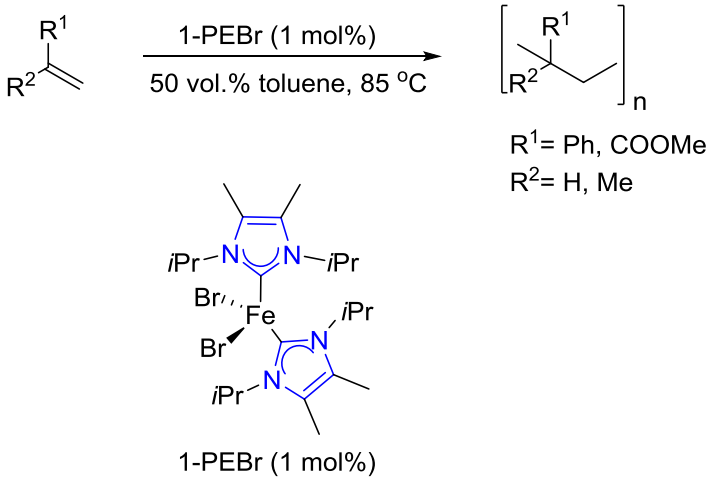

Scheme 1.19. Fe-NHC catalysed atom radical transfer polymerization (ATRP) of olefins.

In 2006, Shen *et al*. reported NHC complexes of Fe(II) and their catalytic activity for ring-opening polymerization of ε-caprolactone.[139] They used a synthesise bis-ligand Fe(II) complex (Scheme 1.20) to catalyse ring-opening polymerisation reaction of ε -caprolactone achieving 100% monomer conversion.[140]

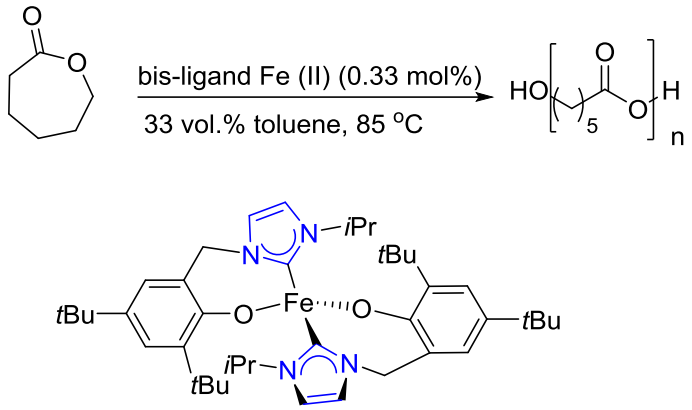

Scheme 1.20. Fe-NHC catalysed ring-opening polymerisation reaction of ε -caprolactone.

As photosensitizers: Recently the work of Liu *et al.* on the photophysics and photochemistry of transition metal complexes, utilizes strongly σ-donating *N*-heterocyclic carbene (NHC) ligands to make strong-field $Fe^{II}L$ complexes with significantly extended triplet metal to ligand charge transfer (^{3}MLCT) lifetimes that serves as promising photosensitizers.[126] This study opens up the possibility of developing solar energy-converting materials from Fe-NHCs. Figure 1.11 shows examples of three prototypical $Fe^{II}L_6$ complexes.

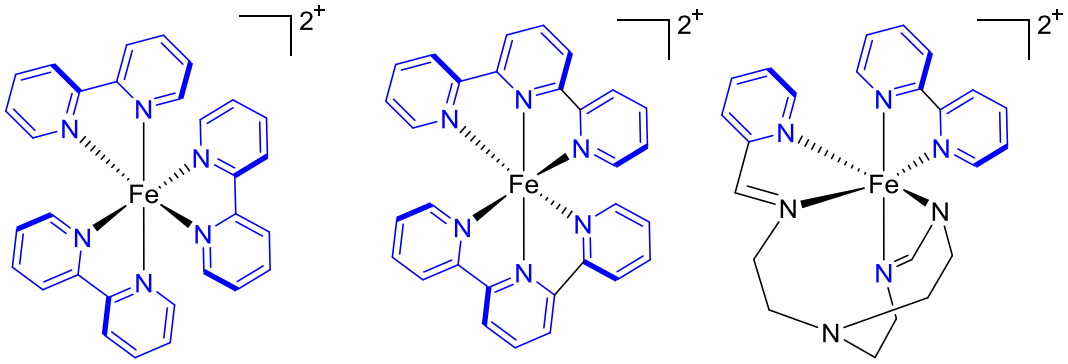

Figure 1.11. Strong-field $Fe^{II}L_6$ complexes with significantly extended ^{3}MLCT.

1.2.3. Objectives

Thus, the objectives of this research are to:

1. Synthesise a range of novel Fe-NHC catalysts (Scheme 1) immobilized on renewable supports (expanded high amylose corn starch, Starbon™ 350, Starbon 400, mango peel cellulose and orange peel cellulose) as outlined in scheme 1.21. A convergent strategy will be used starting with the appropriate renewable resource support, e.g., (**4a**-**e**) and 1-(3-aminopropyl) imidazole (**7**) to afford the precursor nitrogen heterocyclic carbene, e.g., (**13a**-**e**), which will be treated with $FeCl_3$ to furnish the desired Fe-NHC, e.g., (**1a**-**e**). Scheme 1.21 is adapted from Kim *et al*.[48] who used non-*green* solvents (DCM, chloroform) in their synthesis of Fe-NHC's. In our proposed strategy we have replaced these with *greener* solvents (propylene carbonate and CPME) in order to partly adhere with Principle 5 (Safer solvents and Auxillaries) – partly because the synthetic strategy still uses many auxillaries to achieve its intended aim).

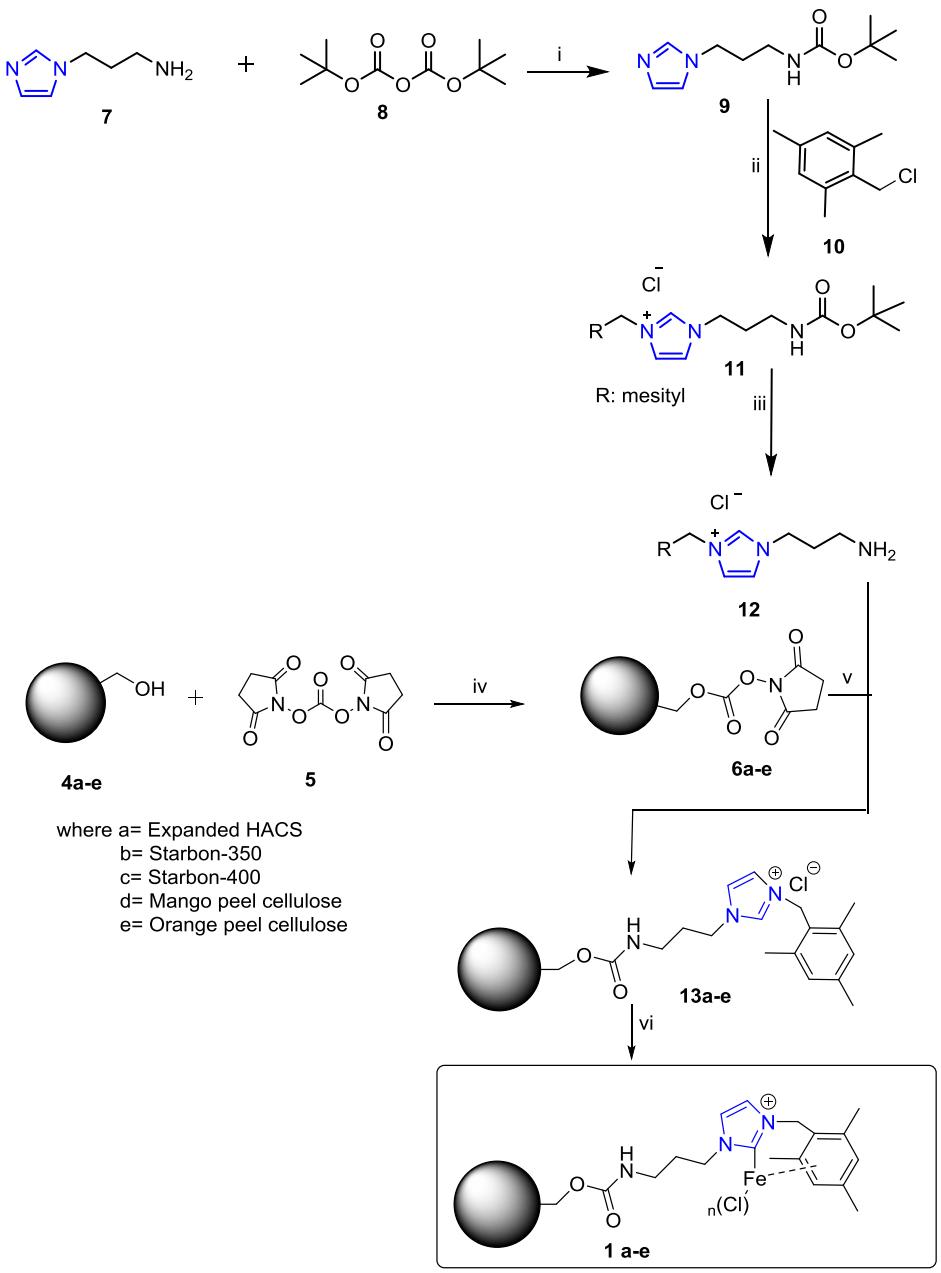

Reaction conditions and reagents: i) $NaHCO_3$,CPME, 25°C, 4 h; ii) CPME, 80°C, 18 h; iii) MeOH, TFA,50 °C, 6 h; iv) DMAP, propylene carbonate, 80 °C, 18 h; v) TEA, propylene carbonate, 80 °C, 18 h; vi) K^{t}OBu, $FeCl_3$, propylene carbonate, 80 °C, 18 h.

Scheme 1.21. Convergent synthesis of Fe-NHCs (**1a-e**) immobilised on renewable supports (**4a-e**)

The support material is a critical aspect in heterogeneous catalysis.[141] Functional mesoporous materials provide many opportunities in a wide variety of fields including catalysis.[142] Mesoporous solids present advantages with respect to conventional porous solids when they are used as catalyst supports, due to their high surface area, large pore size and thermal and hydrothermal stabilities.[38, 143-144] In this research

expanded high amylose corn starch, Starbon™ 350, Starbon™ 400, mango peel cellulose and orange peel cellulose will be exploited.

Expanded High Amylose Corn Starch: Starch is one of Nature's three biggest products, the other two being cellulose and chitin. Starch is an inexpensive commodity that has been used for food and many non-food purposes for centuries.[145-147] Starch is biodegradable, abundant and a renewable resource. [148-151]

Lots of various chemical modifications can be conducted on starch due to their inherently abundant hydroxyl groups.[152] However, the accessibility of the hydroxyl groups is limited due to the low surface area of native starch (<1 m^2 g^{-1}). It has been reported that the surface area of native starch could be dramatically increased to around 180 m^2 g^{-1}, via a process known as expansion which involves three steps: i. gelatinization; ii. retrogradation, and; iii. solvent exchange, yielding expanded starch.[153] This process of expansion significantly increases the accessibility of the hydroxyl groups and therefore makes expanded starch a cheap, abundant and bio-renewable support for heterogeneous catalysis.

Starbons™: The Clark group has developed a range of mesoporous carbonaceous materials derived from waste polysaccharides termed Starbon™, possessing large surface areas ranging from 150 up to 500 m^2 g^{-1} obtained via controlled pyrolysis of expanded polysaccharide precursors (Figure 1.12).[153] The large surface area and mesoporous nature of Starbon™ in addition to its thermal stability makes it an important and efficient support for heterogeneous catalysis.

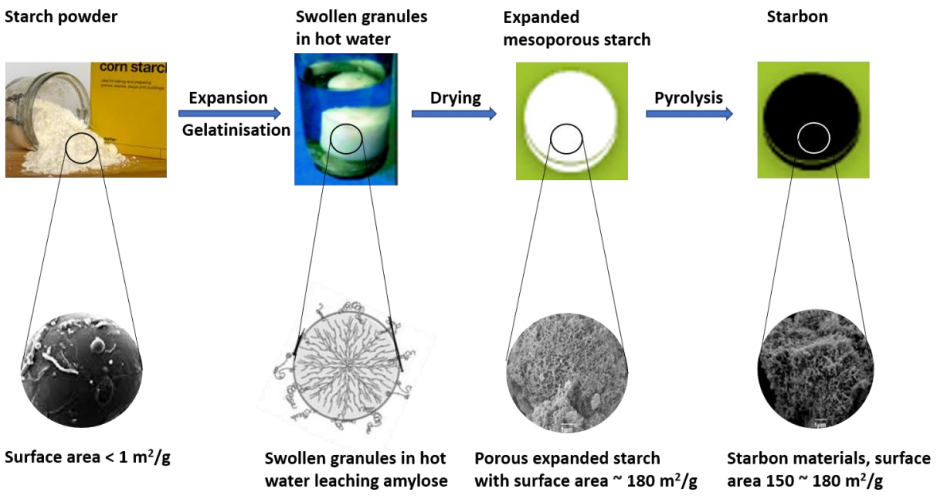

Figure 1.12. Production of Starbon™ through controllable pyrolysis of expanded starch.

Orange and mango peel cellulose: Orange peels and mango peels are byproducts of orange and mango processing industries, respectively. There is an estimated 70 million tonnes of citrus crop of which 60-70% are sweet oranges used mostly for juice production.[154,155] This leads to about 50 % of their total mass as waste that constitutes peels, pulp (juice sac residue), rag (membranes and cores residue) and seeds.[156] For mango there is an estimated 40 million tonnes production and the number is on the rise.[157,158] Asian countries produce the largest volumes of mangoes worldwide with India as the world's largest producer by a wide margin, with more than 40% of global production in 2013.[158] Similar to oranges, the processing of mangoes produced a lot of waste in the form of peels and seeds.

Matharu *et al.* have recently reported mesoporous cellulose from mango peels[159] and nanocellulose from depectinated orange peels.[160] The availability of these materials in the GCCE warranted their use as a potential renewable support. Cellulose is the most abundant natural polymer in nature.[161] Cellulose is a homopolymer composed of D-glucopyranose units linked by β-(1 → 4) glycosidic bonds (Figure 1.13).[162]

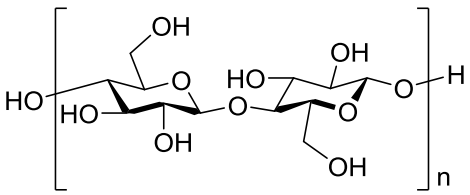

Figure 1.13 D-glucopyranose units linked by β (1 → 4) glycosidic bonds

Most cellulosic materials consist of crystalline and amorphous domains, in varying proportions, depending on the process of extraction/isolation. The physical properties of cellulose, as well as their chemical behaviour and reactivity, are strongly influenced by the arrangement of the cellulose molecules with respect to each other and to the fiber axis, as well.[163] Native cellulose (cellulose I) occurs in two forms: Iα (triclinic) and Iβ (monoclinic). The Iα phase contains a single cellulose chain in a triclinic cell, while a two-chain monoclinic cell is found for Iβ. The relative ratio of the two forms depends on the origins of the cellulose.[164]

The low density and high specific surface area of porous cellulose coupled with its favourable properties including biodegradability, non-toxicity, low cost, and easy

modification has made it to have various applications, such as separation, filtration, and load-bearing.[165] Due to its porosity, relatively chemical and mechanical stability, mesoporous cellulose presents an interesting and cheap bio-renewable support for heterogeneous catalysis. This is because in any chemical reaction, the accessibility of reactant molecules to the catalytically active site is highly important in the process and efficiency of the conversion. Therefore, the mesoporous orange and mango peel cellulose were chosen for the fabrication of the catalyst. The network of pores will facilitate the diffusion of the reactants to the active Fe catalytic sites located on the immobilised Fe-NHC ligand.

2. Fully characterize the synthesized Fe-NHCs (**1a-e**) using a diverse range of complementary analytical techniques: FT-IR (detection of functional groups) solid state ^{13}C CPMAS NMR spectroscopy (minimum number of carbons, carbon framework and surrounding environment), liquid NMR spectroscopy (^{1}H & ^{13}C) (C-H framework), X-ray photoelectron spectroscopy (chemical state and electronic state of the elements within a material – direct evidence for C, O, N and Fe), Mössbauer spectroscopy (chemical, structural, magnetic and time-dependent properties of a material – direct evidence for iron), ICP-MS (elemental composition - direct evidence for iron), thermogravimetric analysis (mass loss versus decomposition - evidence of structural changes in the renewable support upon modification and indirect evidence for iron), scanning electron microscopy and transmission electron microscopy (image the surface of the material and to *observe* porosity), nitrogen adsorption porosimetry (to evidence mesoporosity) and CHN elemental analysis (evidence for nitrogen incorporation).

3. Utilize the fabricated Fe-NHCs (**1a-e**) as potential heterogeneous catalysts for the dehydration of fructose (**2**) (and glucose) to HMF in order to determine their efficacy (conversion, selectivity, kinetics, turnover frequency (TOF), catalytic cycling).

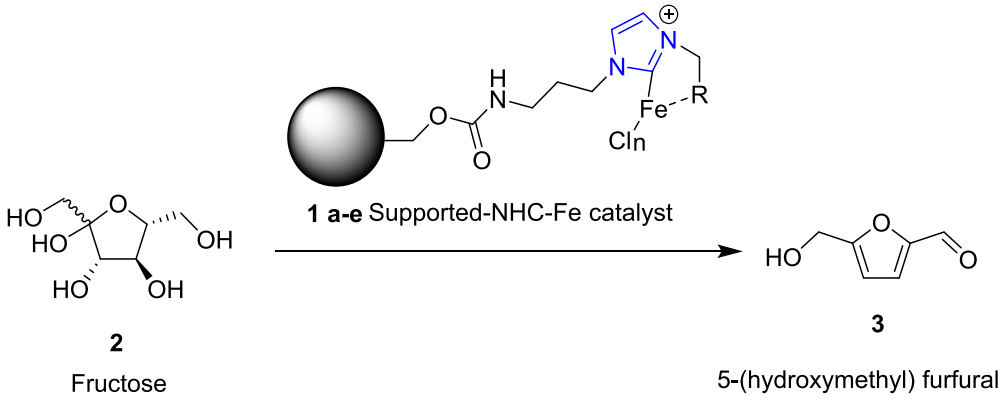

Scheme 1.22. Fructose dehydration to 5-hydroxymethyl furfural using Fe-NHC

4. Apply the catalyst towards glucose dehydration to HMF which still remains the stumbling block towards the successful and efficient valorization of lignocellulosic biomass.[166] The advantages of glucose as a substrate over fructose is due to the low cost and abundance of glucose when compared to fructose. However, the difficult step towards the conversion of glucose into 5-HMF is its isomerization to fructose prior to dehydration. As such a comprehensive understanding of effective solvent system and catalyst characteristics, e.g., active species, active sites, pore size, and surface area, are critical to ensure a high-performance heterogeneous catalyst for glucose dehydration system to HMF. Research shows that Lewis acids (e.g. $AlCl_3$, $CrCl_3$, and Sn-beta) promote isomerization of glucose to fructose.[167]

5. Preliminary investigate the use of Fe-NHCs (**1a-e**) in the synthesis of 5-(chloromethyl) furfural (CMF) (**14**) from glucose and fructose using the immobilized Fe-NHC catalyst (**1b**) and aqueous HCl as the source of the chlorine.

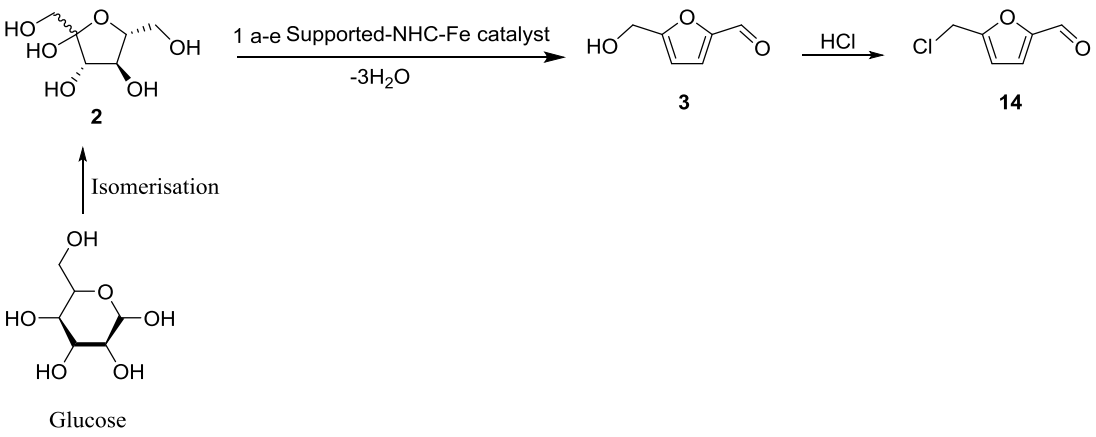

Scheme 1.23 Glucose and fructose dehydration to 5-(chloromethyl)furfural using Fe-NHC.

CHAPTER 2. EXPERIMENTAL

2.1. REAGENTS and MATERIALS

Ethanol, acetone, 1-(3-aminopropyl) imidazole (97%), di-*tert*-butyl dicarbonate, sodium bicarbonate, mesityl chloride (98%), *N,N'*-disuccinimidyl carbonate (purum, ≥95.0%) (DSC), propylene carbonate (99%), potassium *tert*-butoxide (reagent grade, ≥98%), ($KOBu^t$), 4-*N*,*N*'-dimethylaminopyridine (DMAP), ferric chloride anhydrous ($FeCl_3$), triethylamine (anhydrous, ≥ 99.9 %) (TEA), and cyclopentyl methyl ether (anhydrous, ≥ 99.9 %) (CPME), were purchased from Sigma Aldrich, UK (now known as Merck). All other reagents and solvents were used as received without further purification. Expanded HACS and Starbon^{TM} 350 & 400 were obtained from the Green Chemistry Centre, University of York and used as received. Oranges and mangos were purchased from Aldi, York, UK.

2.2. CHARACTERISATION TECHNIQUES

2.2.1. ATR-FTIR

Fourier transform-infrared spectroscopy was conducted on a Bruker Vertex 70 FT-IR/ATR spectrometer. All the spectra were recorded in attenuated total reflectance (ATR) mode, using a resolution of 2 cm^{-1} and 64 scans each for background and sample.

2.2.2. Solid-state ^{13}C CPMAS

Solid-state ^{13}C CPMAS spectra were acquired using a 400 MHz Bruker Avance III HD spectrometer equipped with a Bruker 4 mm H(F)/X/Y triple-resonance probe and 9.4 T Ascend® superconducting magnet. The CP experiments employed a 1 ms linearly-ramped contact pulse, spinning rates of 12000 ± 2 Hz, optimized recycle delays of 7 seconds, spinal-64 heteronuclear decoupling (at ν_{rf}=85 kHz) and are a sum of 600 co-added transients. Chemical shifts are reported with respect to TMS and were referenced using adamantane (29.5 ppm) as an external secondary reference.

2.2.3. X-ray photoelectron spectroscopy (XPS)

XPS measurements were performed on the compressed pellets of powdered orange peel cellulose, mango peel cellulose and expanded HACS before and after modification to detect the presence and state of the coordinated Fe using a VG Escalab

250 EPS instrument equipped with a high intensity monochromated Al Ka source focused to a spot 120-600 μm in diameter on the sample.

The pellets were prepared using a KBr press. However, for the Starbon™ 350 and 400 samples, the powder samples did not compress into suitable pellets and as such the powdered samples were dispersed on XPS-suitable carbon tape before analysis. The XPS experiments were conducted at room temperature with a base pressure of 9−10 mbar. The monochromatic Al K X-ray source was operated at 300 W (15 kV, 20 mA). Quantitative and qualitative XPS analyses were performed with CasaXPS software (version 2.3.16PR1.6). The atomic concentrations were calculated from the photoelectron peak areas by using Gaussian–Lorentzian deconvolution. The carbon 1s spectra were resolved into different contributions of bonded carbon, namely carbon without oxygen bonds (C–C), carbon with one oxygen bond (C–O), carbon with two oxygen bonds (O–C–O) and carbon with double bond oxygen (C=O). The chemical shifts were taken from the literature and the spectra were charge-corrected by setting the carbon-without-oxygen-bond contribution in the C1s emission at 284.5 eV.

2.2.4. Thermogravimetric Analysis (TGA)

Thermogravimetric analysis (TGA) was performed on the expanded HACS, Starbon™ 350 and 400 samples using Netzsch STA 409 instrument at scan rates of 10 ^{o}C min^{-1}, with typically 20 mg sample under flowing N_2 and subsequently air at 100 mL min^{-1}.

For the mango and orange peel cellulosic samples, thermogravimetric analysis (TGA) was performed using Stanton Redcroft STA 625 at heating rates of 20 ^{o}C min^{-1} to 600 ^{o}C, with typically 10 mg sample under a flowing N_2 purge at 50 mL min^{-1}.

2.2.5. Scanning & Transmission Electron Microscopy (SEM & TEM)

SEM and TEM were conducted on all the modified and unmodified samples with the assistance of Dr Meg Stark from the Department of Biology, University of York. SEM studies were performed on a JEOL JSM-6490LV scanning electron microscope with 5 kV scanning electron microscope. Samples were put on SEM stubs and coated with gold and palladium prior to analysis.

TEM studies were conducted on a Tecnai 12 BioTWIN instrument equipped with a field emission gun operated at 120 kV, with a SIS megaview 3 camera using A 200 mesh copper grid with pioloform coating.

2.2.6. N_2 Porosimetry

N_2 porosimetry were carried out at 77 K using a Tristar volumetric adsorption analyser from Micromeritics, and Micromeritics ASAP 2020 surface area and porosity analyzer. All samples were degassed at 120 ^oC under nitrogen flow (100 mL min^{-1}.) for 4 h prior to recording measurements. Degassing is necessary to remove vapours and gases which may have adsorbed onto the surface from the ambient air. Without this, the surface area result can be low and non-reproducible since an indeterminate amount of the surface will be covered by the vapours or gases. The surface area of the samples was calculated directly by the system software using Brunauer-Emmett-Teller (BET) surface area equation (Eq. 1), while the pore size and pore volume of the samples were obtained from Barrett-Joyner-Halenda (BJH) pore size and volume analysis.

$$\frac{1}{v\left[\left(\frac{p_o}{p}\right)-1\right]} = \frac{c-1}{v_m\, c}\left(\frac{p}{p_o}\right) + \frac{1}{v_m\, c} \ldots\ldots\ldots\ldots\ldots (Eq.\,1)$$

The BET equation was plotted as an adsorption isotherm typically at a relative pressure (P/P0) between 0.05-0.35. According to the BET theory this plot should form a straight line. Using which the following are calculated;

a. Slope (S g cm^{-3} STP)
b. Y-intercept (Y_{INT} g cm^{-3} STP)
c. Error of the slope (S_{ERR} g cm^{-3} STP)
d. Error of y-intercept (YI_{ERR} g cm^{-3} STP)
e. Correlation coefficient (Cc)

Where (p) and (p0) are the equilibrium and the saturation pressure of adsorbates at the temperature of adsorption, v is the adsorbed gas quantity (in volume units), v_m is monolayer adsorbed gas quantity, and c is the BET constant.

$$\text{Where } v_m = \frac{1}{gradient - intercept}$$

$$and \quad C = \frac{S + Y_{INT}}{Y_{INT}} \; or \; 1 + \frac{gradient}{intercept}$$

The surface area was calculated using the molecular cross-sectional area.

$$S_{total} = \frac{v_m \, Ns}{V}$$

Where *N* is Avogadro's number, *s* is the adsorption cross section of the adsorbing species, and *V* the molar volume of the adsorbate gas. The exact form of this equation will vary depending on the units being used.

For ASAP2020 analyser the BET surface area (m^2 g^{-1}) is calculated using the BET equation (Eq.2).

$$SA_{BET} = \frac{CSA \; X \; (6.023 \; X \; 10^{23})}{(22414 \; cm^3 \;\; STP) \; X \; (10^{18} \; nm^2 \; / \; m^2) \; X \; (S + Y_{INT})} \; \ldots\ldots\ldots\ldots\ldots (Eq. 2)$$

Where *CSA* = analysis gas molecular cross-sectional area (nm^2), (value entered on the Adsorptive properties dialog box).

Volume of N_2 monolayer (cm^3 g^{-1} STP) was calculated as;

$$v_m = \frac{1}{C \; X \; Y_{INT}} = \frac{1}{S + Y_{INT}}$$

$$\text{where } \; C = \frac{S + Y_{INT}}{Y_{INT}}$$

Where as the Error of BET surface area (m^2 g^{-1}) was calculated as;

$$BET_{ERR} = \frac{SA_{BET} \; X \; \left(S_{ERR}^2 + YI_{ERR}^2\right)^{0.5}}{Y_{INT} + S}$$

BJH analysis determine pore area and specific pore volume using adsorption and desorption techniques. This technique characterises pore size distribution independent of external area due to particle size of the sample.

2.2.7. CHN and ICP-MS elemental analysis

Inductively Coupled Plasma-Mass Spectroscopy (ICP-MS)

The loading level of Fe in the fabricated Fe-NHC catalyst (**1a-e**) was determined using an Agilent 7700x instrument fitted with standard Ni sample and skimmer cones and

coupled to a Mass Spectrometer (MS). The samples were run in He mode. The sample introduction line was rinsed for 60 s between samples using 5% HCl and 2% HNO_3 (30 s with each compound). Typically 50 mg of the sample was digested in 10 mL aqua regia (HNO_3 : 3 HCl) solution at 80 ^oC. The digested sample was treated with ultrapure deionized water (20 mL), filtered and the filtrate was subjected for ICP analysis.

CHN analysis

CHN analysis were conducted by Dr Graeme McAllistair, Department of Chemistry, University of York using Heraeus Megafuge 40R CHN analyser from Thermoscientific. Measurements were conducted in duplicate and the mean is reported.

2.2.8. High Performance liquid chromatography (HPLC)

High Performance liquid chromatography (HPLC) was conducted to determine degree of fructose conversion using Aminax HPX-87H ion exclusion column (300 mm x 7.8 mm) with a 0.005 M H_2SO_4 solution as eluent at a flow rate of 0.6 mL min^{-1}. C18 standard column was also used with 25:75 % MeCN: H_2O solution as eluent at a flow rate of 0.8 mL min^{-1}.

$$\text{Sugar conversion } C = \frac{[sugar]_i - [sugar]_f}{[sugar]_i} X\ 100$$

$$\text{HMF selectivity } S = \frac{[HMF]_f}{[sugar]_i - [sugar]_f} X\ 100$$

Whereas the HMF yield was calculated from the peak arear using internal standard employed.

2.3. PROCEDURES

2.3.1. Microwave assisted hydrothermal extraction of cellulose from Orange and Mango peels

Fresh wet mango and orange peels were milled (<5 mm) in blender, and the milled peels were soaked in warm ethanol at 60 ^oC (50 mL) and subsequently washed with deionized water (4 x 100 mL) before microwave heating (3 g per vessel at a temperature of 180 ^oC for 10 minutes at a peel to water ratio of 1:20, high stirring, 300

W). Post the microwave extraction the solid residue was isolated by filtration and washed with ethanol (3 x 200 mL), acetone (3 x 200 mL) and dried in a vacuum oven at 70 ^{o}C to afford the desired orange and mango cellulose as an off-white solid with yield of 36 % and 33 %, respectively.

2.3.2. Convergent synthesis of immobilized Fe-NHCs (Scheme 1.21)

2.3.2.1. Synthesis of 1-[(*N*-*tert*-butoxycarbonyl)aminopropyl]-imidazole (9)

In an inert atmosphere of nitrogen, a solution of di-*tert*-butyl dicarbonate (**8**) (4.3 g, 19.7 mmol) dissolved in CPME (25 mL) was added, dropwise, to a stirred mixture of 1-(3-aminopropyl) imidazole (**7**) (API, 2.4 mL, 20 mmol), $NaHCO_3$ (4.0 g, 47.6 mmol) and CPME (50 mL) and allowed to stir for 4 h. Thereafter, the reaction mixture was extracted with ethyl acetate and water. The combined organic extract was dried ($MgSO_4$) and the solvent was removed *in vacuo* to afford the desired 1-[(*N*-*tert*-butoxycarbonyl)aminopropyl]imidazole (**9**), 4.1 g (90%), as a pale yellow oil.[168] ^{1}H NMR (400 MHz, $CDCl_3$, TMS): δ (ppm)= (9H, s), 1.94 (2H, tt, *J* = 6.6, 2.7 Hz), 3.09 (2H, t, *J* = 6.6 Hz), 3.95 (2H, t, *J* = 2.7 Hz), 6.91 (1H, dd, *J* = 3.4, 1.9 Hz), 7.02 (1H, dd, *J* = 3.4, 1.1 Hz), 7.45 (1H, dd, *J* = 1.9, 1.1 Hz). ^{13}C NMR (100 MHz, $CDCl_3$, TMS): δ (ppm) = 27.57, 28.45, 32.00, 44.43, 56.39, 118.88, 129.65, 137.18, 156.14; HRMS, found 226.1554 g mol^{-1} ($C_{11}H_{19}N_3O_2$, $[M]^+$), calculated exact mass = 225.2874 g mol^{-1}.

2.3.2.2. Synthesis of 1-[(*N*-*tert*-butoxycarbonyl)aminopropyl]-3- (2,4,6-trimethylbenzyl)imidazolium chloride (11)

A mixture of 1-[(*N*-*tert*-butoxycarbonyl)aminopropyl]imidazole (**9**) (2.0 g, 10 mmol), 2,4,6-trimethylbenzyl chloride (**10**) (1.86 g, 11 mmol) and CPME (50 mL) was stirred at room temperature for 12 h. The resulting crude product was washed with CPME (5 x 50 mL) and dried under vacuum at 40 ^{o}C to afford the desired 1-[(*N*-*tert*-butoxycarbonyl)aminopropyl]-3-(2,4,6-trimethylbenzyl) imidazolium chloride (**11**), 3.29 g (84%) as a viscous, dark brown oil/semi-solid. ^{1}H NMR (400 MHz, $CDCl_3$, TMS): δ 1.31 (9H, s), 2.07 (2H, tt, *J* = 6.6, 4.4 Hz), 2.19-2.20 (9H, 2.19 (s), 2.20 (s)), 3.09 (2H, t, *J* = 6.6 Hz), 4.36 (2H, t, *J* = 4.4 Hz), 5.45 (2H, s), 6.85 (2H, d, *J* = 1.2 Hz), 6.68 (1H, dd, *J* = 1.8, 1.0 Hz), 6.71 (1H, dd, *J* = 1.8, 1.0 Hz), 7.69 (1H, t, *J* = 1.2 Hz). ^{13}C NMR (100 MHz, $CDCl_3$, TMS): δ (ppm) = 19.84, 21.09, 28.45, 31.97, 37.63,

48.60, 56.37, 82.99, 122.10, 124.63, 125.50, 129.98, 136.80, 137.51, 138.12, 156.11; HRMS, found 358.2487 g mol^{-1} $C_{21}H_{32}N_3O_2$, $[M]^+$, calculated exact mass = 358.4976 g mol^{-1}

2.3.2.3 Synthesis of 1-[aminopropyl]-3-(2,4,6-trimethylbenzyl)-imidazolium chloride (12)

A mixture of 1-[(*N*-*tert*-butoxycarbonyl) aminopropyl]-3-(2,4,6-trimethylbenzyl)imidazolium chloride (1.97 g, 5 mmol) (**11**), trifluoroacetic acid (10 mL) and methanol (30 mL) were heated under reflux for 6 h at 50 ^oC. The ensuing product was obtained after rotary evaporation of the solvent (methanol and residual trifluoroacetic acid). The crude product was washed with CPME (5 x 50 mL) and dried under vacuum at 40 ^oC to yield the desired 1-[aminopropyl]-3-(2,4,6-trimethylbenzyl) imidazolium chloride (**12**), 1.18 g (80 %), as a viscous, dark brown oil. ^1H NMR (400 MHz, methanol-d4, TMS): δ 2.01 (2H, tt, *J* = 6.8, 6.7 Hz), 2.26-2.27 (9H, 2.27 (s), 2.27 (s)), 2.97 (2H, t, *J* = 6.7 Hz), 4.31 (2H, t, *J* = 6.8 Hz), 5.45 (2H, s), 6.97 (2H, d, *J* = 1.2 Hz), 7.44 (1H, dd, *J* = 1.8, 0.9 Hz), 7.69 (1H, dd, *J* = 1.8, 1.2 Hz), 7.76 (1H, t, *J* = 0.9 Hz).^{13}C NMR (100 MHz, Methanol-d4, TMS): δ (ppm) = 19.82, 20.97, 29.85, 36.19, 48.51, 118.14, 122.60, 125.74, 129.58, 130.06, 135.65, 138.20, 139.82; HRMS, found 258.1973 g mol^{-1} ($C_{16}H_{24}N_3$, $[M]^+$,), calculated exact mass = 258.3818 g mol^{-1} (see Figures F1-F6 in Appendix for NMR spectra).

2.3.2.4. Synthesis of succinimidyl carbonate (DSC) activated mesoporous solid support (6a-e)

4-*N*,*N*'-Dimethylaminopyridine (1.2 g, 9.8 mmol) and propylene carbonate (50 mL) were added to a mixture of the appropriate mesoporous support (e.g., **4a-e**) and *N*,*N'*-disuccinimidyl carbonate (**5**) in a stoichiometric ratio of 1:1.16 (i.e. with a slight excess of 0.16 mol DSC) contained in a 500 ml round-bottomed flask and heated to 80 ^oC for 18 h with constant stirring. Thereafter, the resultant mixture was centrifuged at 1643 *x g* (centrifugal force), the supernatant from each was decanted and discarded whilst the pellet was further subjected to centrifugation with deionized water (2 x 40 mL) and acetonitrile (2 x 40 mL), in each case decanting and discarding the supernatant. The purified pellet was dried in a vacuum oven at 70 ^oC for 4 h to afford the desired succinimidyl carbonate activated mesoporous support (**6a-e**) with yields of 456, 398, 395, 393 and 390 mg, respectively.

From the results of the DSC activation, the degree of substitution on the expanded HACS were calculated using equation 3. Theoretically, the degree of substitution on starch is a maximum of 3. This is with respect to 3 hydroxyl groups per each anhydro glucose unit.

$$DS = \frac{162\ X\ W}{[100\ X\ M - (W\ X\ M_{SC})]} \ldots\ldots\ldots\ldots\ldots (Eq.3)$$

Where W is % nitrogen, M is molecular weight of nitrogen, M_{SC} is the molecular weight of succinimidyl carbonate groups, 162 is molecular weight of anhydroglucose units and 100 is percentage factor.

2.3.2.5. Synthesis of NHC ligand grafted mesoporous solid support (13a-e)

The appropriate succinimidyl carbonate activated mesoporous support (e.g. **6a-e**) (300 mg), 1-[aminopropyl]-3-(2,4,6-trimethylbenzyl) imidazolium chloride (**12**) (1.2 g, 4 mmol), triethyl amine (1 mL, 7 mmol) and propylene carbonate (50 mL) were heated to 80 ^{o}C in a round bottom flask for 24 h. Thereafter, the resultant mixture was centrifuged at 1643 *x g* (centrifugal force), the supernatant was decanted and discarded whilst the pellet was further subjected to centrifugation with deionized water (2 x 40 mL) and acetonitrile (2 x 40 mL), in each case decanting and discarding the supernatant. The purified pellet was dried in vacuum oven at 70 ^{o}C for 4 h to afford the dried NHC ligand grafted solid support (**13a-e**) with yields of 484, 453, 426, 420 and 419 mg, respectively.

For optimisation purpose, 100 mg of each of the succinimidyl carbonate activated support was first reacted with 400 mg of (**12**), 1 mL of triethylamine in 50 mL propylene carbonate. After the successful ligand binding, the process was scaled up to 300 mg and then 3000 mg of support.

2.3.2.6. Synthesis of Fe-NHCs (1a-e)

In an inert atmosphere of nitrogen, a stirred mixture of the appropriate ligand grafted support material (e.g., **13a-e**) (300 mg), K^{t}OBu (75 mg, 0.66 mmol), iron(III) chloride (96 mg, 0.60 mmol) and propylene carbonate (50 mL) was heated at 80 ^{o}C for 18 h. Thereafter, the resultant mixture was centrifuged at 1643 *x g* (centrifugal force) and the supernatant was decanted (and discarded) whilst the pellet was further subjected to

washing and centrifugation with brine solution (1 x 40 mL) to ensure removal of the uncoordinated $FeCl_3$, deionized water (2 x 40 mL) and with methanol (2 x 40 mL), in each case decanting and discarding the supernatant. The purified pellet was dried in vacuum oven at 70 ^oC for 4 h to afford the desired immobilised Fe-NHC catalysts (**1a-e**) with yields of 504, 477, 441, 443 and 456 mg, respectively.

For optimisation purposes, was first reacted with 400 mg of (**12**), 1 mL of triethylamine in 50 mL propylene carbonate. After the Fe coordination on 100 mg of each of the ligand binded support, the process was scaled up to 300 mg and then 3000 mg of ligand binded support. The immobilised Fe-NHC catalysts (**1a-e**), were characterised using ATR FT-IR, solid ^{13}C CP-MAS NMR spectroscopy, XPS, Mossbauer spectroscopy, ICP-MS and TEM/SEM analysis.

2.4. Fructose dehydration reaction in DMSO with fabricated Fe-NHC catalysts.

The amounts of the catalysts **1a-e** in mg equivalent to 0.01 mmol Fe active centre were determined from the Fe loading levels of the different catalysts **1a-e**. The table below shows the amount of each catalyst (mg) equivalent to 0.01 mmol.

Table 2.1. Amounts of the catalysts **1a-e** in mg equivalent to 0.01 mmol Fe centre

Catalysts	**Fe loading mmol g^{-1}**	**Mass (mg) equivalent to 0.01 mmol active Fe**
Fe-NHC HACS **1a**	0.68	14.7
Fe-NHC S350 **1b**	0.31	32.2
Fe-NHC S400 **1c**	0.32	31.3
Fe-NHC MPC **1d**	0.30	33.3
Fe-NHC OPC **1e**	0.52	19.2

The appropriate immobilised Fe-NHC catalyst (e.g., **1a-e**) (14.7 to 33.3 mg, 0.01 mmol) was added to a solution of D-fructose (180 mg, 1 mmol) in DMSO (4 mL) contained in separate glass vials. The reaction was allowed to run for 6 h at 100 ^oC, from which 0.5 mL samples were taken periodically and immediately quenched with ice-cold water to stop further reaction. The samples were then subjected to ^1H and ^{13}C NMR spectroscopy and HPLC analysis.

To assess the performance of the Fe-NHC catalysts (**1a-e**), diverse types of heterogeneous catalysts such as ZSM-5, Amberlyst-15, and Montmorillonite K10, were employed under the same reaction conditions. For the comparison, 30 mg of each

of ZSM-5, Amberlyst-15 and Monmorillonite K10 were measured and added to 1 mmol of fructose in 4 mL of DMSO. The dehydration was carried out at 100 ^{o}C for 6 hours from which samples were taken at time intervals of 10 min, 20 min, 30 min, 1 h, 3 h and 6 h.

Catalyst recycling experiments were also carried out using the same reaction conditions (1mmol fructose, 0.01 mmol catalyst, 4 mL DMSO at 100 ^{o}C, 1 hour). After each cycle the catalyst is recovered by centrifugation, washed 4 times with 20 mL ethanol and dried in vacuum oven at 70 ^{o}C for 4 hours. The dried recovered catalyst is then weighed, and the required amount of fructose is then reacted with the catalyst again for another cycle using same reaction conditions.

Control experiment was also carried out under the same reaction conditions using the unmodified support that do not contain the Fe-NHC group.

2.5. Glucose dehydration reaction in DMSO with fabricated Fe-NHC catalysts.

The appropriate immobilised Fe-NHC catalyst (**1a**-**e**) (14.7 to 33.3 mg, 0.01 mmol) was added to a solution of D-glucose (180 mg, 1 mmol) in DMSO (4 mL) contained in separate glass vials. The reaction was allowed to run for 6 h at 100 ^{o}C, from which samples were taken periodically and immediately quenched with ice-cold water to stop further reaction. The samples were then subjected to ^{1}H and ^{13}C NMR spectroscopy and HPLC analysis.

2.6. Fructose and glucose conversion to CMF with fabricated Fe-NHC catalysts and 1M HCl

The immobilised Fe-NHC catalyst (**1b**) (64 mg, 0.1 mmol) was added to a solution of D-glucose or D-fructose (180 mg, 1 mmol) in DMSO (4 mL) contained in separate glass vials. 0.5 mL of 1M HCl was then added and the reaction was allowed to run for 4 h at 100 ^{o}C, from which samples were taken periodically and immediately quenched with ice-cold water to stop further reaction. The samples were then subjected to ^{1}H and ^{13}C NMR and HPLC. Control experiments were run with only the substrates and 1M HCl with no catalysts.

2.7. Attempted amide synthesis using the fabricated supported Fe-NHC catalyst (1b)

A mixture of the appropriate amine (either aniline or benzylamine (12 mmol), appropriate carboxylic acid (either acetic acid or benzoic acid) (12 mmol) and Fe-NHC catalyst (**1b**) (0.38 g 0.12 mmol) and toluene (20 mL) contained in a 100 ml round bottom flask fixed with a reflux condenser was heated under reflux. The reaction progress was monitored by HPLC at 1 h, 2 h, 3 h, 4 h, 5 h, 6 h, 12 h, and 24 h by removal of an aliquot (10 μL) which was diluted to 1 mL in methanol before injection.

CHAPTER 3. RESULTS and DISCUSSION

Parts of the work in this chapter has been published:

"Novel Starbon™/HACS-supported *N*-heterocyclic carbene-iron(III) catalyst for efficient conversion of fructose to HMF."

Avtar S. Matharu, Suleiman Ahmed, Badriya Almonthery, Duncan J. Macquarrie, Yoon-Sik Lee and Yohan Kim, *ChemSusChem,* 2017.

DOI: 10.1002/cssc.201702207

(impact factor 2016, 7.226)

3.1 Introduction

This chapter presents and discusses in detail the synthesis, characterisation and catalytic applications of novel Fe-NHC heterogeneous catalysts (**1a-e**) immobilised on renewable supports which is the primary aim of this thesis as stated in Chapter 1. To achieve its objectives (also highlighted in Chapter 1), this chapter is sub-divided in to three parts, namely:

i. Part 1: Synthesis and characterisation of Fe-NHCs. The successful synthesis (Scheme 1 and as shown by experimental procedures in Chapter 2) and characterisation of Fe-NHCs immobilised on expanded starch, Starbon™ 350, Starbon™ 400, orange peel cellulose and mango peel cellulose are discussed. A diverse range of complementary characterisation techniques applied (ATR FT-IR, ^{13}C CP-MAS NMR, STA, TGA, CHN and ICP-MS, XPS, Mossbauer spectroscopy, and SEM/TEM) during every step of the synthetic strategy for each catalyst type (**1a-e**) is explored.

ii. Part 2: Catalytic Study. This chapter presents and discusses in detail the catalytic application of all the supported Fe-NHC heterogeneous catalysts synthesised, towards fructose dehydration to produce 5-(hydroxymethyl)furfural. The reaction was investigated with respect to reaction time at fixed temperature via NMR (^{1}H and ^{13}C) spectroscopy and the disappearance of signals for fructose concomitant with the appearance of HMF. HPLC results are discussed with respect to yield, conversion and selectivity. The efficacy of the Fe-NHCs immobilised on renewable supports (**1a-e**) with other heterogeneous catalysts (Amberlyst-15, Montmorillonite K10 and ZSM-5) with respect to fructose (**2**) to HMF (**3**) dehydration is presented. Catalyst recycling and re-use monitored by NMR spectroscopy (qualitative) and HPLC (quantitative) in DMSO-d_6 at 100 °C is discussed. Catalyst leaching, and catalyst reuse is reported to determine stability of the catalyst. A brief kinetic study is reported for Starbon 350 catalyst (**1b**) which shows an experimental activation energy (26.8 kJ mol^{-1}) for Starbon 350 catalyst (**1b**) to be much lower than that reported in the literature for HZSM-5 (Si/Al = 25) (70 kJ mol^{-1}) and MIL-101(Cr)-SO_3H

(55 kJ mol^{-1}). To conclude this part a mechanism for fructose (**2**) to HMF (**3**) dehydration is proposed.

iii. Part 3: Glucose and fructose dehydration to CMF (**14**). This chapter presents and discusses in detail the catalytic applications of the supported Fe-NHC heterogeneous catalysts synthesised towards; fructose and glucose dehydration to 5-(chloromethyl)furfural (**14**); and glucose dehydration reaction to produce 5-(hydroxymethyl)furfural (**3**).

3.2. Part 1: Synthesis and characterisation of Fe-NHCs (1a-e)

3.2.1. Fe-NHCS immobilised on expanded HACS (1a)

Although the use of disuccinimidyl carbonate activation to couple primary amines is widely reported in literature,[169, 170] to the best our knowledge this is first time this reaction has been applied to expanded HACS (**4a**) in the context of making an Fe-NHC (see scheme 1.21). Thus, initially a set of optimisation experiments were conducted to ascertain best conditions, i.e., solvent, DSC concentration (mmol g^{-1}), reaction temperature, reaction time.

3.2.1.1. Solvent selection study for the DSC (5) activation of expanded HACS (4a), i.e., preparation of (6a)

To select the best reaction solvent in terms of reactivity and sustainability, many different solvents (propylene carbonate, DMF, ethyl acetate and CPME) were employed for the DSC (**5**) activation of the expanded HACS support (**4a**) to afford **6a**.

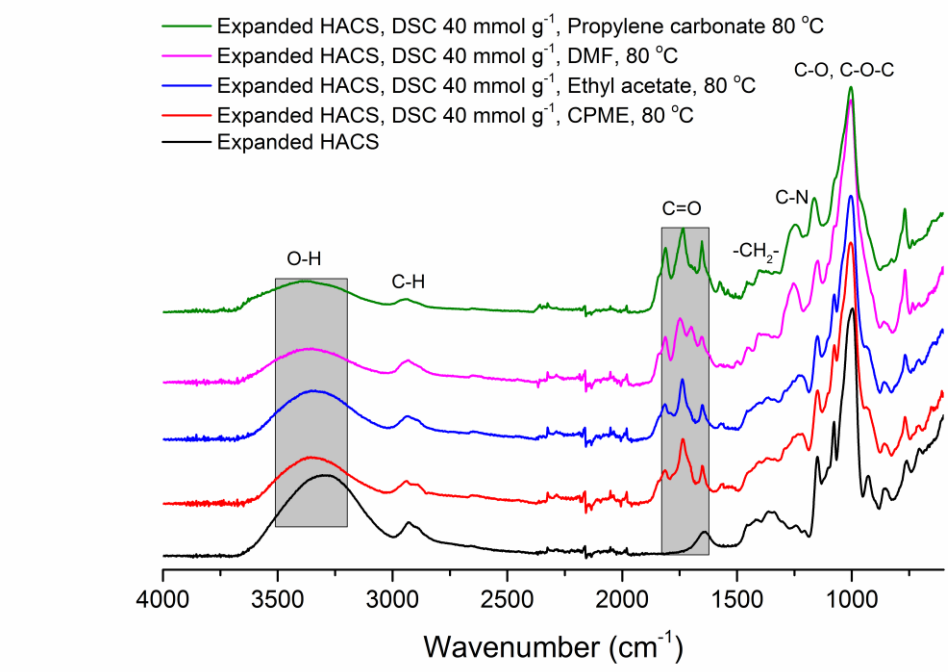

Figure 3.1. ATR-IR spectroscopy of expanded HACS after DSC activation in various solvents.

ATR-IR spectroscopy (Figure 3.1) was used as a simple probe technique to explore the intensity and number of absorbance bands (1813, 1738, 1653 cm^{-1}) in the carbonyl region characteristic of imide and carbamate stretching vibration associated with

incorporation of DSC (**5**). At a simplistic level, it was assumed that the greater the area of absorbance bands the greater the amount of DSC activation. Thus, as shown in Figure 3.1 best DSC activation was achieved when DMF or propylene carbonate were used as reaction solvent which is also complementary with a decrease in the intensity of O-H stretching vibration mode (centred at 3300 cm^{-1}) synonymous hydroxyl groups on expanded starch (**4a**).[171-173] There are several absorbance bands arising from starch in the region 1000-1200 cm^{-1}, which corresponds to C-O, C-C, C-O-H bond stretching and C-O-H bending,[174] Furthermore, an absorbance band at 1239 cm^{-1} is noted which may be assigned to the imide (C-N) vibration. [175-177] Although, all the other solvents show activation, the decrease in intensity of the O-H stretch is not as strong and thus assumed not to be as good as propylene carbonate.

To further investigate the effect of the solvent selection on the DSC activation of expanded HACS (**4a**) to afford (**6a**) the samples of the latter were submitted for CHN elemental analysis (Table 3.1), as an increase in nitrogen content would be indicative of succinimyl carbonate loading (mmol g^{-1}) and from which also the degree of OH substitution with the succinimidyl carbonate group is also calculated.

Table 3.1. Succinimidyl carbonate loading (mmol g^{-1}) and degree of substitution in (**6a**) with respect to reaction solvent at 80^{o}C and 24 h reaction time.

Reaction solvent	**Yield (g)**	**Nitrogen (%)**	**Degree of substitution (DS)**	**Succinimidyl carbonate loading (mmol g^{-1})**
Ethyl acetate	0.11	0.90	0.11	0.64
Cyclopentyl methylether	0.13	1.19	0.16	0.85
Propylene carbonate	0.15	2.61	0.41	1.86
Dimethyl formamide	0.16	2.93	0.48	2.09

Assuming that (**6a**) is pure and dry, i.e., solvent free, then as shown by % nitrogen content (Table 3.1) it is evident that dimethyl formamide (2.09 mmol g^{-1}, DS 0.48) and propylene carbonate (1.86 mmol g^{-1}, DS 0.41) are far superior than ethyl acetate (0.64 mmol g^{-1}, DS 0.11) and cyclopentyl methyl ether (0.85 mmol g^{-1}, DS 0.16). It appears that DMF and propylene carbonate, dipolar aprotic solvents, better solvate HACS (**4a**) and DSC (**5**) than polar aprotic solvents (ethyl acetate and CPME).

A plausible mechanism for DSC activation in the presence of DMAP is given in Scheme 3.1. The two possible mechanisms A and B are shown below. However, due to the tendency of the intermediate in mechanism A to be stabilised in polar aprotic solvents, it is more likely that the reaction proceeds via mechanism A due to CPME which is a polar aprotic solvent.

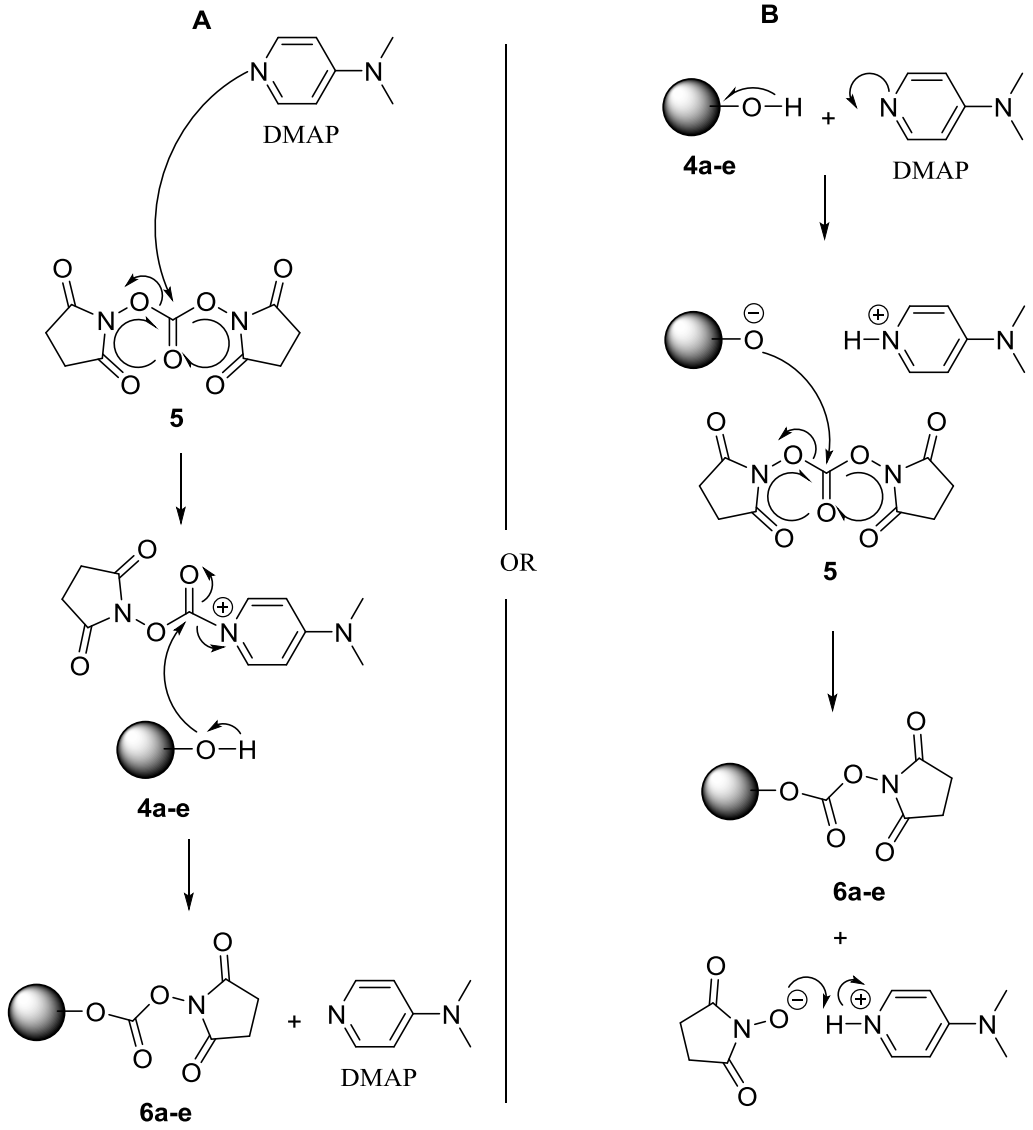

Scheme 3.1. Two plausible mechanisms for DSC activation in the presence of DMAP.

Although dimethyl formamide gave the highest loading level compared to propylene carbonate, the former is a toxic, dipolar, aprotic nitrogen containing solvent. [178, 179] Solvent waste which is usually removed by washing, creates large volume of waste and its incineration produces NOx emissions. Propylene carbonate on the other hand is a green(*er*) alternative produced from (waste) carbon dioxide and propylene oxide.

Unlike DMF, incineration of propylene carbonate affords carbon dioxide and water only. Thus, herein, propylene carbonate was chosen as the best solvent for the DSC activation of all renewable supports (**4a-e**) discussed in this thesis.

3.2.1.2. DSC (5) concentration study for activation of expanded HACS (4a), i.e., preparation of (6a)

To better ascertain the best succinimidyl carbonate loading (mmol g^{-1}) of the DSC towards achieving the best starch OH activation, various loading levels of the DSC were employed (10 mmol g^{-1}, 20 mmol g^{-1}, 40 mmol g^{-1} and 80 mmol g^{-1}).

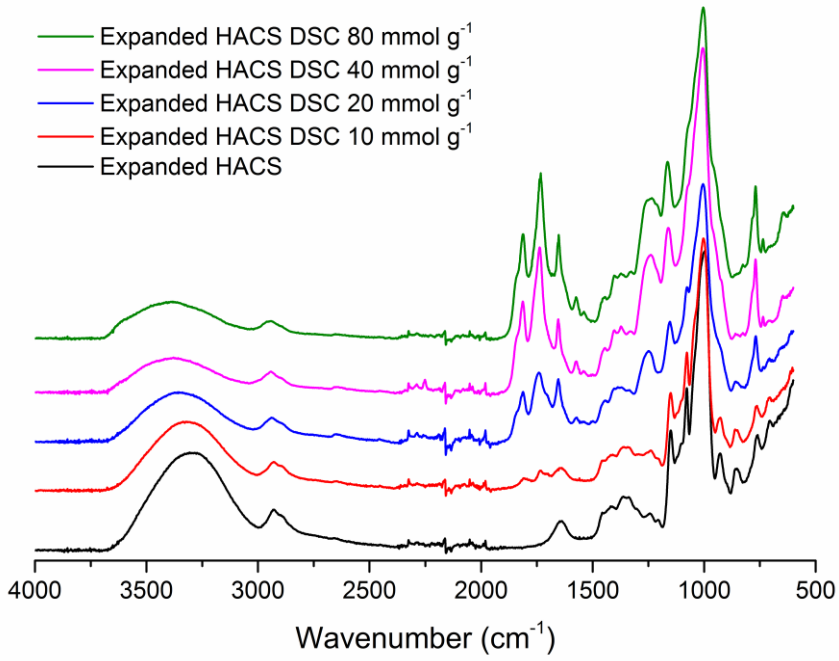

Figure 3.2. FT-IR spectra for succinimidyl carbonate derivative of HACS **6a** with respect to DSC concentration (mmol g^{-1} starch).

Figure 3.2. indicates that 40 mmol of DSC for each 1 g of expanded starch is the best. The stoichiometry of starch with respect to *N*,*N*'-disuccinimidyl carbonate (**5**) is 1:3 (on the basis of hydroxyl groups to succinimidyl carbonate). As such the conversion to its succinimidyl carbonate derivative (**6a**) at 40 mmol DSC per g of starch was performed using a slight excess i.e., 3.16 molar equivalents or 0.16 molar excess of the succinimidyl carbonate. It is evident from Figure 3.2. that the 10 mmol DSC loading is insufficient to result in OH activation as the OH band at 3300 cm^{-1} does not show any significant decrease coupled with an almost absence of the carbonyl

absorption band of succinimidyl carbonate groups. 20 mmol show some activation with appearance of new succinimidyl carbonate groups absorption bands at 1813, 1738, 1653 cm^{-1} and a band at 1239 cm^{-1} assigned to imide (C-N) vibration and a decrease in OH band at 3300 cm^{-1}. Both 40 mmol and 80 mmol DSC loading proved the most effective for DSC activation of the expanded HACS as evident by the significant decrease in the broad OH absorbance band at 3300 cm^{-1} with a corresponding increase in intensity of newly attached carbonyl bands of succinimidyl carbonate[180, 181] at 1813, 1738, 1653 cm^{-1} and a band at 1239 cm^{-1} assigned to imide (C-N) vibration. However, the lack of significant increase in activation on going from 40 mmol to 80 mmol DSC loading on 1g expanded HACS suggests that the 40 mmol DSC loading is probably the optimum DSC loading required for the best DSC activation of the expanded HACS under those conditions.

Table 3.2 shows the succinimidyl carbonate loadings and degree of substitution (based on % N as determined by CHN analysis) of the expanded HACS for the different DSC loadings (mmol g^{-1} HACS).

Table 3.2. Succinimidyl carbonate loadings (mmol g^{-1}) and degree of substitution based on varying DSC loadings (mmol g^{-1} HACS).

DSC (mmol/100 mg HACS)	Yields (g)	Nitrogen (%)	Degree of substitution (DS)	Succinimidyl carbonate loading (mmol g^{-1})
2	0.11	0.64	0.08	0.46
4	0.15	2.93	0.48	2.09
8	0.16	3.25	0.56	2.32

Note: 1 mmol not reported due in-significant loading.

Effort was not made to obtain the succinimidyl carbonate loading of 10 mmol DSC g^{-1} of support due to very low activation as evidenced by the FT-IR spectrum (Figure 3.2). It is evident that 40 mmol and 80 mmol DSC g^{-1} of support provides the best succinimidyl carbonate activation with loadings of 2.09 mmol g^{-1} and 2.32 mmol g^{-1} of expanded HACS, and degree of substitution of 0.48 and 0.56 respectively. A significant increase in succinimidyl carbonate loading is achieved from 2 mmol to 4 mmol DSC g^{-1} of HACS (0.46 mmol g^{-1} to 2.09 mmol g^{-1}). However, no significant increase in loading is achieved on going from 40 mmol to 80 mmol DSC loading with respect to succinimidyl carbonate activation. As such it is considered a waste to continue the activation at 8 mmol DSC g^{-1} of support. Thus, herein, succinimidyl

carbonate activation of the all renewable supports (**4a-e**) were carried out with a maximum of 40 mmol of DSC g^{-1} of renewable support.

3.2.1.3. Reaction temperature optimisation study for DSC activation

The DSC activation was further subjected to temperature optimisation study at fixed concentration (4 mmol) for 24 h reaction time.

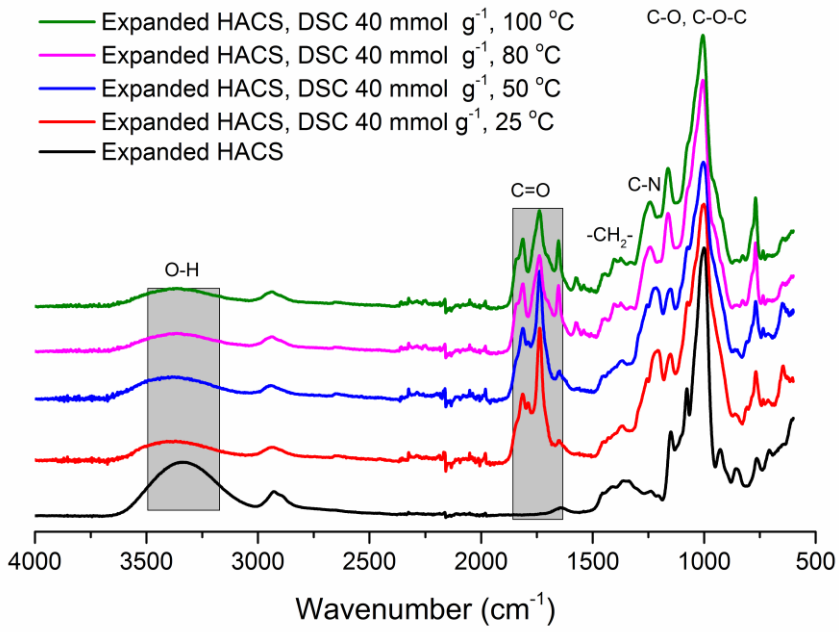

Figure 3.3. FT-IR results of the optimisation of DSC activation temperature on Expanded HACS.

The FT-IR spectra depicted in Figure 3.3 indicates that 80 ^{o}C is probably the optimum temperature for the DSC activation reaction. This is evident from the spectra as at 80-100 ^{o}C there exists three absorption bands at 1813, 1738, 1653 cm^{-1} assigned to carbonyl (C=O), and another at 1239 cm^{-1} assigned to imide (C-N) vibration corresponding to newly attached carbonyl and imide groups on HACS surface. At 25 to 50 ^{o}C, only two carbonyl absorption bands at 1813 and 1738 cm^{-1} were observed, indicating that potentially activation of the OH group only occurred at the more accessible position 6 rather than the proposed activation at position 2 and 6 of the glucose monomer units of the expanded HACS. This observation is further supported

by the much-decreased intensity of the broad band at 3340 cm^{-1} assigned to OH at 80-100 ^oC reaction temperature as compared to the 25-50 ^oC reaction temperature.

The nitrogen content (as determined by elemental analysis) in **6a** at fixed concentration (40 mmol) with respect to different reaction temperatures are given in Table 3.3. It is evident that 80 ^oC and 100 ^oC give the best succinimidyl carbonate activation with loadings of 1.86 mmol g^{-1} (DS 0.41) and 2.09 mmol g^{-1} (DS 0.48) of expanded HACS, respectively. Thus, the results are complementary with the IR spectra shown in Figure 3.3 which also suggested 80 ^oC and 100 ^oC as optimal temperatures. A significant increase in succinimidyl carbonate loading is achieved on going from 50 ^oC to 80 ^oC (1.86 mmol g^{-1} to 2.09 mmol g^{-1}). However, no significant increase in loading is achieved on increasing the temperature from 80 ^oC to 100 ^oC.

Table 3.3. Succinimidyl carbonate loading (mmol g^{-1}) and degree of substitution at fixed concentration (40 mmol g^{-1}) with respect to temperature (^oC) at 24 h reaction time.

Reaction temperature (^oC)	**Nitrogen (%)**	**Degree of substitution (DS)**	**Succinimidyl carbonate loading (mmol g^{-1})**
25	1.80	0.25	1.29
50	1.88	0.27	1.34
80	2.61	0.41	1.86
100	2.93	0.48	2.09

The results above (Table 3.3) shows that even at 100 ^oC, only about 2.09 mmol g^{-1} of succinimidyl carbonate group reacted with the expanded HACS support, representing a 5.2 % incorporation.

3.2.1.4. Reaction time optimisation study for DSC activation

A reaction time optimisation was carried out from 6 h to 24 h at 6 h intervals. FT-IR spectroscopy (Figure 3.4) of the succinimidyl carbonate derivatives (**6a**) shows variations in the intensity of the key absorption bands as described earlier.

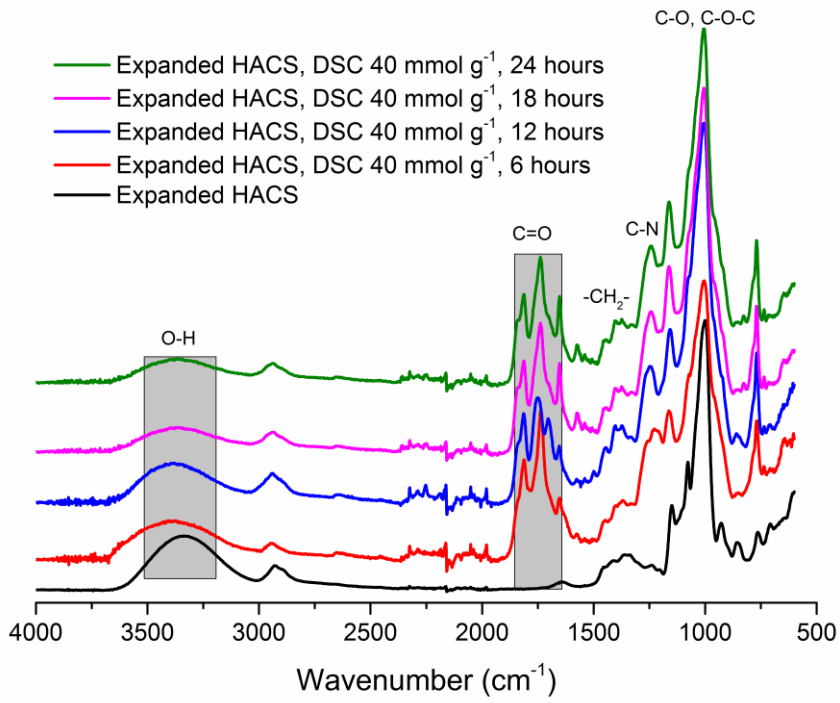

Figure 3.4. FT-IR spectra for optimisation of DSC activation of HACS (**4a**) with respect to reaction time

As seen in Figure 3.4, only two carbonyl absorption bands at 1813 and 1738 cm^{-1} were observed at lesser reaction times 6-12 h, indicating that potentially activation of the OH group only occurred at the more accessible position 6 rather than the proposed activation at position 2 and 6 of the glucose monomer units of the expanded HACS. However, at relatively longer reaction time 18-24 h all the three absorption bands at 1813, 1738, 1653 cm^{-1} assigned to carbonyls (C=O) of the imide and carbamate were distinctly evident. No notable change was observed on increasing reaction time from 18-24 h reaction time, making 18 h as the optimum DSC activation reaction time. Similarly, this observation is further supported by the much-decreased intensity of the broad band at 3340 cm^{-1} assigned to O-H stretching vibration mode at 18-24 h reaction time as compared to the 6-12 h reaction time.

Table 3.4 gives the succinimidyl carbonate loadings on expanded HACS (**4a**) with respect to reaction time indicating that 18 h and 24 h gave best succinimidyl carbonate loadings of 1.80 mmol g^{-1}, DS 0.39 and 1.86 mmol g^{-1}, DS 0.41 of expanded HACS, respectively. Significant increase in succinimidyl carbonate loading is achieved on going from 12 h to 18 h (1.47 mmol g^{-1}, DS 0.30 to 1.86 mmol g^{-1}, DS 0.41). However,

no significant increase in loading is achieved on increasing the reaction time from 18 h to 24 h.

Table 3.4. Results of starch DSC activation at different temperatures.

Reaction time (h)	Nitrogen (%)	Degree of substitution (DS)	Succinimidyl carbonate loading (mmol g^{-1})
24	2.61	0.41	1.86
18	2.51	0.39	1.80
12	2.06	0.30	1.47
6	1.94	0.28	1.38

The combined results of the FT-IR spectroscopy and CHN elemental analysis indicates that 18 h is the optimum reaction time for succinimidyl carbonate activation of the OH groups on expanded HACS.

3.2.1.5. Summary of DSC optimisation study

Thus, to summarise the best conditions for the formation of succinimidyl carbonate derivative (**6a**) of expanded HACS (**4a**) using DSC (**5**) as reagent are: DSC 40 mmol g^{-1}; reaction time, 18 h; reaction temperature, 80 ^{o}C, and; reaction solvent, propylene carbonate.

3.2.1.6. Ligand grafted HACS (13a) and Fe-NHC immobilised on HACS (1a)

FT-IR (Figure 3.5) spectroscopy was used to analyse the modification stages of succinimidyl carbonate derivative (**6a**) to afford ligand grafted HACS (**13a**) and thereafter the desired Fe-NHC immobilised on HACS (**1a**) (see scheme 1.21). Notably, the decrease in the intensity of the O-H absorbance band, and the appearance of new carbonyl absorption bands and C-N absorption bands were used to analysed and ascertain the successful modification of the expanded HACS support.

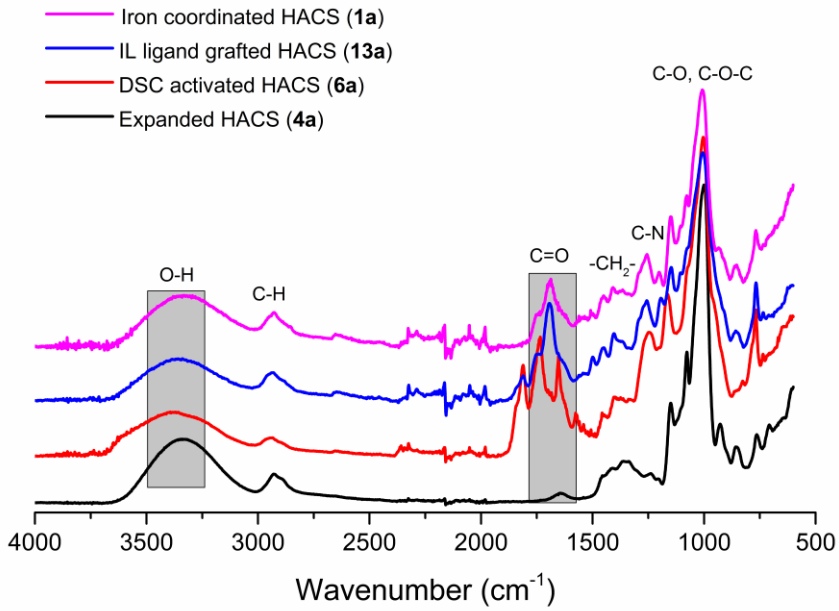

Figure 3.5 FT-IR spectra of expanded HACS (**4a**), DSC activated HACS (**6a**), ligand grafted HACS (**13a**) and Fe coordinated HACS (**1a**).

The absorption band patterns of the ligand grafted HACS (**13a**) with respect to those of its precursor (**6a**) showed significant difference in the carbonyl region. Ligand grafted HACS (**13a**) showed one notable carbonyl absorption band at 1695 cm^{-1} corresponding to the carbamate moiety compared to three carbonyl peaks in **6a**. Although, hidden within the fingerprint region weak absorbance bands characteristic of an imidazolium ring (1257, 1192 cm^{-1})[182-184] are observed. After the formation of NHC-iron(III) complex (**1a**), the absorbance band at 1192 cm^{-1} corresponding to the quaternary ammonium of imidazolium disappeared, indicating possible iron(III) coordination to the NHC ligand. However, actual iron incorporation and its oxidation state is evidenced later.

3.2.1.7. Solid-state ^{13}C NMR spectroscopy investigation for the formation of (1a) from (4a) via intermediates (6a) and (13a)

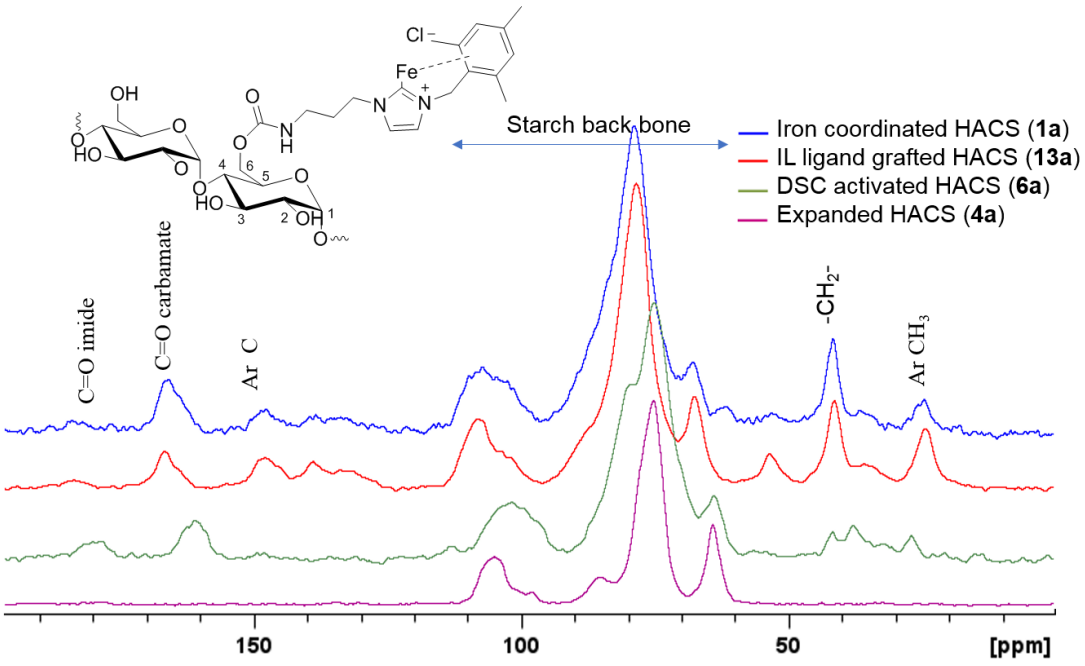

Figure 3.6 ^{13}C CPMAS spectra of expanded HACS (**4a**), succinimidyl carbonate derivative (**6a**), ligand grafted derivative (**13a**) and Fe-NHC immobilised on HACS (**1a**).

Figure 3.6 shows ^{13}C CPMAS spectra of expanded HACS (**1a**) and chemically modified HACS. Signals observed at 61.8, 82.1 and 101 ppm were assigned to C-6, C-4 and C-1 in expanded HACS (**1a**), respectively.[185-187] The signal at 72.5 ppm is assigned to C-2, -3, -5. Upon transformation of (**4a**) in to (**6a**) new signals at 172 and 160 ppm characteristic of –C=O moieties within succinimidyl carbonate appear. However, C-1 signal of starch was affected by the succinimidyl carbonate groups as it shifted from 101 ppm to 98 ppm. After ligand binding (**13a**), the carbonyl signal at 172 ppm assigned to the imide of the succinimidyl carbonate disappeared leaving the signal at 156 ppm assigned to the carbamate. On the starch support C-2, -3, -5 shifted from 72.5 ppm to 75.6 ppm, with C6 also shifted from 61.8 ppm to 65.2 ppm.

The successful ligand binding was further confirmed by the appearance of signals at 23, 40-51, 127-133 ppm and 142 ppm corresponding to aromatic CH_3, imidazole -CH_2-, carbons of imidazole ring,[188] and aromatic carbon of the attached imidazole ligand, respectively. [189-192]

3.2.1.8. CHN and ICP-MS elemental analysis of succinimidyl carbonate activated HACS 6a, ligand binded HACS 13a and Fe-NHC HACS 1a.

From the results of the CHN elemental analysis of **6a** and **13a**, the succinimidyl carbonate and NHC ligand loadings of the modified expanded HACS were found to be 2.09 mmol g^{-1} and 1.23 mmol g^{-1}, respectively. The presence and quantity of iron loaded was determined by ICP-MS elemental analysis which gave and iron loading of 0.63 mmol g^{-1} for the desired Fe-NHC immobilised on HACS (**1a**).

3.2.1.9. Thermogravimetric analysis of conversion of 4a to 1a via intermediates 6a and 13a

The thermogravimetric behaviour of expanded HACS (**4a**) and its modified forms, i.e.., **6a**, **13a** and **1a**, are shown in Figures 3.7 and 3.8 and key data summarised in Table 3.5.

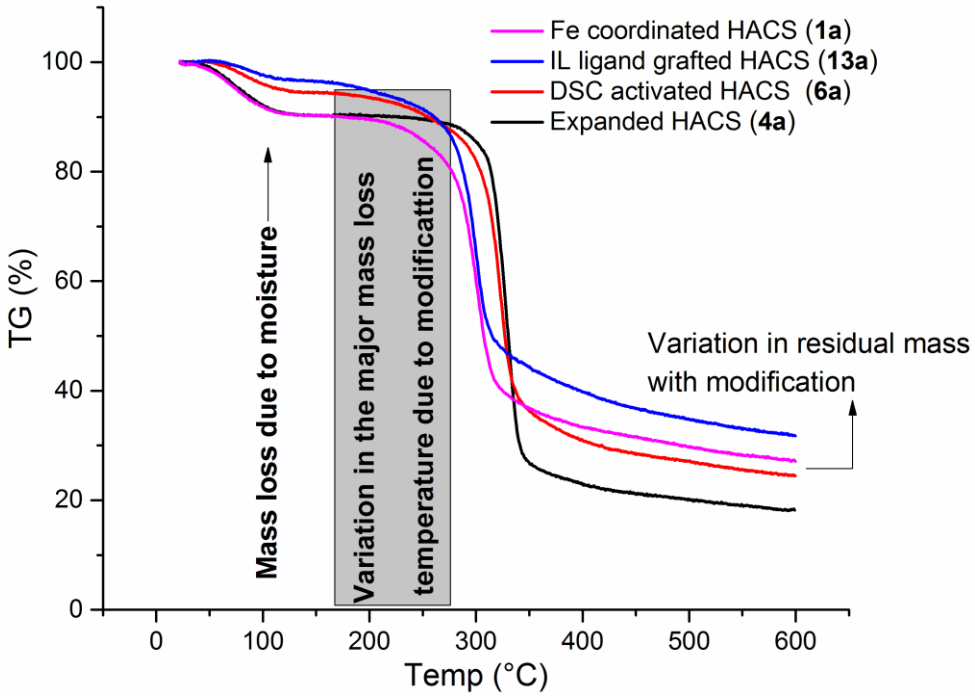

Figure 3.7. Thermograms for expanded HACS (**4a**) and modified expanded HACS, i.e., (**6a**), (**13a**), (**1a**) in N_2.

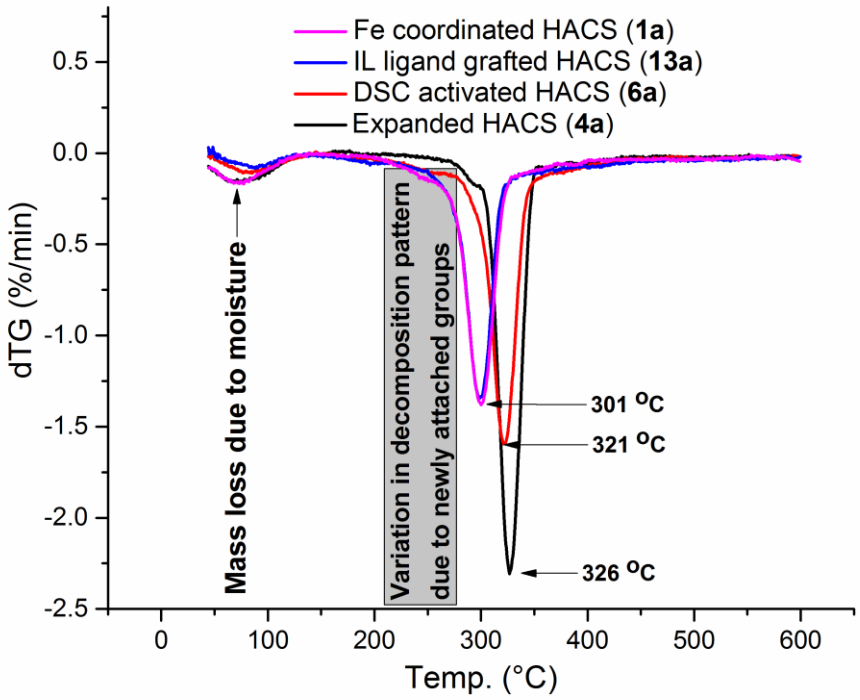

Figure 3.8. Differential thermograph (dTG) curves for expanded HACS (**4a**) and modified expanded HACS, (**6a**), (**13a**), (**1a**) in N_2.

For all thermograms (Figure 3.7) and dTG curves (Figure 3.8), the first decomposition stage which occurs from ambient to approximately 150 °C is associated with loss of physi-sorbed and chemi-sorbed water, and any residual solvent. Starch is known to contain approximately 10% bound water in its native state. The next major decomposition corresponds to the breakdown of the HACS backbone.[193] The point of inflection for HACS (**4a**) was 326 °C which decreased by 5 °C upon conversion in to its succinimidyl derivative (**6a**, point of inflection 321 °C) suggesting disruption of starch chains leading to a reduction in intermolecular attraction. Slight variation in decomposition is noted in the range 200-270°C which corresponds to derivatisation of HACS in to **6a**, **13a** and **1a**. Modification of **6a** in to its ligand grafted derivative (**13a**) and Fe-NHC **1a** saw a further decrease in temperature at point of inflection 301 °C and thus suggest further weakening of intermolecular interactions

Moreover, to indirectly determine the presence of iron all samples were additionally heated in air (Table 3.5). Combustion of organic samples in an air atmosphere should affords carbodioxide and water thus leaving no residue. Residues should only be seen

for non-combustible materials, in this case iron-containing, which will be present as oxides. As shown in Table 3.4, no residue was obtained for the expanded HACS (**4a**), succinimidyl carbonate derivative (**6a**), and ligand grafted HACS (**13a**). However, for the Fe coordinated HACS (**1a**), a reddish-brown residue (approx.3%) was obtained, which resembles the colour of iron oxide.

Table 3.5. Summary of the thermogravimetric data for expanded HACS (**4a**), succinimidyl carbonate derivative (**6a**), ligand grafted HACS (**13a**), and Fe coordinated HACS (**1a**).

Sample	**T_d (°C)**	**Residue (%)**		**Water Content (%)**
		N_2	air	
4a	326	18.2	-	9.7
6a	321	26.1	-	5.5
13a	301	28.7	-	2.1
1a	301	33.0	3	9.8

3.2.1.10. X-Ray Photoelectron Spectroscopy of (13a) and (1a)

X-Ray photoelectron spectroscopy was used for confirmatory analysis for the success of the imidazolium ligand binding (**13a**) and iron complexation on the expanded HACS support (**1a**).

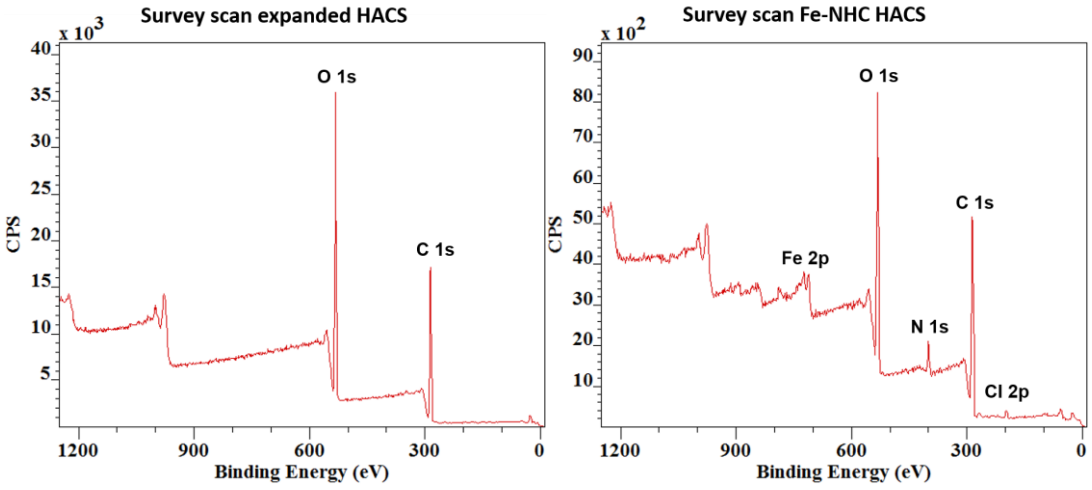

Figure 3.9. Fitted carbon 1s peaks for the expanded HACS and Fe-NHC expanded HACS.

The survey spectra (Figure 3.9), corresponding to the expanded HACS (**4a**) and the Fe-NHC immobilised on HACS (**1a**) shows an interesting difference with two new additional binding energy peaks that appear at 400 eV and 711 eV corresponding to nitrogen and iron, respectively, thus re-affirming successful fabrication of material **1a**.

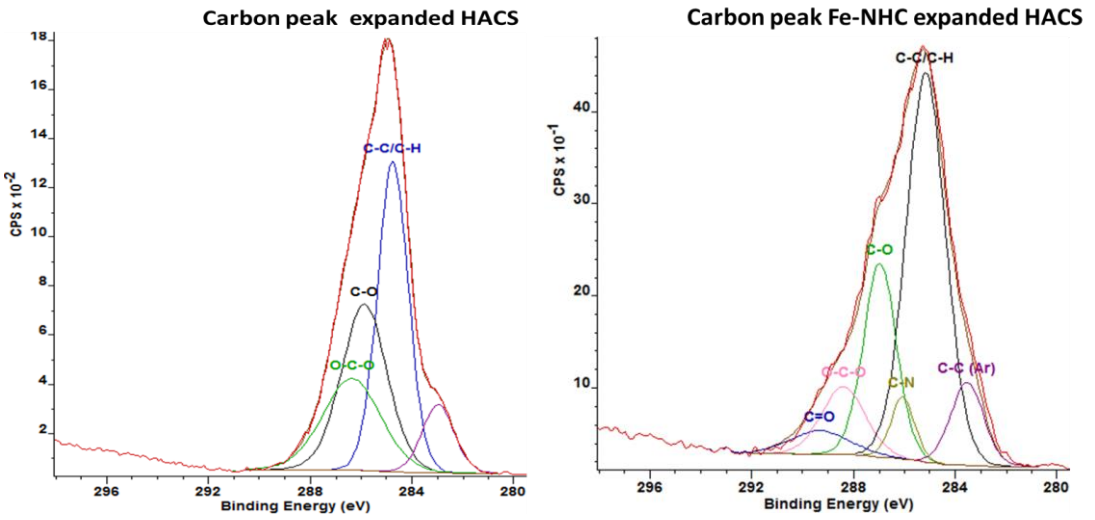

Figure 3.10. Fitted carbon 1s peaks for the expanded HACS (**4a**) and Fe-NHC immobilised HACS (**1a**)

The deconvolution and fitted XPS spectra (Figure 3.10) for C 1s of the expanded HACS (**4a**) and Fe-NHC immobilised HACS (**1a**), shows additional carbon binding energy peaks at 283.6, 286.1 and 289.2 eV assigned to C-C(Ar), C-N and C=O. [170, 194, 195] characteristic of compound **12** attached (see scheme 1.21).

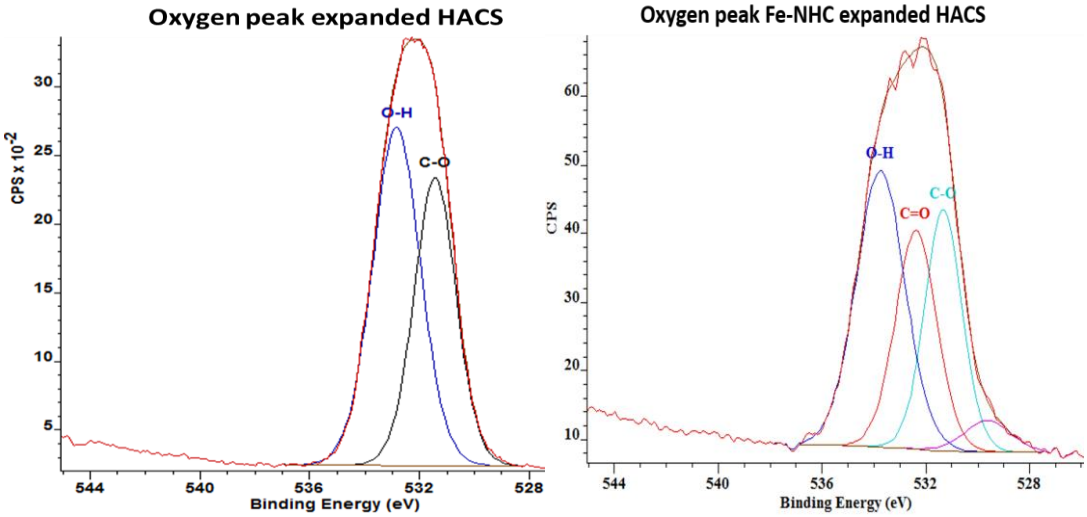

Figure 3.11. Fitted oxygen 1s peaks for the expanded HACS and Fe-NHC expanded HACS.

The deconvoluted and fitted O 1s spectra for expanded HACS (**1a**) (Figure 3.11) shows two binding energy peaks at 531.5 and 533.5eV assigned to C-O and O-H bonds in the expanded HACS (**1a**). However, the deconvoluted O 1s peak of the Fe-NHC immobilised HACS shows two additional binding energy peaks at 533 and 529 eV corresponding to C=O and possible metal oxide (iron oxide), respectively.[196] Another important and striking difference is the decrease in the O-H binding energy peak intensity which possibly may be attributed to the loss of some hydroxyl groups from the expanded HACS. This decrease in the intensity of the hydroxyl peak in the expanded HACS and the corresponding appearance of a new C=O peak in the Fe-NHC expanded HACS, indicates and further proves the successful attachment of **12** on the expanded HACS surface which leads to the eventual formation of **1a**.

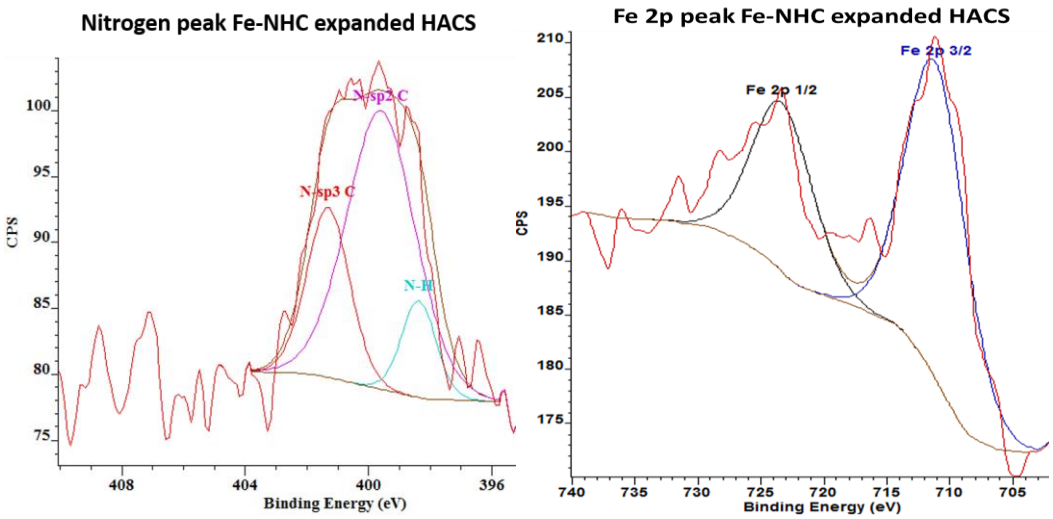

Figure 3.12. Fitted nitrogen 1s and iron 2p peaks for the Fe-NHC expanded HACS **1a**.

The appearance of a nitrogen 1s binding energy peak at 400 eV in the XPS survey spectra of the Fe-NHC expanded HACS (**1a**) which was originally absent as can be seen in the survey spectrum of the unmodified expanded HACS (Figure 3.12), is a clear indication that a new compound containing nitrogen has been attached to the expanded HACS. Further deconvolution of the N 1s peak indicates three different nitrogen bonding environments at 398.3, 399.2 and 401.3 eV assigned to N-H, C-N, and C=N, respectively. This however, is believed to have come from compound **12** attached to the expanded HACS.

Importantly, the appearance of a Fe doublet binding energy peaks with the Fe 2p 1/2 at 711 eV in the spectrum of the Fe-NHC immobilised HACS (**1a**) confirms the

presence of iron predominantly in the +3 oxidation state.[197-199] Mössbauer spectroscopy (see section 3.2.1.11) was undertaken to further confirm the presence of iron.

3.2.1.11. Mössbauer Spectroscopy of (1a)

Mössbauer spectroscopy is a versatile technique that can be used to provide precise information about the chemical, structural, magnetic and time-dependent properties of a material. Mössbauer effect is only detected in isotopes with very low energy gamma-ray and long-lived excited states. Similarly, the resolution is dependent upon the lifetime of the excited state. These two factors limit the number of isotopes that can be used successfully for Mössbauer spectroscopy. Interestingly, Fe which is the active metal chosen for the fabrication of our catalyst, is the most used isotope in Mössbauer spectroscopy (^{57}Fe), because it has both a very low energy gamma-ray and long-lived excited state, matching both the requirements well. As such, Mössbauer spectroscopy was employed to further investigate the presence and state of the Fe in the fabricated supported Fe-NHC catalyst (**1a**).

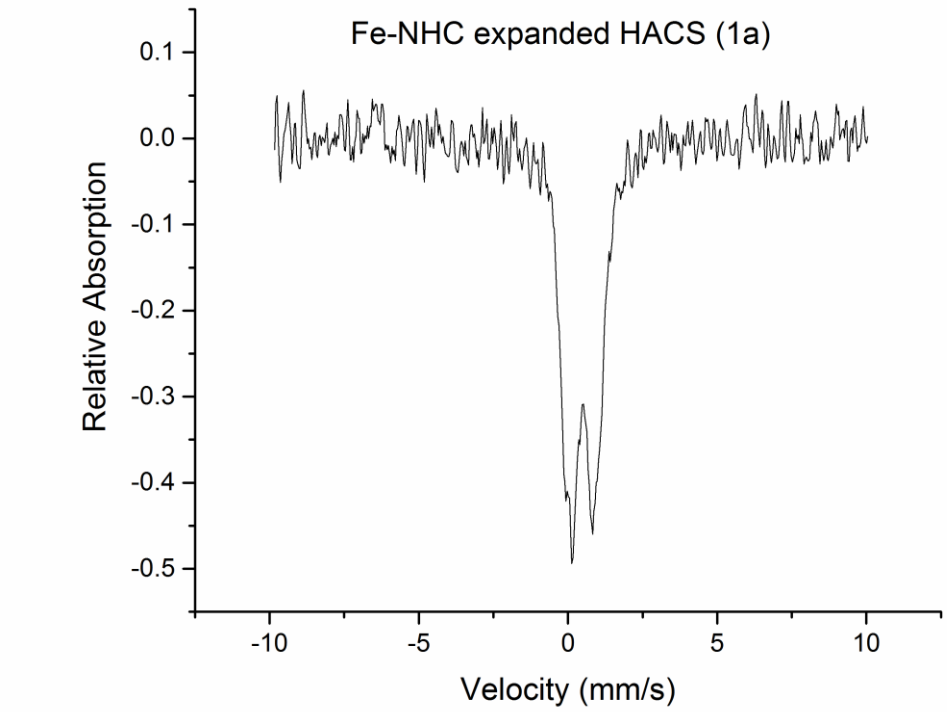

Figure 3.13. Mössbauer spectrum of Fe-NHC immobilised on HACS (**1a**)

The Mössbauer spectrum of **1a** (Figure 3.13), confirms the presence of iron in the form of Fe^{3+}. A characteristic isomer shift of 0.47 coupled with quadrupolar splitting of 0.81 are representative of Fe^{3+}.[200] The presence of iron, as well as oxygen and nitrogen, was further evidenced by XPS analysis as discussed earlier in Section 3.2.1.10.

3.2.1.12. Scanning Electron Microscopy (SEM) of (1a)

Scanning electron microscopy was used to explore the trends in porosity as the expanded HACS support undergoes modification to the desired fabricated expanded HACS supported Fe-NHC catalyst. This allows for a visible examination into the porosity of the support and whether the chemical and mechanical processes during the modification has effect on the porosity of the support material in question.

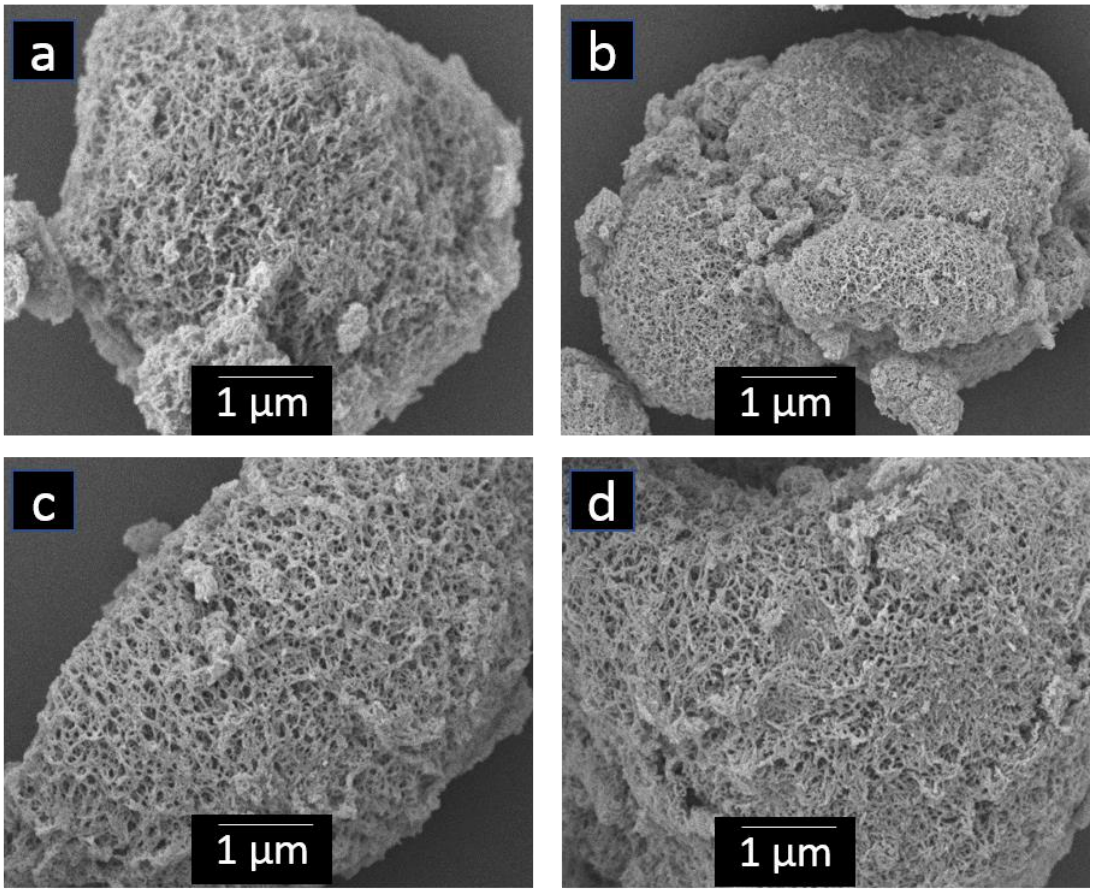

Figure 3.14. SEM micrographs of (A) expanded HACS (**4a**) (B) Succinimidyl carbonate activated HACS (**6a**) (C) Ligand grafted HACS (**13a**) and (D) Fe-NHC HACS (**1a**)

The SEM images (Figure 3.14) qualitatively prove that the surface modification process on the expanded HACS does not significantly collapse pore structure of the expanded HACS. Good network of pores is expected to facilitate diffusion of reactants to the catalytically active Fe centre and the diffusion of the products out after reaction.

3.2.1.13. Transmission Electron Microscopy (TEM) of (1a)

The iron complexation reactions were carried out under nitrogen purged conditions to prevent the formation of iron oxide nanoparticles. However, to investigate and ascertain the absence or otherwise of the formation of iron and iron oxide nanoparticles, transmission electron microscopy was employed to visibly investigate presence of nanoparticles in the Fe-NHC Starbon™ catalysts. Figure 3.15 shows the TEM images of the Fe-NHC expanded HACS.

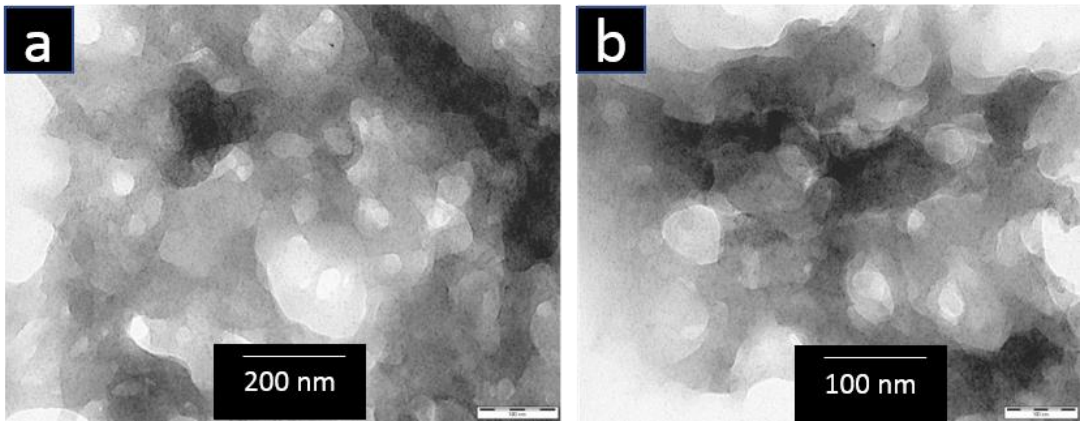

Figure 3.15. TEM micrographs of Fe-NHC HACS (**1a**), at 200 nm (a) and 100 nm (b).

The TEM images taken at 200-100 nm scale show absence of iron oxide nanoparticles. However, the limitation on the ability to zoom further due to the loss of particle of the material as a result of higher transmission that causes the particle to heat-up and bust prevents from drawing a general conclusion that the measured iron obtained from the ICP-MS, and XPS analysis only comes from the intended complexed iron covalently bonded to the imidazolium ligand on the expanded HACS support forming **1a**.

3.2.1.14. N_2 Porosimetry of (4a) and (1a)

The BET surface area, pore diameter and pore volume of expanded HACS (**4a**) and its subsequent Fe-NHC modified form (**1a**) determined by nitrogen adsorption porosimetry are listed in Table 3.6 and their isotherms are shown in Figures 3.16.

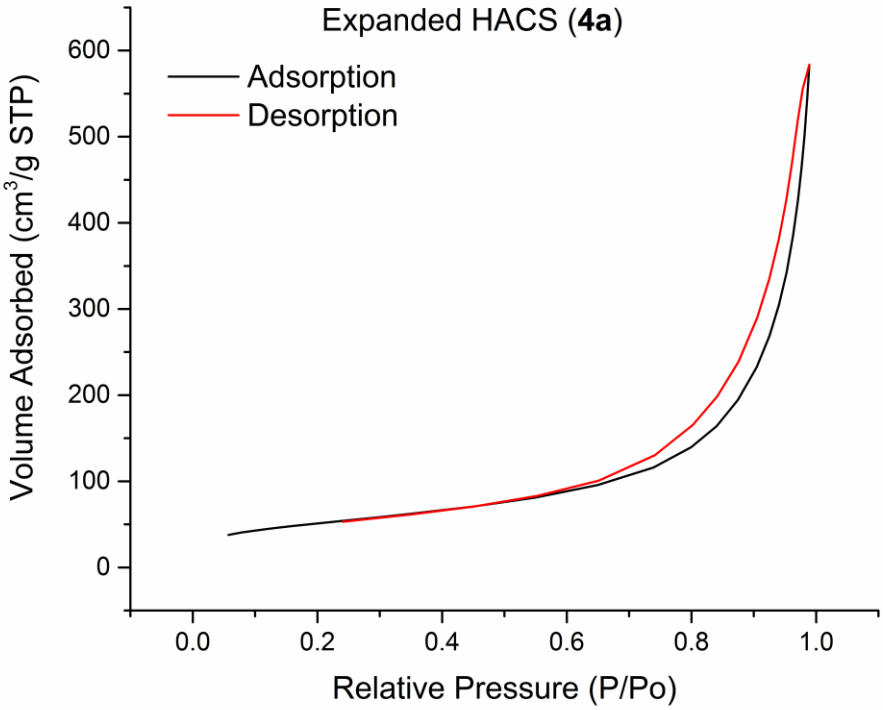

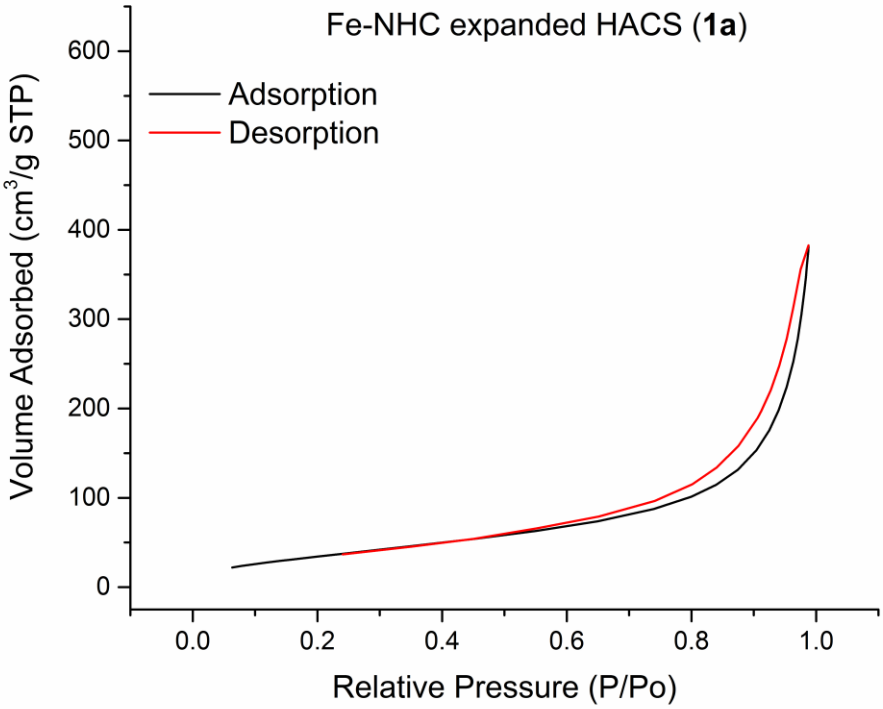

Figure 3.16. Adsorption/desorption isotherms for expanded HACS (**4a**) and Fe-NHC HACS (**1a**)

Generally, there are four main adsorption types isotherm plots that help to suggest the likely mechanism involved in the adsorption/desorption process. The isotherms shown in Figure 3.16 are characteristic of Type IV isotherm showing mild hysteresis (delay) on the desorption isotherm due to possible capillary condensation and typically indicating moderate physisorption abilities with mesoporosity of somewhat irregular organization.[201] More irregular ink bottle type pores with narrow necks and wide bodies can cause much larger desorption hysteresis.

Table 3.6. Summary of the porosity data for expanded HACS and modified forms.

Sample	**BET surface area (m^2/g)**	**Desorption pore volume (cm^3/g)**	**Desorption average pore diameter (nm)**
Expanded HACS (**4a**)	186	0.91	18.4
Fe-NHC expanded HACS (**1a**)	135	0.60	16.3

On modification of expanded HACS (**4a**) through to the desired Fe-NHC immobilised on HACS (**1a**) the BET surface area decreased: 186 m^2/g (**4a**); and; 135 m^2/g (**1a**). The subsequent decrease in surface area and pore volume may be explained by the attachment of the imidazolium ligand (and iron) on the HACS surface leading to blockage and filling of the porous structure.

3.2.2. Fe-NHCS immobilised on Starbon 350 (1b) and 400 (1c)

3.2.2.1 ATR FT-IR Spectroscopy

As previously discussed the decrease in intensity of the O-H stretching absorbance band and the appearance of new C=O stretch and C-N stretch absorption bands were used to analysed and ascertain the successful modification of the Starbon^{TM} supports **4b** and **4c** and their modification to the desired Fe-NHC catalysts immobilised **1b** and **1c**.

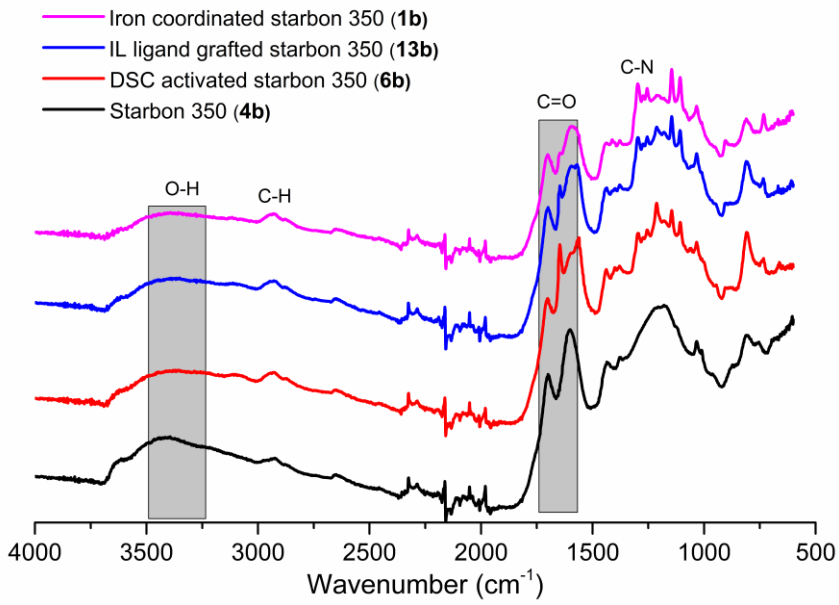

Figure 3.17 FT-IR spectra of Starbon™-350 (**4b**), DSC activated Starbon™-350 (**6b**), ligand grafted Starbon™-350 (**13b**) and Fe-NHC immobilised on Starbon™-350 (**1b**)

The FT-IR spectrum of Starbon™-350 (**4b**) (Figure 3.17), shows a broad, shallow, O-H stretching vibration centred around 3300 cm^{-1}, followed by carbonyl stretching vibration at 1702 cm^{-1} and possibly at 1600 cm^{-1}. However, the latter is more akin to C=C stretching. In the DSC activated Starbon™-350 or succinimidyl carbonate derivative **6b**, a new C=O stretching absorbance band is noted at 1678 cm^{-1} associated with the carbonyl moiety of succinimidyl carbonate. This assigment is also supported by a decrease in the intensity of the O-H absorbance band at 3300 cm^{-1} from Starbon™-350 (**4b**) to the succinimidyl carbonate derivative (**6b**). Moreover, the IR

spectrum of the ligand grafted Starbon™-350 (**13b**) indicates a disappearance of a band at 1567 cm^{-1} and a corresponding decrease of the band at 1678 cm^{-1} assigned to the C=O stretching of the carbamate derivative (**6b**).

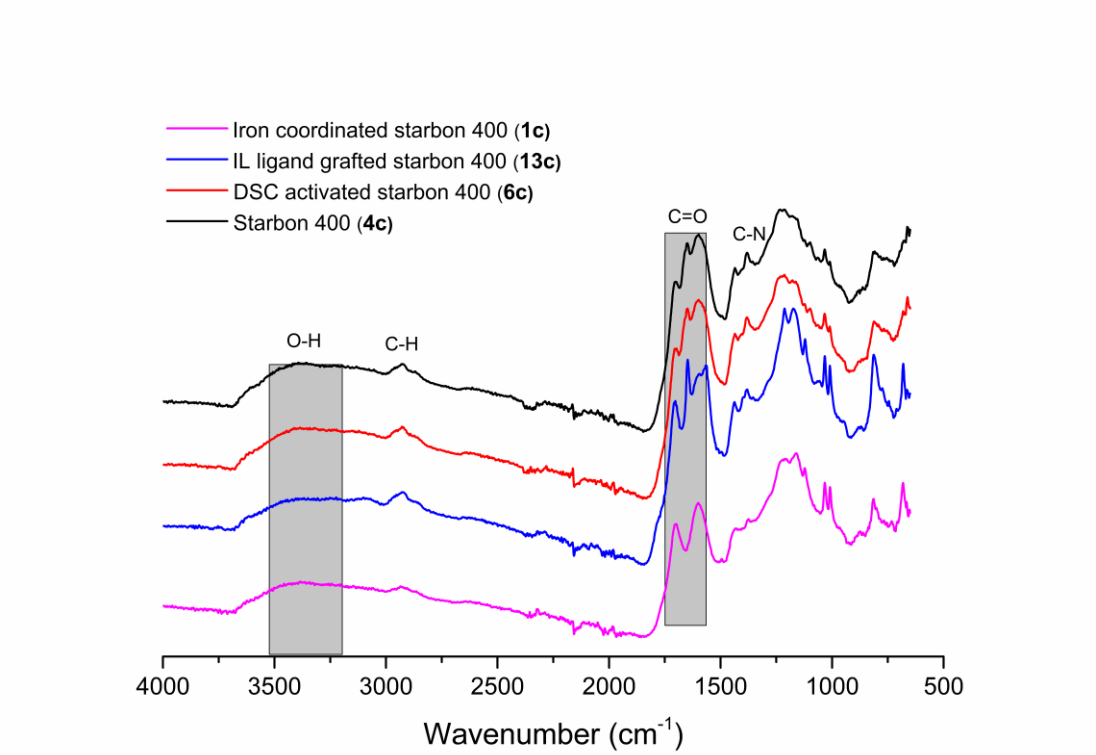

Figure 3.18. FT-IR spectra of Starbon™-400 (**4c**), DSC activated Starbon™-400 (**6c**), ligand grafted Starbon™-400 (**13c**) and Fe-NHC immobilised on Starbon™-400 (**1c**).

The FT-IR spectrum of Starbon™-400 (**4c**) (Figure 3.18), shows C=C stretching vibrational mode at 1599 cm^{-1} and one carbonyl stretching bands 1703 cm^{-1}. Conversion of **4c** in to **6c** shows appearance of a new absorbance band at 1678 cm^{-1} characteristic of the carbonyl moiety of succinimidyl carbonate group.[202] The intensity of the O-H stretching (3353 cm^{-1}) mode decreases and the intensity of the C-H stretching mode at approximately 2900 cm^{-1} becomes more evident. Thereafter, conversion of **6c** in to **13c** is characterised by the loss (or reduction in intensity) of the carbonyl absorbance band at 1678 cm^{-1}.

3.2.2.2. Solid-state ^{13}C NMR spectroscopy investigation for the formation of 1b and 1c from 4b and 4c via intermediates 6b and 6c and 13b and 13c

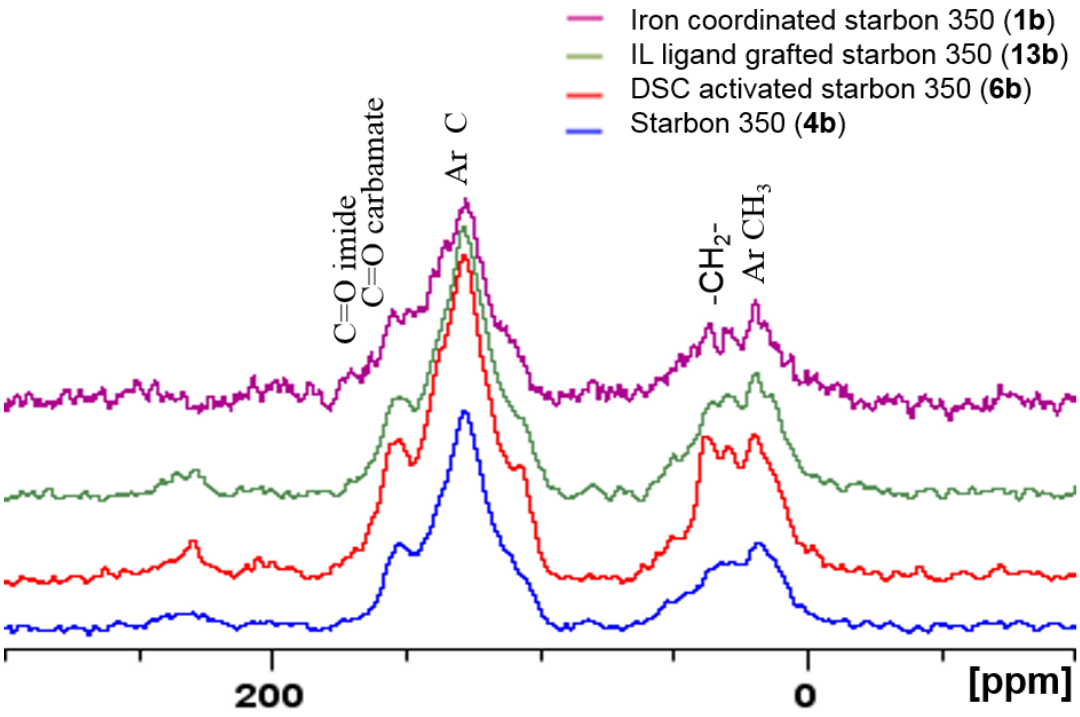

Figure 3.19 ^{13}C CP-MAS NMR spectra of Starbon™-350 (blue line), DSC activated Starbon™-350 (red line), ligand grafted Starbon™-350 (green line) and Fe coordinated NHC Starbon™-350 (purple line).

The ^{13}C CPMAS spectra of Starbon™350 (**4b**) and Starbon 400 (**4c**) and its modified forms (Figure 3.19 and 3.20) show similar resonance changes as described for the HACS materials earlier (Figure 3.6). The ligand grafted Starbon™ 350 (**13b**) shows new resonances at 23, 40-51 ppm, assigned to aromatic CH_3, imidazole CH_2, and carbons of imidazole ring, respectively. It was difficult to assign all the aromatic carbons, and most importantly the carbonyls of the imide and carbamate group of the succinimidyl carbonate were masked within the signals for Starbon™ itself.[153]

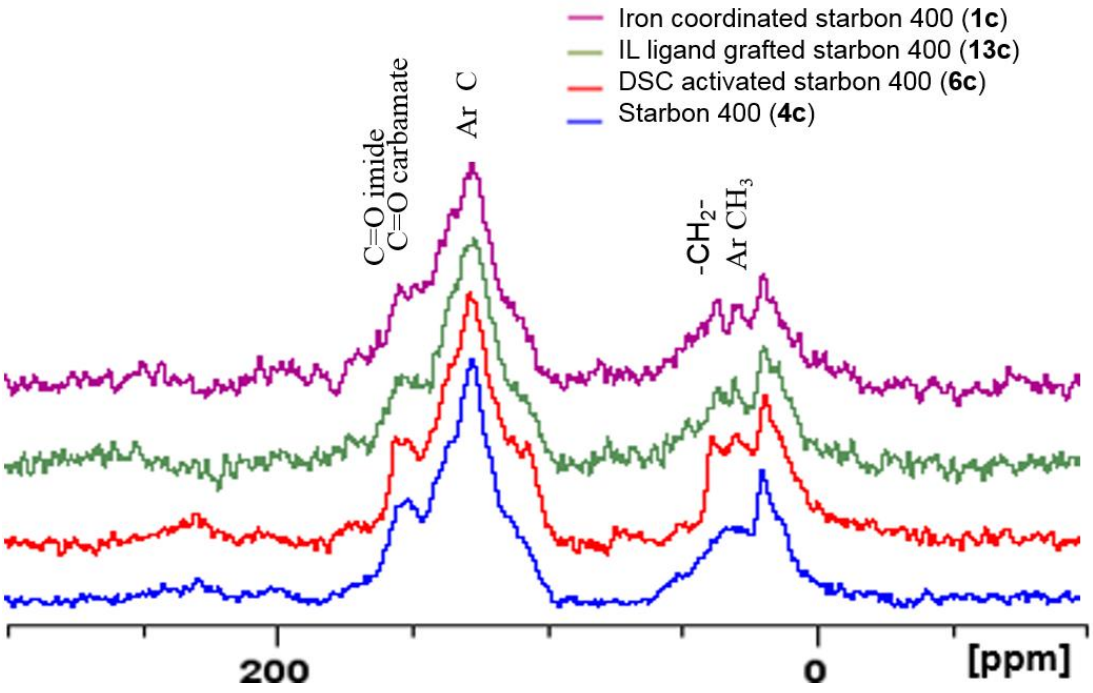

Figure 3.20. ^{13}C CP-MAS NMR spectra of Starbon™-400 (blue line), DSC activated Starbon™-400 (red line), ligand grafted Starbon™-400 (green line) and Fe coordinated NHC Starbon™-400 (purple line).

3.2.2.3. CHN and ICP-MS elemental analysis of Fe-NHC immobilised on Starbon-350 (1b) and Fe-NHC immobilised on Starbon-400 (1c)

Table 3.7. Loading levels (mmol g^{-1}) of succinimidyl carbonate, NHC ligand and Fe on Starbon 350 and Starbon 400.

Support	Loading level (mmol g^{-1})		
	Succinimidyl carbonate	NHC ligand	Fe
Starbon™ 350 (**4b**)	1.18 (**6b**)	0.63 (**13b**)	0.31 (**1b**)
Starbon™ 400 (**4c**)	1.36 (**6c**)	0.46 (**13c**)	0.32 (**1c**)

The loading levels (mmol g^{-1}) as determined by CHN elemental analysis are listed in Table 3.7. Slightly higher siccinimidyl carbonate loading is achieved with Starbon™ 400 (**6c**) (1.36 mmol g^{-1}) as compared to Starbon™ 350 (**6b**) (1.18 mmol g^{-1}), which may be due to differences in porosity and/or accessibility of OH groups. However, surprisingly the NHC ligand loading of Starbon™ 350 (**13b**) is slightly higher (0.63 mmol g^{-1}) as compared to Starbon™ 400 (**13c**) (0.46 mmol g^{-1}). The Fe loading

obtained from ICP-MS on the other hand, indicates almost comparable Fe loading between Starbon™ 350 catalyst (**1b**) and Starbon™ 400 catalyst (**1c**).

3.1.2.4. Thermogravimetric analysis of Fe-NHC immobilised on Starbon-350 (1b) and Fe-NHC immobilised on Starbon-400 (1c)

The thermograms and differential thermal curves are given in Figures 3.21 – 3.22 for Starbon 350 **4b** and its conversion to **1b** and for Starbon 400 **4c** and its conversion to **1c**.

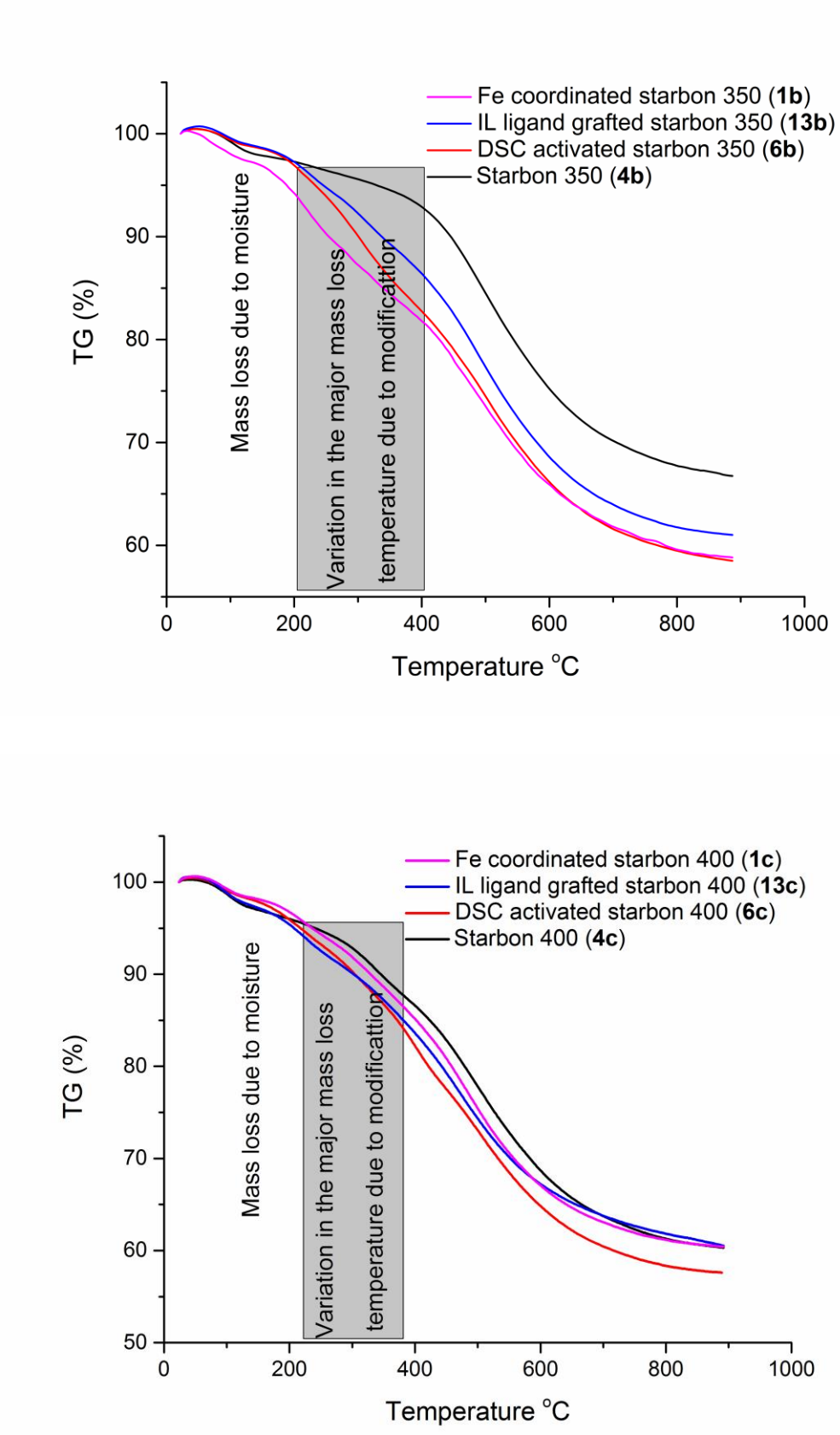

Figure 3.21. Thermal analysis data (TG) of Starbon™ 350 (Top) and Starbon™ 400 (Bottom) in N_2.

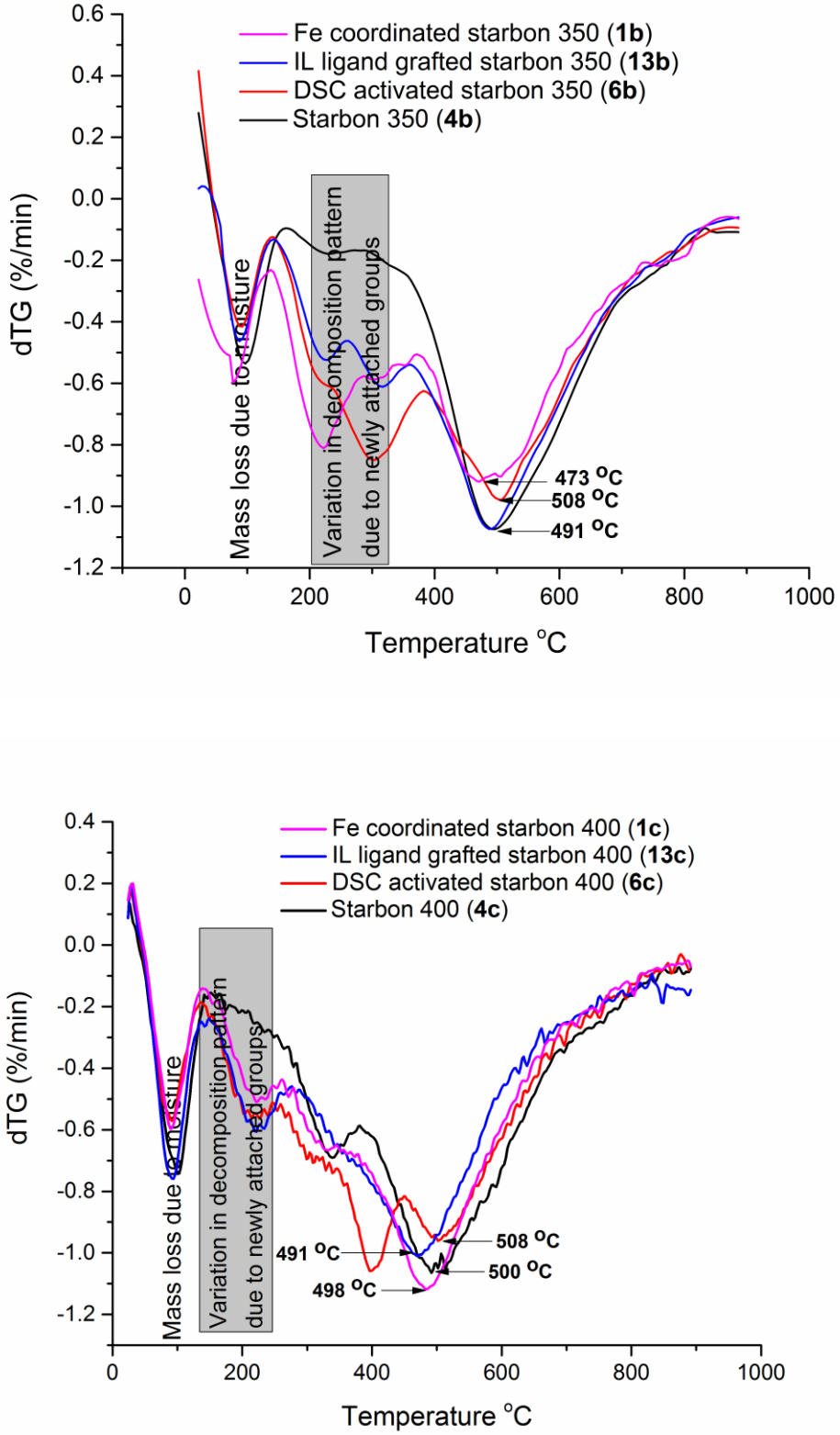

Figure 3.22. Thermal analysis data (dTG) of Starbon™ 350 (Top) and Starbon™ 400 (Bottom) in N_2.

The point of inflection which corresponds to the major mass loss temperature, signifying the breakdown of Starbon™ back bone, is decreased by the chemical modification; 492 ºC (Starbon™ 350, **4b)**, 491 ºC (ligand grafted Starbon™ 350, (**13b**)), and 473 ºC (Fe-NHC immobilised Starbon™ 350, (**1b**)). However, an increase in the temperature at the point of inflection is observed for succinimidyl carbonate derivative (**6b**) 508 ºC.

A clear difference is observed in the decomposition of Starbon™ 400 which shows that the support itself starts to decompose at a very low temperature of about 120 ºC, a behaviour that is not expected of a material that has been carbonised at 400 ºC. This unusual behaviour could perhaps be due to different ways in which the materials were prepared (e.g. different furnaces used to carbonise the Starbon materials). The exact reason may be difficult to prove since the Starbon materials used in this research were obtained and used as received.

In terms of the points of inflection, similar trends were observed with the Starbon™ 400 and its modified forms: 500 ºC (**4c**), 508 ºC (**6b**), 491 ºC (**13b**), and 498ºC (**1b**). All the modified Starbon^{TM} samples analysed showed decompositions at around 220-300 ºC attributed to the decomposition of the various groups (succinimidyl carbonate and NHC ligand) attached during modification. This observation further proves the successful modification of the supports.

While heating in air, no residue is obtained for the Starbon™-350, succinimidyl carbonate activated Starbon™-350, and Ligand grafted Starbon™-350. However, for the Fe coordinated Starbon™-350, reddish brown residue (4%) was obtained confirming the presence of iron (see appendix G) in proportion that agrees with the reported iron contents from ICP-MS analysis.

3.2.2.5. Mössbauer Spectroscopy of (1b) and (1c)

Mössbauer spectroscopy was used to ascertain the presence of iron and its oxidation state in the materials **1b** and **1c**.

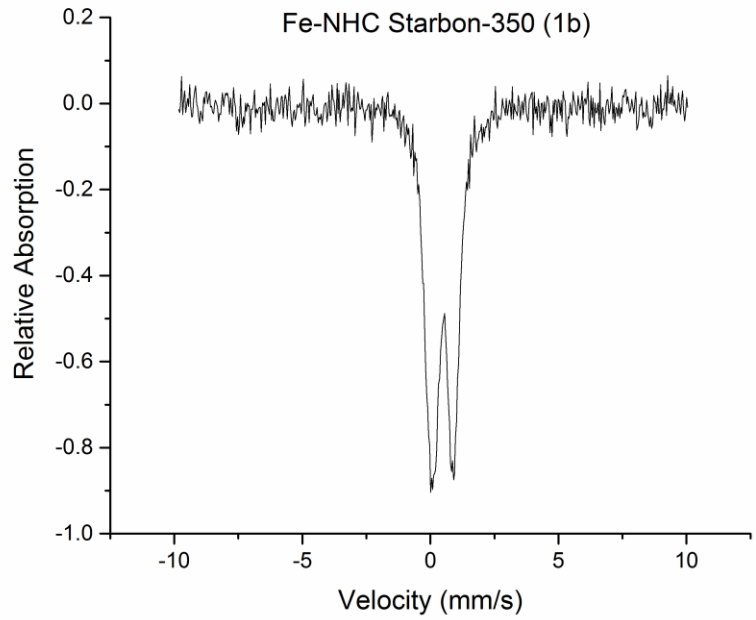

Figure 3.23. Mössbauer trace for the fabricated Starbon™-Fe catalyst.

The Mössbauer spectrum for Starbon™-350 Fe fabricated catalyst (**1b**) (Figure 3.23) confirms the presence of iron in the form of Fe^{3+}. A characteristic isomer shift of 0.47 coupled with quad. splitting of 0.81 are representative of Fe^{3+}.[200] The presence of iron, as well as oxygen and nitrogen, was further evidenced by XPS analyses.

3.2.2.6. X-ray photoelectron spectroscopy of 1b, 1c and 4b and 4c

X-Ray photoelectron spectra (Figures 3.24-3.25) were obtained for both the Starbon™-350 (**4b**) and Starbon™-400 (**4c**), and subsequently for the Fe-NHC Starbon™-350 (**1b**) and Fe-NHC Starbon™-400 (**1c**), to evaluate their chemical composition before and after modification.

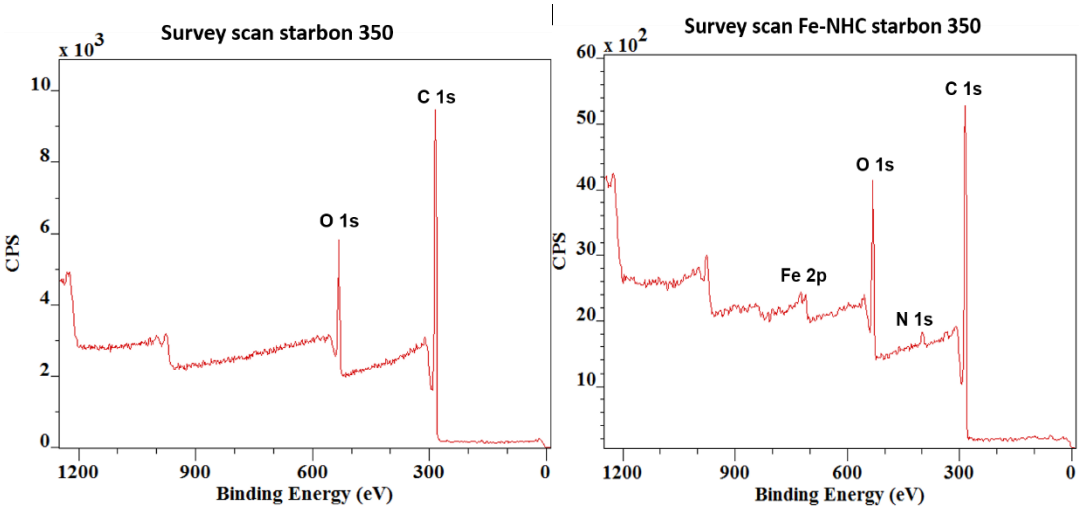

Figure 3.24. XPS survey scan for the Starbon™-350 **4b** and Fe-NHC Starbon™-350 **1b**.

The survey spectra above (Figure 3.24) corresponding to the Starbon™-350 and the Fe-NHC Starbon™-350, shows an interesting difference in the fact that two new additional binding energy peaks appear at 400 eV and 711 eV corresponding to nitrogen and iron, respectively. The presence of a nitrogen peak at 400 eV confirms that the imidazolium ligand was successfully grafted on Starbon™-350 whilst a Fe doublet peak at 711 eV entails a successful Fe complexation on the ligand.

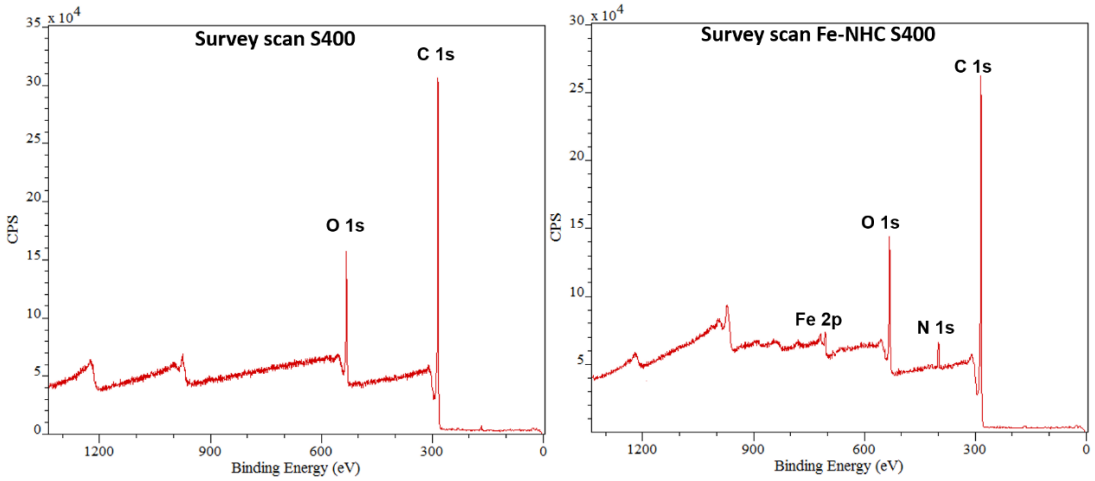

Figure 3.25. XPS survey scan for Starbon™-400 **4c** and Fe-NHC Starbon™-400 **1c**.

Figure 3.25 corresponding to the XPS survey scans for Starbon™-400 **4c** and the Fe-NHC Starbon™-400 **1c**, shows similar trends with two newly observed additional binding energy peaks which appear at 400 eV and 711 eV corresponding to nitrogen and iron, respectively. The presence of a nitrogen peak at 400 eV confirms that the

imidazolium ligand was successfully grafted on Starbon™-400 whilst an Fe doublet peak at 711 eV entails a successful Fe complexation.

As discussed earlier for the XPS analysis of Fe-NHCs immobilised on HACS (see section 3.1.1.11) the deconvoluted carbon 1s peaks of the Starbon™ 350 and Starbon™ 400 (Figure D1 and D4 in Appendix D) shows similar binding energy peaks at 289.1, 286.5, 284.7 and 283.6 eV assigned to C=O, C-O, C-C, and C-C(Ar). For the Fe-NHC Starbon™ 350 and Fe-NHC Starbon™ 400 additional carbon binding energy peaks at 283.9, and 285.6 eV assigned to C-C(Ar), and C-N,[195] were observed. These additional binding energy peaks are assigned to compound **12** attached on the various Starbon™ supports. Another interesting and further supportive evidence of the ligand binding on the support material is the decrease in the intensity of the C-O peak at 286.5 eV and a corresponding increase in C-C(Ar) peak at 283.6 eV, attributed to the successful activation of hydroxyl groups on the support and increasing aromatic character due to the mesityl group of the imidazole ligand **12,** respectively.

The O 1s spectra of the Starbon™ 350 and Starbon™ 400 (Figure D2 and D5 in Appendix D) shows three binding energy peaks at 529.5, 531.5 and 534.2 eV assigned to C=O, C-O and O-H bonds respectively.[196] However, the deconvolution of the oxygen peak of the Fe-NHC Starbon™ 350 shows another important and striking difference with the decrease in the O-H peak intensity which confirms the loss of some hydroxyl groups from the Starbon™ 350. This decrease in the intensity of the hydroxyl peak and the corresponding increase of the C=O peak observed in both the deconvoluted oxygen peaks of the Fe-NHC Starbon™ 350 and 400, indicates and further prove the successful attachment of **12** on the Starbon™ 350 support which leads to the formation of **1b.**

The appearance of a nitrogen 1s peak at 400eV in the XPS survey spectra of the Fe-NHC Starbon™-350 and Fe-NHC Starbon™-400 (Figure D3 and D6 in Appendix D) which was originally absent as can be seen in the survey spectra of the unmodified Starbon™ 350 and 400, is a clear indication that a new compound containing nitrogen has been attached to the Starbon™-350 and Starbon™-400 supports. Further deconvolution of the N 1s peak indicates two different nitrogen bonding environments at 398.3, and 401.3eV assigned to C-N and C=N, respectively. This however, is

believed to have come from compound **12** attached to the Starbon™-350 and Starbon™-400 supports.

The appearance of an Fe doublet peaks with the Fe 2p1/2 at 711eV in the spectra of the Fe-NHC Starbon™-350 and Fe-NHC Starbon™-400 (Figure D3 and D6 in Appendix D) confirms the presence of the coordinated iron predominantly in the +3 oxidation state.

3.2.2.7. Scanning Electron Microscopy (SEM)

Figures 3.26 and 3.27 show the SEM images of the Starbon™ supports and their modified forms.

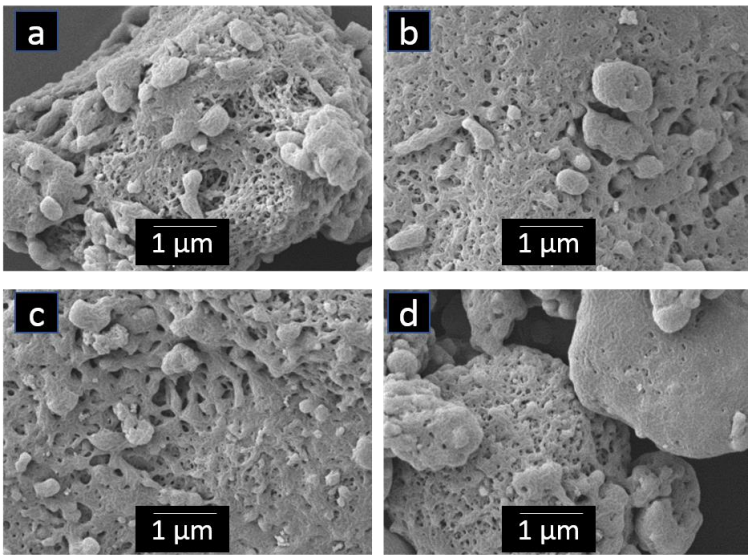

Figure 3.26. SEM micrographs of (A) Starbon™-350 (**4b**) (B) Succinimidyl carbonate activated Starbon™-350 (**6b**) (C) Ligand grafted Starbon™-350 (**13b**) and (D) Fe-NHC Starbon™-350 (**1b**).

Figure 3.26 indicate that both Starbon™-350 and Starbon-400 supports remain visually porous and despite the several chemical and mechanical processes they underwent during the succinimidyl carbonate activation, imidazolium ligand binding and iron coordination reactions.

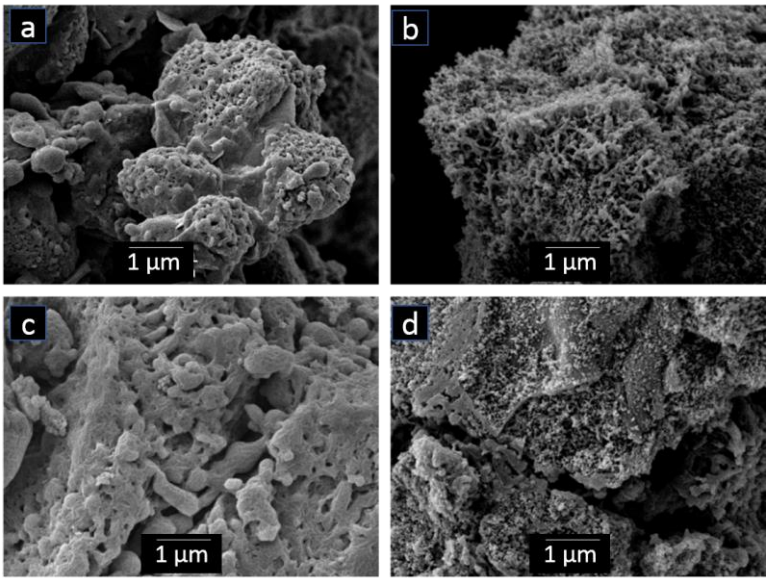

Figure 3.27. SEM micrographs of (A) Starbon™-400 (**4c**) (B) Succinimidyl carbonate activated Starbon™-400 (**6c**) (C) Ligand grafted Starbon™-400 (**13c**) and (D) Fe-NHC Starbon™-400 (**1c**).

3.2.2.8. Transmission Electron Microscopy (TEM)

Figure 3.28 shows the TEM images of the FE-NHC Starbon™-350 (**1b**) and Fe-NHC Starbon™-400 (**1c**).

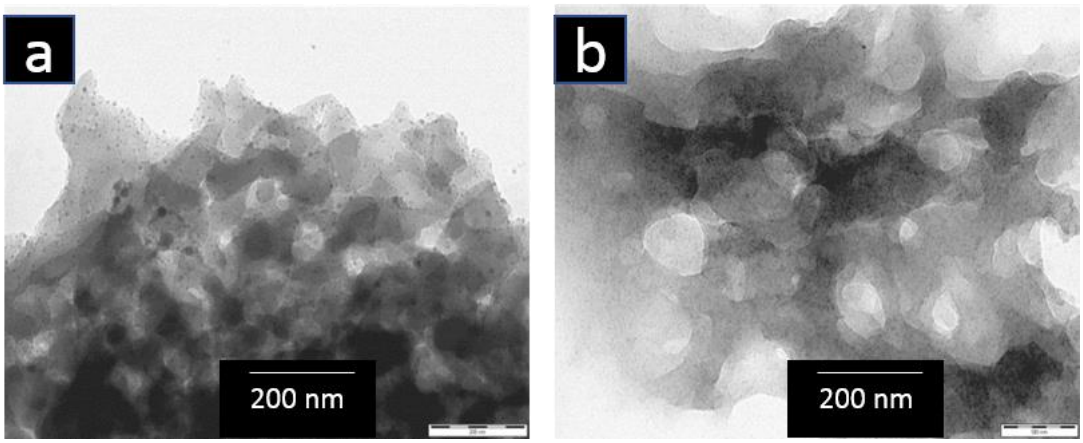

Figure 3.28. TEM microimages of (A) Fe-NHC Starbon™-350 (**1b**) and (B) Fe-NHC Starbon™-400 (**1c**).

The TEM image of the Fe-NHC Starbon™-350 (**1b**) shows scattered dense particles, which are expected to be iron oxide nanoparticles form during the iron complexation reaction. This may occur due the rapid oxidation of residual iron particles on exposure of the iron coordinated Starbon™-350 to the atmosphere during drying process.

Interestingly, the TEM image of the Fe-NHC Starbon™-400 (**1c**), shows absence of nanoparticles as no dense particles were observed. This confirms that the iron contained in the Fe-NHC Starbon™-400 (**1c**) is purely the intended complexed iron covalently bonded to the imidazolium ligand (**12**).

3.2.2.9. N_2 Adsorption Porosimetry

Table 3.8 summarizes the textural (surface area (S_{BET}), pore diameter (D_{BJH}), and pore volume (V_{BJH})) properties of the Starbon™-350 (**4b**), Fe-NHC Starbon™-350 (**1b**), Starbon™-400 (**4c**) and Fe-NHC Starbon™-400 (**1c**).

Table 3.8. Porosity data for the Starbon™ and modified Starbons.

Sample	**Pore volume ($cm^3\ g^{-1}$)**	**Adsorption pore diameter (nm)**	**Desorption pore diameter (nm)**	**BET surface area ($m^2\ g^{-1}$)**
Starbon™-350 (**4b**)	0.3	11	11	337
Fe-NHC Starbon™-350 (**1b**)	0.3	9	9	132
Starbon™-400 (**4c**)	0.2	64	48	60
Fe-NHC Starbon™-400 (**1c**)	0.2	77	48	13

From the unmodified Starbon supports (**4b** and **c**) through to the desired Fe-NHC (**1b** and **c**) the BET surface area decreased; 337 $m^2\ g^{-1}$ (**4b**) to 132 $m^2\ g^{-1}$ (**1b**) and 60 $m^2\ g^{-1}$ (**4c**) to 13 $m^2\ g^{-1}$ (**1c**). The observed decrease in surface area and pore volume may be explained by the attachment of the imidazolium ligand on the Starbon™ surface leading to blockage and filling of the porous structure.

Again, an unusual behaviour in the porosity values is observed in Starbon 400, very low surface area and an increase rather than a decrease in the pore diameters with modification. This could perhaps be due to different ways in which the materials were prepared as mentioned earlier.

3.2.3. Fe-NHCS immobilised on mango peel (1d) and orange peel cellulose (1e)

3.2.3.1. ATR-FTIR spectroscopy

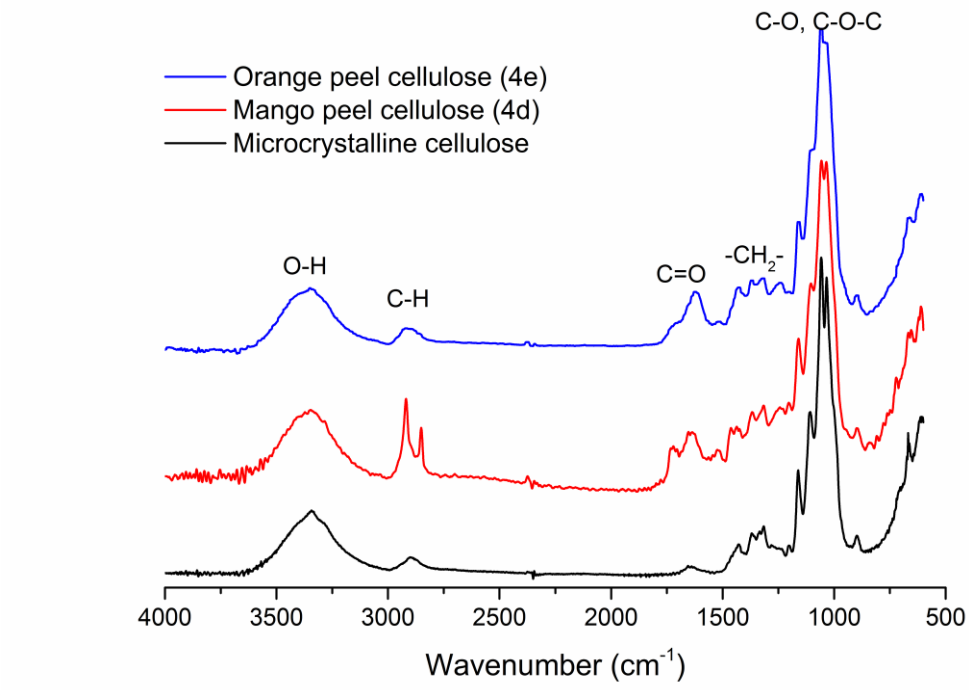

Figure 3.29 FT-IR spectra of microcrystalline cellulose (black line), mango peel cellulose (**4d**) and orange peel cellulose (**4e**)

FTIR spectroscopy was used to investigate the similarity in the structure of the isolated mango peel (**4d**) and orange peel cellulose (**4e**) in comparison with that of microcrystalline cellulose (Figure 3.29). The IR spectra of the mango peel cellulose (**4d**) and orange peel cellulose (**4e**) as compared to microcrystalline cellulose, shows similar absorption bands with only an increase in the intensity of the absorption bands at 1650-1750 cm^{-1} assigned to carbonyl stretching associated with residual pectinaceous matter and 2850-2920 cm^{-1} assigned to CH_2 symmetric and asymmetric stretching. The broad band at 3600-3100 cm^{-1} region is due to the OH-stretching vibration. The nature of the O-H stretching band gives considerable information concerning the hydrogen bonds, and as such can give a useful information regarding the crystalline or amorphous nature of the cellulose. The bands characteristic of hydrogen bonds from the spectrum of amorphous cellulose became sharper and with lower intensity, and usually they are shifted to higher wavenumbers. The absorption band at 1430 cm^{-1} is assigned to a symmetric CH_2 bending vibration, it is also known

as the "crystallinity band", indicating that a decrease in its intensity indicates a reduce degree of crystallinity of the samples while an increase in its intensity indicates a higher degree of crystallinity.[163, 203] The various contributions from the glucopyranose ring of cellulose (C-O, O-C-O) are at 1250-750 cm^{-1}.[204]

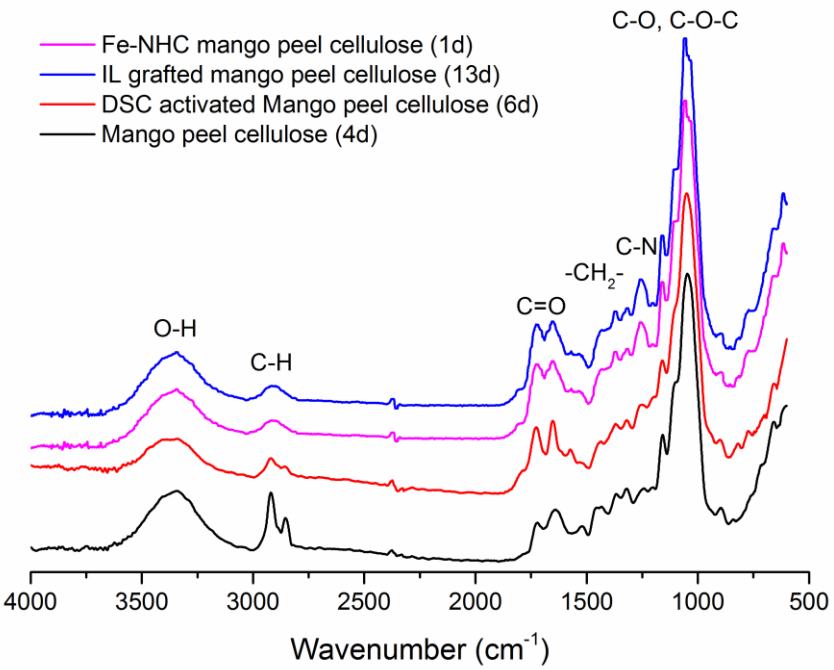

Figure 3.30 FT-IR spectra of mango peel cellulose (**4d**), DSC activated mango peel cellulose (**6d**), ligand grafted mango peel cellulose (**13d**) and Fe-NHC immobilised on mango peel cellulose (**1d**)

Figure 3.30 shows the FT-IR spectroscopy of the derivatives of **4d** leading to the formation of **1d**. The appearance of new carbonyl stretching bands at 1601, 1650 and 1700 cm^{-1} in the succinimidyl carbonate activated mango cellulose (**6d**) and a band at 1239 cm^{-1} assigned to imide C-N vibration[175, 177] are noted. This is further supported by the disappearance of the band at 1601 cm^{-1} in the spectrum of the ligand grafted mango cellulose (**13d**) due the loss of the carbonyl of the succinimidyl carbonate as the ligand is successfully attached.

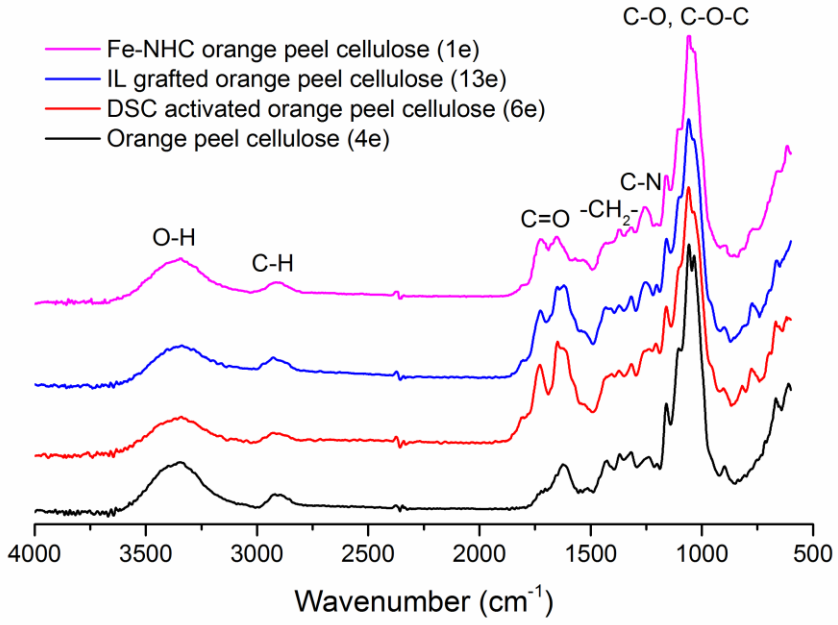

Figure 3.31 FT-IR spectra of orange peel cellulose (**4e**), DSC activated orange cellulose (**6e**), ligand grafted orange peel cellulose (**13e**) and Fe-NHC immobilised on orange peel cellulose (**1e**).

Like the observations made in the FT-IR spectra of mango cellulose and its modified forms, the FTIR spectra of orange peel cellulose and its modified forms (Figure 3.31) also shows new carbonyl stretching bands at 1650 and 1700 cm^{-1} in the succinimidyl carbonate activated orange peel cellulose. These changes occur due to the additional new carbonyl groups from the succimidyl carbonate group attached during activation. Displacement of the succininidyl carbonate by the ligand to afford (**13e**) is less discernible by FT-IR spectroscopy but is evidenced by elemental analysis and XPS as discussed later. Conversion of **13e** in to **1a** interestingly shows an increase in the intensity of the carbonyl absorption at 1700 cm^{-1}.

3.2.3.2. ^{13}C CPMAS Spectroscopy

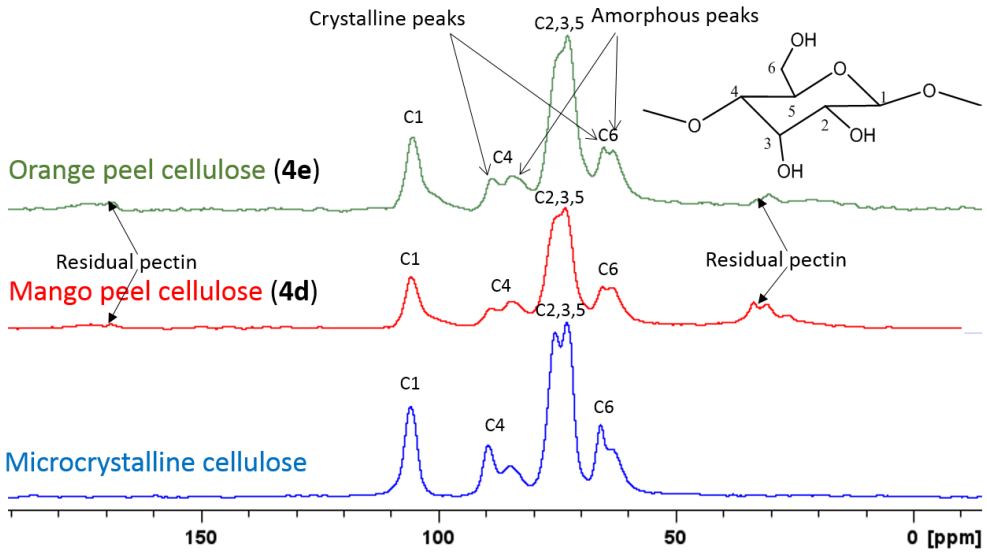

Figure 3.32 ^{13}C CP-MAS NMR spectra of microcrystalline cellulose (blue line), mango peel cellulose (**4d**) and orange peel cellulose (**4e**).

To further characterise the isolated mango peel cellulose, cross polarisation magic angle spinning ^{13}C NMR spectroscopy was performed and the result compared to commercial grade microcrystalline cellulose (Figure 3.32). The spectra for mango peel cellulose (**4d**) and orange peel cellulose (**4e**) are similar to that of microcrystalline cellulose. Some evidence, albeit very minor, of residual pectinaceous matter is seen in **4d** and **4e** with signals at 20-30 ppm characteristic of CH_3 of rhamnose and at 170 ppm characteristic of carboxylic acid and ester moieties. Otherwise, signals observed around 65, 88 and 106 ppm are assigned to C-6, C-4 and C-1 of the glucose monomer unit of the cellulose, respectively. The major peak in 72.5 ppm is assigned to C-2, -3, -5 of the glucose monomer unit of the cellulose.[205] Information with respect to crystallinity can be gleaned from interrogation of the C-4 and C-6 signals. For C-4, signals at 80~86 ppm relate to its amorphous nature whilst signals at 86~92 ppm confer more crystallinity. Similarly, for C-6 signals at 63~65 ppm relate to amorphous character but when at 65~67 ppm are akin to crystallinity.[206]

These findings however, indicates that the isolated cellulose from the orange peels contain almost equal proportions of amorphous to crystalline cellulose. Unlike the microcrystalline cellulose which contain only a small proportion of the amorphous type.

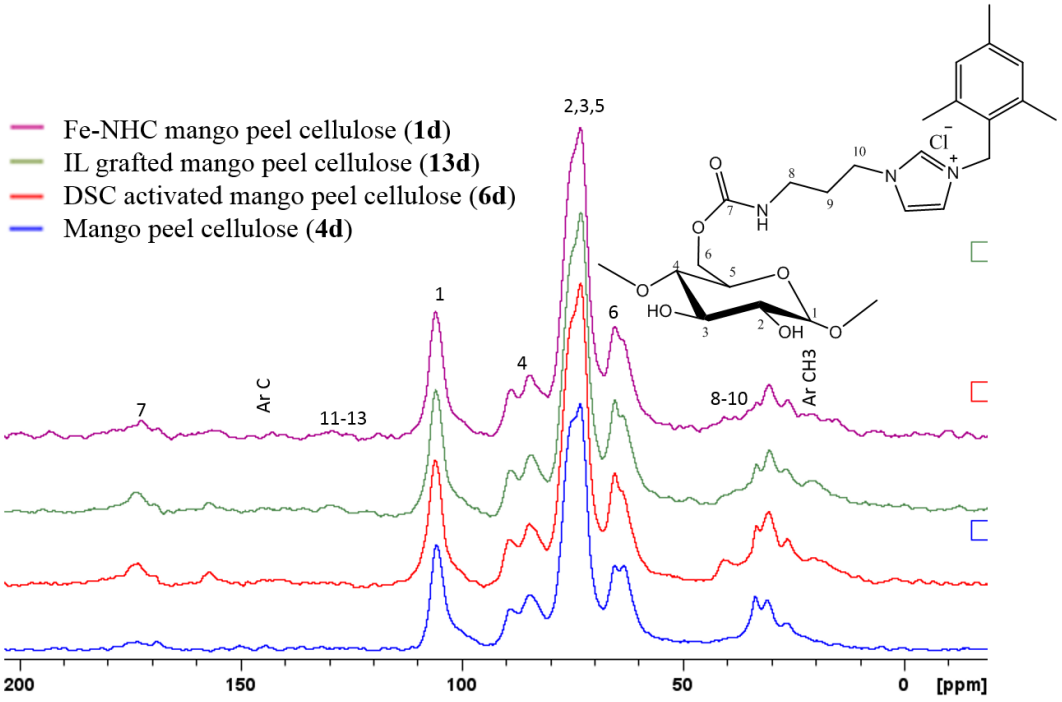

Figure 3.33 ^{13}C CP-MAS NMR stacked spectra of mango peel cellulose (**4d**), DSC activated mango peel cellulose (**6d**), ligand grafted mango peel cellulose (**13d**) and Fe-NHC immobilised on mango peel cellulose (**1d**).

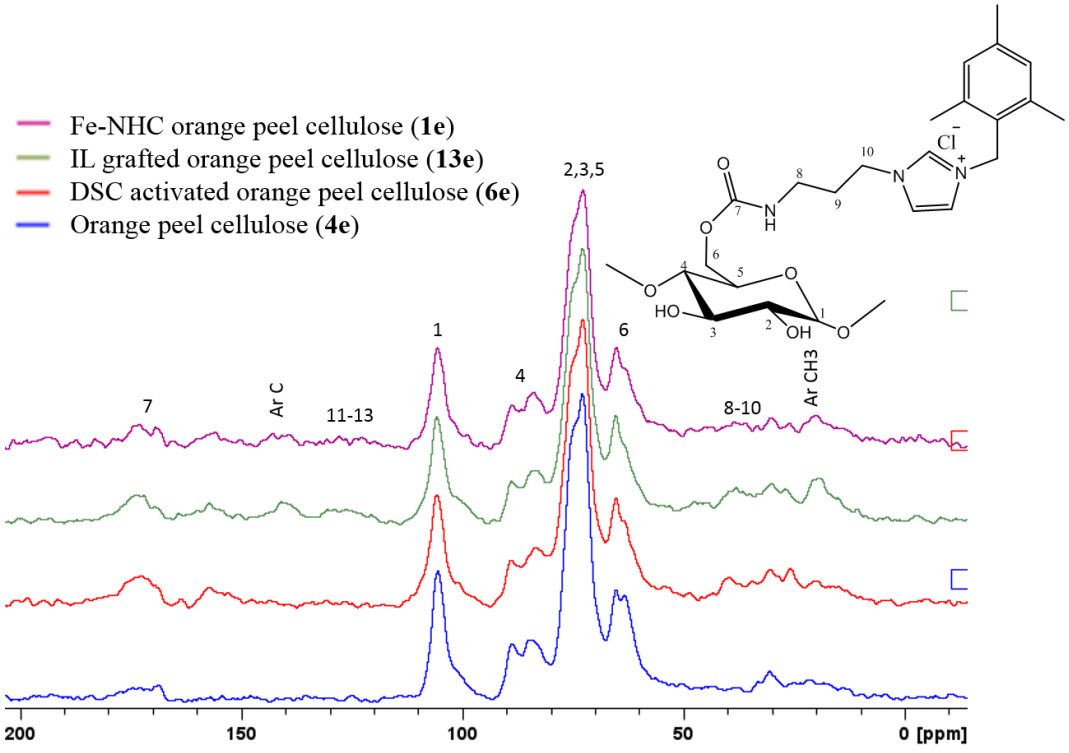

Figure 3.34 ^{13}C CP-MAS NMR spectra of orange peel cellulose (**4e**), DSC activated orange peel cellulose (**6e**), ligand grafted orange peel cellulose (**13e**) and Fe-NHC immobilised on orange peel cellulose (**1e**).

Figures 3.33 and 3.34 show the ^{13}C CP-MAS spectra of mango peel and orange peel cellulose and its conversion in to **1d** and **1e**, respectively. The spectra of the succinimidyl carbonate activated mango peel (**6d**) and orange peel cellulose (**6e**) showed new signals in the carbonyl region corresponding to carbonyl of the carbamate and imide respectively, and the signal at 40 ppm which corresponds to CH_2 group of the imide thus confirming the successful attachment of the succinimidyl group during activation. The spectra of the imidazolium ligand grafted mango peel (**13d**) and orange peel cellulose (**13e**) showed the loss of carbonyl signal of the imide. The signals numbered 8,9 and 10 correspond to CH_2 groups of the aminopropyl group of the imidazole ligand and peaks at 23 ppm, assigned to aromatic CH_3. The spectra confirm the successful attachment of the ligand on the activated mango and orange peel cellulose support. After modification of the cellulose surface, C-6 (to which the most accessible OH is attached to) signal at around 65 ppm was affected by the succinimidyl carbonate and imidazole ligand groups, causing a change in the proportion of the amorphous to crystalline region, with the cellulose support becoming more amorphous.

3.2.3.3. CHN and ICP-MS elemental analysis.

From the results of the CHN elemental analysis of **6d** (succinimidyl carbonated activated) and **13d** (ligand grafted) mango cellulose, the succinimidyl carbonate and NHC ligand loadings of the modified cellulose samples were found to be 1.49 mmol g^{-1} and 0.56 mmol g^{-1}, respectively. The Fe loading as determined by ICP-MS for Fe-NHC immobilised in mango peel cellulose (**1d**) and orange peel cellulose (**1e**) were 0.30 mmol g^{-1} and 0.52 mmol g^{-1}, respectively. Thus, once again confirming successful synthesis of the desired NHC's despite IR and NMR spectroscopy not always being so conclusive.

3.2.3.4. Thermogravimetric Analysis (TGA)

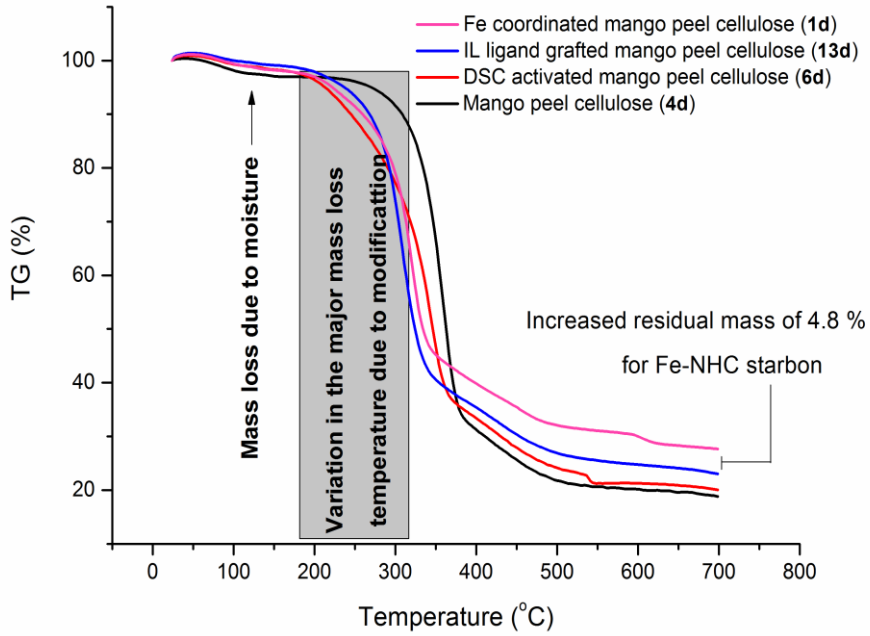

Figure 3.35. Thermograms for mango peel cellulose (**4d**) and its derivatives **6d** and **13d** leading to Fe-NHC immobilised on mango peel cellulose (**1d**) in N_2.

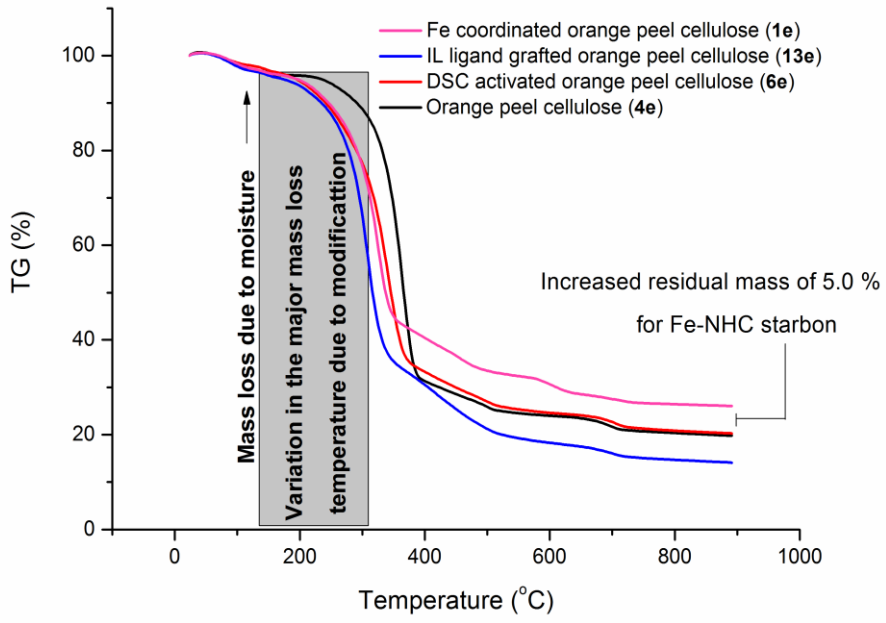

Figure 3.36. Thermograms for orange peel cellulose (**4e**) and its derivatives **6e** and **13e** leading to Fe-NHC immobilised on orange peel cellulose (**1e**) in N_2.

The thermograms of the mango and orange peel cellulose samples analysed (Figures 3.35 and 3.36) showed weight loss within the temperature range of 50 to 100 ^{o}C owing to water loss. Thereafter, both the unmodified mango and orange cellulose were stable until the onset of the major decomposition temperature around 300 ^{o}C corresponding to cellulose decomposition. However, their chemically modified forms (succinimidyl carbonate activated **6d** and **6e**, ligand grafted **13d** and **13e** and Fe-NHC immobilised **1d** and **1e**), variable decomposition temperatures were observed, with degradation starting earlier at 200 ^{o}C. This lower temperature decompositions are attributed to the breakdown of the succinimidyl carbonate and imidazolium ligand groups attached to the cellulosic supports. These changes in the decomposition profile with modification, suggests a successful succinimidyl carbonate activation and ligand binding. The increased residual mass at 650^{o}C of 4.8 and 5.0 % in Fe-NHC mango peel cellulose (**1d**) and Fe-NHC orange peel cellulose (**1e**), respectively, may indicate presence of Fe.

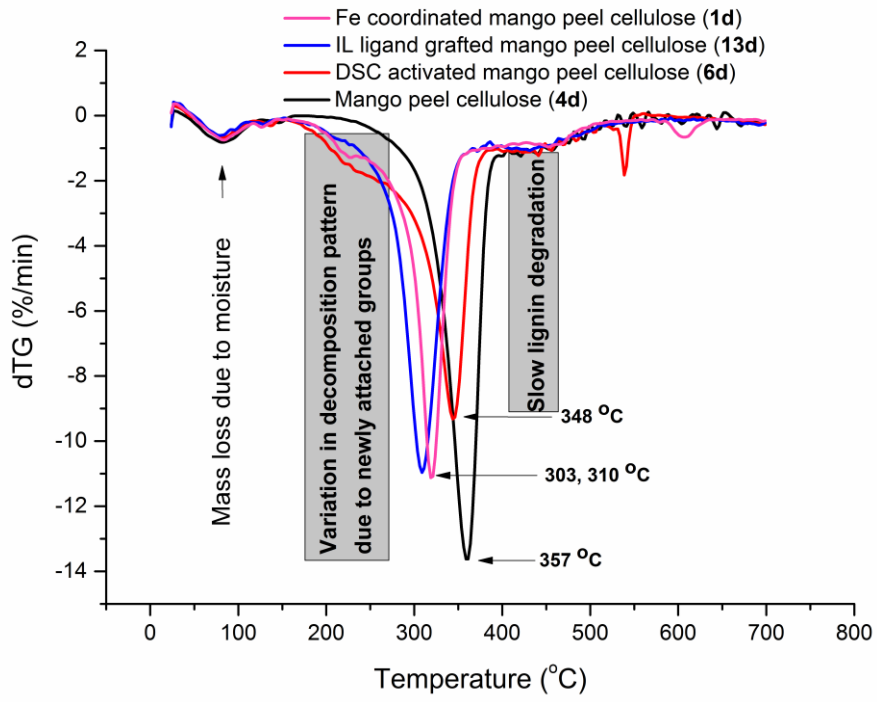

Figure 3.37. Differential thermographs for mango peel cellulose (**4d**) and its derivatives **6d** and **13d** leading to Fe-NHC immobilised on mango peel cellulose (**1d**) in N_2.

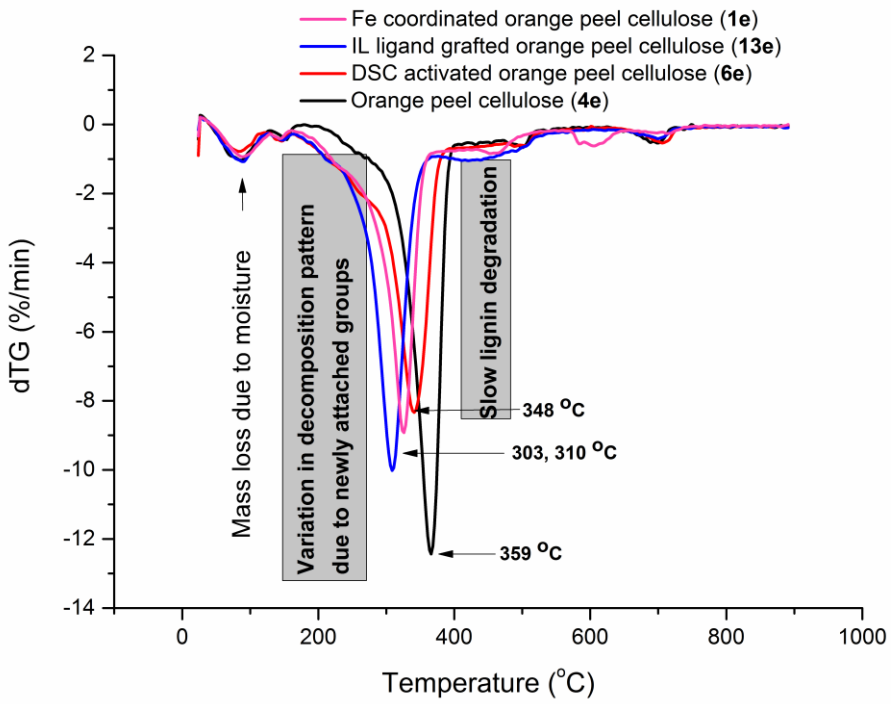

Figure 3.38. Differential thermographs (dTG) for mango peel cellulose (**4e**) and its derivatives **6e** and **13e** leading to Fe-NHC immobilised on mango peel cellulose (**1e**) in N_2.

The differential thermograms of the mango and orange peel cellulose samples analysed (Figures 3.37 and 3.38), showed that both the mango peel and orange peel cellulose togother with their modified forms have almost an identical decomposition profile. This further confirms the similarity of the two cellulose supports and the effectiveness of the modification process. The major decompostion occurs at 357°C **4d** and 359 °C **4e**. On modification T_d decreases and is the same for both supports, e.g., T_d for **6d** and **6e** is 348 °C. The T_d of the ligand grafted derivatives (**13d** and **13e**) is 303 °C and increases upon iron co-ordination to 310 °C for both **1d** and **1e**.

3.2.3.5. X-Ray photo electron spectroscopy

X-Ray photoelectron spectra were obtained for both the mango and orange peel cellulose, and subsequently for the Fe-NHC mango and orange peel cellulose, to evaluate their chemical composition before and after modification.

Figure 3.39 corresponds to the XPS survey scans for mango peel cellulose (**4d**) and orange peel cellulose (**4e**). Similar C 1s and O 1s peaks composition were observed in both the unmodified supports. Interestingly, N 1s and Ca 2p peaks were also

observed which are attributed to possible proteins and calcium deposits[160] remaining in the cellulose.

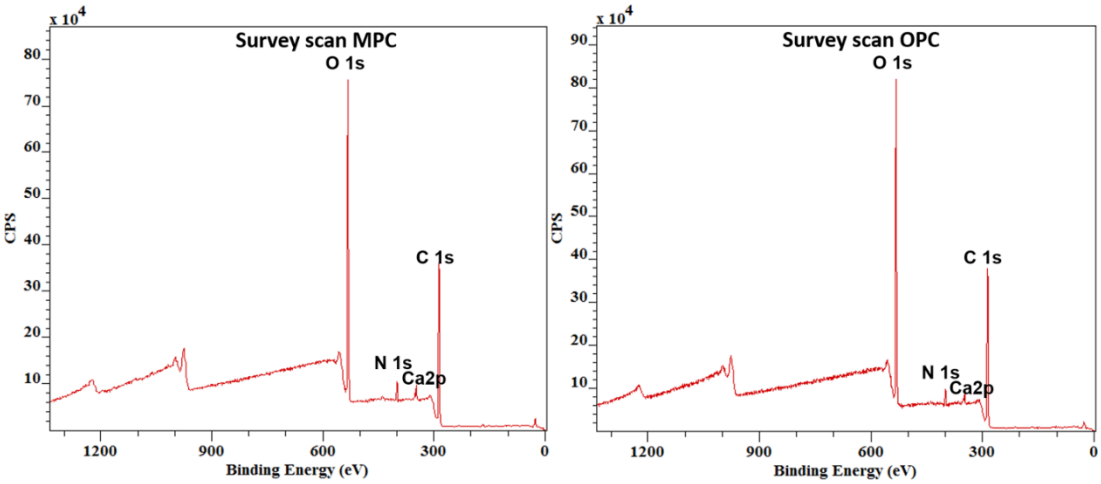

Figure 3.39. XPS survey scan for the mango peel cellulose (**4d**) and orange peel cellulose (**4e**).

Figure 3.40 showed two newly observed additional binding energy peaks which appear at 200 eV and 711 eV corresponding to chlorine and iron, respectively. A significant increase in the intensity of the nitrogen peak at 400 eV is also observed confirming that the imidazolium ligand was successfully grafted on to the mango and orange peel cellulose. Likewise, a Fe doublet binding energy peak at 711 eV and presence of chlorine peak at 200 eV entails a successful Fe complexation on the ligand bonded on both the mango and orange peel cellulose supports.

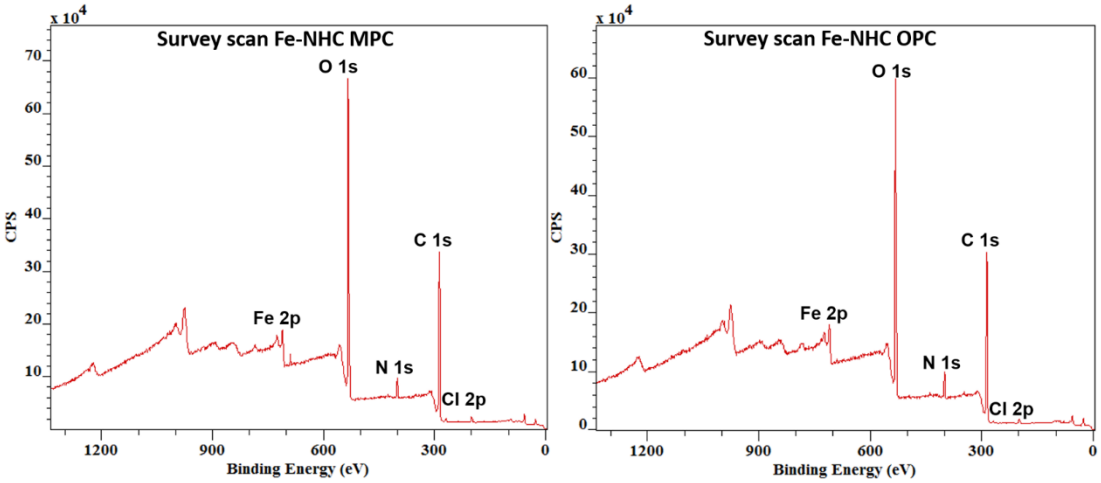

Figure 3.40. XPS survey scan for the Fe-NHC mango peel cellulose (**1d**) and Fe-NHC orange peel cellulose (**1e**).

The deconvoluted spectra for both mango and orange peel cellulose together with their derivatives are shown in Figure E1 to E6 in Appendix E. The C1s peak of the mango and orange peel cellulose shows various contributions of bonded carbon, namely carbon without oxygen bonds (C–C), carbon with one oxygen bond (C–O) and carbon with two oxygen bonds (O–C–O) in proportions which are a characteristic of cellulose.[207] However, the deconvolution of carbon peaks of the Fe-NHC mango cellulose and Fe-NHC orange cellulose shows additional peaks at 289.1, 283.9, and 285.6 eV assigned to C-C(Ar), C=O and C-N.[195] These additional peaks are assigned to compound **12** attached on the various cellulose supports. Another interesting and further supportive evidence of the ligand binding on the support material is the decrease in the intensity of the C-O peak at 286.5 eV and a corresponding increase in C-C(Ar) peak at 283.6 eV, attributed to the successful activation of hydroxyl groups on the support and increasing aromatic character due to the mesityl group of the imidazole ligand **12**, respectively.

The O 1s peak of the orange and mango peel cellulose and Fe-NHC modified orange and mango peel cellulose shows similar contributions of bonded oxygen, namely carbon oxygen bonds (C–O), carbon with double bond oxygen (C=O) and oxygen hydrogen bond (O-H). A significant difference that suggests successful modification is an increase in the (C=O) peak and a decrease in (O-H) peak due to successful ligand bonding on the activated OH group of the cellulose support which lead to loss of OH groups.

The significant increase in the nitrogen 1s peak (Figure E3 and E6 in Appendix E) at 400 eV in the XPS survey spectra of the Fe-NHC mango peel cellulose and Fe-NHC orange peel cellulose which was originally low as can be seen in the survey spectra of the unmodified mango and orange peel cellulose, is a clear indication that a new compound containing nitrogen has been attached to the cellulose supports. Further deconvolution of the nitrogen 1s peak indicates three different nitrogen bonding environments at 398, 399, and 401.3eV assigned to N-H, C-N, and C=N respectively. This however, is assigned to compound **12** attached to the cellulose supports.

The appearance of a Fe doublet peaks with the Fe 2p 1/2 at 711 eV in the spectra of the Fe-NHC mango peel cellulose (**1d**) and Fe-NHC orange peel cellulose (**1e**), (Figure

E3 and E6 in Appendix E) confirms the presence of the coordinated iron predominantly in the +3 oxidation state.

3.2.3.6. Scanning Electron Microscopy

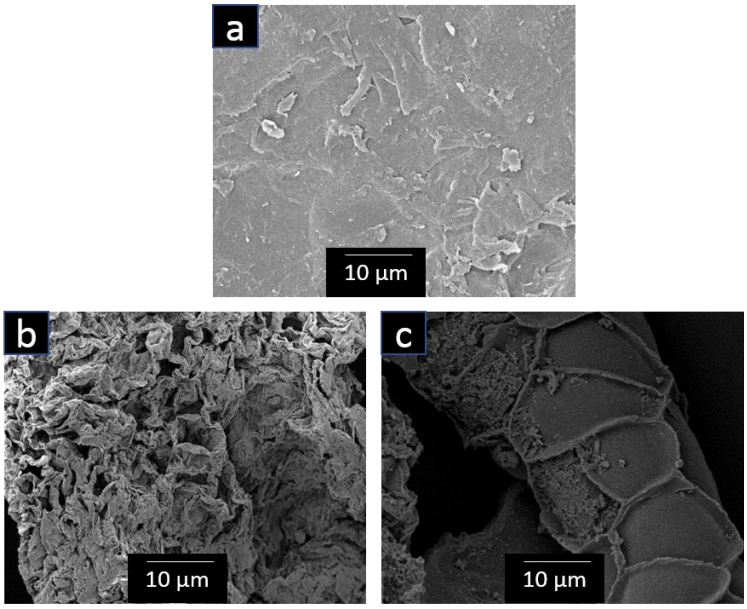

Figure 3.41. SEM images of commercial microcrystalline cellulose (a) mango peel cellulose (b) and orange peel cellulose (c).

The SEM images (Figure 3.41) shows that the extracted mango and orange peel cellulose are visually porous compared to the commercial microcrystalline cellulose which appear to be non-porous. However, some of the pores appear to be occluded within the cellulose inner structure and not accessible from the external surface.

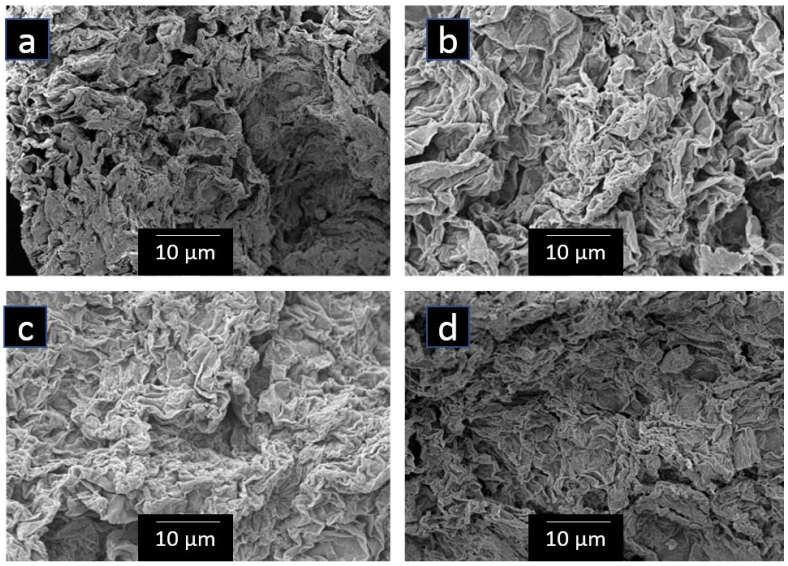

Figure 3.42. SEM images of (a) mango peel cellulose, (b) DSC activated mango peel cellulose, (c) IL grafted mango peel cellulose, and (d) Fe-NHC mango peel cellulose.

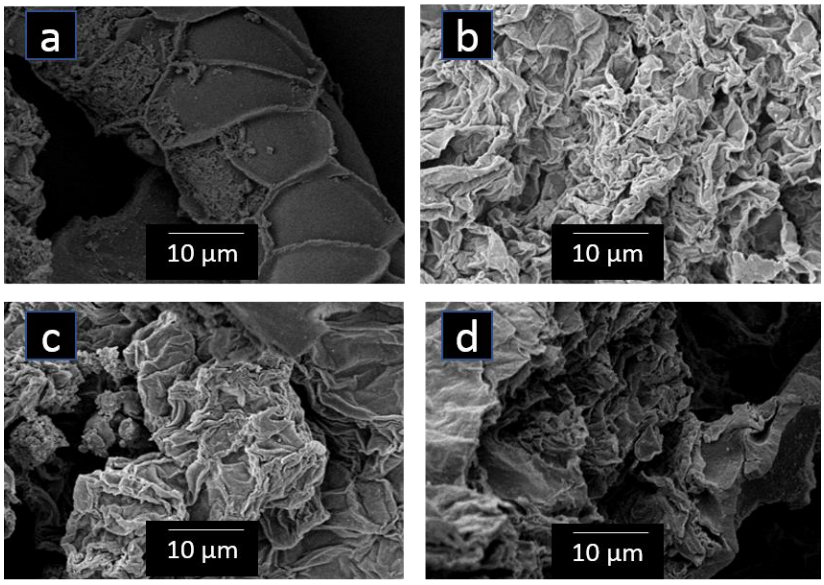

Figure 3.43. SEM images of (a) orange peel cellulose, (b) DSC activated orange peel cellulose, (c) IL grafted orange peel cellulose, and (d) Fe-NHC orange peel cellulose.

The SEM images (Figures 3.42 and 3.43) of the surface modified mango and orange peel cellulose indicates that the porous structure of the mango and orange peel cellulose is relatively stable towards the mechanical, chemical and thermal treatment it underwent during the modification processes.

3.2.3.7. Transmission Electron Microscopy (TEM)

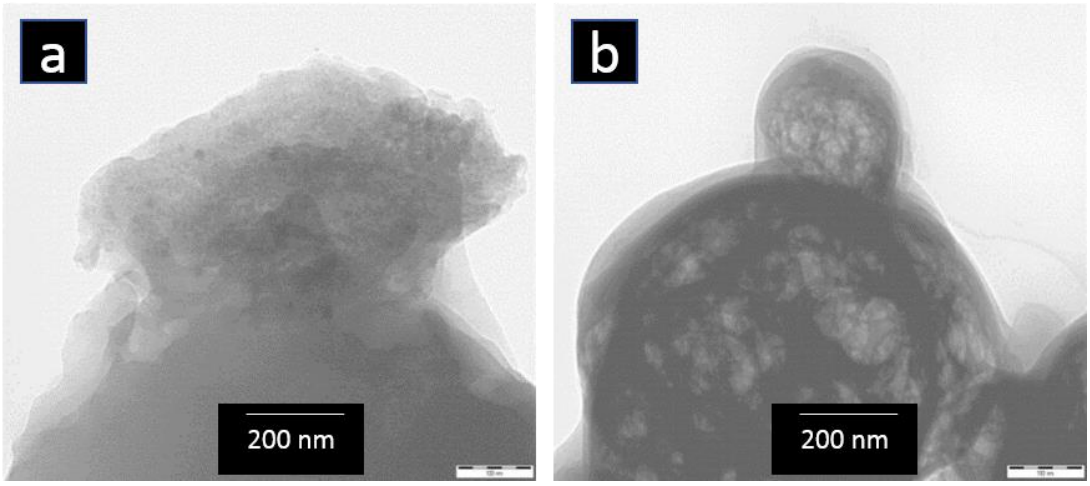

Figure 3.44. TEM images of (a) Fe-NHC mango peel cellulose, (b) Fe-NHC orange peel cellulose.

The TEM images above for Fe-NHC mango cellulose and Fe-NHC orange cellulose (Figure 3.44) showed absence of Fe nanoparticles. However, as earlier stated, the inability to zoom further due to the loss of particle of the material as a result of higher transmission that causes the particle to heat-up and thus prevents from drawing a general conclusion that the measured iron obtained from the ICP-MS, and XPS analysis only comes from the intended complexed iron covalently bonded to the imidazolium ligand and not from some Fe nano-particles.

3.2.3.8. N_2 adsorption porosimetry

The BET surface area, pore volume, adsorption and desorption pore diameters of the mango peel cellulose (**4d**), orange peel cellulose (**4e**) and their subsequent Fe-NHC modified forms, (**1d**) and (**1e**) were determined using nitrogen adsorption porosimetry (see Table 3.9). From the unmodified mango and orange peels cellulose supports through to the desired Fe-NHC (**1d** and **1e**) the BET surface area decreased; 51 m^2 g^{-1} (**4d**) to 44 m^2 g^{-1} (**1d**) and 151 m^2 g^{-1} (**4e**) to 80 m^2 g^{-1} (**1e**). The observed decrease in the BET surface area and pore volume may be explained by the attachment of the succinimidyl carbonate and subsequently the imidazolium ligand on the cellulose surface leading to blockage and filling of the porous structure.

Table 3.9. Summary of the surface and porosity properties of the samples analysed.

Sample	**Adsorp. pore diameter BJH (nm)**	**Desorp. pore diameter BJH (nm)**	**Adsorp. pore volume BJH ($cm^3\ g^{-1}$)**	**Desorp. pore volume BJH ($cm^3\ g^{-1}$)**	**BET surface area ($m^2\ g^{-1}$)**
(**4d**)	8.63	6.26	0.13	0.13	51
(**6d**)	7.05	4.73	0.06	0.06	30
(**13d**)	7.11	4.82	0.06	0.06	30
Fe-NHC mango (**1d**)	5.95	4.32	0.07	0.07	44
(**4e**)	9.37	8.45	0.34	0.34	151
(**6e**)	10.31	8.48	0.32	0.30	119
(**13e**)	9.47	7.97	0.26	0.26	95
Fe-NHC orange (**1e**)	9.99	8.22	0.22	0.22	80

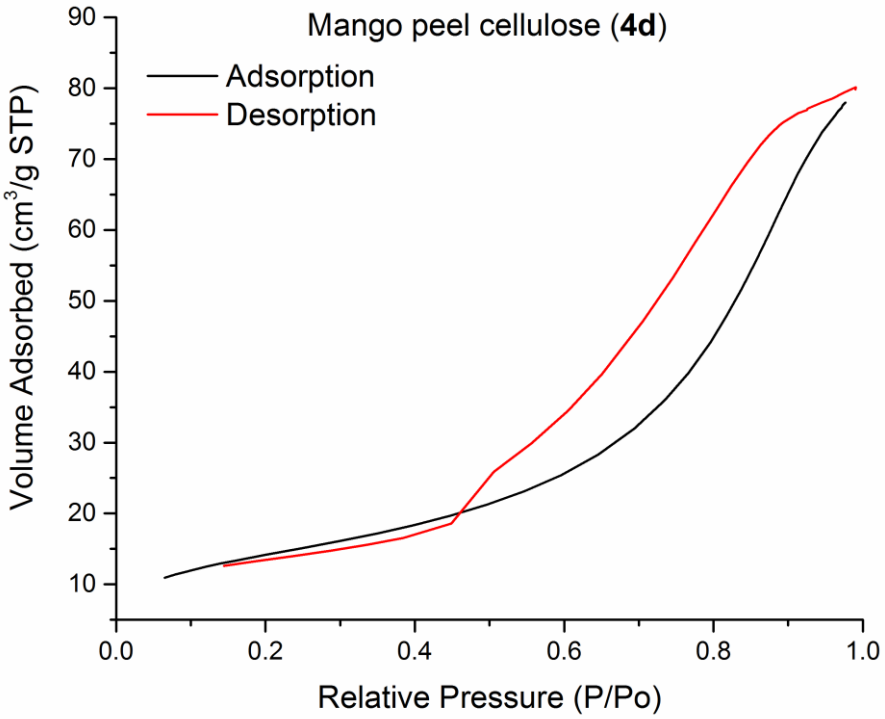

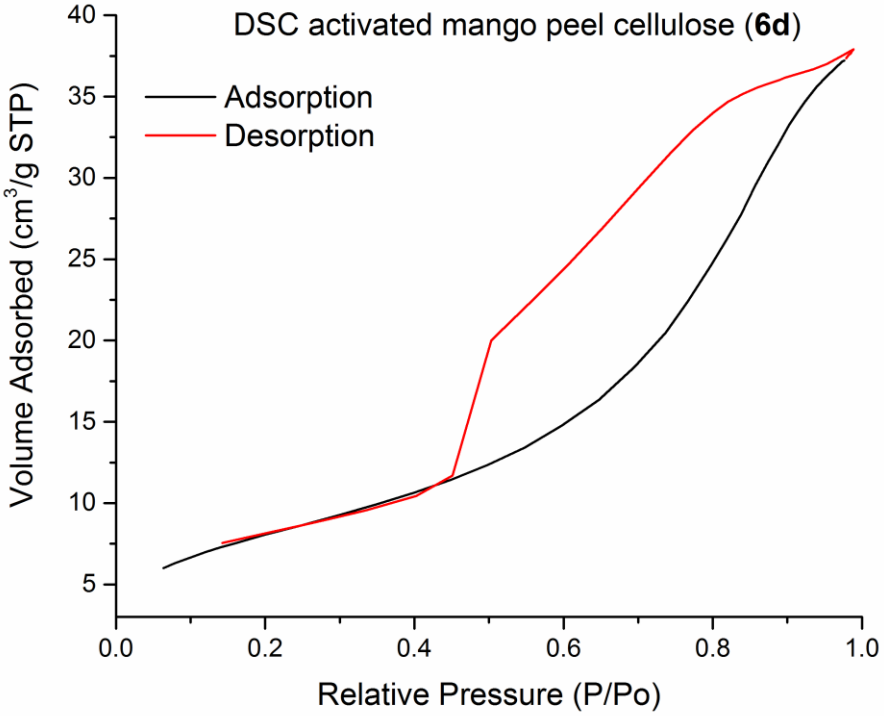
DSC activated mango peel cellulose (**6d**)
Adsorption
Desorption
Volume Adsorbed (cm³/g STP)
Relative Pressure (P/Po)
40
35
30
25
20
15
10
5
0.0
0.2
0.4
0.6
0.8
1.0

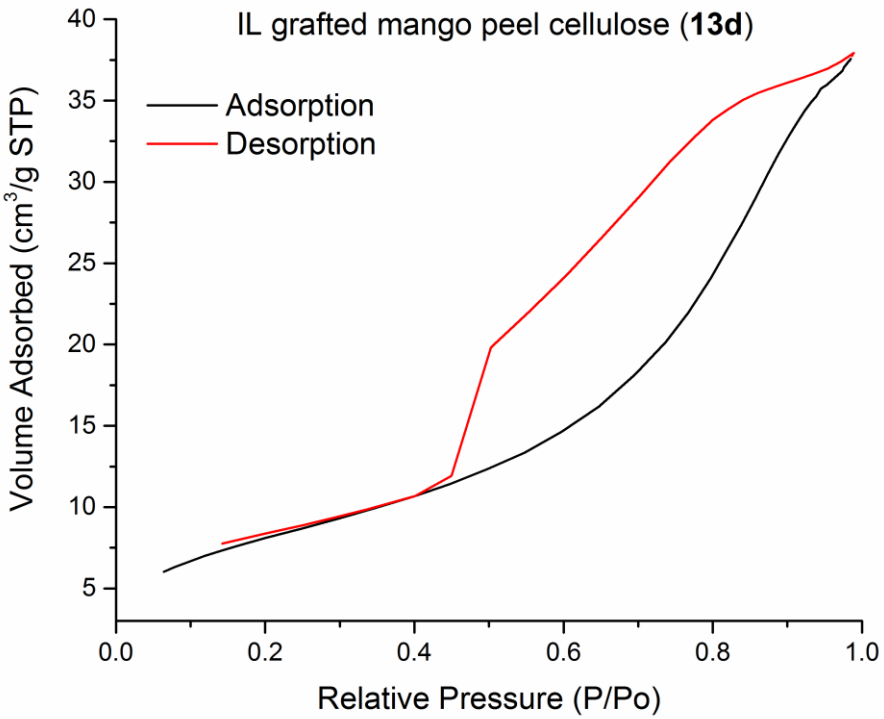
IL grafted mango peel cellulose (**13d**)
Adsorption
Desorption
Volume Adsorbed (cm³/g STP)
Relative Pressure (P/Po)
40
35
30
25
20
15
10
5
0.0
0.2
0.4
0.6
0.8
1.0

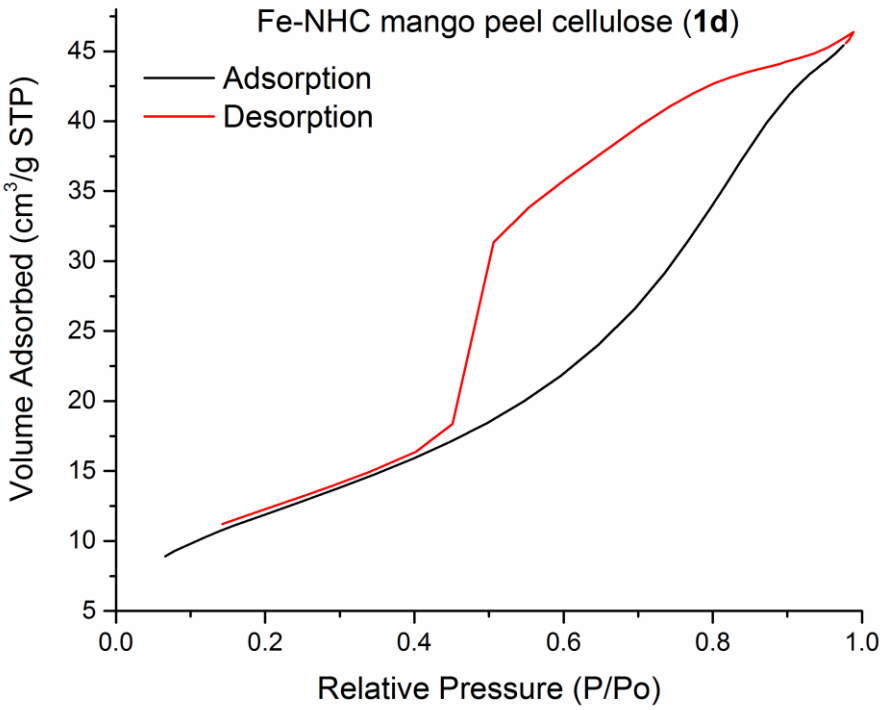

Figure 3.45: Nitrogen adsorption/desorption isotherm of mango cellulose (**4d**), DSC activated mango cellulose (**6d**), IL grafted mango cellulose (**13d**) and Fe-NHC mango cellulose (**1d**).

Figures 3.45 shows nitrogen adsorption isotherm obtained by measuring the amount of N_2 gas adsorbed across a wide range of relative pressures at a constant temperature (liquid N_2, 77K). Conversely desorption isotherms are achieved by measuring gas removed as pressure is reduced. The nitrogen isotherm indicates mesoporosity of narrow size distribution across all the samples analysed. However, noticeable changes in the desorption pattern can be seen between the mango peel cellulose and the surface modified mango cellulose grades. These changes are attributed to the reduction of the pore sizes as different groups are attached to the surface of the mango cellulose.

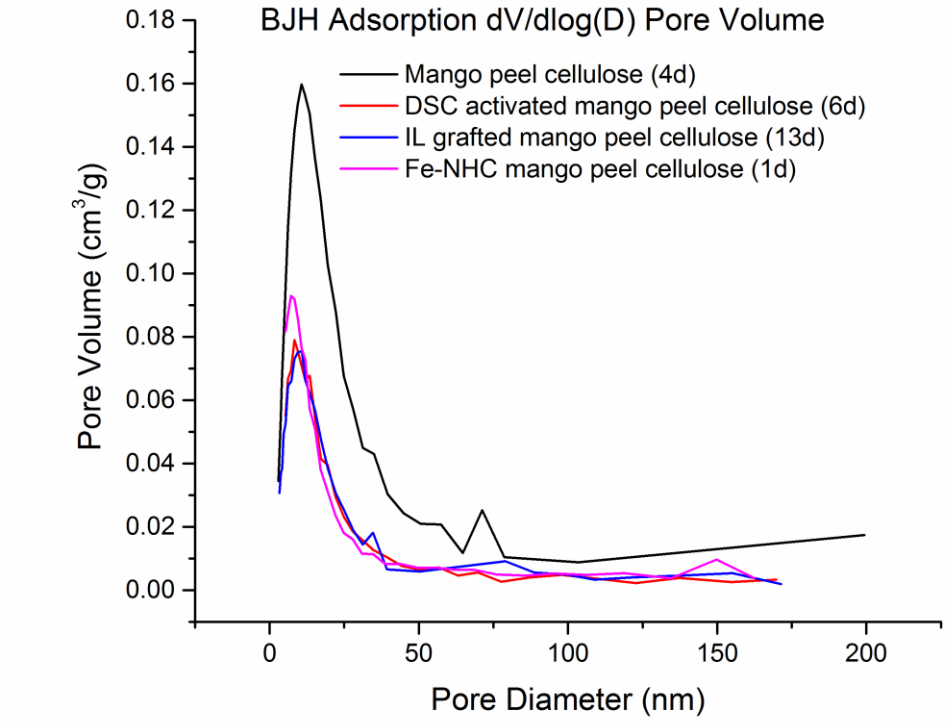

Figure 3.46. BJH adsorption dV/dlog(D) pore volume distribution for mango cellulose (**4d**), activated mango cellulose (**6d**), ligand grafted mango cellulose (**13d**) and Fe-NHC mango cellulose (**1d**).

In Figure 3.46 the BJH adsorption pore volume of the mango cellulose shows a mono-modal distribution around 10 nm while that of the DSC activated, IL grafted and Fe-NHC mango cellulose each shows a poly-modal distribution between 2-50 nm within the mesoporous region.

The mango peel BET surface area was 51.04 m^2 g^{-1} and pore volume (0.125 m^2 g^{-1}) with pores confined to the mesopore range. Indeed t-plot analysis showed micropores contributed relatively little the porosity, having negligible volume and area. The BJH pore volume agreed with the total pore volume from the adsorption isotherm at 0.9935 P/P0 (<300 nm pore diameter), further highlighting the absence of microporosity. BJH size distribution was indeed within a narrow range, having an average diameter of 7.45 nm. Moreover, the BJH adsorption pore volume of the mango cellulose shows a mono-modal distribution at 10 nm while the BJH desorption pore volume showing a characteristic tri-modal distribution with volume maxima at 2.7 nm and 10 nm.

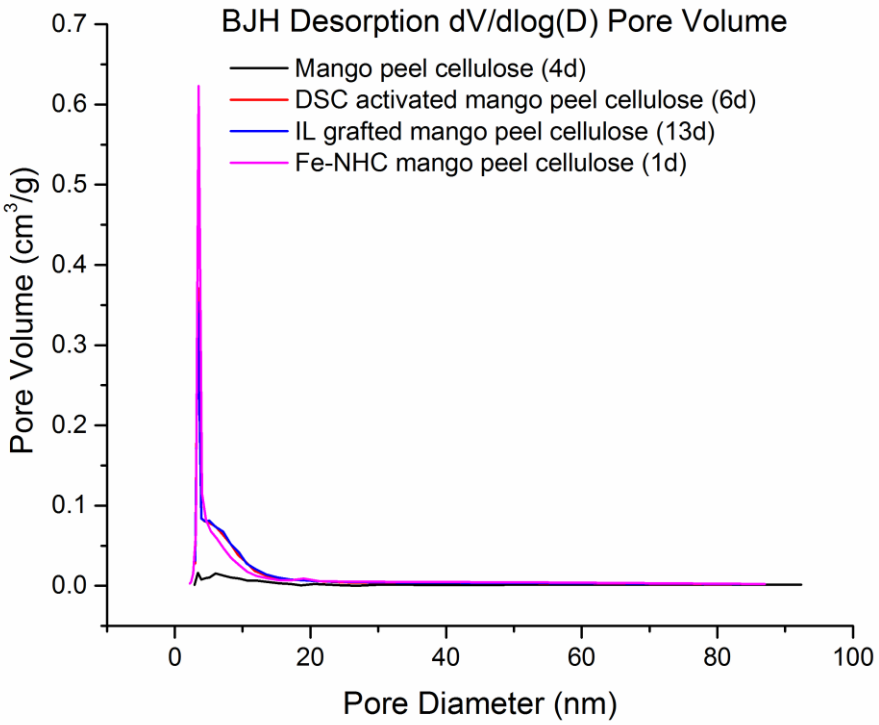

Figure 3.47. BJH adsorption dV/dD pore volume distribution of mango cellulose (**4d**), activated mango cellulose (**6d**), ligand grafted mango cellulose (**13d**) and Fe-NHC mango cellulose (**1d**)

Figure 3.47 shows BJH desorption pore volume of the four samples analysed, with mango peel cellulose (**4d**) showing a characteristic tri-modal distribution with volume maxima at 2.7 nm and 10 nm. The other three samples namely; DSC activated mango peel cellulose (**6d**), ligand grafted mango peel cellulose (**13d**) and Fe-NHC mango peel cellulose (**1e**) shows almost a mono-modal distribution.

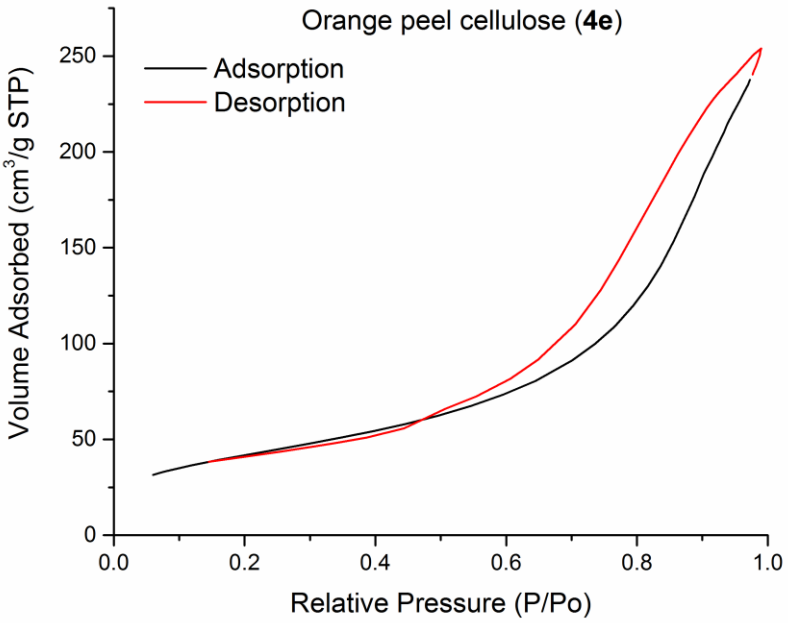
Orange peel cellulose (4e)
Adsorption
Desorption
Volume Adsorbed (cm3/g STP)
Relative Pressure (P/Po)
0
50
100
150
200
250
0.0
0.2
0.4
0.6
0.8
1.0

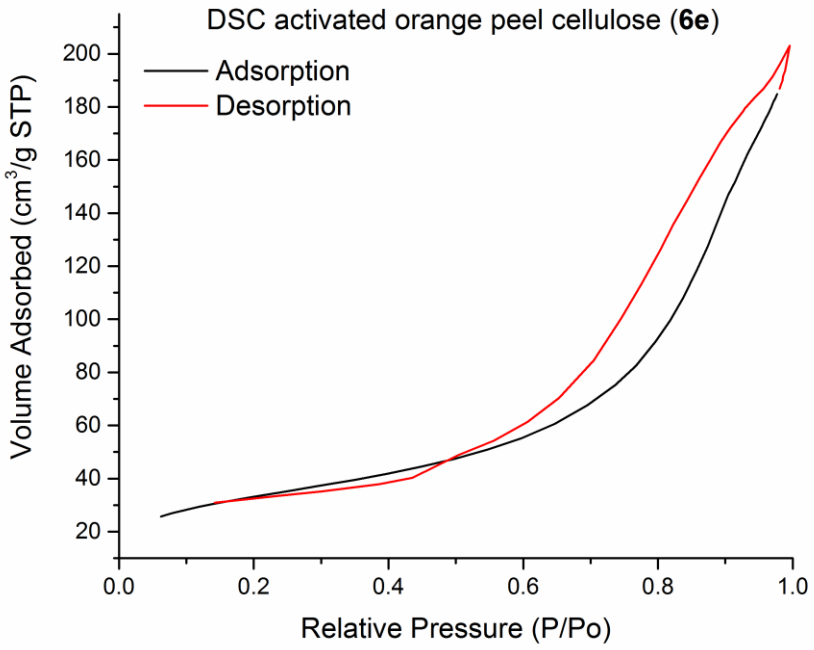
DSC activated orange peel cellulose (6e)
Adsorption
Desorption
Volume Adsorbed (cm3/g STP)
Relative Pressure (P/Po)
20
40
60
80
100
120
140
160
180
200
0.0
0.2
0.4
0.6
0.8
1.0

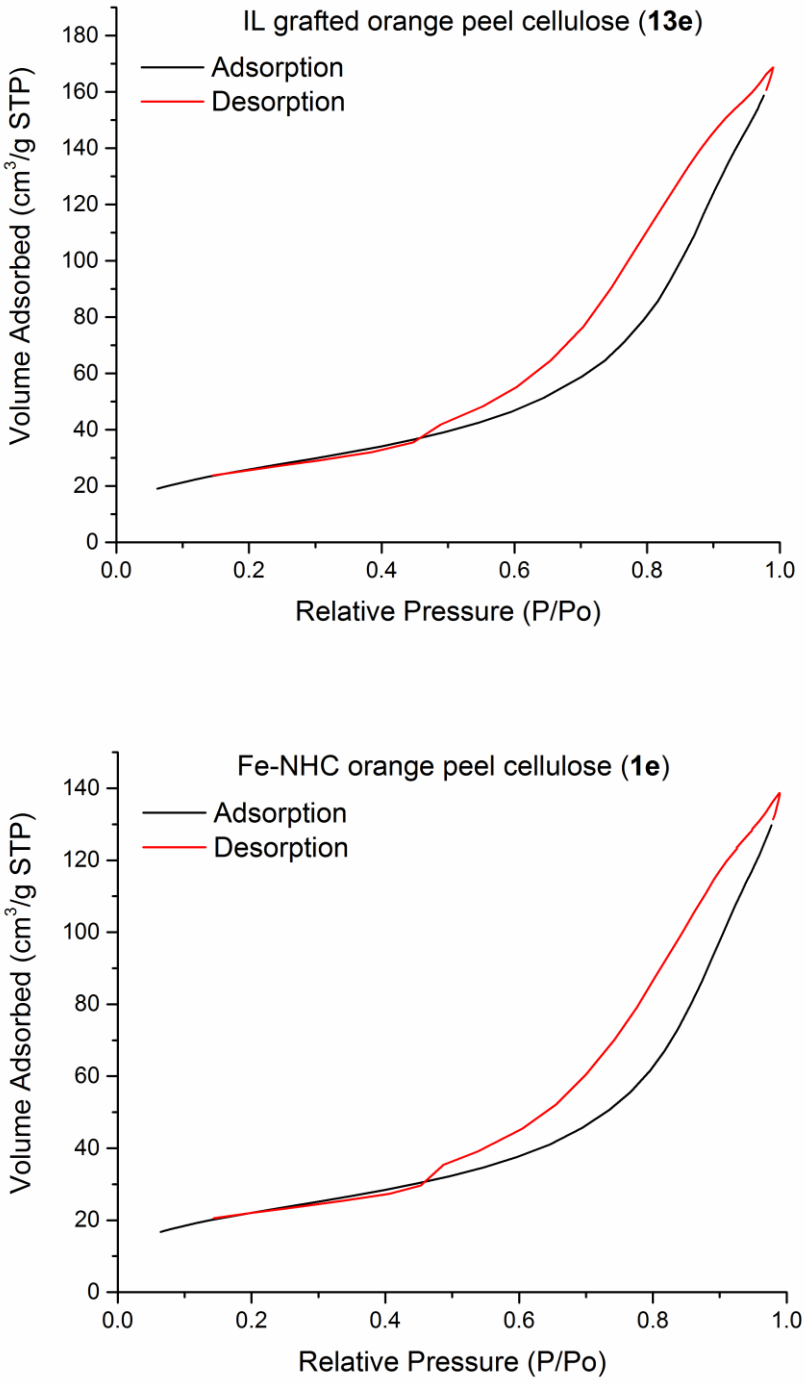

Figure 3.48. Nitrogen adsorption/desorption isotherms of orange peel cellulose (**4e**), DSC activated orange peel cellulose (**6e**), ligand grafted orange peel cellulose (**13e**) and Fe-NHC orange peel cellulose (**1e**).

Figure 3.48 indicates meso-porosity of narrow size distribution across all the samples analysed. However, noticeable slight changes in the desorption pattern can be seen between the orange peel cellulose and the surface modified orange peel cellulose

grades. These slight changes are attributed to the reduction in the pore sizes as different groups are attached to the surface of the orange peel cellulose. In contrast with the isotherms of the mango peel cellulose (Figure 3.45), isotherms of orange peel cellulose showed only a slight change in the desorption pattern because it has larger pore sizes almost twice that of the mango cellulose, as such no great hindrance on desorption even after attaching other groups in the modified forms (DSC, IL and Fe-NHC modified).

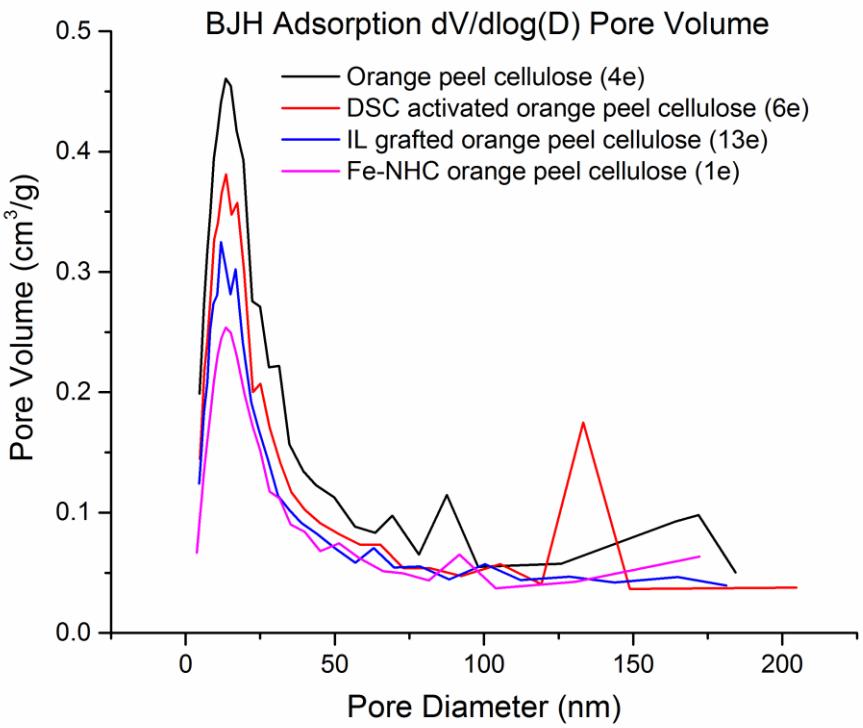

Figure 3.49. BJH adsorption dV/dD pore volume distribution of orange cellulose (**4e**), activated orange cellulose (**6e**), ligand grafted orange cellulose (**13e**) and Fe-NHC orange cellulose (**1e**)

The BJH adsorption pore volume of the orange peel cellulose and Fe-NHC orange peel cellulose shows a mono-modal distribution around 10 nm while that of the DSC activated and IL grafted each shows a poly-modal distribution between 2-50 nm. These

however, shows that all the samples analysed have pore diameters within the mesoporous region.

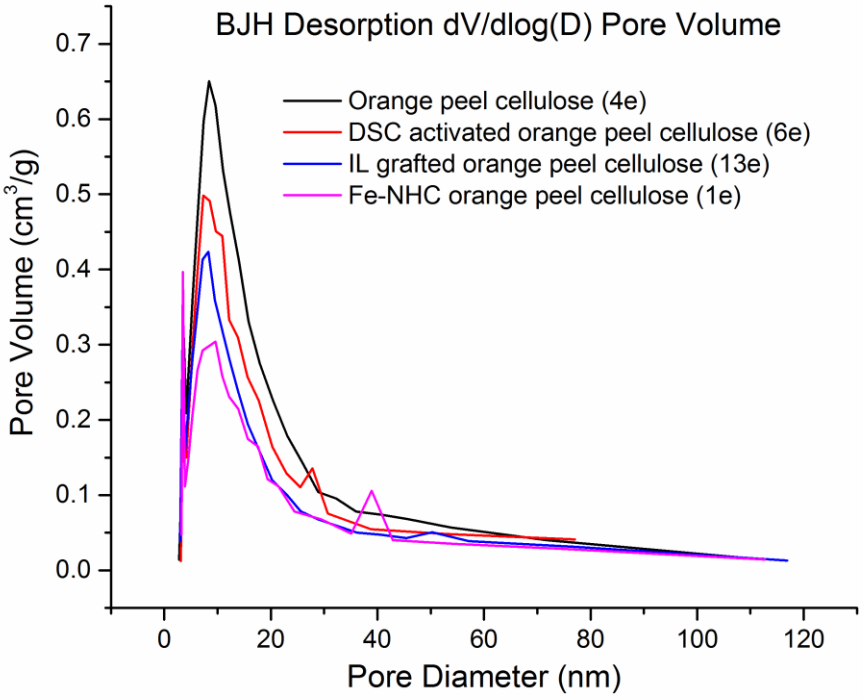

Figure 3.50. BJH desorption dV/dlog(D) pore volume distribution of orange cellulose (**4e**), activated orange cellulose (**6e**), ligand grafted orange cellulose (**13e**) and Fe-NHC orange cellulose (**1e**).

Figure 3.50 shows BJH desorption pore volume of the four samples analysed, with orange peel cellulose and IL grafted orange peel cellulose showing a characteristic bi-modal distribution with volume maxima at 2.7 nm and 8 nm. The other two samples namely; DSC activated orange peel cellulose and Fe-NHC orange peel cellulose shows almost a tri-modal distribution with volume maxima at 2.5 nm and 7 nm.

The orange peel cellulose was particularly of high surface area (151.12 m^2 g^{-1}) and pore volume (0.34 m^2 g^{-1}) with pores confined to the mesopore range. Similar to mango cellulose, t-plot analysis showed micropores to contribute little to porosity, having negligible volume and area. The BJH pore volume agrees with the total pore volume from the adsorption isotherm at 0.9935 P/P0 (<300 nm pore diameter), further highlighting the absence of micro-porosity. BJH size distribution was indeed within a narrow range, having an average diameter of about 8 nm. Moreover, the BJH

adsorption pore volume of the orange peel cellulose shows a mono-modal distribution at 10 nm while the BJH desorption pore volume showing a characteristic bi-modal distribution with volume maxima at 2.7 nm and 8 nm.

3.3. Part 2: Catalytic study: Fructose (2) to HMF (3) conversion

3.3.1. ^{1}H and ^{13}C NMR spectroscopy study of catalytic conversion of fructose (2) to HMF (3) with respect to time

The effectiveness of the catalytic conversion of fructose (**2**) to HMF (**3**) using the various fabricated Fe-NHC supported catalysts (**1a-e**) at fixed temperature (100 ^{o}C) was monitored initially by ^{1}H and ^{13}C NMR spectroscopy.

Figures 3.52 to 3.54 show stacked ^{1}H NMR spectra for the dehydration of fructose (**2**) in the presence of Fe-NHC catalyst immobilised on expanded HACS (**1a**), Starbon™ 350 (**1b**), Starbon™ 400 (**1c**), mango peel cellulose (**1d**) and orange peel cellulose (**1e**) at t= 10 min, 20 min, 0.5 h, 1 h, 3 h and 6 h. As shown in Figure 3.51, qualitatively the dehydration of fructose (**2**) to HMF (**3**) is characterized by a visible colour change from colourless to pale yellow solution (0.5 h), light brown (1 h to 3 h) to dark brown (6 h) reaction time. The onset of the dark brown colour is characteristic of HMF decomposition to formic and levulinic acid and humins, as discussed below.[208,209]

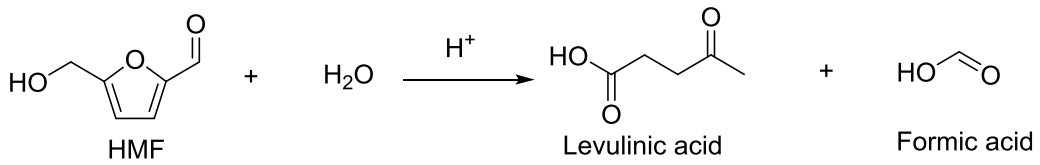

Scheme 3.2. HMF rehydration to levulinic acid and formic acid.

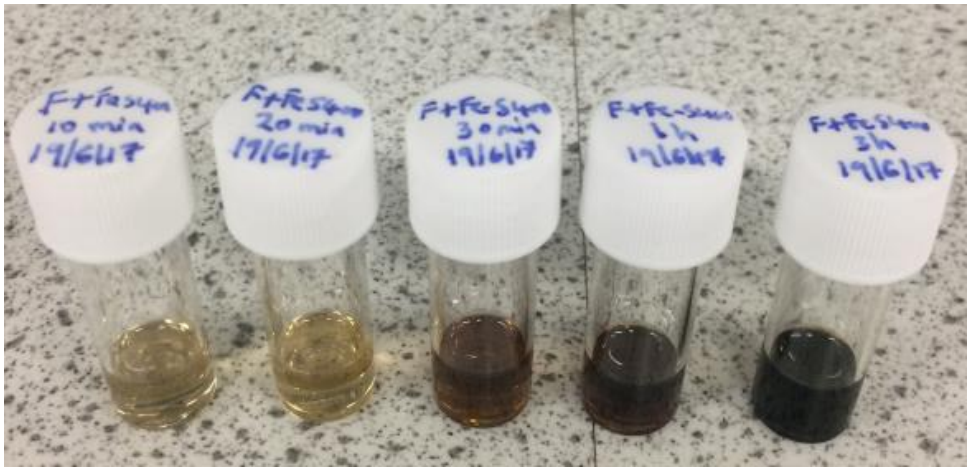

Figure 3.51 Colour change as fructose is converted to HMF with time. From pale straw (LHS) to dark brown (RHS).

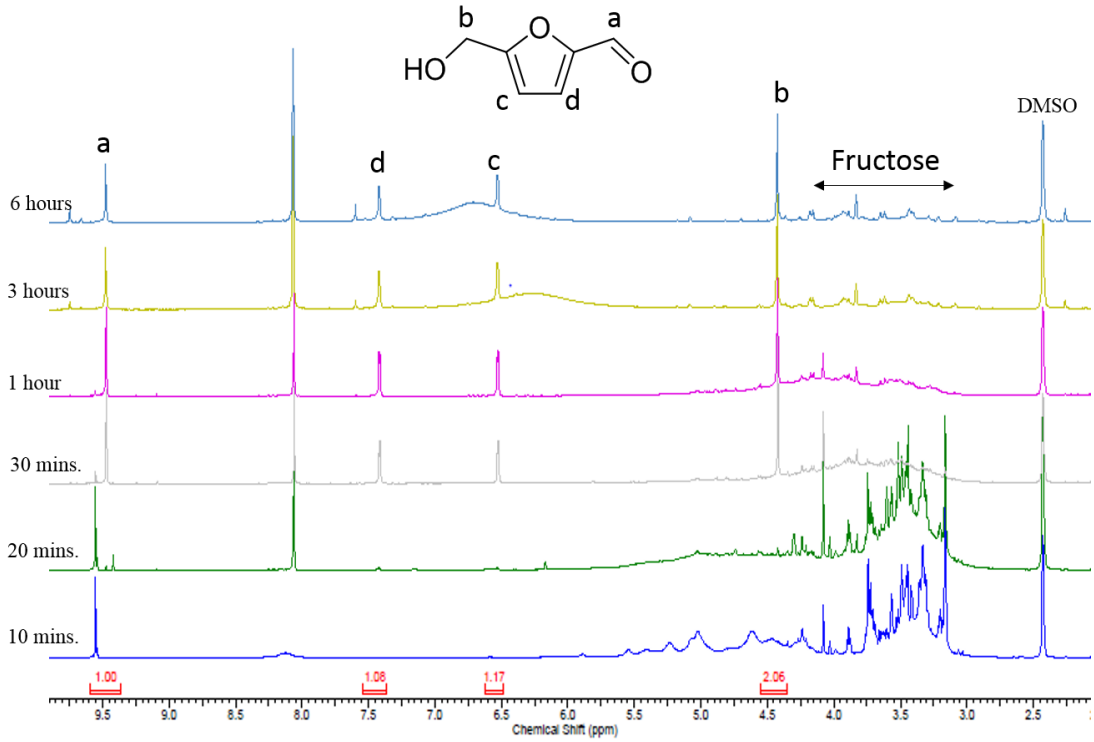

Figure 3.52. Stacked ^{1}H NMR spectra for fructose (**2**) conversion to HMF (**3**) with Fe-NHC HACS catalyst (**1a**).

As can be seen from figure 3.52 corresponding to fructose (**2**) conversion using the Fe-NHC immobilised on expanded HACS (**1a**), weak signals at 7.44 ppm, 6.55 ppm and 4.46 ppm characteristic of HMF (**3**) start to appear within 20 minutes reaction time which then develop in intensity as the reaction proceeds over time. HMF (**3**) is clearly evident after 30 min ((1 H, **H**-C=O, 9.49 ppm), (1H, O=C-C=C**H**, 7.44 ppm), (1H, H_2C-C=C**H**-, 6.55 ppm) and (2H, HO-C**H**$_2$ -C=CH, 4.46 ppm)) coupled with significant reduction in the signals for fructose (**2**). The signal at 8.08 ppm was assigned to formic acid which is formed as a consequence of the reverse hydrolysis reaction of HMF (**3**), considered as one of the side reactions of fructose dehydration.[210, 211] While the signal at 2.45 ppm is assigned to DMSO- d_6 [212], complex multiplets for fructose are in the region 3-5 ppm. [213] Interestingly, as the reaction progresses over time, the intensity of HMF (**3**) signals starts to decline slightly after 1 h reaction time which may be due to the re-hydration side reaction to formic acid and levulinic acid as mentioned earlier. However, the presence of formic acid and absence of levulinic acid suggests that formic acid is formed via a different route that involves breakdown of humins to release formic acid, not the rehydration of HMF. The formation of humins is further supported by the darkening of the reaction media as shown in Figure 3.51.

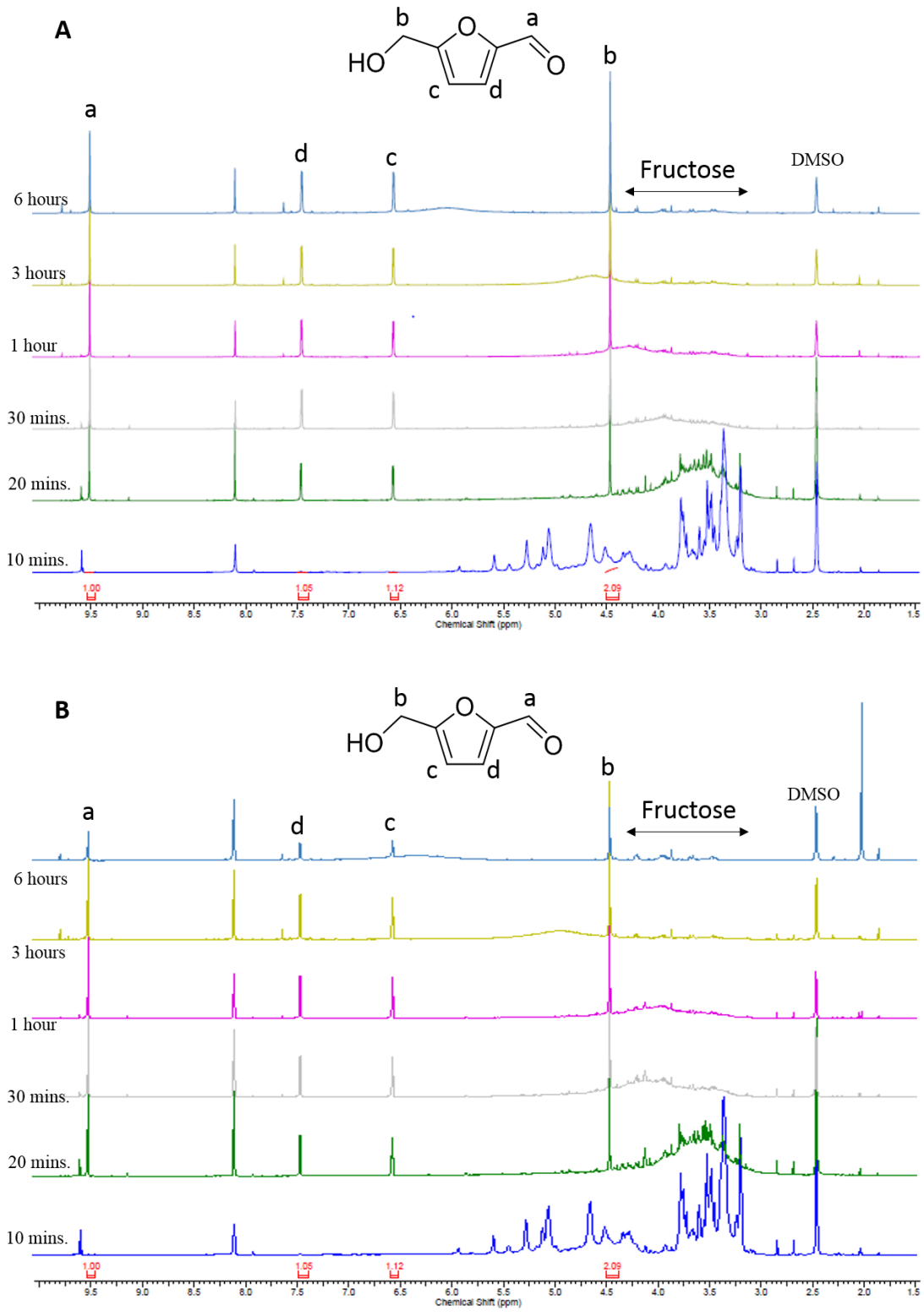

Figure 3.53 Stacked ^{1}H NMR spectra for fructose (**2**) conversion to HMF (**3**) with Fe-NHC Starbon™ 350 catalyst (1**b,** Figure A) and Starbon™ 400 catalyst (**1c,** Figure B), respectively.

In Figure 3.53A corresponding to fructose (**2**) conversion to HMF (**3**) with Fe-NHC Starbon™ 350 (**1b**), product signals were evident at t= 20 min, coupled with almost near disappearance of signals from fructose in the region 3.3-4.3 ppm. Interestingly,

the intensity of HMF (**3**) signals also declined after 1 h reaction time which may be due to the re-hydration side reactions. Prolonging the reaction from 1 h through 3 h to 6 h did not prove beneficial to HMF (**3**) production, with longer reaction time resulting in decrease of the HMF (**3**) signals and increased intensity of the signal at 8.0 ppm assigned to formic acid. Again, this validates the increasing susceptibility of HMF (**3**) re-hydration with respect longer reaction time.

A similar pattern of fructose dehydration was observed for the corresponding fructose (**2**) conversion with Fe-NHC Starbon™ 400 (**1c**) (Figure 3.53B). HMF signals were also evident at t= 20 min, coupled with almost the disappearance of the signals from fructose at 3.3-4.3 ppm. However, interestingly, for Fe-NHC Starbon™ 400 (**1c**), at 6 h reaction time, a much greater decrease in intensity of the HMF (**3**) signals was observed with corresponding increase in formic acid signal (8.1 ppm).

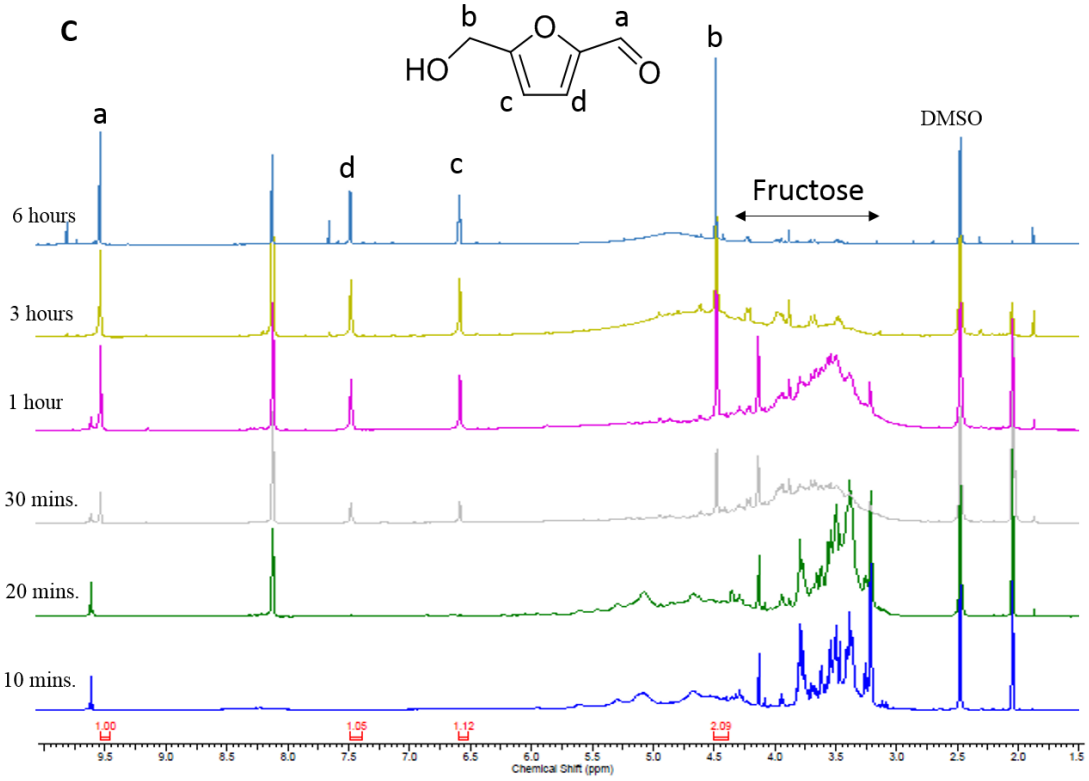

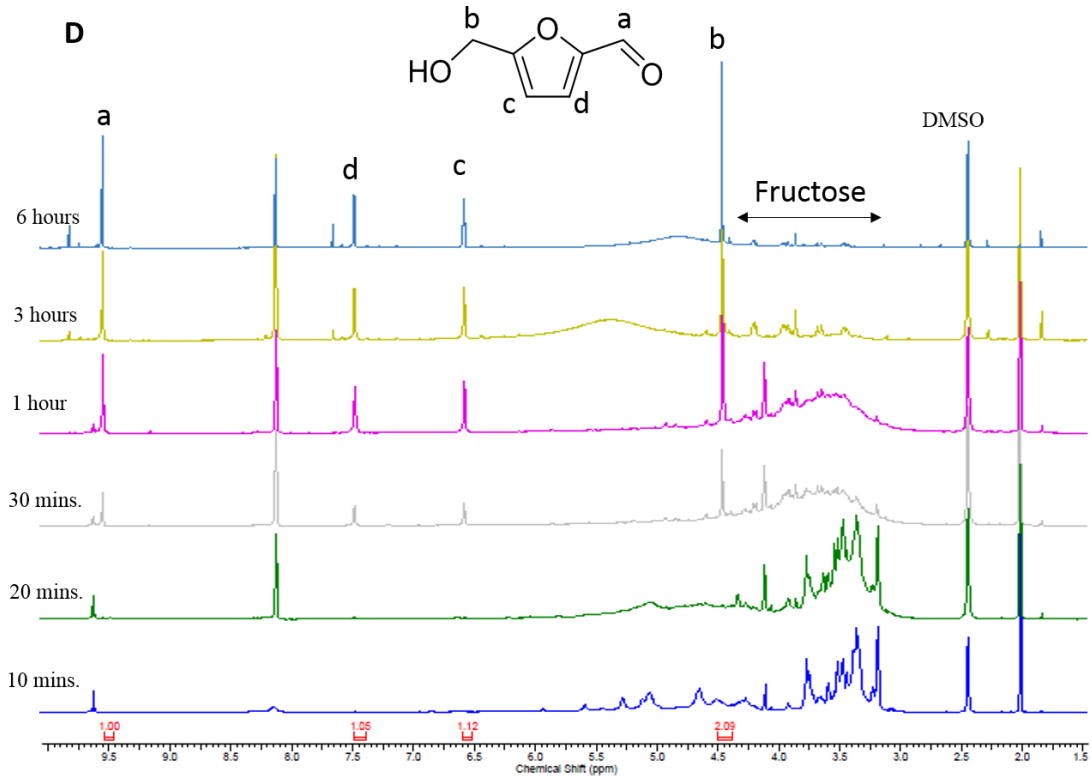

Figure 3.54 (C and D). Stacked ^{1}H NMR spectra for fructose (**2**) conversion to HMF (**3**) with Fe-NHC mango peel cellulose catalyst (**1d,** Figure C) and orange peel cellulose catalyst (**1e,** Figure C) respectively.

Figures 3.54C and 3.54D shows the fructose (**2**) conversion with Fe-NHC mango peel cellulose (**1d**, **C**), and Fe-NHC orange peel cellulose catalyst (**1e**, **D**). Signals for HMF (**3**) were evident at t= 30 min instead of t= 20 min as observed for expanded HACS (Figure 3.52) and Starbon™350 and 400 (Figure 3.53A and B) immobilised Fe-NHC counterparts. This indicates that the orange and mango peel Fe-NHC catalysts are *kinetically slower* in activity than expanded HACS (**1a**) and Starbon™ supported catalysts (**1b** and **1c**), which may be attributed to the low porosity of the mango and orange peel cellulose support as compared to HACS and Starbon™ supports (see Table 3.8). Low porosity limits diffusion of molecules towards the catalytically active iron centre. The difference in porosity is supported by the lesser perforations of the orange and mango peel cellulose as observed from the SEM images and the lower pore volume, diameter and surface area as compared to the HACS and Starbon™ supports. Similarly, the intensity of HMF (**3**) signals also declined after 1 h.

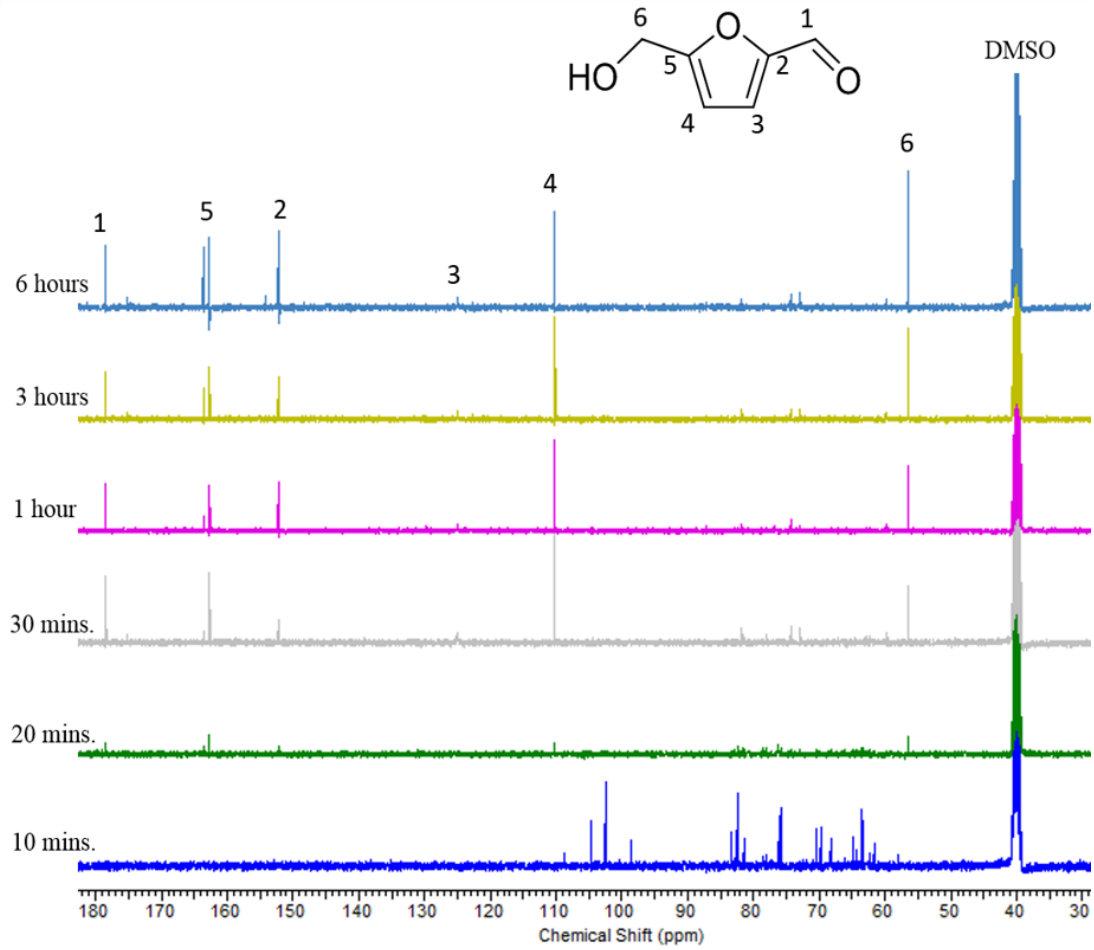

Figure 3.55. Stacked ^{13}C NMR spectra for fructose (**2**) conversion to HMF (**3**) with Fe-NHC HACS catalyst (**1a**).

Similarly, a supporting ^{13}C NMR spectroscopy study was conducted to evidence fructose (**2**) to HMF (**3**) conversion. Figure 3.55 for catalyst (**1a**) revealed a decrease in fructose (**2**) resonances (60 - 105 ppm) coupled with an increase in those for HMF (**3**) with respect to time. HMF signals were evident at t=0.5 h (56.43 ppm, HO-**C**H_2-C=CH-), (110.24 ppm, HO-CH_2-C=**C**H-), (152.25 ppm, O=HC-**C**H=C-), (162.66 ppm, HO-CH_2-**C**=CH_2-) and 178.53 ppm, O=**C**H-C=CH)).[214] The signal at 163.45 ppm most likely corresponds to formic acid which agrees with its resonance observed by ^{1}H NMR spectroscopy at 8.0 ppm.

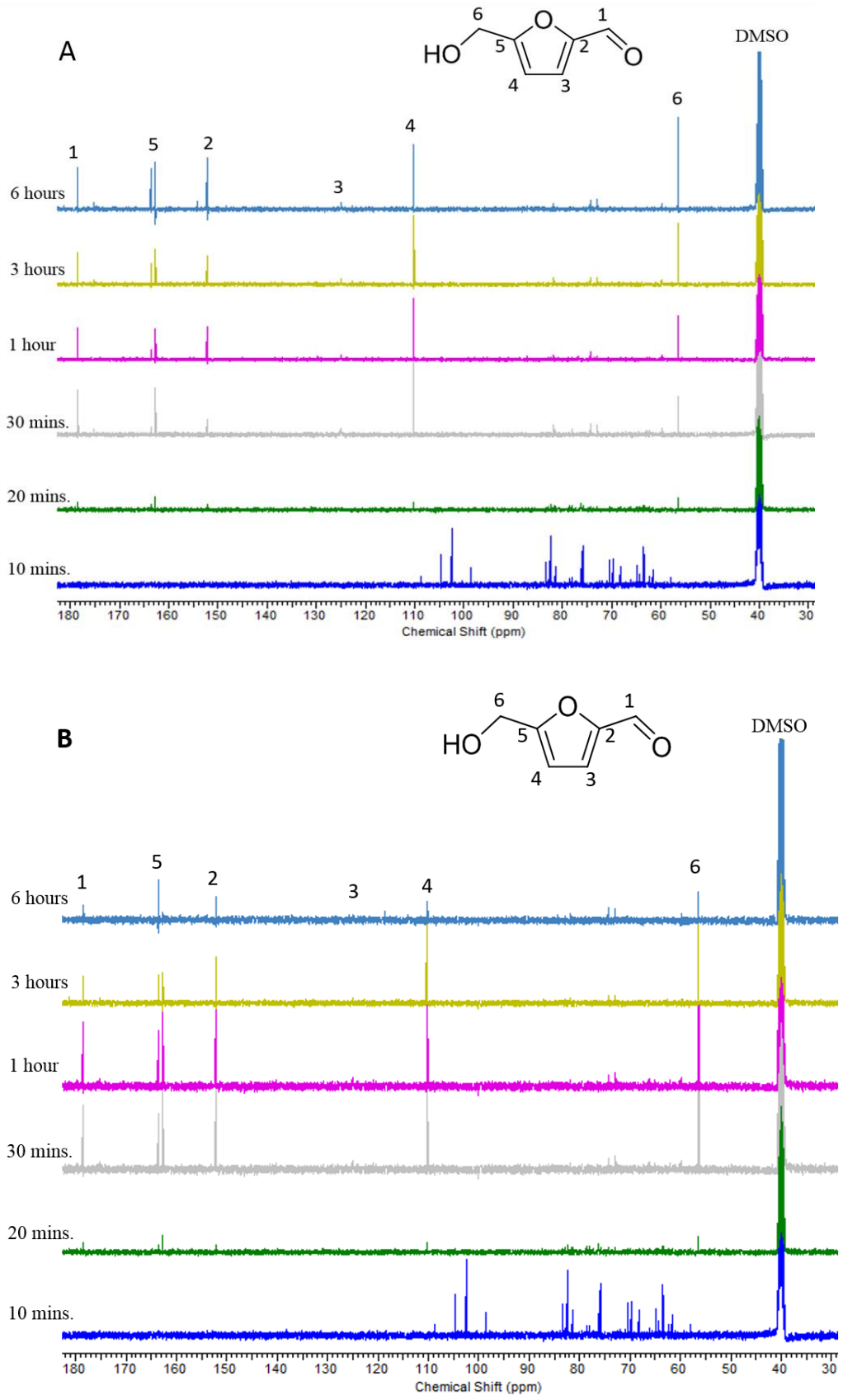

Figure 3.56. (A and B) Stacked ^{13}C NMR spectra for fructose (**2**) conversion to HMF (**3**) with Fe-NHC Starbon™ 350 catalyst (1**b**, A) and Starbon™ 400 catalyst (**1c**, B) respectively.

Very few changes were observed in figure 3.56 A and B when compared to Figure 3.55. All the signals for HMF are evident, with only a decreased in the intensities when compared to Figure 3.55.

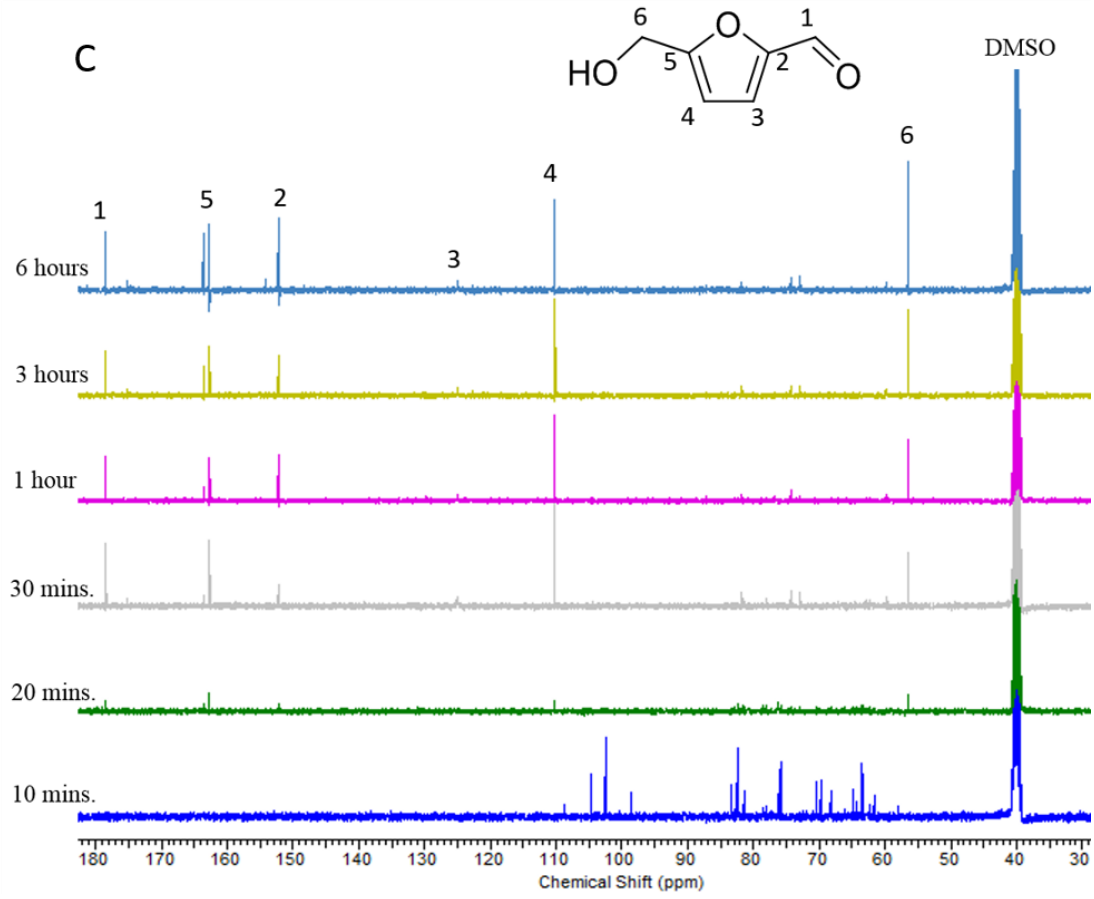

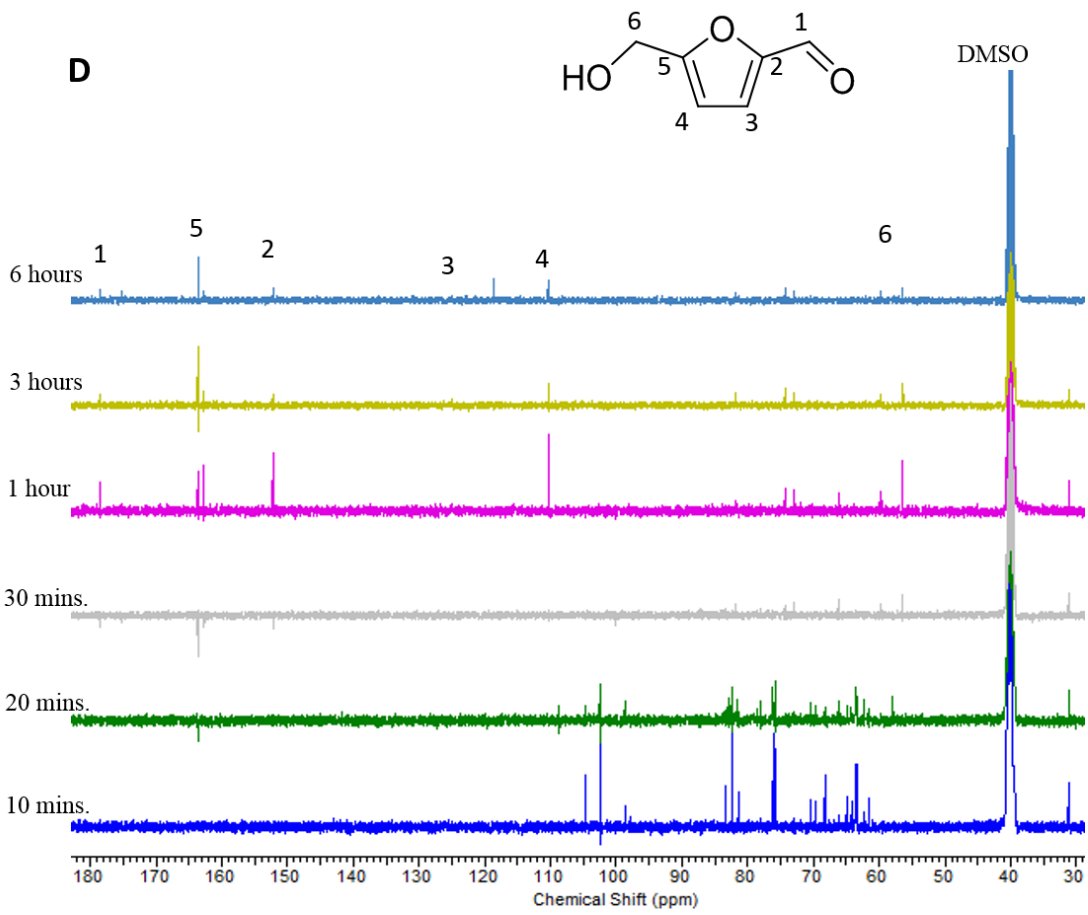

Figure 3.57. (C and D). Stacked ^{13}C NMR spectra for fructose (**2**) conversion to HMF (**3**) with Fe-NHC mango peel cellulose catalyst (1**d**) and orange peel cellulose catalyst (**1e**), respectively.

Similarly, the ^{13}C NMR spectra of fructose (**2**) conversion to HMF (**3**) using Fe-NHC mango peel cellulose catalyst (1**d**) and orange peel cellulose catalyst (**1e**) (Figure 3.57C and D), fructose loss and HMF production resonances are as discussed for catalysts **1a-c** earlier. Interestingly and similar to the complementary proton NMR (Figure 3.54 C and D), the intensity of HMF signals also declined after 1 h reaction time due to the re-hydration side reactions.

3.3.2. HPLC analysis of fructose to HMF

In order to investigate yield and selectivity the dehydration of fructose (**2**) to HMF (**3**) was investigated by HPLC.

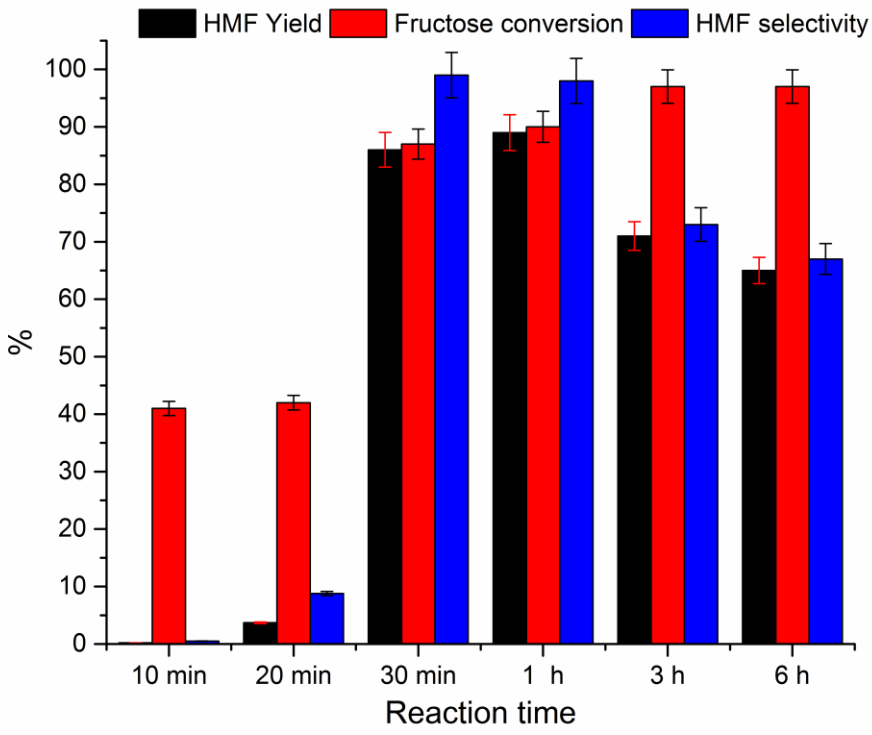

Figure 3.58. HPLC results of fructose conversion to HMF with Fe-NHC HACS catalyst (**1a**). Condition: Fructose 180 mg, catalyst 14.7 mg, DMSO 4 mL, 100 ^{o}C.

For Fe-NHC expanded HACS (**1a**) (Figure 3.58), at 0.5-1 h, high HMF (**3**) yield and selectivity was obtained thus indicating effectiveness of (**1a**) as a catalyst for fructose (**2**) dehydration to HMF (**3**). The high selectivity at this time could be explained by the low probability of re-hydration at this point compared to proceeding times. The best HMF (**3**) yield (90%) was obtained at t= 1 h. Thereafter, although fructose conversion is the highest (97 %) for 6 h reaction time both HMF yield and selectivity drop significantly. As proposed earlier this may be due to re-hydration to formic acid which is seen at 4.74 min retention time and supported by NMR (^{1}H and ^{13}C) analysis discussed earlier.

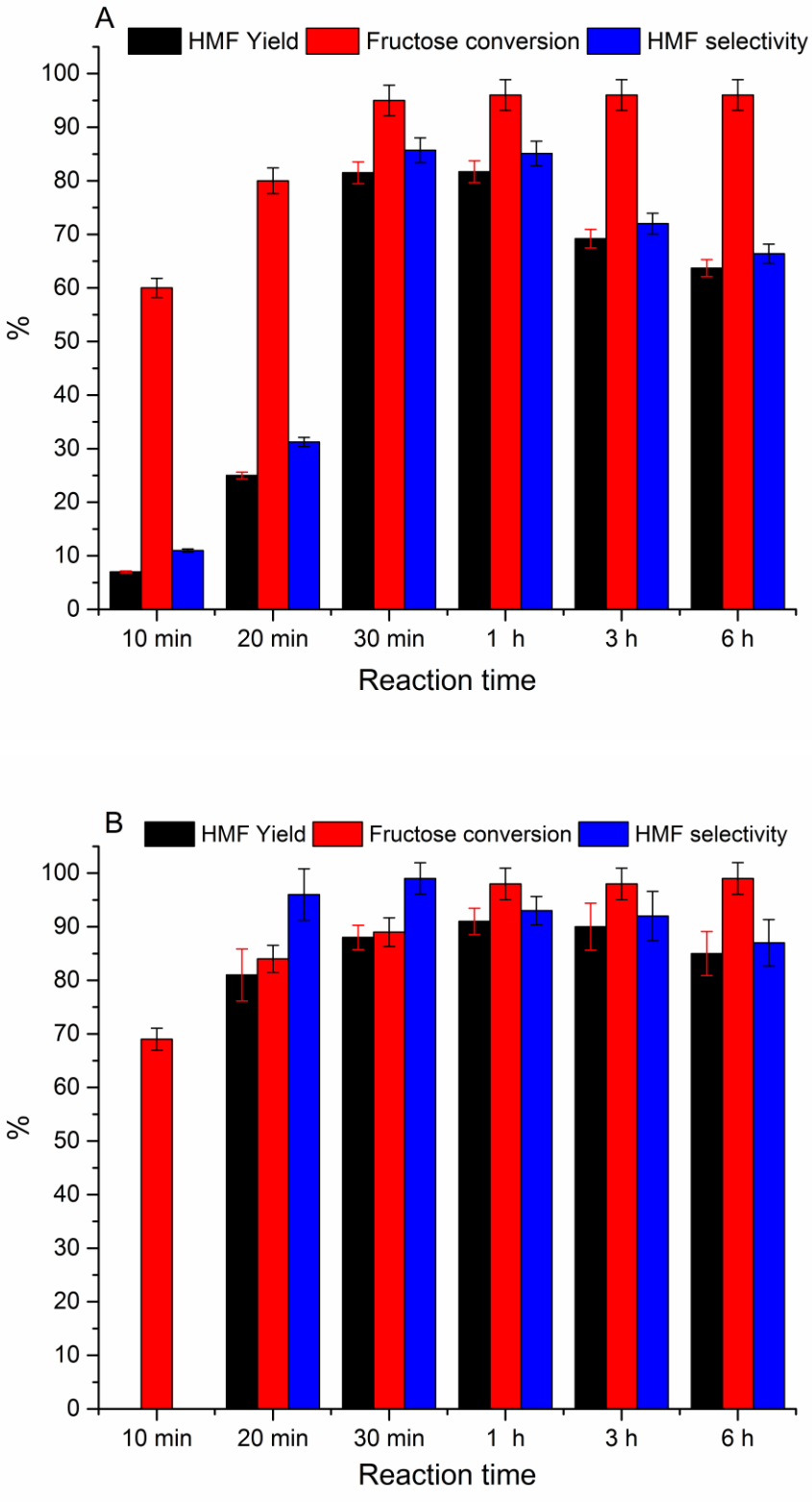

Figure 3.59. (A and B) Consolidated HPLC results for fructose (**2**) conversion to HMF (**3**) with Fe-NHC Starbon™ 350 catalyst (1**b**, A) and Starbon™ 400 catalyst (**1c**, B), respectively. Condition: Fructose 180 mg, catalyst 31 to 32 mg (depending on catalyst Fe loading), DMSO 4 mL, 100 ºC.

Figure 3.59A which corresponds to the catalytic conversion using the Fe-NHC Starbon™ 350 catalyst (1**b**) indicates best catalytic activity with HMF yield of 82 % (TOF=169 h^{-1}), fructose conversion of 95 % and HMF selectivity of 86 % at t=0.5 h. No significant changes occur on taking the reaction further to t=1 h. Thereafter, at t=3 h and t=6 h, both HMF yield and selectivity drops significantly. As earlier stated, this may be due to formation of humins.

Figure 3.59B on the other hand, corresponding to the catalytic with Starbon™ 400 catalyst (**1c**), gave similar conversion, yield and selectivity at 0.5 h to 6 h reaction time when compared to its Starbon™ 350 counterpart. However, a significant difference in conversion, yield and selectivity is noted at time t = 20 minutes, where Starbon™ 400 (**1c**) performs more effectively than the Starbon™ 350 (**1b**) giving a HMF yield of about 80% as compared to 25% obtained with Starbon™ 350 catalyst. This observation may be attributed to the absence of iron oxide nanoparticles in Fe-NHC Starbon 400 (see TEM, Section 3.1.2.8), suggesting that all the iron present is catalytically active coordinated iron. While the presence of nanoparticles (possibly iron oxide, see TEM, section 3.1.2.8) in Fe-NHC Starbon 350 means that not all of the iron contained is catalytically active.

A HMF yield of 81 % (TOF=241 h^{-1}), fructose conversion of 87 % and HMF selectivity of 98 % at t=0.20 mins were obtained with Starbon™ 400 catalyst (**1c**). Taking the reaction to 0.5 h the yield increases to 88 %. No significant changes occur on taking the reaction further to t=1 h. Thereafter, at t=3 h and t= 6 h, both HMF yield and selectivity drops significantly, again due to rehydration side reactions.

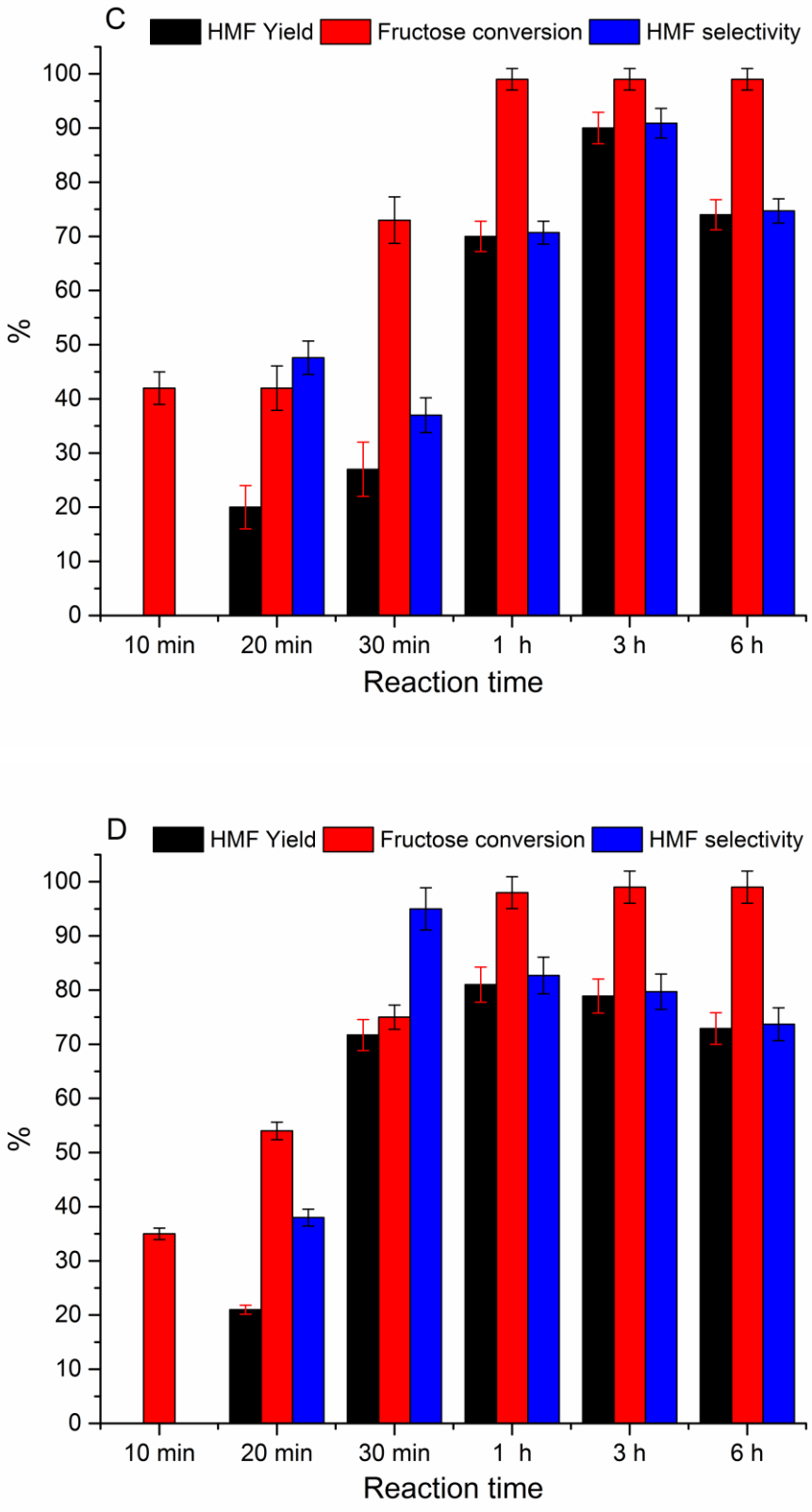

Figure 3.60. (C and D) Consolidated HPLC results for fructose (**2**) conversion to HMF (**3**) with Fe-NHC mango peel cellulose catalyst (**1d**, C) and orange peel cellulose catalyst (**1e**, D) respectively.

Condition: Fructose 180 mg, catalyst 19 to 33 mg (depending on catalyst Fe loading), DMSO 4 mL, 100 ^{o}C.

Overall the mango and orange peel cellulose supported catalysts (**1d** and **1e**, respectively) showed lower catalytic activity compared to HACS and Starbon™ supported catalysts (**1a**, and **1b** and **1c**, respectively), which may due to decreased porosity (see Table 3.8, in Section 3.1.1.8), therefore creating a barrier to diffusion of the reagents to catalytic sites. However, it seems that given enough time a significant increase in HMF yield is noted for mango peel supported catalyst (**1d**) after 3 h reaction time (Figure 3.60C). Thereafter, taking the reaction to 6 h results in significant decrease in the HMF yield and selectivity. Figure 3.60C indicates a HMF yield of 71 %, fructose conversion of 72.5 % and HMF selectivity of 97.5 % at t=1 h, TOF= 79.2 h^{-1} for Fe-NHC mango cellulose catalyst (1**d**). Figure 3.60D shows similar conversion: HMF yield 71.7 % (t=0.5 h), TOF= 146 h^{-1} for Fe-NHC orange peel cellulose catalyst (**1e**).

3.3.3. Comparative study of Fe-NHCs immobilised on renewable supports (1a-e) with other heterogeneous catalysts (Amberlyst-15, Montmorillonite K10 and ZSM-5) for fructose (2) to HMF (3) dehydration

Figure 3.61 A-C shows the results (yield, selectivity and conversion) for fructose (**2**) dehydration to HMF (**3**) (determined by HPLC) using a variety of heterogeneous catalysts, namely: Amberlyst-15, Montmorillonite K10 and ZSM-5 (SiO_2:Al_2O_3=30) and compared with **1a-e**. Thus, to compare activity between all catalysts, a series of standard reactions were undertaken using the same amount of fructose and DMSO at 100 ˚C. To ensure consistency in the amount of Fe added in moles, the amount of catalysts added (in mg) changes based on the Fe loading of each catalyst used. Literature data was not used because lack of knowledge of exactly how the study was performed would add huge uncertainty when trying to compare data.

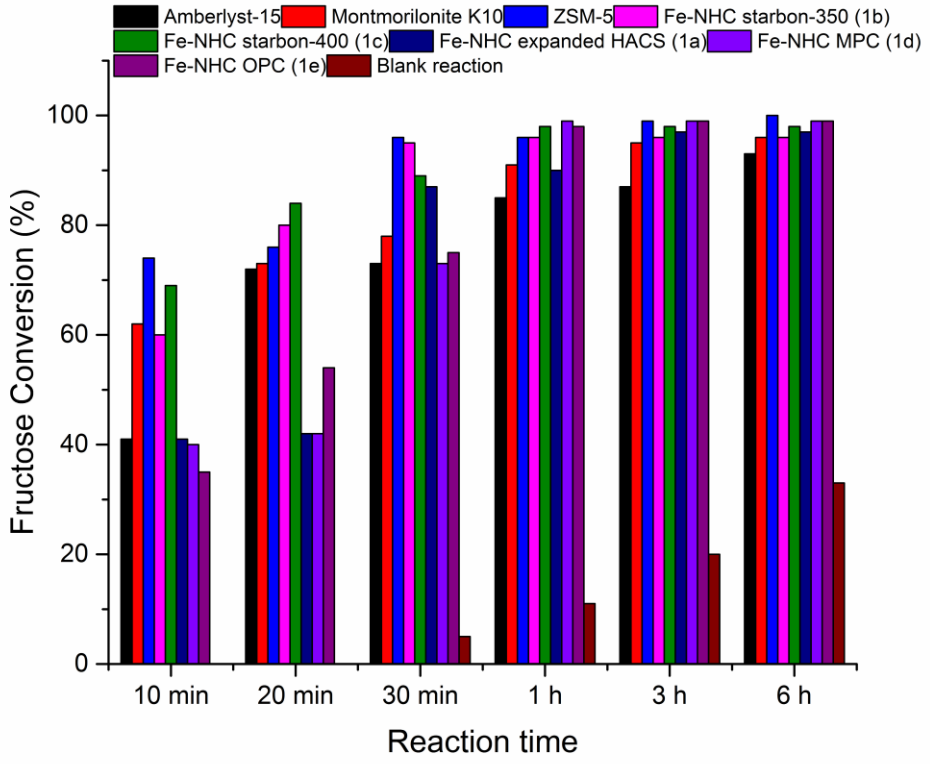
Amberlyst-15
Montmorilonite K10
ZSM-5
Fe-NHC starbon-350 (1b)
Fe-NHC starbon-400 (1c)
Fe-NHC expanded HACS (1a)
Fe-NHC MPC (1d)
Fe-NHC OPC (1e)
Blank reaction
Fructose Conversion (%)
0
20
40
60
80
100
10 min
20 min
30 min
1 h
3 h
6 h
Reaction time

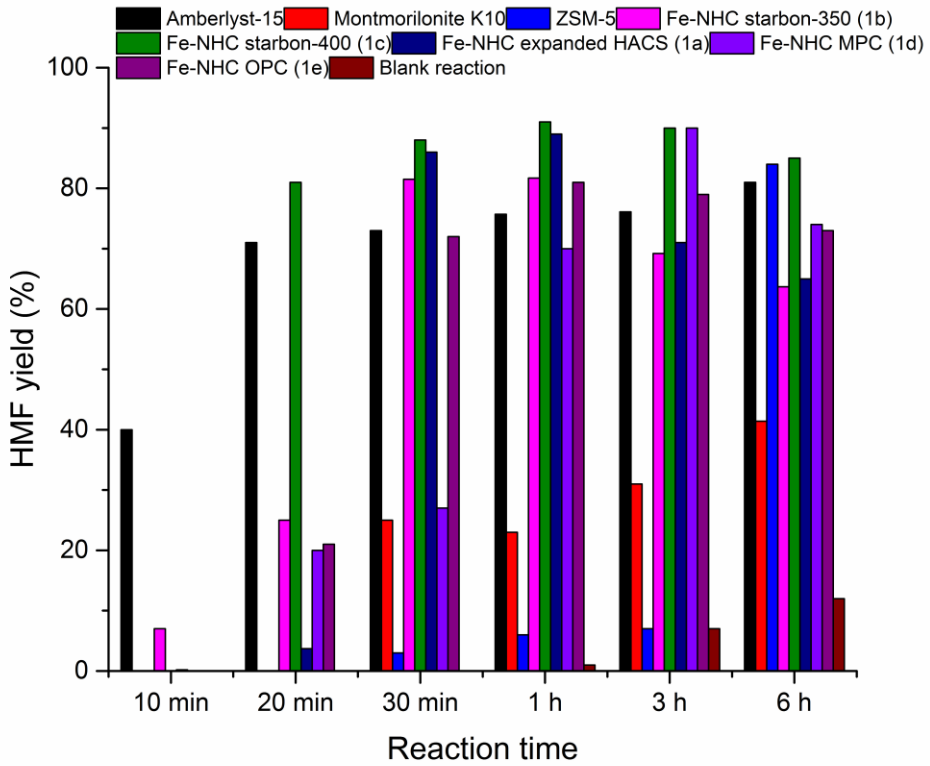
Amberlyst-15
Montmorilonite K10
ZSM-5
Fe-NHC starbon-350 (1b)
Fe-NHC starbon-400 (1c)
Fe-NHC expanded HACS (1a)
Fe-NHC MPC (1d)
Fe-NHC OPC (1e)
Blank reaction
HMF yield (%)
0
20
40
60
80
100
10 min
20 min
30 min
1 h
3 h
6 h
Reaction time

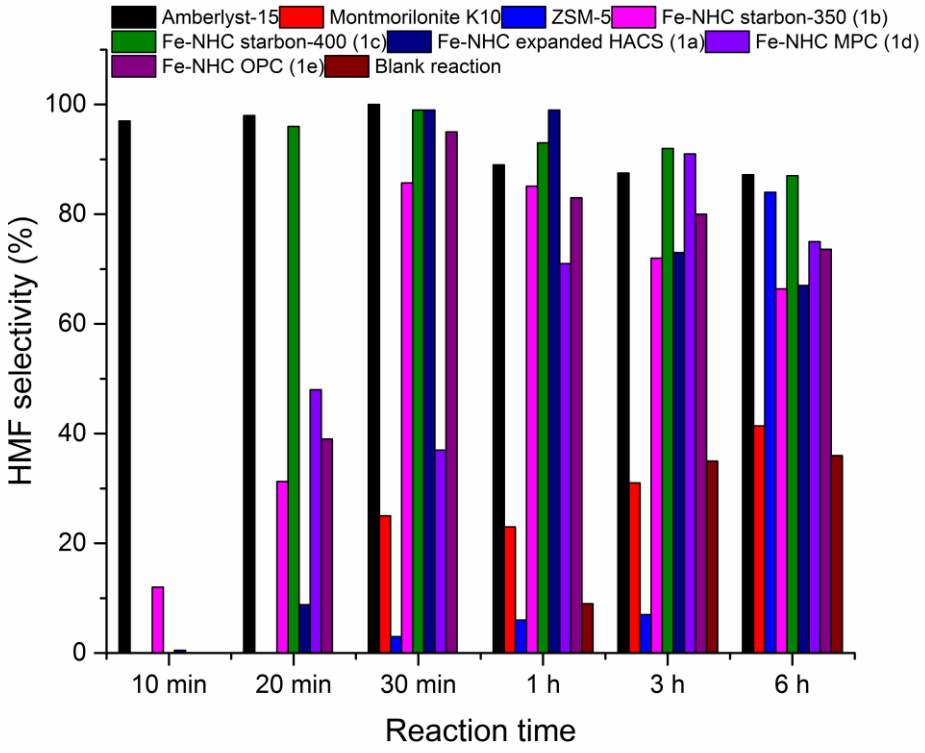

Figure 3.61A-C. HPLC results for fructose conversion (A), HMF yield (B) and HMF selectivity (C) for **1a-e** and selected commercially available catalysts. Condition: Fructose 180 mg, catalyst 14 to 32 mg (depending on catalyst Fe loading), DMSO 4 mL, 100 ^{o}C.

For Amberlyst-15, maximum yield of HMF (80%) occurred after 6 h, however, even after 20 mins HMF yield had reached 72%. Thus, it is fair to conclude that no appreciable increase in yield occurs after 20 mins. The behaviour of Montmorillonite K-10 shows HMF formation at T= 30 mins and longer. An almost linear increment in HMF yield, but with a bit of abnormality at t=1 h at which the yield and selectivity seemed to drop a little, was seen up to t=6 h. ZSM-5 catalyst attains a good yield at t=6 h but no significant yield up to t=3 h. Expanded HACS supported Fe-NHC catalyst (**1a**) had its highest HMF yield at t= 1 h. However, for Starbon 400 Fe-NHC catalyst (**1c**) the fructose conversion, HMF yield and HMF selectivity, started very high at initial reaction time of t=20 min to 1 h and thereafter the HMF yield started to drop significantly with increasing reaction time.

Orange peel cellulose Fe-NHC catalyst (**1e**) and Starbon™ 350 catalyst (**1b**) showed a near similar activity in terms of fructose conversion and HMF yield and selectivity. Fe-NHC mango cellulose (**1d**) had the lowest activity among the fabricated supported

NHC-Fe catalysts which is attributed to its very low pore size making diffusion of reactant and product in and out of the active centres very slow.

Importantly, at highest fructose conversion levels (after t= 1 h, Figure 3.61A), the novel Fe-NHC catalysts immobilised on expanded HACS (**1a**), Starbon 350 (**1b**) and Starbon 400 (**1c**) show better performance than their commercial counterparts with respect to HMF yield (see Figure 3.61B).

3.3.4. Catalyst recycling study

The importance of catalyst recycling is to determine the stability of the catalyst in the reaction conditions employed against leaching or poisoning. Catalyst recycling and re-use was investigated in DMSO-d_6 at 100 ˚C with each experiment run for 1 h reaction time and monitored by NMR (qualitative) and HPLC (quantitative). As shown by the quantitative data. Figure 3.62A shows that the desired Fe-NHC expanded HACS catalyst (**1a**) can be re-used up to four times (4x) without significant loss in performance. The other catalysts (**1b-e)** (Figure 3.62 B-E) however, showed that they can be recycled up to five times (5x) without any significant reduction in their catalytic activity towards fructose (**2**) to HMF (**3**) conversion.

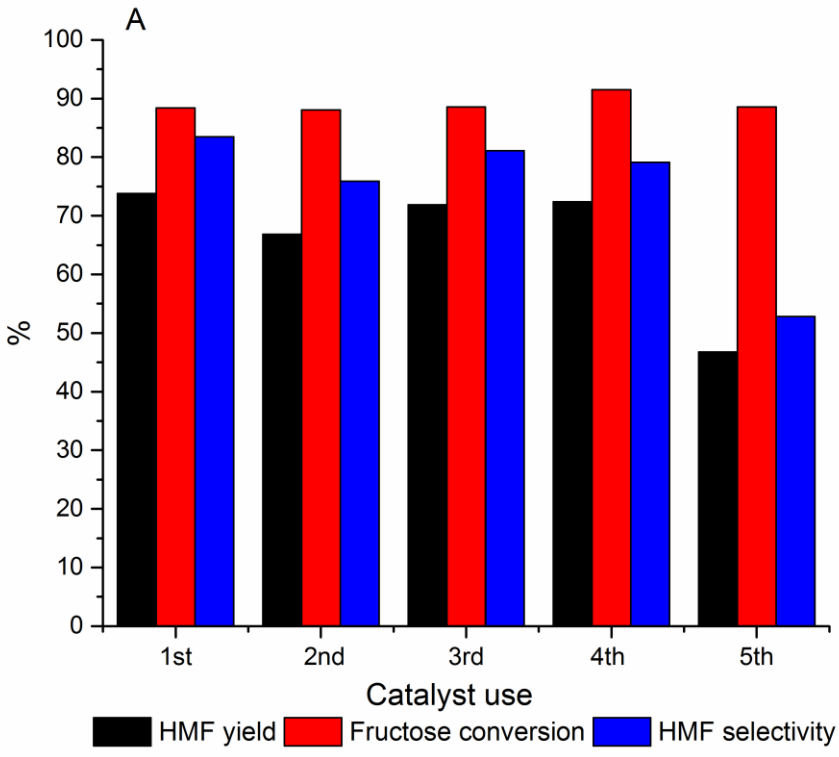

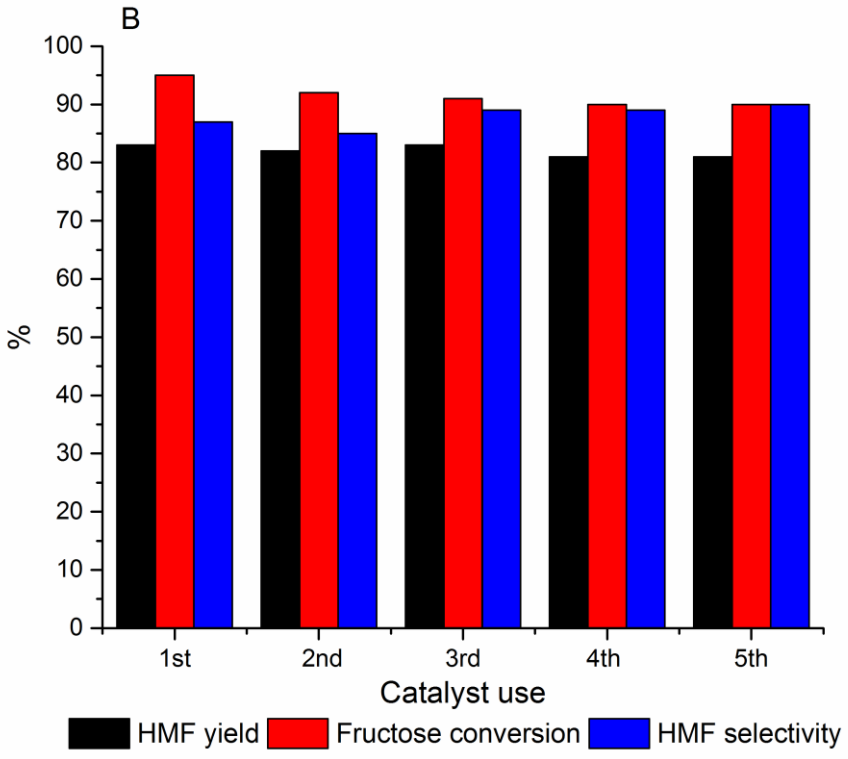
B
100
90
80
70
60
50
40
30
20
10
0
%
1st
2nd
3rd
4th
5th
Catalyst use
HMF yield
Fructose conversion
HMF selectivity

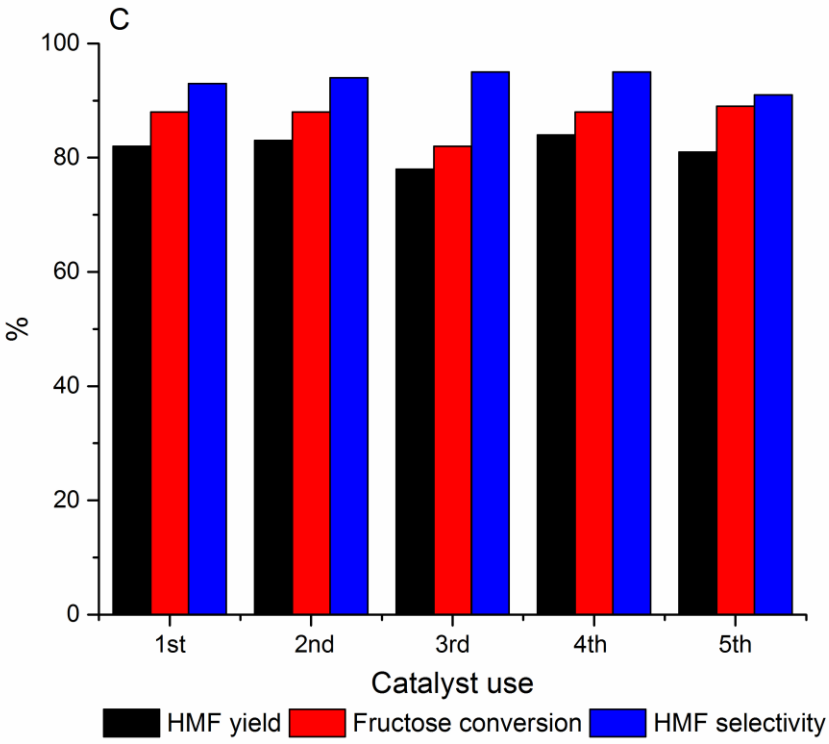
C
100
80
60
40
20
0
%
1st
2nd
3rd
4th
5th
Catalyst use
HMF yield
Fructose conversion
HMF selectivity

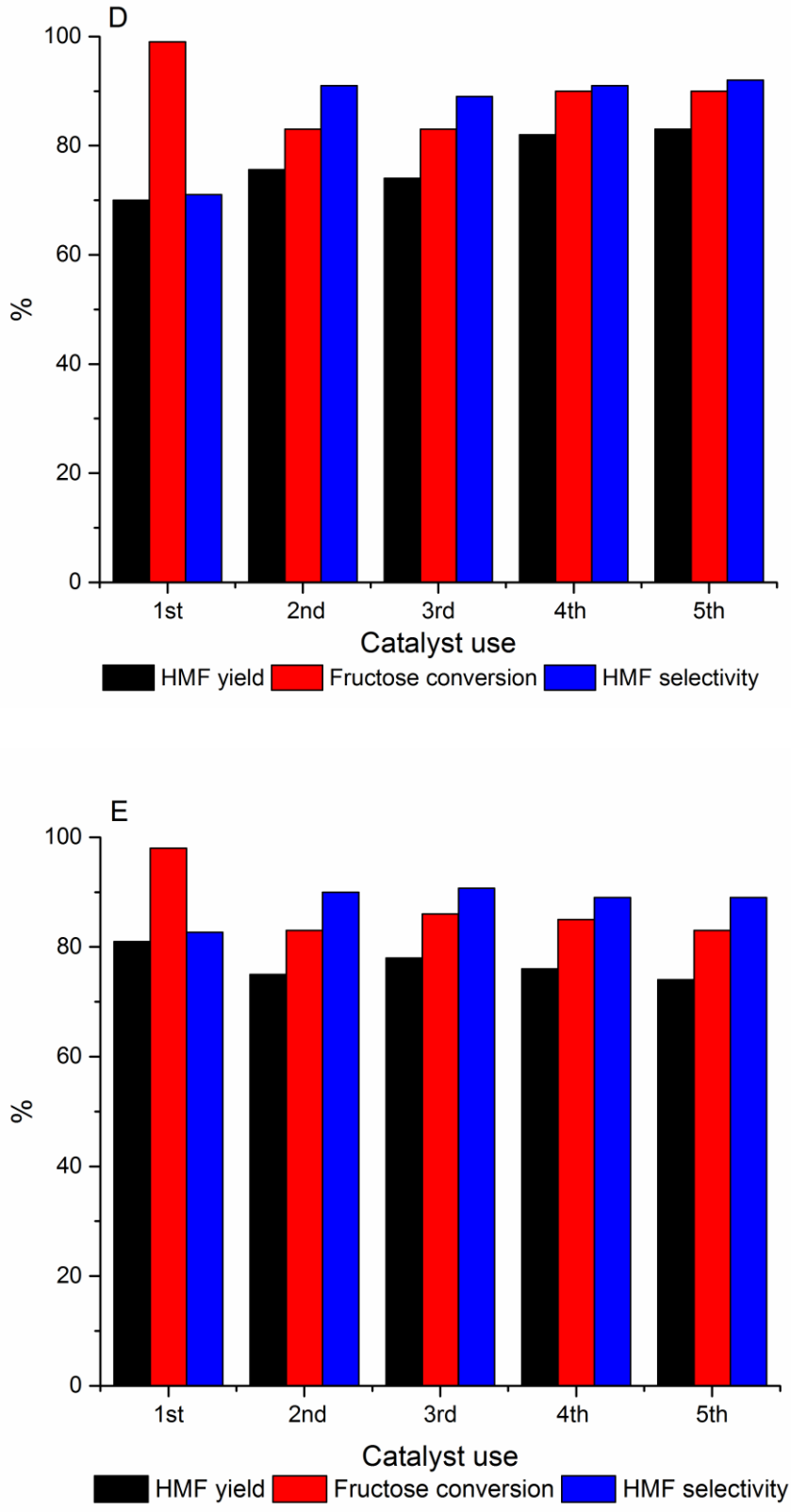

Figure 3.62. (A-E) Catalytic (re)use data for fructose conversion, HMF yield and selectivity over (A) Fe-NHC expanded HACS (**1a**), (B) Fe-NHC Starbon™ 350 (**1b**), (C) Fe-NHC Starbon™ 400 (**1c**), (D) Fe-NHC MPC (**1d**) and (E) Fe-NHC OPC (**1e**).

3.3.5. Catalysts leaching test

In order to confirm that the novel Fe-NHC catalysts are heterogeneous and the iron is firmly immobilised, i.e., no or limited leaching, post fructose to HMF conversion (at 100^{o}C) the reaction mixture was filtered whilst hot and the filtrates were subjected to ICP analysis. The leachate showed insignificant amounts of Fe (35-79.49 ppb) confirming strong co-ordination on the iron within the NHC.

3.3.6. Temperature and reaction time study for the catalytic conversion of fructose (2) to HMF (3) with Fe-NHC immobilised on Starbon 350 (1b)

A brief, and partly representative study of the other Fe-NHCs (**1a**, 1**c**-**e**), study of optimum temperature for conversion of fructose to HMF (yield, conversion and selectivity, Figure 3.63) with respect to Fe-NHC immobilized on Starbon 350 (**1b**) was done. It can be inferred from the results (Figure 3.63) that increasing the reaction temperature from 80 to 100 ^{o}C for all temperatures except 3 h is beneficial if not crucial to achieving higher conversion (max, 96%), yield (max, 82%) and selectivity (max, 85%), except at 3 h. Significant differences in fructose conversion, HMF yield and HMF selectivity are seen between 20 min to 1 h, thereafter the difference in much less. With respect to reaction time, at 100 ^{o}C, prolonging the reaction after 1 h did not result in any beneficial effect but results in decrease in HMF yield and selectivity. At 80 ^{o}C reaction temperature however, good fructose conversion, HMF yield and HMF selectivity were only achieved after a longer reaction time of 3 h. Prolonging the reaction from 3 h resulted in decreasing yield and selectivity.

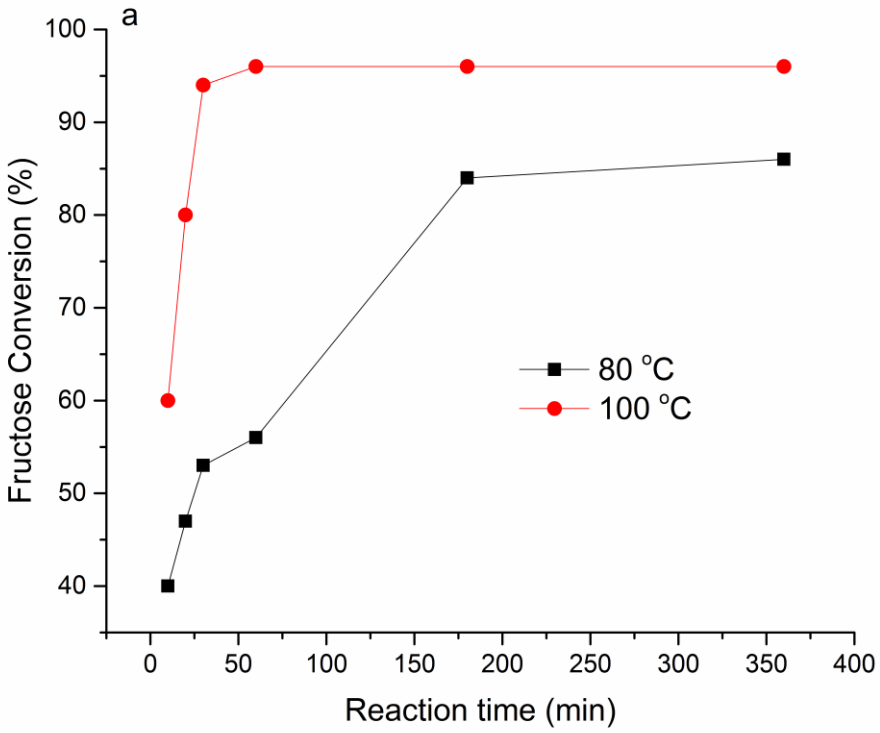
a
Fructose Conversion (%)
Reaction time (min)
80 °C
100 °C
100
90
80
70
60
50
40
0
50
100
150
200
250
300
350
400

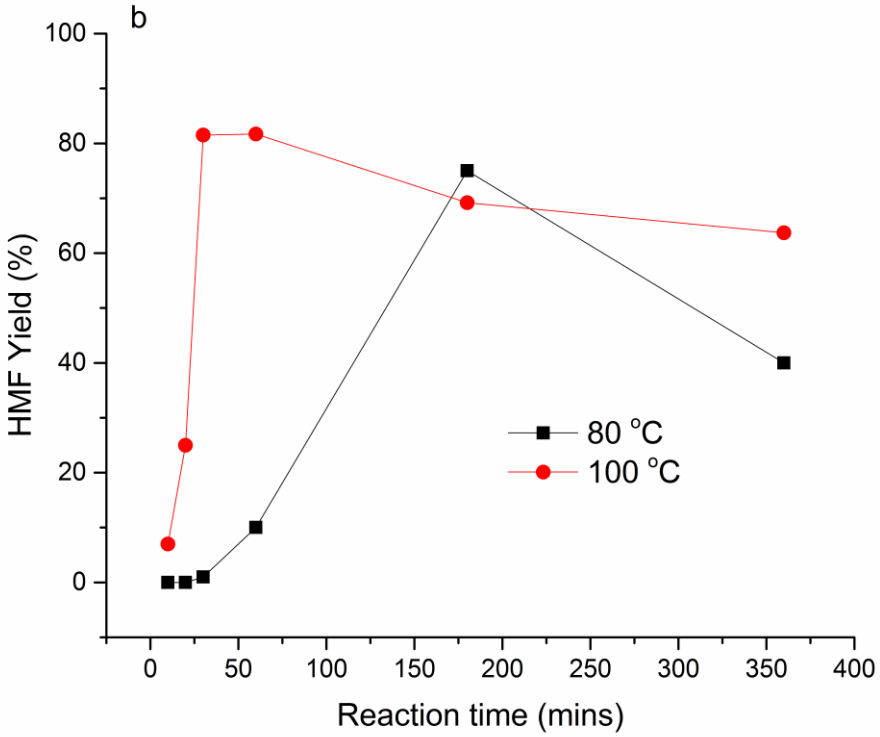
b
HMF Yield (%)
Reaction time (mins)
80 °C
100 °C
100
80
60
40
20
0
0
50
100
150
200
250
300
350
400

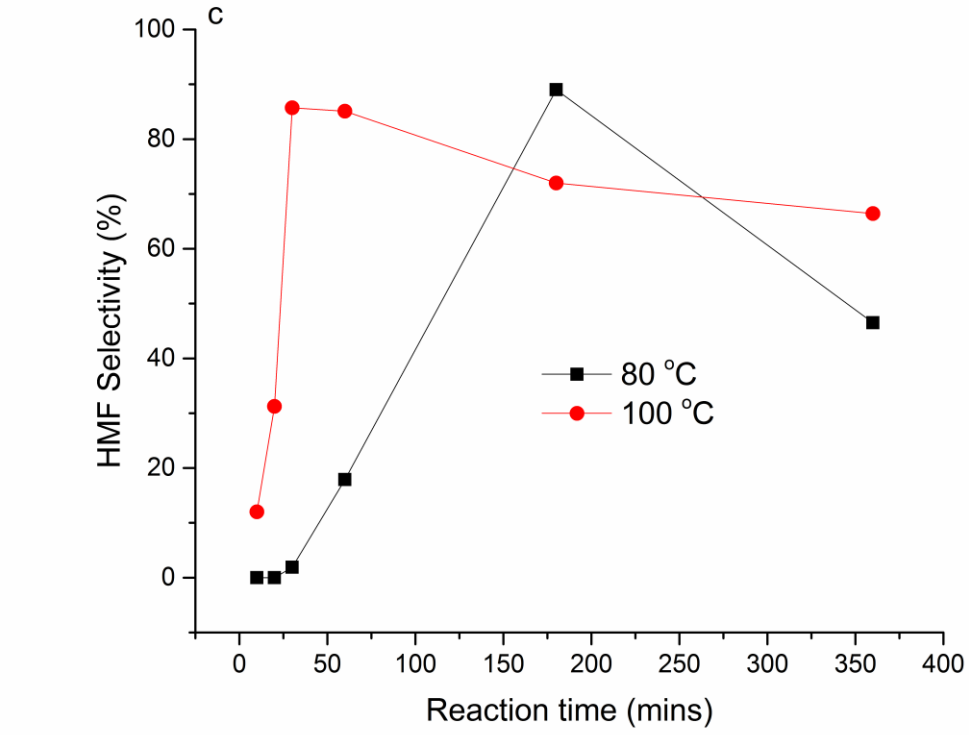

Figure 3.63. A, B and C. Comparative study of the fructose to HMF conversion with other catalysts. Conditions: Fructose 180 mg, Fe-NHC S350 **1b** 32 mg, DMSO 4 mL, 80 °C then 100 °C.

3.3.7. Kinetic studies

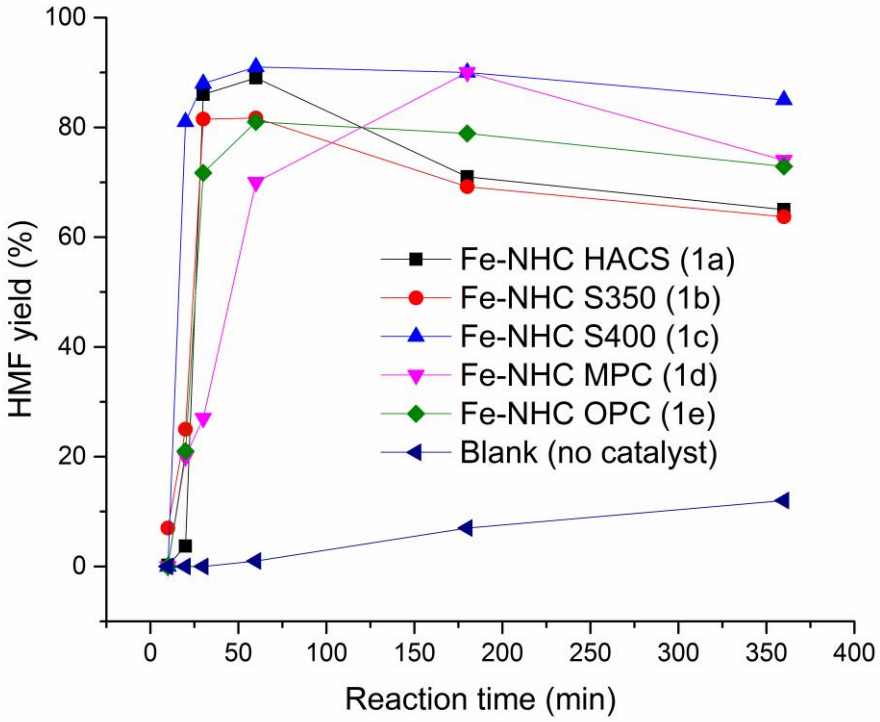

Figure 3.64. Reaction kinetic curve (yield vs time) for Fe-NHC HACS (**1a**) and Fe-NHC-Starbon™-350 (**1b**), Fe-NHC Starbon™ 400 (**1c**), Fe-NHC mango peel cellulose (**1d**) and Fe-NHC orange peel cellulose (**1e**). Conditions: Fructose 180 mg, catalyst 14 to 33 mg (depending on Fe loading in each catalyst), DMSO 4 mL, 100 °C

The kinetic profile (Figure 3.64) based on HMF yield efficiency for the five different supports employed (**1a-e**), showed a similar pattern. At 20 minutes HMF yield (81%) was highest for Starbon-400 support (**1c**), with Fe-NHC HACS (**1a**) having the lowest yield (3.7%). At 30 minutes good yields were obtained with all the catalysts except Fe-NHC mango peel cellulose (**1d**) with a lower yield of 27 % at 30 minutes reaction time. Highest yields were obtained at 1 h reaction time except for the Fe-NHC mango peel cellulose (**1d**) which attained its highest yield at 3 h reaction time. Generally, it was noted that for all catalysts employed, prolonging the reaction to 3 h and 6 h resulted in decreased yields of HMF. This is attributed possible rehydration to formic and levulinic acid or formation of humic substances as evidenced by darkening of the reaction mixture. In the absence of catalyst (blank) there were significantly lower HMF yields even at longer reaction times of 3 h and 6 h.

Further temperature kinetic analysis of fructose dehydration to HMF catalyzed by Fe-NHC Starbon 350 (**1b**) was performed using DMSO as reaction solvent. To conduct the kinetic studies of the fructose to HMF conversion using the fabricated Fe-NHC supported catalyst, it was assumed that fructose (**2**) to HMF (**3**) dehydration follows pseudo-first order reaction kinetics as there is only one starting material, *i.e*, fructose giving one predominant product (HMF).[215]

The rate of fructose conversion (*Eq .4*) can thus be expressed as:

$$-r[\text{fructose}] = -\frac{d[\text{fructose}]}{dt} = k[\text{fructose}] = \frac{d[\text{HMF}]}{dt} \quad \ldots\ldots\ldots\ldots\ldots (Eq.4)$$

where [fructose] and [HMF] represents molar concentrations of fructose and HMF respectively, *k* is the rate constant of fructose dehydration at a temperature.

$$\text{Ln } k = -\frac{Ea}{RT} + \ln A \quad \ldots\ldots\ldots\ldots\ldots (Eq.5)$$

According to the above Arrhenius equation (*Eq. 5*), *Eq 4* can be transformed in to a linear equation of the form y = mx+c (*Eq. 6*), where *X* is fructose conversion, *t* is reaction time, *k* is the rate constant, and C is an arbitrary constant.[215]

$$-\ln(1 - X) = kt + C \quad \ldots\ldots\ldots\ldots\ldots (Eq.6)$$

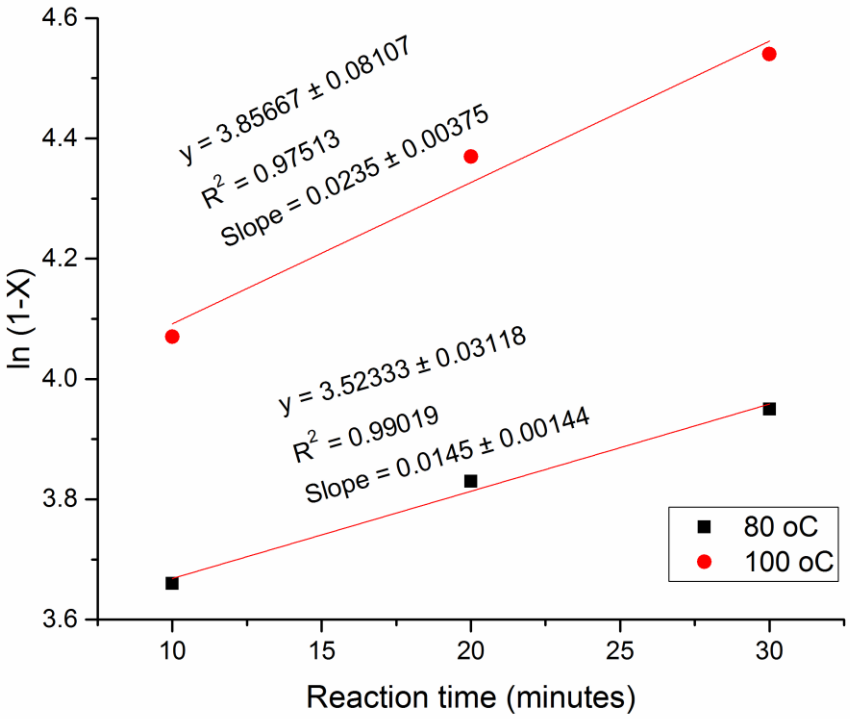

Figure 3.65. Kinetic parameters for fructose (**2**) to HMF (**3**) conversion at 80 ºC and 100 ºC based on first-order assumption for Starbon 350 (**1b**).

The values of ln (1 - *X*) were plotted against the reaction time (t) to obtain the pseudo first-order rate constant (*k*) (Figure 3.65) which, as expected, shows that *k* (rate constant) for fructose (**2**) to HMF (**3**) increases with increase in reaction temperature from 80 ºC (0.0145 M s^{-1}) to 100 ºC (0.0235 M s^{-1}).

The activation energy was calculated from the observed rate constant k_1 (0.0145 ± 0.00144 M s^{-1}) and k_2 (0.0235 ± 0.00375 M s^{-1}) at 80 and 100 ºC, respectively using the equation 7.

$$\ln(k_2/K_1) = Ea/R \times (1/T_1 - 1/T_2) \ldots\ldots\ldots\ldots\ldots (Eq.\ 7)$$

where

Ea is the activation energy of the reaction in J mol^{-1}

R is the ideal gas constant = 8.3145 J K^{-1}·mol^{-1}

T_1 and T_2 are absolute temperatures

k_1 and k_2 are the reaction rate constants at T1 and T2

The observed activation energy for Starbon 350 catalyst (**1b**) is found to be 26.8 kJ mol^{-1}. Though the activation energy is lower than that reported in some literature at similar reaction conditions, the result only presents very preliminary data but would suggest that the catalyst may be superior to those previously reported for HZSM-5 (Si/Al = 25) (70 kJ mol-1) and MIL-101(Cr)-SO_3H (55 kJ mol^{-1}). [215]

3.3.8. Summary

Thus, in summary although not all the intermediates on route from fructose to HMF have been characterised, in comparison with the work of Guan *et al.*[214] the following mechanism (Scheme 3.3) for conversion of fructose (**2**) to HMF (**3**) is proposed. The iron (Fe^{3+}) coordinates with the carbonyl and adjacent OH within fructose to form a metal-fructofuranose complex. A series of three dehydrations (-3 H_2O) induced by the catalyst attaching and detaching the fructose ring structure affords the desired HMF (**3**). This further implies the need for the catalytic centre to be an ion, hence the presence of Fe nanoparticles (Fe_2O_3 or FeO) aren't catalytically active.

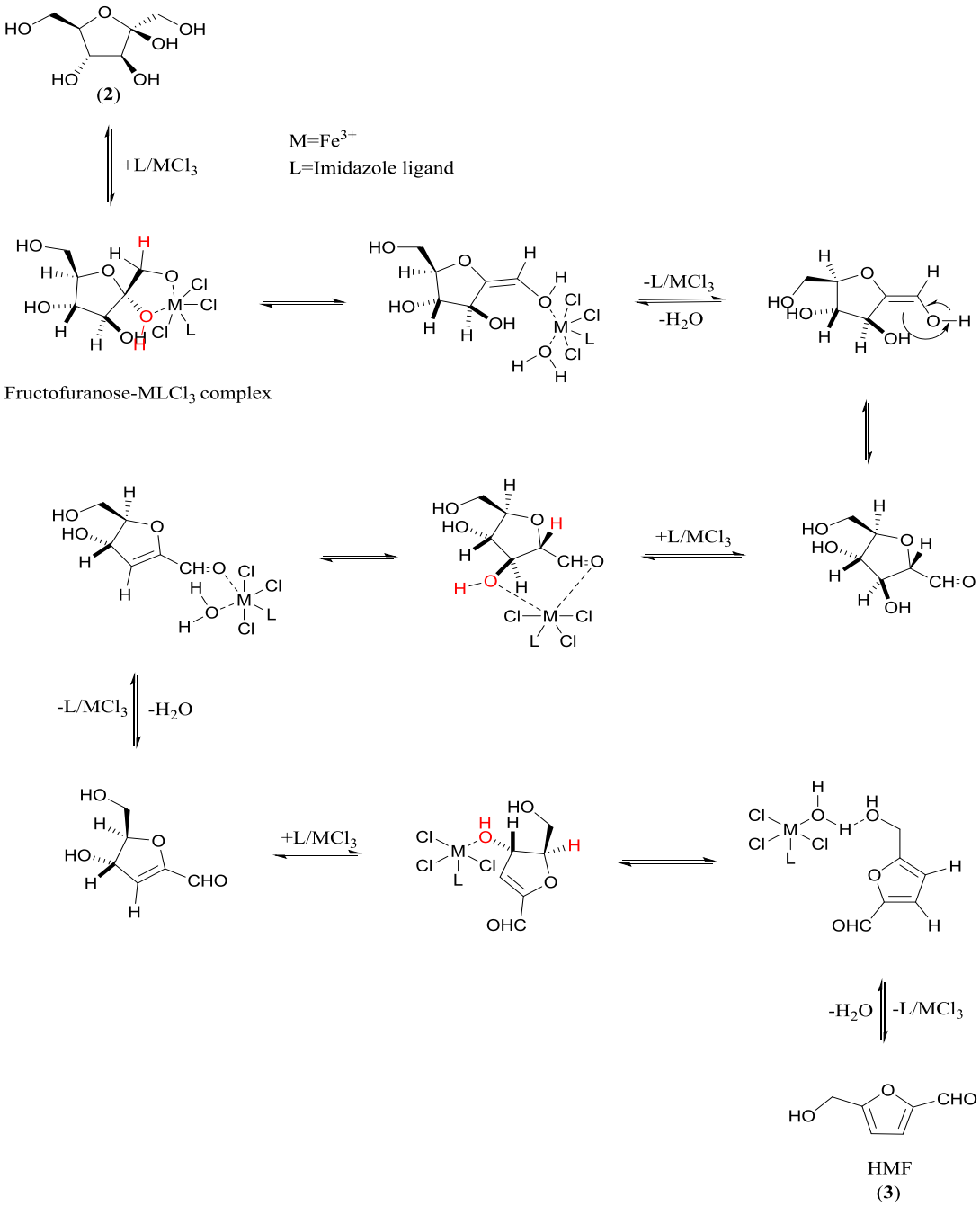

Scheme 3.3. Proposed fructose (**2**) dehydration mechanism to HMF (**3**) by Fe-NHC catalyst.

3.4. Part 3: Glucose and fructose dehydration to 5-CMF

The thermal and chemical instability issues, coupled with the high solubility in water, and low melting point of HMF have become a hinderance towards the successful generation of fuels and chemicals from carbohydrates and other ligno-cellulosic materials. This limitation has in recent years paved the way for CMF as better alternative to HMF in this regard. CMF has better thermal and chemical stability, lower polarity (immiscible in water), and it can be more readily produced from glucose and cellulose biomass due to its lipophilicity.[55, 56] As reported by Mascal *et al.* CMF serves as a precursor to the new generation bio-fuels and high value chemicals.[57]

NHC metal complexes has been shown to catalyse the conversion of fructose to HMF through a mechanism that involves attaching and detaching of the NHC metal complex on fructose leading to successive dehydration stages (Scheme 3.3).[214] NHC metal complexes ability to also catalyse the isomerisation of glucose to fructose (see later scheme 3.5) warrants the use of the fabricated Fe-NHC catalyst for glucose to CMF conversions.[214]

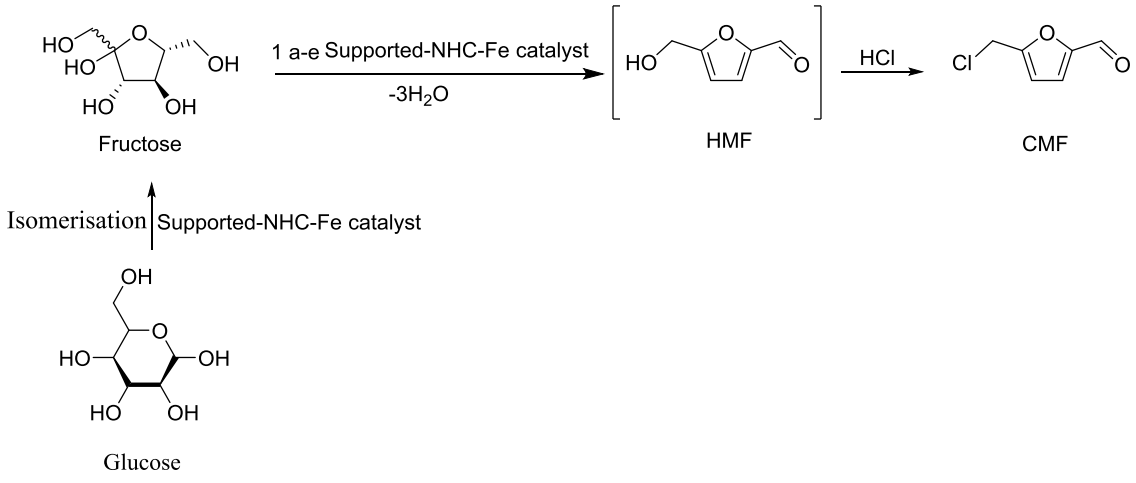

Scheme 3.4. Fructose and glucose dehydration to HMF and conversion to CMF.

3.4.1. Application of the fabricated catalyst towards fructose dehydration to 5-(chloromethyl)furfural (CMF)

3.4.1.1. ^{1}H NMR spectroscopy results on the fructose conversions to CMF

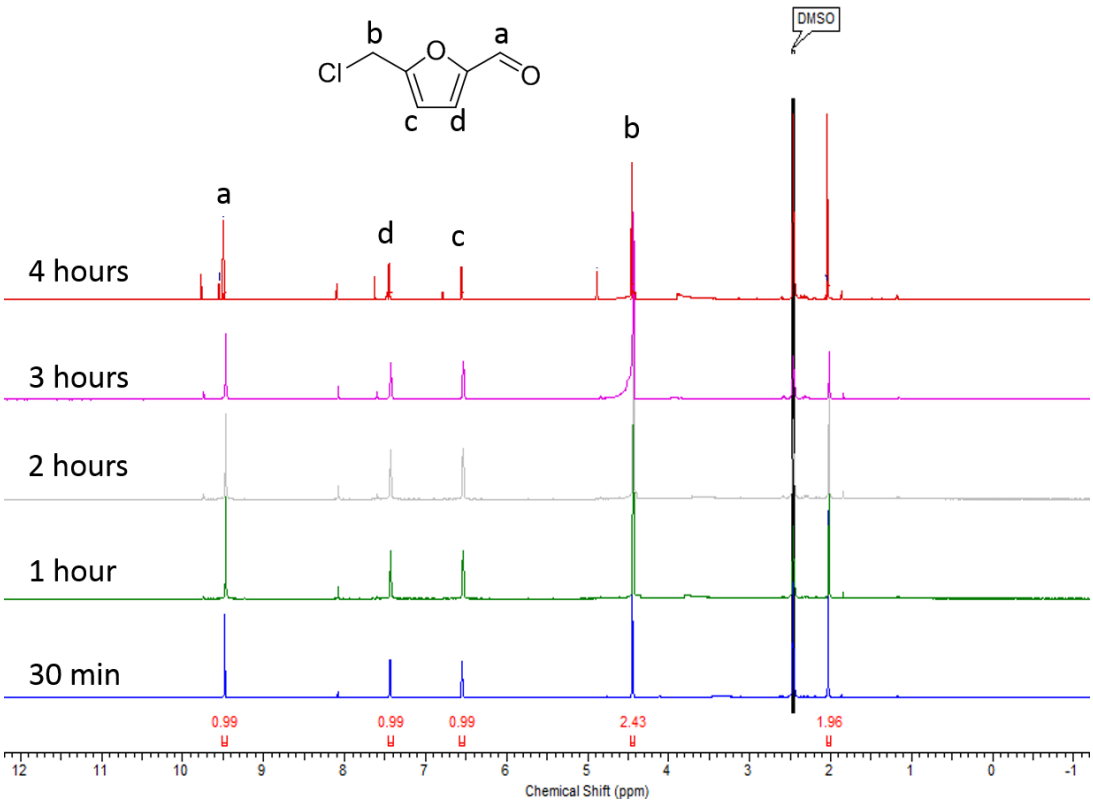

Figure 3.66 [1]H NMR of fructose to CMF conversion using aqueous HCl.

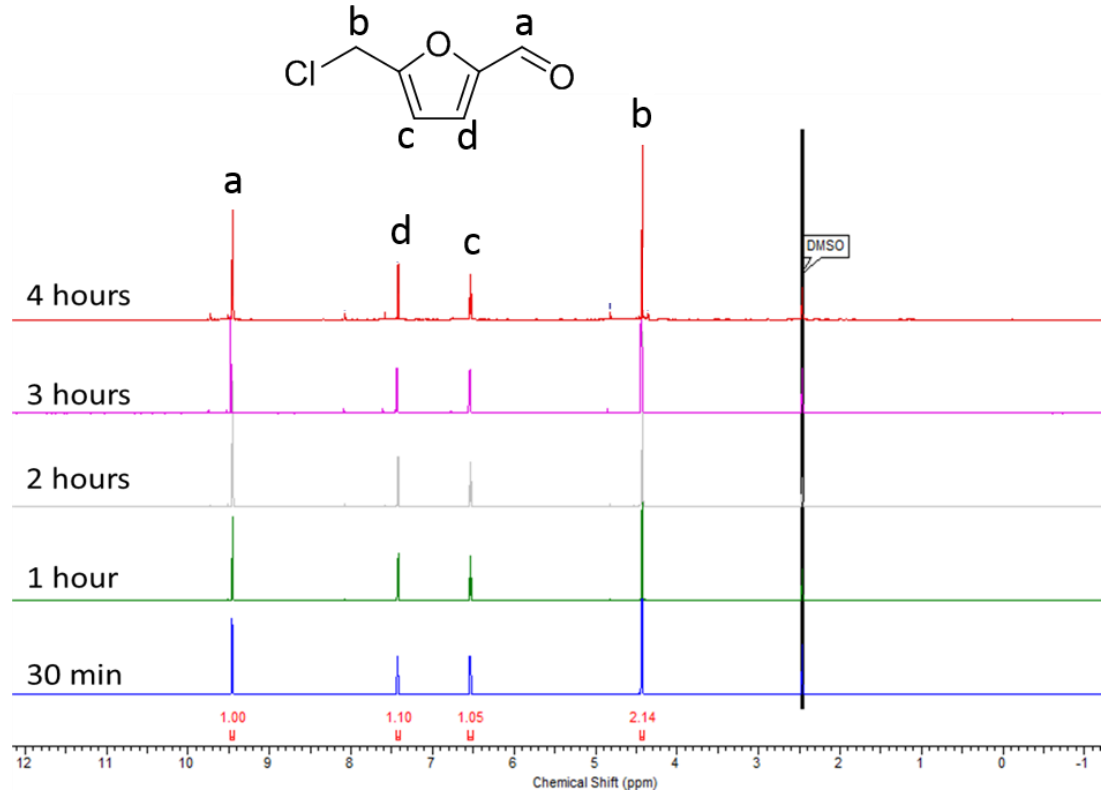

Figure 3.67 [1]H NMR of fructose to CMF conversion using aqueous HCl and Fe-NHC Starbon 350 catalyst (**1b**).

As can be seen from figures 3.66 & 3.67 corresponding to fructose (**2**) conversion to CMF (**14**) using HCl and HCl/Fe-NHC Starbon 350 catalyst (**1b**), CMF (**14**) is evident at 30 min ((1 H, **H**-C=O, 9.45 ppm), (1H, O=C-C=C**H**, 7.42 ppm), (1H, H_2C-C=C**H**-, 6.53 ppm) and (2H, Cl-C**H_2**-C=CH, 4.48 ppm)) coupled with almost depletion of the signals for fructose. The signal at 8.08 ppm was assigned to formic acid. While the signal at 2.45 ppm is assigned to DMSO- d_6. [212]

The NMR data shows that there is no need to even prolong the reaction above 30 minutes as the fructose has almost been fully converted to other products including the CMF at 30 minutes reaction time.

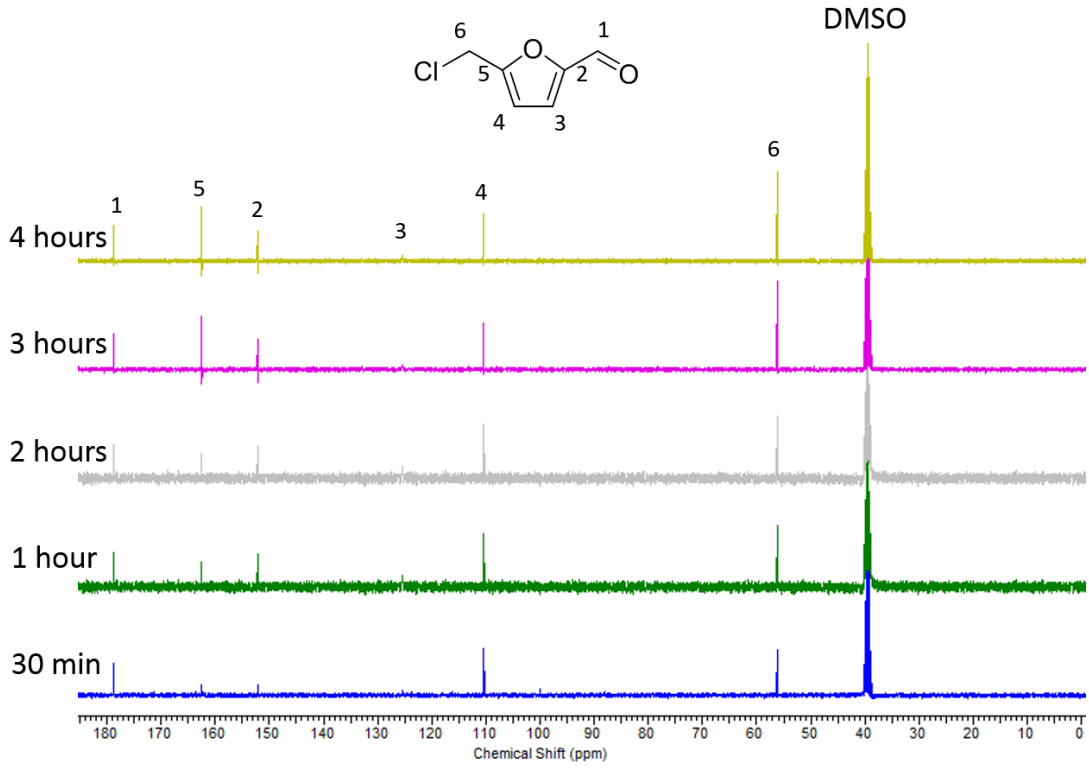

Figure 3.68 ^{13}C NMR of fructose to CMF conversion using aqueous HCl.

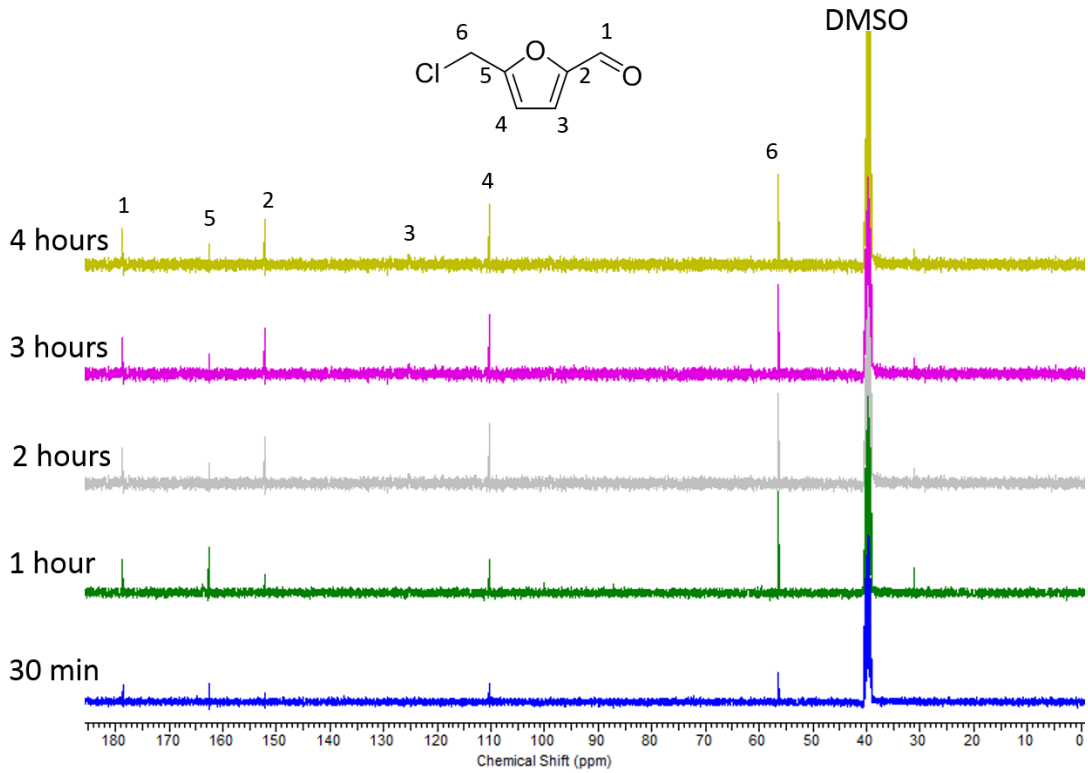

Figure 3.69 ^{13}C NMR spectroscopy of fructose to CMF conversion using aqueous HCl and Fe-NHC Starbon 350 catalyst (**1b**).

The complementary ^{13}C NMR spectroscopy study was conducted simultaneously with the ^{1}H NMR to further evidence fructose (**2**) conversion to CMF (**14**). Figures 3.68 & 3.69 revealed a decrease in fructose (**2**) resonances (60 - 105 ppm) coupled with an increase in those for CMF (**14**) with respect to time. CMF signals were evident at t=0.5 h (56.13 ppm, Cl-**C**H_2-C=CH-), (110.47 ppm, Cl-CH_2-C=**C**H-), (152.10 ppm, O=HC-**C**H=C-), (162.57 ppm, Cl-CH_2-**C**=CH_2-) and 178.77 ppm, O=**C**H-C=CH)).[214] The signal at 163.43 ppm most likely corresponds to formic acid which agrees with its resonance observed by ^{1}H NMR spectroscopy at 8.0 ppm.

3.4.1.2. HPLC results for the fructose conversion to CMF using the fabricated supported Fe-NHC catalyst.

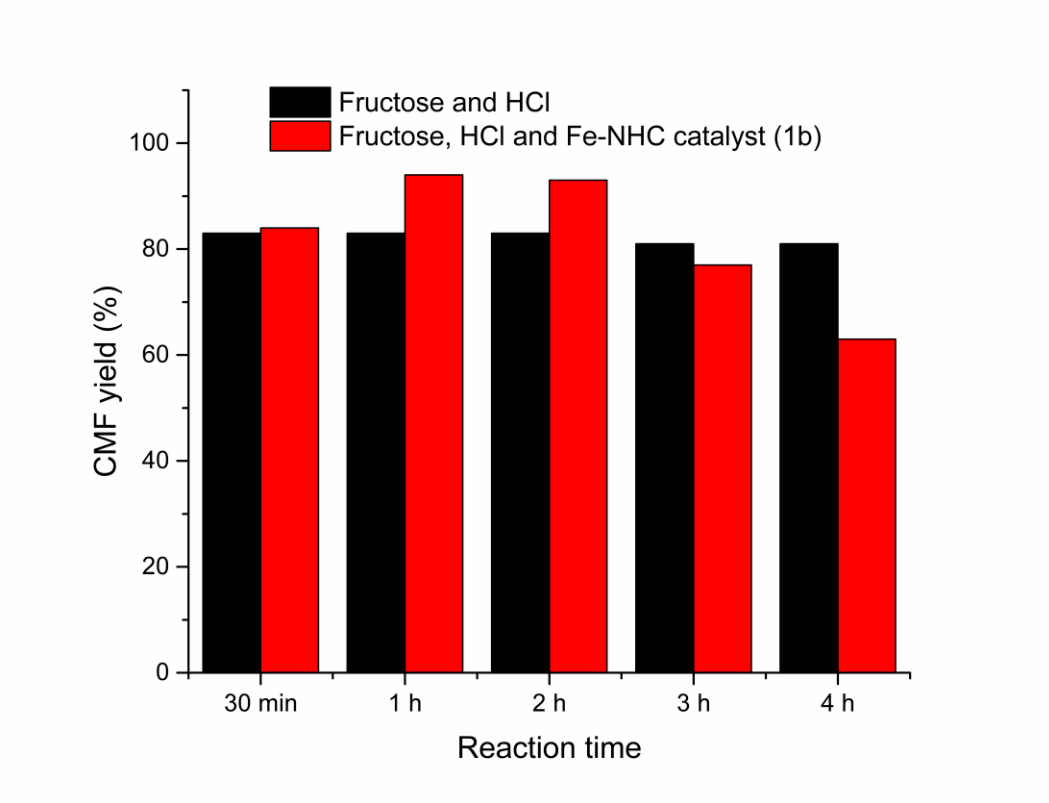

Figure 3.70. Fructose conversion to CMF study using aqueous HCl.

The results in Figures 3.70 shows the HPLC results of the fructose conversion to CMF. The fructose has the highest conversion to CMF up to 92 % yield at 1 h reaction time using both HCl and the Starbon 350 immobilised catalyst (**1b**). Without the Fe-NHC catalyst however, relatively 10 % lower yields where obtained at 1 h and 2 h reaction times.

3.4.2. Application of the fabricated catalyst towards glucose dehydration to 5-(chloromethyl)furfural (CMF)

The availability and low cost of glucose makes it more sustainable source of platform molecules than fructose. As such the research sought to use glucose as a substrate for the production of CMF.

3.4.2.1. ^{1}H NMR spectroscopy results on the glucose conversions to CMF

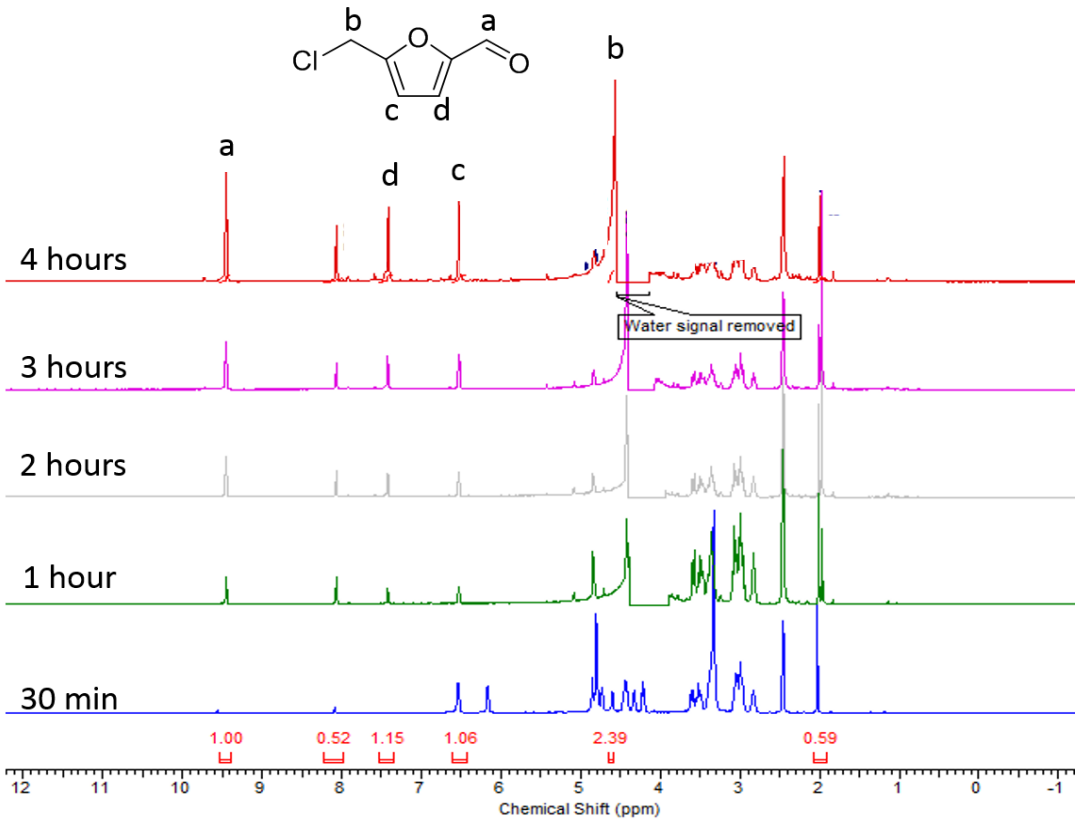

Figure 3.71 ^{1}H NMR of glucose to CMF conversion using aqueous HCl.

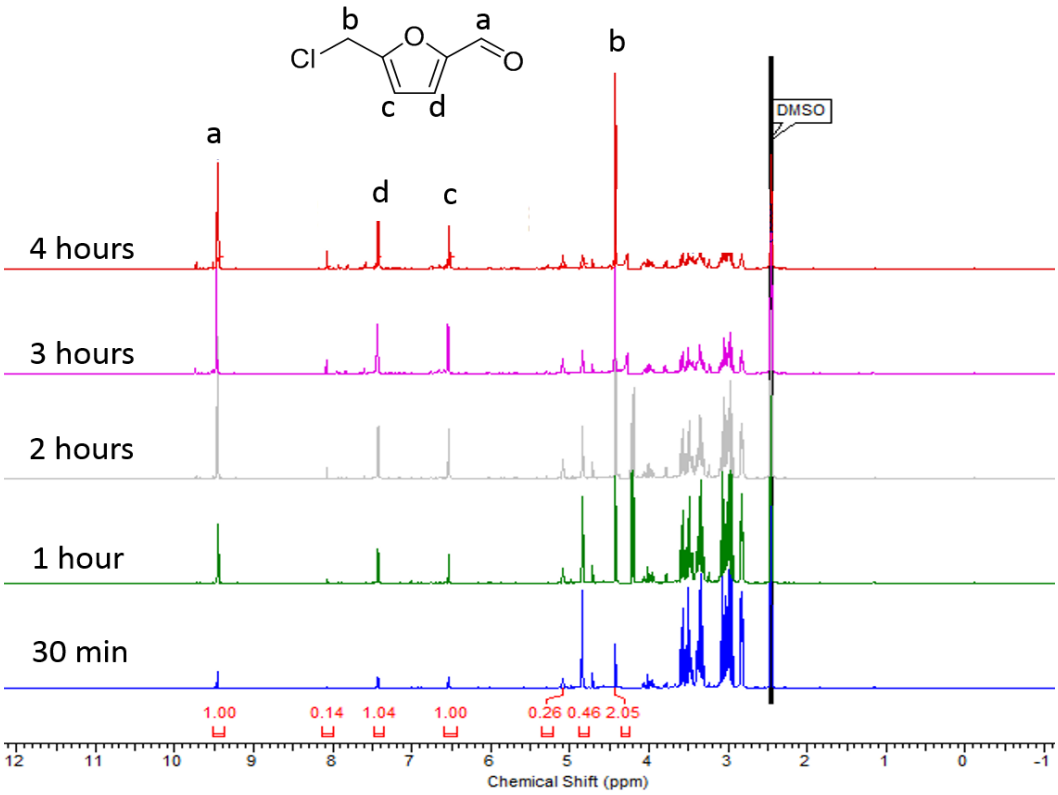

Figure 3.72 ^{1}H NMR of glucose to CMF conversion using aqueous HCl and Fe-NHC Starbon 350 catalyst (**1b**).

In both Figure 3.71 corresponding to glucose conversion to CMF (**14**) using only HCl and Figure 3.72 corresponding to glucose conversion to CMF (**14**) using the Fe-NHC Starbon 350 catalyst (**1b**), weak signals at 7.42 ppm, 6.55 ppm and 4.56 ppm starts to appear at 30 min reaction time which develop in intensity as the reaction proceeds over time. CMF (**14**) was evident at 1 h reaction time (1 H, **H**-C=O, 9.45 ppm), (1H, O=C-C=C**H**, 7.42 ppm), (1H, H_2C-C=C**H**-, 6.52 ppm) and (2H, Cl-C**H**$_2$-C=CH, 4.57 ppm) coupled with much reduction of the signals for glucose at t= 6 h. The signal at 8.06 ppm was assigned to formic acid. While the signal at 2.45 ppm is assigned to DMSO-d_6. [212]

The NMR data shows that prolonging the reaction above 30 minutes is crucial to achieving higher yields. After 1 h reaction time, the yields start to reduce with increasing reaction time.

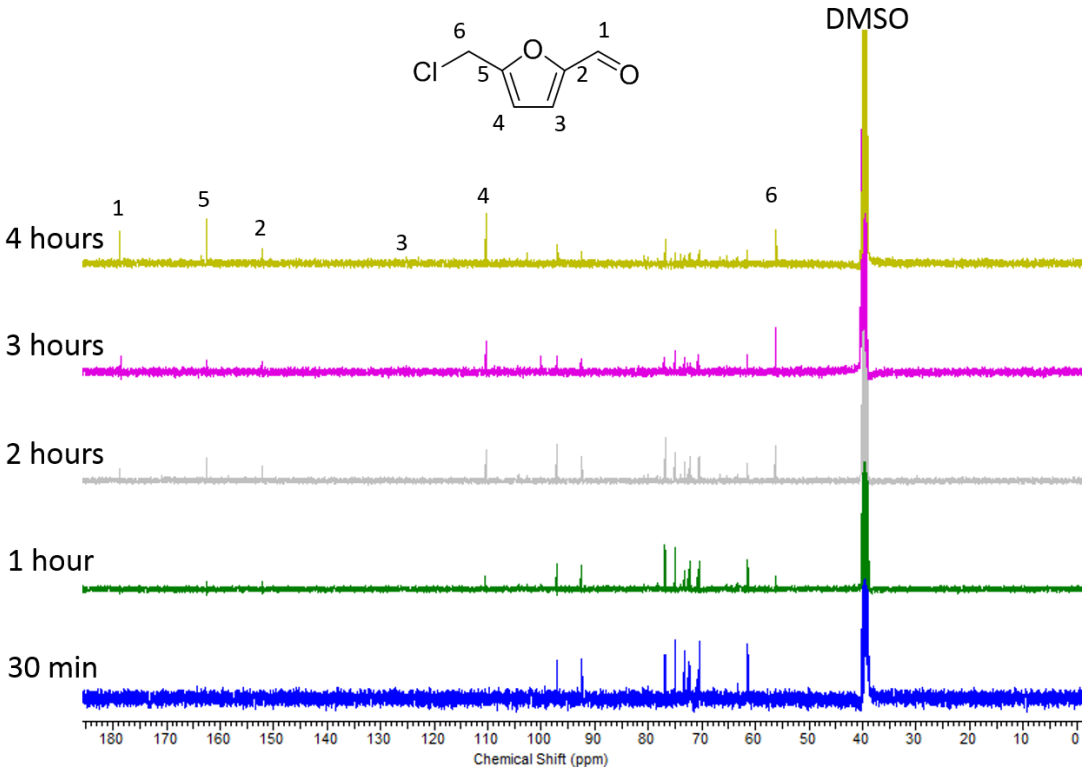

Figure 3.73 ^{13}C NMR of glucose to CMF conversion using aqueous HCl.

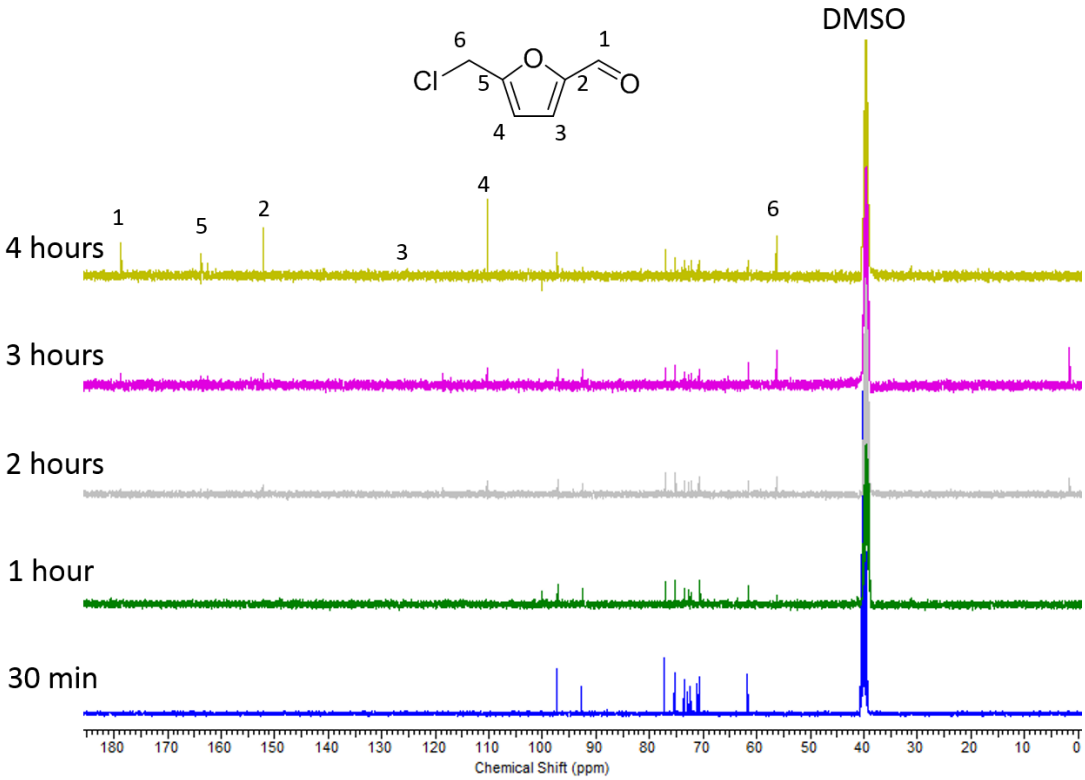

Figure 3.74 ^{13}C NMR of glucose to CMF conversion using aqueous HCl and Fe-NHC Starbon 350 catalyst (**1b**).

Figures 3.73 & 3.74 revealed a decrease in resonances (60 - 105 ppm) assigned to glucose, fructose (resulting from glucose isomerisation) and other intermediates coupled with an increase in those for CMF (**14**) with respect to time. CMF signals were evident at t=0.5 h (56.23 ppm, Cl-**C**H_2-C=CH-), (110.28 ppm, Cl-CH_2-C=**C**H-), (152.14 ppm, O=HC-**C**H=C-), (162.79 ppm, Cl-CH_2-**C**=CH_2-) and 178.78 ppm, O=**C**H-C=CH)). The signal at 163.81 ppm most likely corresponds to formic acid which agrees with its resonance observed by ^{1}H NMR spectroscopy at 8.0 ppm.

3.4.2.2. HPLC results for the glucose conversion to CMF using the fabricated supported Fe-NHC catalyst.

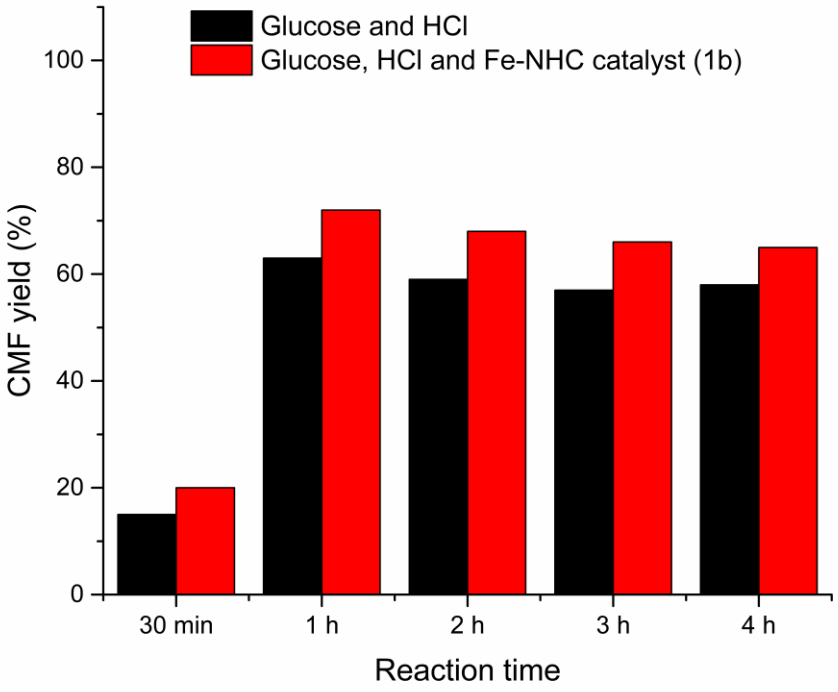

Figure 3.75. Glucose conversion to CMF study using aqueous HCl with Fe-NHC catalyst (**1b**).

Most interesting are the results of the glucose isomerisation and dehydration to CMF Figure 3.75. Glucose being a difficult substrate than fructose due to the difficulty to isomerise to fructose prior to dehydration. A trend of increasing 5-chloromethyl furfural yields by about 10-11% at 1 h and 2 hours reaction time was observed with the fabricated Fe-NHC catalyst as compared to the control experiment done without the catalyst. After 2 hours of the reaction time the yield starts to reduce with increased reaction time, possibly due to the catalyse degradation of CMF into humins.

3.4.3. Application of the fabricated catalyst towards glucose dehydration to 5-(hydroxymethyl)furfural.

The previous section (3.4.2) suggests that the fabricated Fe-NHC catalyst **1b** might aid the glucose to fructose isomerisation which might be the reason for the increased CMF yield when the catalyst is added as compared to the control experiment in absence of catalyst. As such herein we investigated the conversion of glucose to HMF using the fabricated Fe-NHC catalysts **1a** and **1b**.

3.4.3.1. ^{1}H NMR spectroscopy study on the glucose dehydration to HMF.

Figure 3.76 shows the stacked ^{1}H NMR spectra at 100 ˚C for the isomerisation and dehydration of glucose to HMF in the presence of Fe-NHC catalyst at t= 0.5 h, 1 h, 3 h and 6 h.

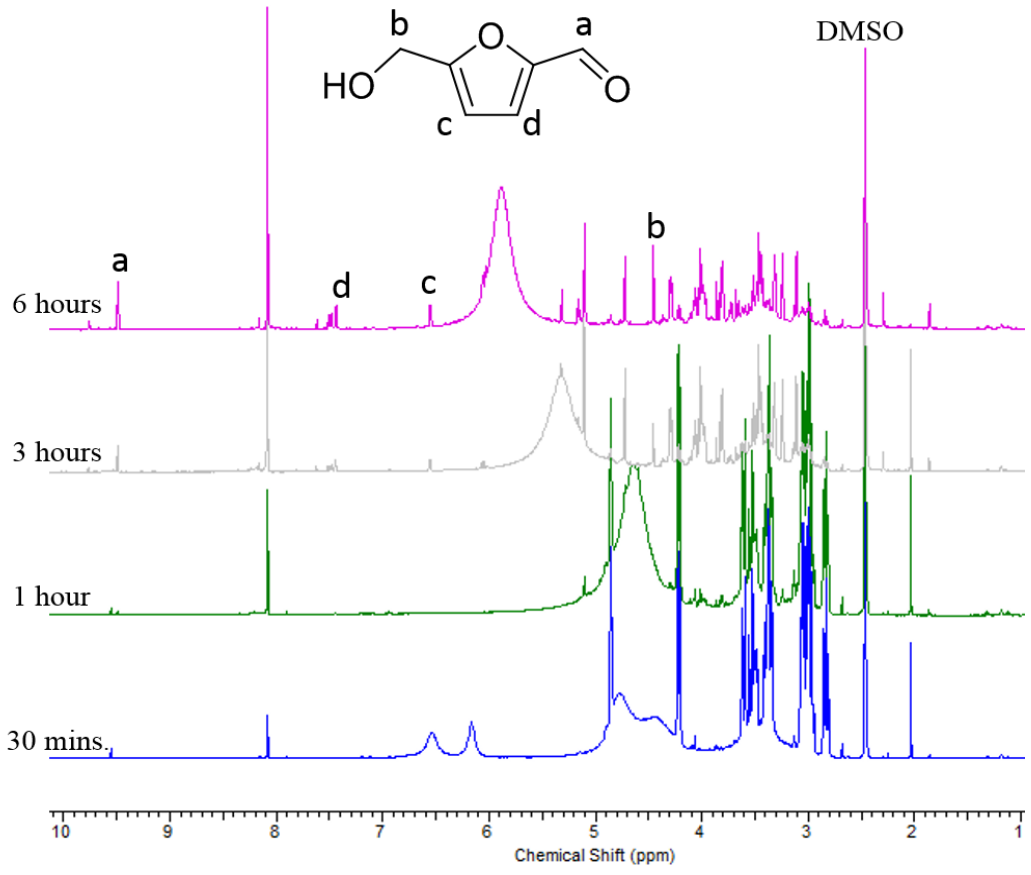

Figure 3.76 ^{1}H NMR spectra results of glucose dehydration to HMF using Fe-NHC catalyst (**1a**).

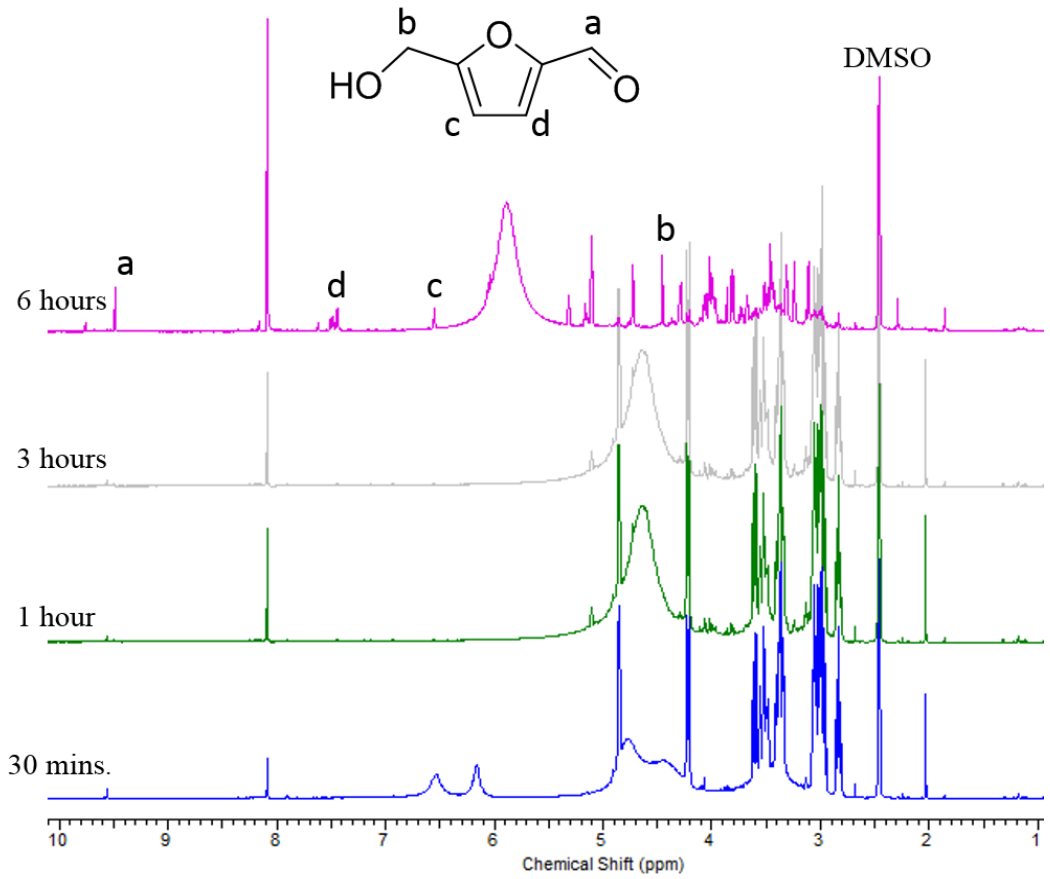

Figure 3.77 ^{1}H NMR spectra results of glucose dehydration to HMF using Fe-NHC catalyst (**1b**).

The proton NMR spectra of the glucose dehydration to HMF (Figure 3.76 & 3.77) using the synthesised immobilised Fe-NHC catalysts (**1a**) and Fe-NHC catalyst (**1b**) respectively, indicates that, weak HMF signals were only evident at reaction time of 3 h to 6 h, (1 H, **H**-C=O, 9.48 ppm), (1H, O=C-C=C**H**, 7.44 ppm), (1H, H_2C-C=C**H**-, 6.55 ppm) and (2H, HO-C**H**$_2$-C=CH, 4.46 ppm). However, the NMR data shows a very high yield of formic acid with signal at 8.09 ppm, suggesting that possibly the isomerisation of the glucose to HMF proceed very slowly such that the isomerised fructose produced continuously undergoes dehydration to HMF and subsequently to humins which later produce formic acid (8.08 ppm).

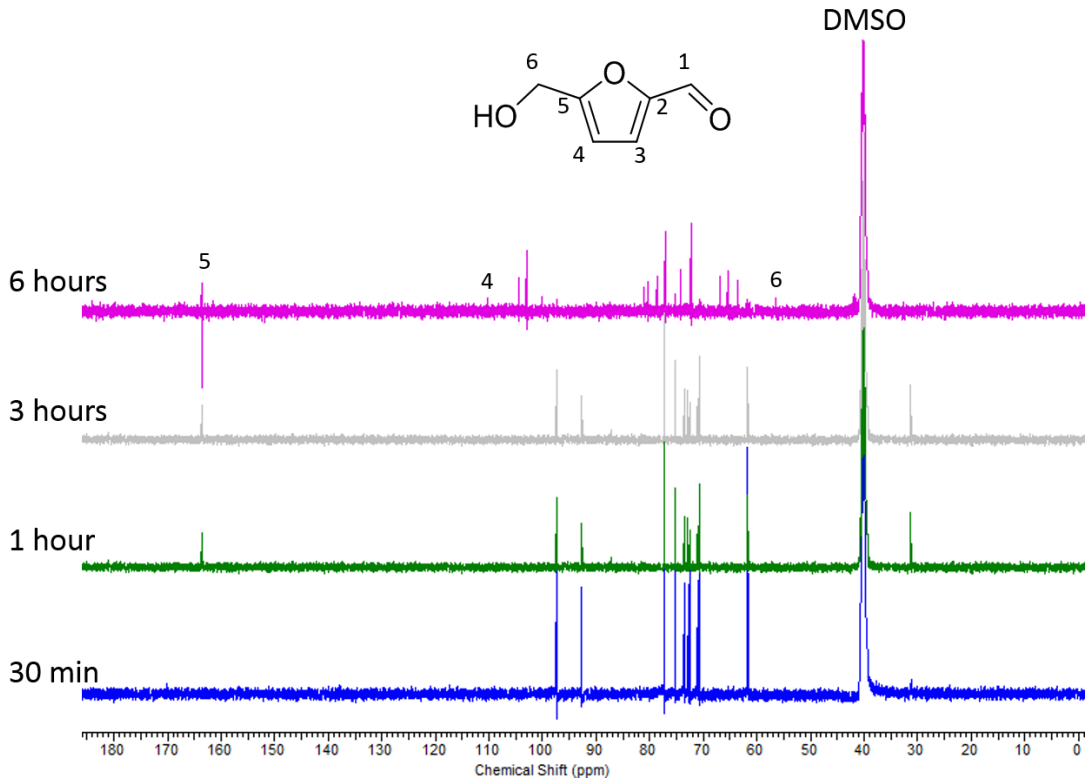

Figure 3.78 ^{13}C NMR spectra of glucose dehydration to HMF using Fe-NHC catalyst (**1a**).

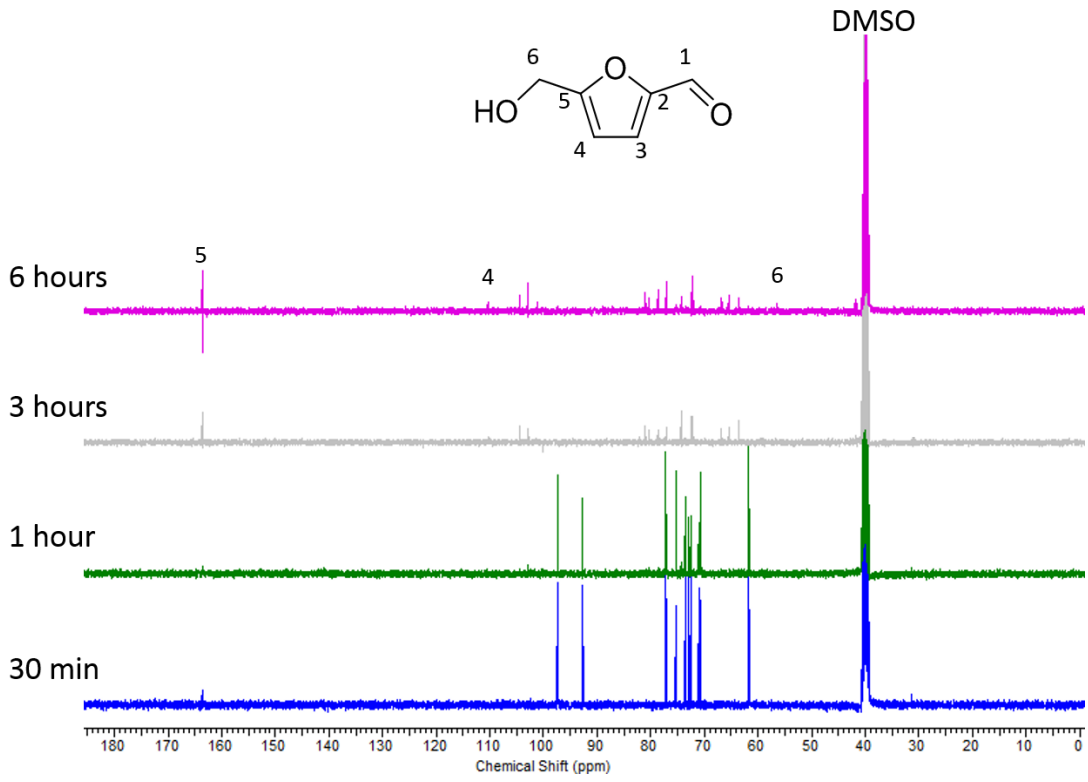

Figure 3.79 ^{13}C NMR spectra of glucose dehydration to HMF using Fe-NHC catalyst (**1b**).

Figures 3.78 & 3.79 revealed a decrease in resonances (60 - 105 ppm) assigned to glucose and other intermediates at 3 h to 6 h reaction time. Very weak, less visible HMF signals start to appear at t= 3 h and 6 h (56.23 ppm, HO-**C**H_2-C=CH-), (110.28 ppm, HO-CH_2-C=**C**H-) and (162.79 ppm, HO-CH_2-**C**=CH_2-). The signal at 163.10 ppm most likely corresponds to formic acid which agrees with its resonance observed by ^{1}H NMR spectroscopy at 8.08 ppm. These weaker HMF signals, further supported the very poor HMF yields obtained through HPLC analysis of the conversion products.

3.4.3.2. HPLC results of the glucose dehydration to HMF using the fabricated Fe-NHC catalyst.

To further qualitatively and quantitatively characterise the catalytic glucose to HMF conversion using the fabricated Fe-NHC supported catalysts, HPLC was used to monitor the progress of the reaction and to obtain conversions and yields.

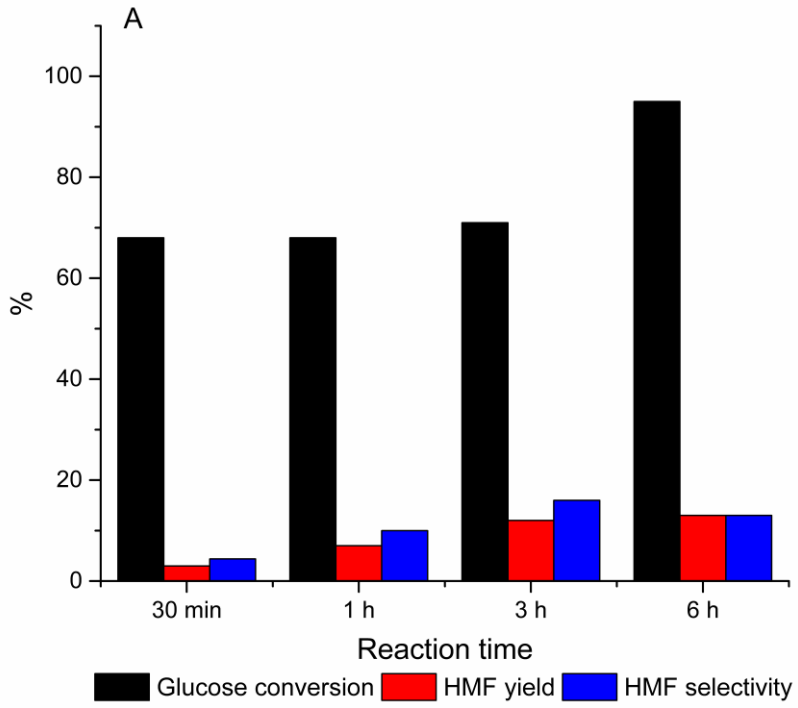

Figure 3.80. HPLC results of glucose dehydration to HMF using Fe-NHC HACS catalyst (**1a**).

The results of the HPLC analysis on the glucose to HMF conversion with the fabricated Fe-NHC HACS catalysts (**1a**) (Figure 3.80), shows that although higher glucose conversion was achieved, the HMF yields were quite low (about 2-15%). This indicates that the glucose is not successfully isomerised to fructose in good yields at

the reaction conditions used. Most of the glucose conversions are therefore into other intermediates rather than the fructose as proposed.

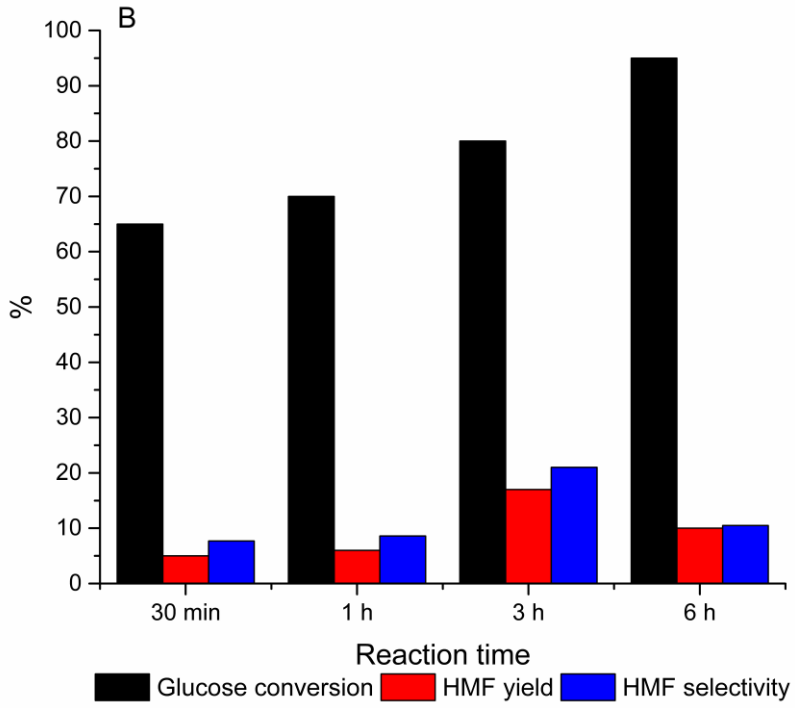

Figure 3.81 HPLC results of glucose dehydration to HMF using Fe-NHC Starbon 350 catalyst (**1b**).

The HPLC analysis on the glucose to HMF conversion with the fabricated Fe-NHC Starbon^{TM} 350 catalyst (**1b**) (Figure 3.81) gives a similar result to that of Fe-NHC HACS catalyst (**1b**) with slight increase in HMF yields at 3 h reaction time obtained from the immobilised Fe-NHC Starbon 350 (**1b**) (18 % HMF yield).

3.4.3.3. Plausible mechanism for glucose isomerisation to fructose

Based on the work of Guan *et al.*[214] we propose the following plausible mechanism for isomerisation of glucose to fructose. The iron (Fe^{3+}) coordinates with the adjacent OH within glucose to form a metal-glucopyranose complex. A series of rearrangement induced by the catalyst attaching and detaching the glucose ring structure affords the desired fructose isomer.

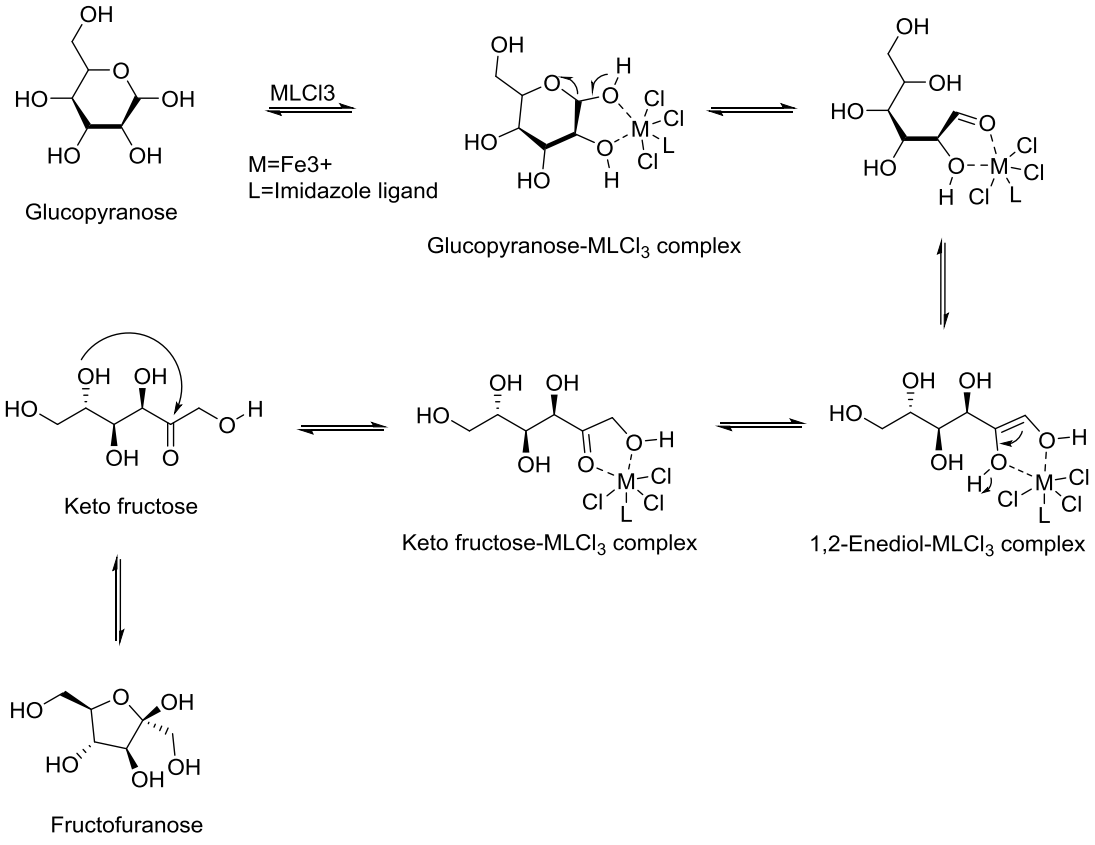

Scheme 3.5. Plausible mechanism for glucose isomerisation to fructose.

CHAPTER 4. Summary, Conclusions and Future Work

4.1. Summary of Research Findings

This chapter presented the results on the synthesis of an Fe-NHC catalyst synthesised through the alkylation of 1-(aminopropyl)imidazole **7** with 2,4,6-trimethylbenzyl chloride **10**, to afford the desired NHC ligand precursor (1-[aminopropyl]-3-(2,4,6-trimethylbenzyl)imidazolium chloride **12**. The desired ligand **12**, was immobilised on various mesoporous supports which were later reacted with $FeCl_3$ to produce the final Fe-NHC catalysts **1a-e**. The different synthesised catalysts were characterised using diverse techniques including NMR spectroscopy, ATR-IR spectroscopy, XPS, Mossbauer spectroscopy, ICP-MS, thermogravimetry and porosimetry etc.

The results on the characterisation of the various successfully synthesised, immobilized heterogeneous supported catalysts and their subsequent application towards fructose (**2**) to HMF (**3**) conversions is presented below in a tabular form (Table 4.1), highlighting the general trends with respect to catalyst nature and activity. A general discussion of the trend is presented.

Table 4.1. Summary of measured parameters of the fabricated Fe-NHC catalysts.

Parameter	**Fe-NHC HACS (1a)**	**Fe-NHC S350 (1b)**	**Fe-NHC S400 (1c)**	**Fe-NHC MPC (1d)**	**Fe-NHC OPC (1e)**
Surface Area $_{BET}$ (m^2/g)	135	132	13	44	80
Pore Volume (cm^3/g)	0.60	0.35	0.19	0.07	0.22
Pore diameter (nm)	16.30	09.30	48.63	4.32	8.22
Fe loading (mmol/g)	0.68	0.31	0.32	0.30	0.52
Fructose convers. (%)	87	95	89	99	75
HMF yield (%)	86	81	88	70	72
HMF selectivity (%)	99	85	99	71	95

Condition: Fructose 180 mg, catalyst 14 to 32 mg (depending on catalyst Fe loading), DMSO 4 mL, 100 ^oC, 0.5 h.
Note: For Fe-NHC MPC conversions and yields are reported at 1 h reaction time.

The results in table 4.1. indicate that, although all the catalysts have the same Fe-NHC complex, the nature of the support plays a very important role in determining the loadings of the NHC ligand and subsequently the Fe itself. Fe-NHC HACS has the highest Fe loading of 0.68 mmol/g, a feature attributed to the substantial number of

OH groups on starch and the large surface area of the expanded HACS that allows for higher accessibility of the OH groups to which the ligand is bonded. The Starbon^{TM} and cellulose immobilised Fe-NHCs have lower Fe loadings compared to expanded HACS due to lower ligand loadings as a result of the former having a limited number of OH groups after the carbonisation process and the latter having a more compact and partly crystalline nature that limits the accessibility of the OH groups.

The results on the application of the supported catalysts towards fructose to HMF conversions showed that Fe-NHC HACS and Fe-NHC Starbon^{TM} 350 have the highest HMF yield at 0.5 h reaction time, both of which have the largest pore diameters and good surface area that allow for effective diffusion towards the catalytically active sites.

The two cellulosic supported catalysts (Fe-NHC MPC (**1d**) and Fe-NHC OPC (**1e**)) which were different in terms of Fe loadings and the surface area and porosity values, also showed different catalytic activities towards fructose to HMF dehydrations. Fe-NHC MPC has the lowest HMF yields (27 %), less than half of the yields obtained with Fe-NHC OPC (71 %) at 0.5 h. The inference here is that Fe-NHC MPC has significantly lower Fe loading, surface area, pore size, and pore volume compared to the Fe-NHC OPC which resulted in its reduced catalytic activity. The catalytic activities of the fabricated supported Fe-NHC catalysts, are very much influenced by their Fe loadings and surface area and porosity values, indicating the diverse nature of the fabricated catalysts.

For the glucose and fructose to CMF conversions, the fabricated Fe-NHC catalyst **1b**, has proven to have some catalytic activity, increasing CMF yields by about 10-11 % as compared with control experiments done without the catalyst. However, for the glucose conversions to HMF using the fabricated Fe-NHC catalysts **1a** and **1b**, highest HMF yields (15% for **1a** and 18 % for **1b**) were obtained at 3 h reaction time.

4.2. Conclusion

The proposed supported Fe-NHC catalyst (**1a-e**) were fabricated successfully as confirmed by the various characterization techniques employed. All mesoporous supports were effective for the immobilization of the Fe-NHC due to accessible OH groups and enhanced surface area and porosity. The performance of the catalysts for

heterogeneous catalytic conversion of fructose (**2**) to HMF (**3**) was investigated with good yields obtained. The supported Fe-NHC catalysts were also employed in other important catalytic reactions; glucose/fructose to CMF conversions and glucose to HMF dehydration.

4.3. Future work

Future work can be focused on many areas including; devising better synthetic routes to the NHC ligand, utilisation of other types of NHC ligands for the synthesis of the Fe catalyst, using other metal centres other than Fe, using other supports like silica, or trying other reactions such as the Diels-Alder reaction, and amidation. However, as part of the future work, some initial screening was done on amide synthesis using carboxylic acids and amines (see appendix A).

Appendix A Preliminary Amidation reaction

Preliminary investigation on the use of Fe-NHCs (1a-e) as catalysts for amidation.

Amides are one of the most important classes of organic compounds in the chemical and particularly pharmaceutical industries.[216] The amide bond is one of the most fundamental functional group linkages. It is the single most common synthetic transformation used within medicinal chemistry.[217] Amide bond has an estimated occurrence of 25% in available drugs.[218] Roughley's analysis of the most common reactions used within synthetic medicinal chemistry research across three of the largest pharmaceutical companies (GSK, AstraZeneca, and Pfizer) indicated that *N*-acylation to prepare amides ranked 1st for frequency of use, accounting for 16% of all reactions performed, with the amide linkage present in 54% of the compound set analysed.[219] However, considering the importance of amides, development of efficient methodologies for their synthesis becomes necessary.[220, 221]

The fabricated catalyst Fe-NHC Starbon-350 **1b** was employed for direct amide synthesis from carboxylic acids and amines.

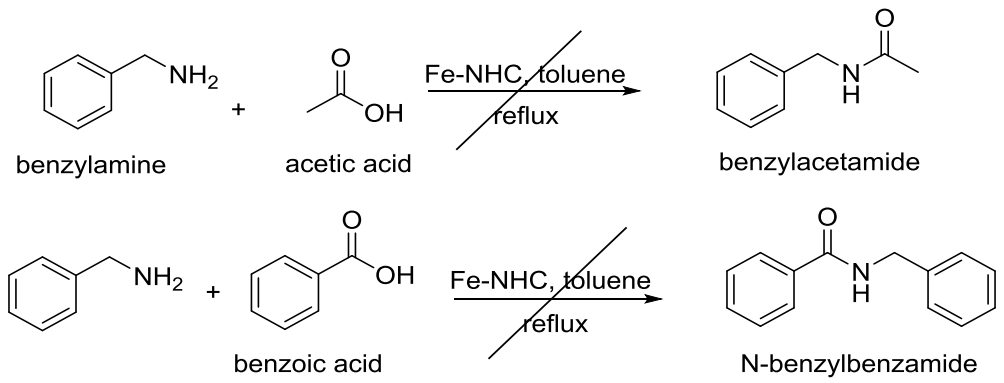

Scheme A1. Amide formation from amines and carboxylic acid.

Amides were synthesised by reacting acetic acid and benzoic acid with benzyl amine to produce benzyl acetamide and benzyl benzamide respectively (Scheme A1). The reactions were carried out using toluene as reaction solvent. Two reaction vessels were used under the same reaction conditions one serving as a control reaction without any

added catalyst and the other reactor containing Fe-NHC catalyst. The reactions were heated under reflux toluene for 12 hours with a sample taken after each hour.

The result of the synthesis of benzanilide shows no conversion even after 12 hours of reaction time. The results however, are not very surprising as aniline is a very difficult substrate to use in amidation reaction especially when using carboxylic acids rather than the more reactive acid halides or anhydrides. This is due to the reduced nucleophilicity of aniline because of the delocalisation of the lone pair on the nitrogen into the delocalised electrons of the benzene ring. As such this result shows that the fabricated Fe-NHC catalyst is not effective in providing alternative pathway through which aniline can effectively react with the carboxylic acids to form amides.

Comparing the results of the amide synthesis, it is apparent that the Fe-NHC catalyst does not promote the amidation reaction of the carboxylic acids and amines in question.

The results above on the application of the synthesised supported Fe-NHC catalyst informed the decision to stop the investigation on the catalytic ability of the Fe-NHC catalyst towards amidation reactions. Focus was diverted on other important reactions that the catalyst might be very effective towards.

Appendix B Fe loading calculations

Calculation of the Fe loading of the Fe-NHC HACS from ICP-MS data.

Table A1. Result of the ICP-MS analysis.

	^{56}Fe [He]	
Sample Name	Conc. [ppb]	Conc. RSD
Fe NHC HACS	37978275.61	3.3

The result of the ICP analysis indicated that the concentration of Fe in the sample is 37978 ppm. Which is 3.8 % wt.

Thus; 1 g has 0.038 g of Fe,

So; $0.038/55.845 = 6.8x10^{-4}$ mol g^{-1} or 0.68 mmol g^{-1}

Calculation of the Fe loading of the Fe-NHC S350 from ICP-MS data.

Table A2. Result of the ICP-MS analysis.

	^{56}Fe [He]	
Sample Name	Conc. [ppb]	Conc. RSD
Fe NHC S350	17392029.55	2

The result of the ICP analysis indicated that the concentration of Fe in the sample is 17392 ppm. Which is 1.7 % wt.

Thus; 1 g has 0.017 g of Fe,

So; $0.017/55.845 = 3x10^{-4}$ mol g^{-1} or 0.30 mmol g^{-1}

Calculation of the Fe loading of the Fe-NHC S400 from ICP-MS data.

Table A3. Result of the ICP-MS analysis.

	^{56}Fe [He]	
Sample Name	Conc. [ppb]	Conc. RSD
Fe NHC S350	17930914.76	2

The result of the ICP analysis indicated that the concentration of Fe in the sample is 17930 ppm. Which is 1.8 % wt.

Thus; 1 g has 0.018 g of Fe,

So; $0.018/55.845 = 3.2\text{x}10^{-4}$ mol g^{-1} or 0.32 mmol g^{-1}

Calculation of the Fe loading of the Fe-NHC mango cellulose from ICP-MS data.

Table A4. Result of the ICP-MS analysis.

	^{56}Fe [He]	
Sample Name	Conc. [ppb]	Conc. RSD
Fe NHC MPC	1614059.11	2

The result of the ICP analysis indicated that the concentration of Fe in the sample is 1614 ppm. Which is 0.16 % wt.

Thus; 1 g has 0.0016 g of Fe,

So; $0.0016/55.845 = 2.8\text{x}10^{-5}$ mol g^{-1} or 0.03 mmol g^{-1}

However, this sample was unlike the other, has been diluted x10 due to the concern expressed by the ICP unit that the samples previously submitted contain too much acid from digestion as such it was diluted further.

Applying the dilution factor for correction; 0.03 x10 = 0.3 mmol g^{-1}

Calculation of the Fe loading of the Fe-NHC Orange cellulose from ICP-MS data.

Table A5. Result of the ICP-MS analysis.

	^{56}Fe [He]	
Sample Name	Conc. [ppb]	Conc. RSD
Fe NHC OPC	29142441.03	2

The result of the ICP analysis indicated that the concentration of Fe in the sample is 37978 ppm. Which is 2.9 % wt.

Thus; 1 g has 0.029 g of Fe,

So; $0.029/55.845 = 5.2 \times 10^{-4}$ mol g^{-1} or 0.52 mmol g^{-1}

Appendix C HPLC standard calculation

Quantitative HPLC using internal standard.

The equation below is used for quantitative HPLC using furfural as internal standard.

$$\frac{\text{Area internal standard peak}}{\text{Area of desired product standard peak}} = F \frac{\text{Concentration of internal standard}}{\text{Concentration of desired product stand.}}$$

For our particular system we have,

$$\frac{\text{Area furfural standard peak}}{\text{Area of HMF standard peak}} = F \frac{\text{Concentration furfural internal standard}}{\text{Concentration of HMF standard}}$$

Here F is a unitless factor used to correct for sensitivity issues during HPLC.

$$\frac{58136468}{25542388} = F \frac{4\text{ mg}}{3\text{ mg}}$$

$$\frac{58136468}{25542388} = \frac{F \times 4\text{ mg}}{3\text{ mg}}$$

F= 1.70

Appendix D XPS deconvolution of S350 and S400

Deconvoluted XPS peaks for Starbon 350 (4b), Starbon-400 (4c) and their subsequent immobilised Fe-NHC catalysts (1b & 1c)

Starbon 350 Deconvoluted Peaks.

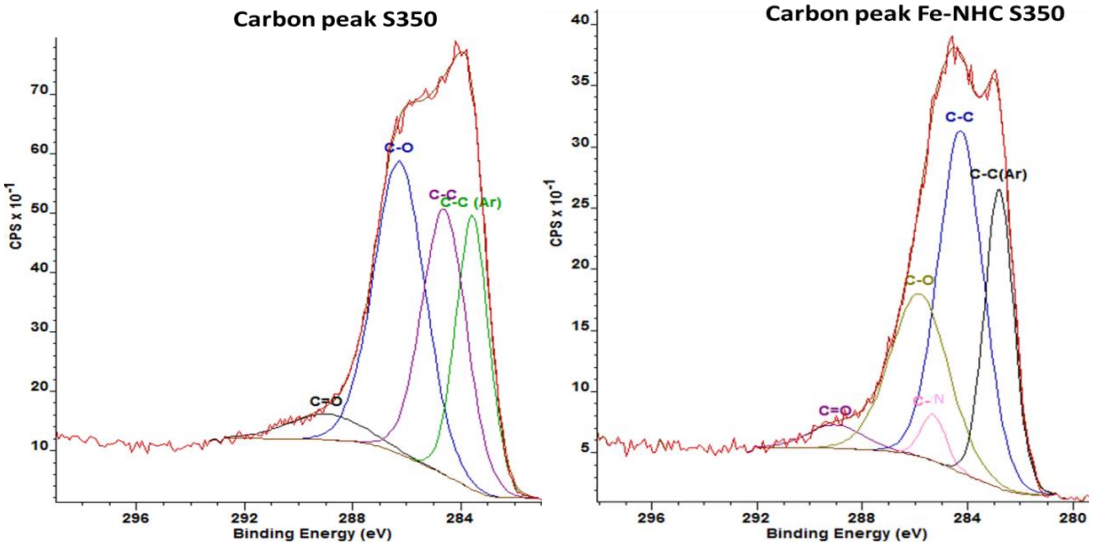

Figure D1. Deconvoluted C 1s peaks for Starbon 350 (**4b**) and Fe-NHC Starbon-350 (**1b**).

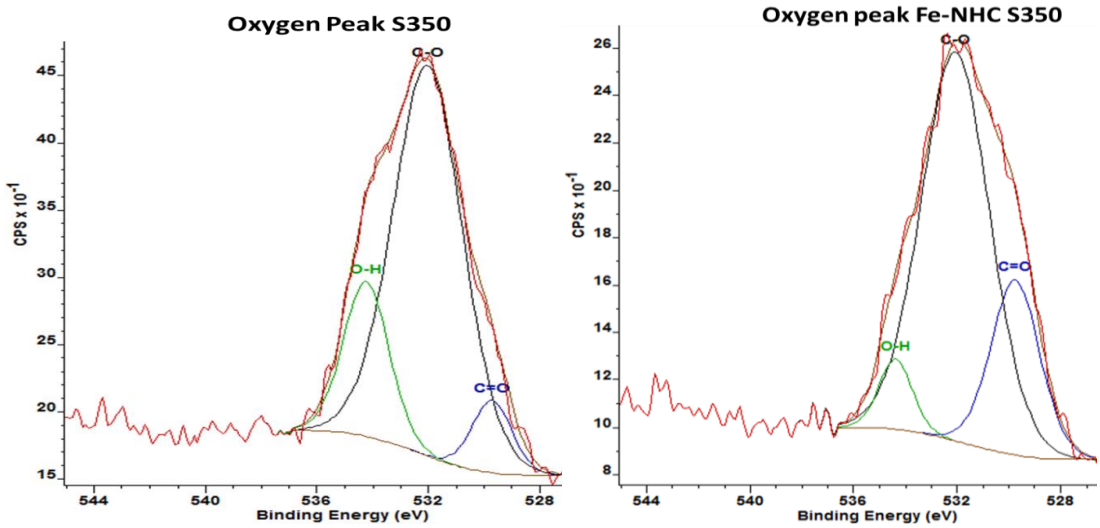

Figure D2. Deconvoluted O 1s peaks for Starbon 350 (**4b**) and Fe-NHC Starbon-350 (**1b**).

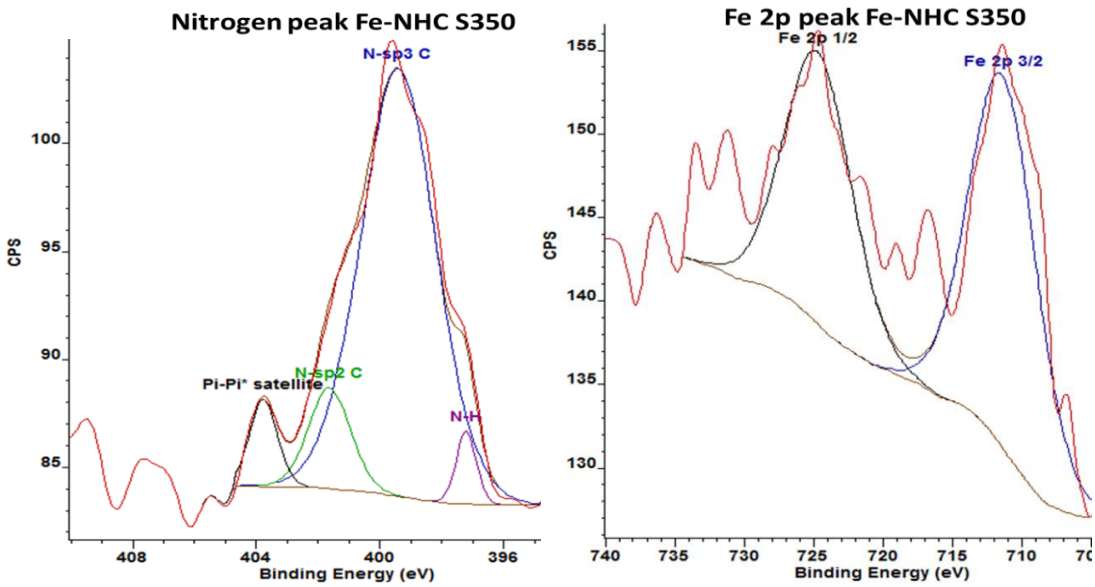

Figure D3. Deconvoluted N 1s and Fe 2 p peaks for Fe-NHC Starbon-350 (**1b**).

Starbon 400 Deconvoluted Peaks.

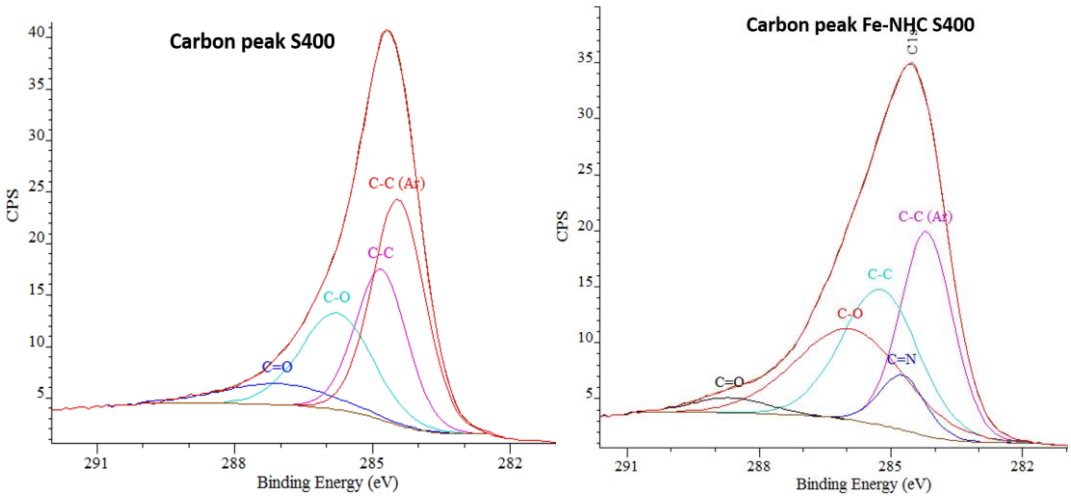

Figure D4. Deconvoluted C 1s peaks for Starbon 400 (**4c**) and Fe-NHC Starbon-400 (**1c**).

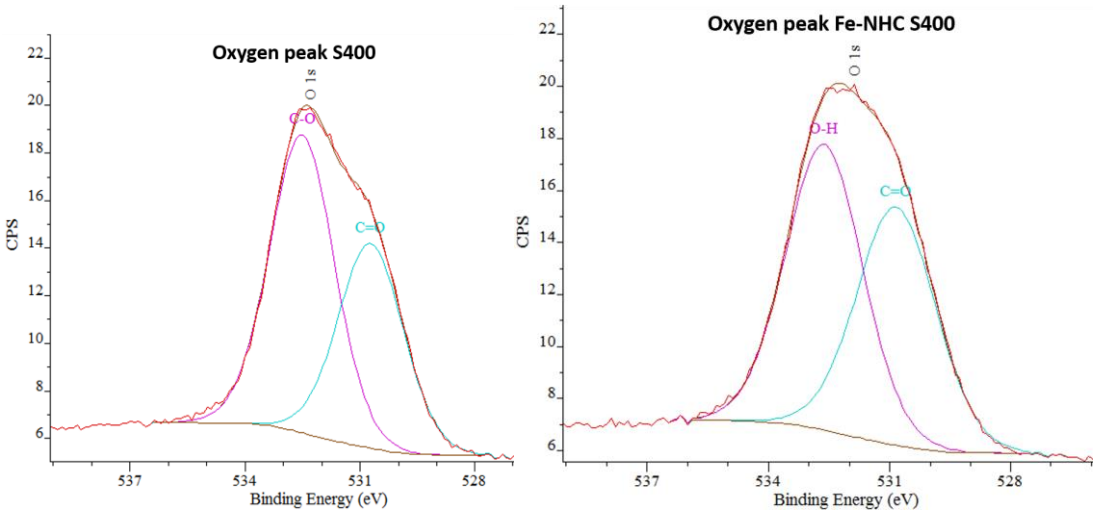

Figure D5. Deconvoluted O 1s peaks for Starbon 400 (**4c**) and Fe-NHC Starbon-400 (**1c**).

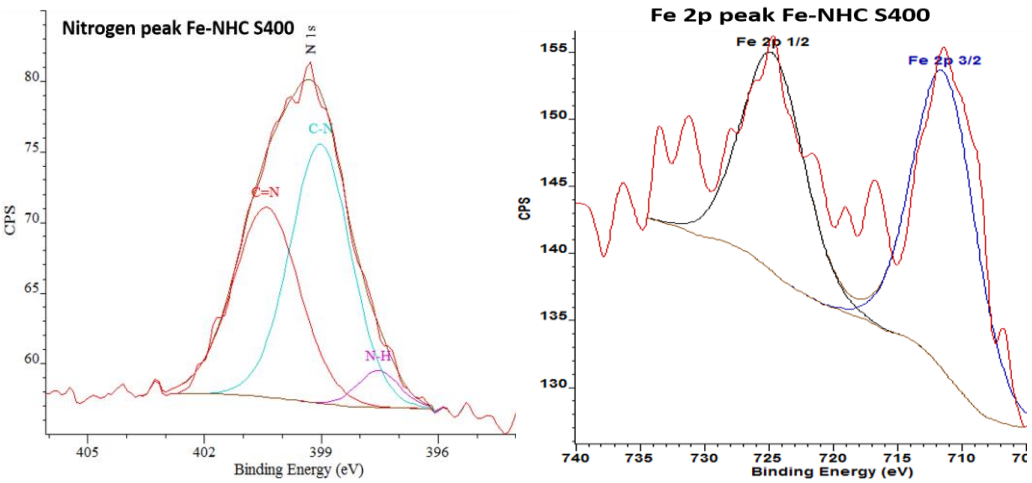

Figure D6. Deconvoluted N 1s and Fe 2 p peaks for Fe-NHC Starbon-400 (**1c**).

Appendix E XPS deconvolution of MPC and OPC

Deconvoluted XPS peaks for mango peel cellulose (4d), orange peel cellulose (4e) and their subsequent immobilised Fe-NHC catalysts (1d & 1e).

Mango Peel Cellulose Deconvoluted Peaks

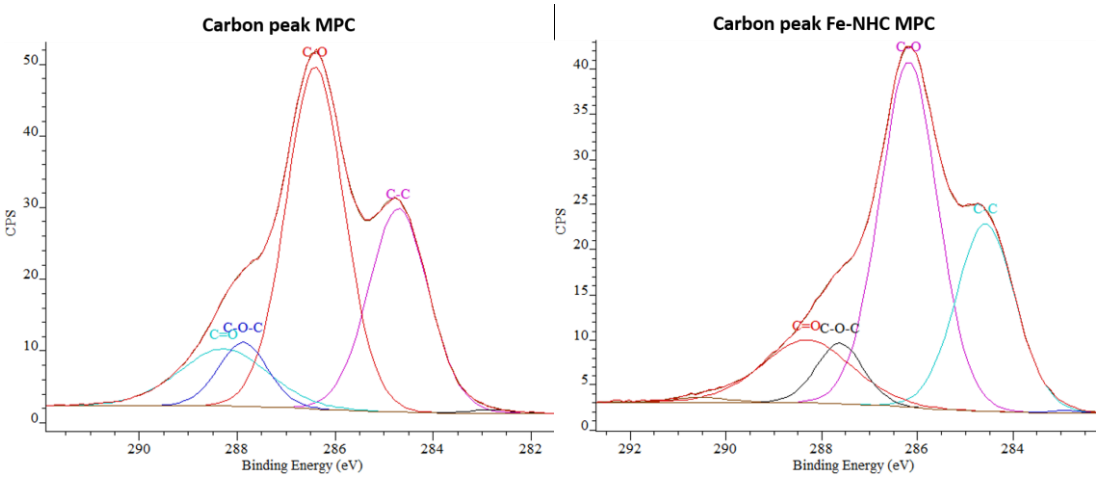

Figure E1. Deconvoluted C 1s peaks for mango peel cellulose (**4d**) and Fe-NHC orange peel cellulose (**1d**).

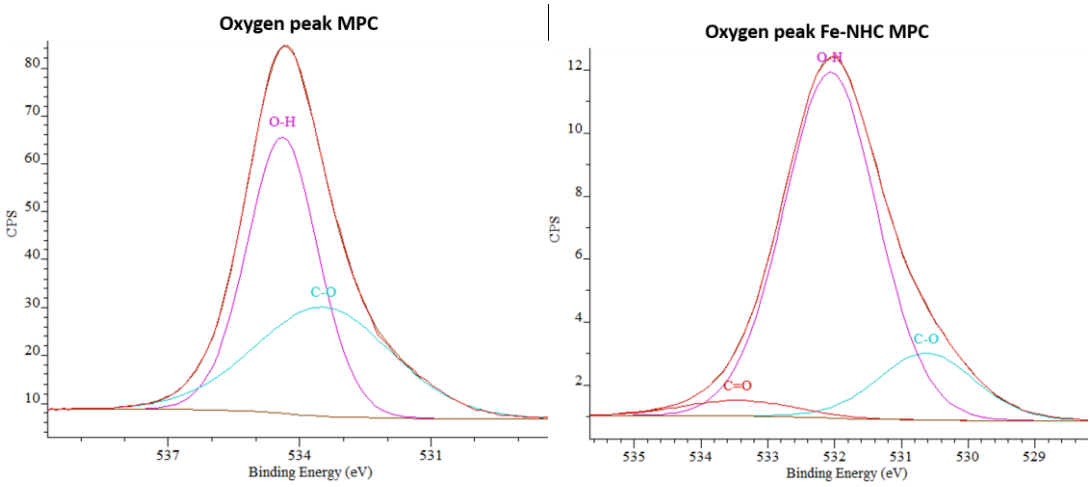

Figure E2. Deconvoluted O 1s peaks for mango peel cellulose (**4d**) and Fe-NHC orange peel cellulose (**1d**).

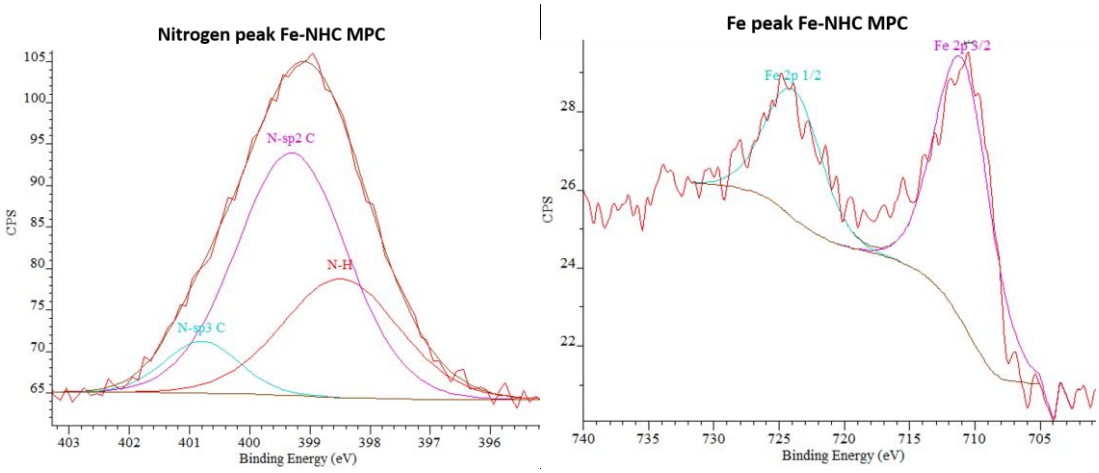

Figure E3. Deconvoluted N 1s and Fe 2 p peaks for Fe-NHC mango peel cellulose (**1d**).

Orange Peel Cellulose Deconvoluted Peaks

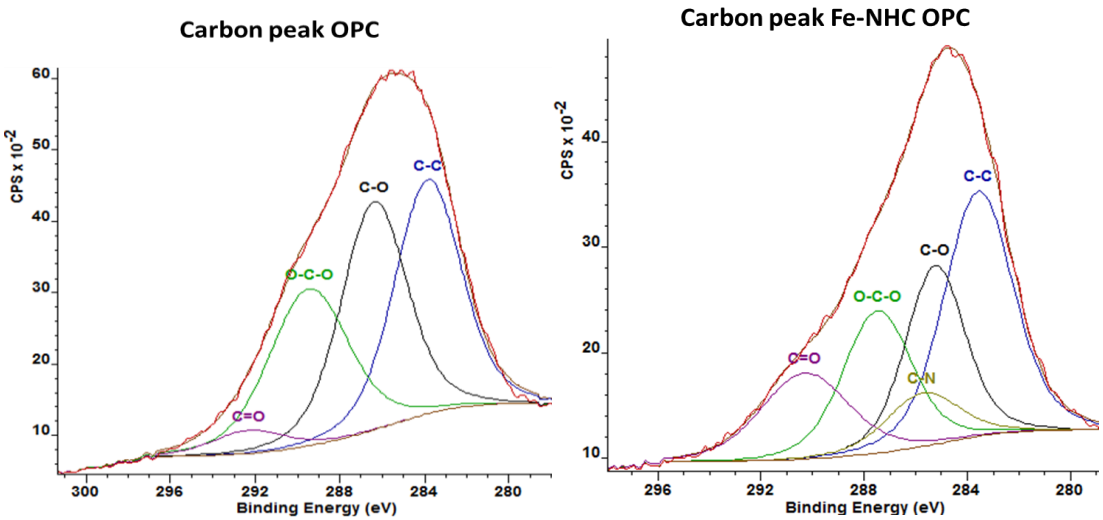

Figure E4. Deconvoluted C 1s peaks for orange peel cellulose (**4e**) and Fe-NHC orange peel cellulose (**1e**).

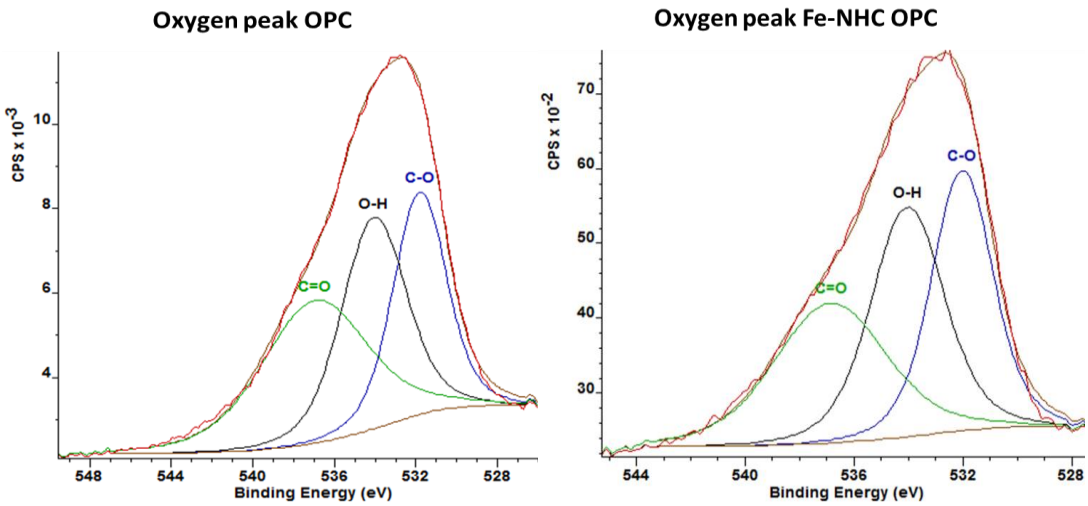

Figure E5. Deconvoluted O 1s peaks for orange peel cellulose (**4e**) and Fe-NHC orange peel cellulose (**1e**).

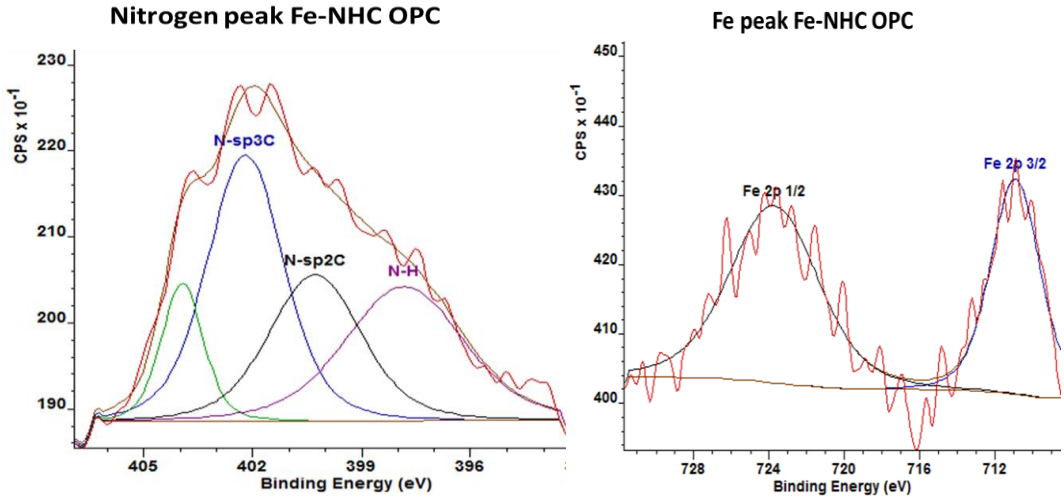

Figure E6. Deconvoluted N 1s and Fe 2 p peaks for Fe-NHC orange peel cellulose (**1e**).

Appendix F ^{1}HNMR and ^{13}C NMR of ligand synthesis

1-[Aminopropyl]-3-(2,4,6-trimethylbenzyl)-imidazolium chloride (**12**)

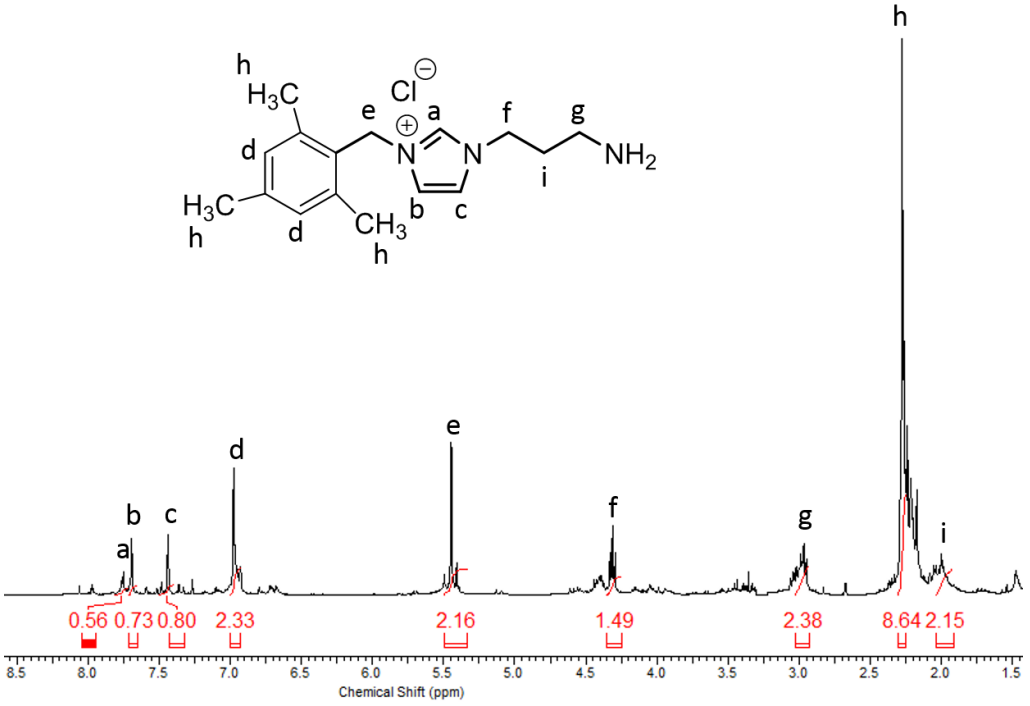

Figure F1. ^{1}H NMR spectrum of the synthesised NHC ligand (**12**). Methanol-$_{d4}$

1-[Aminopropyl]-3-(2,4,6-trimethylbenzyl)-imidazolium chloride (**12**)

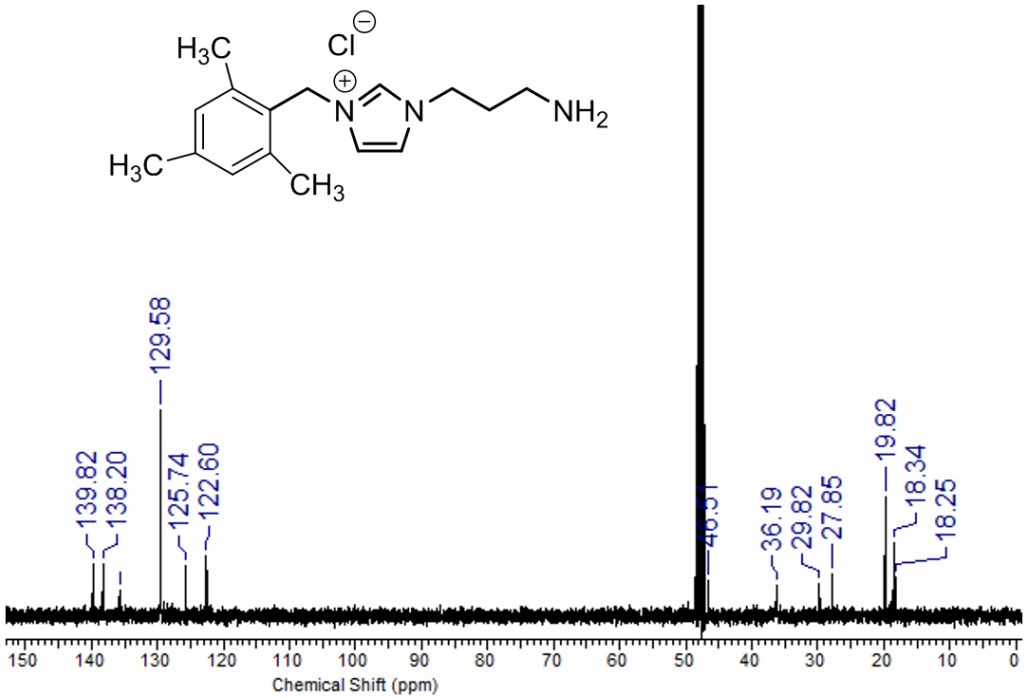

Figure F2. ^{13}C NMR spectrum of the synthesised NHC ligand (**12**) Methanol-$_{d4}$.

1-[(*N-tert*-butoxycarbonyl)aminopropyl]-3-(2,4,6-trimethylbenzyl)imidazolium chloride (**11**)

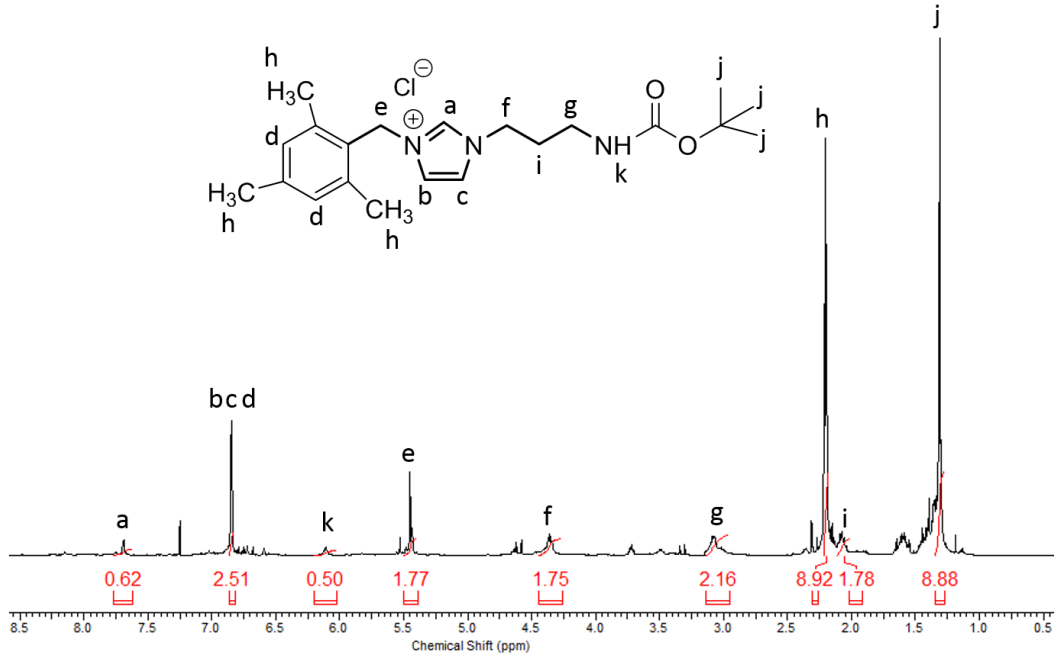

Figure F3. ^{1}H NMR spectrum of the BOC-protected mesityl-imidazole (**11**) $CDCl_3$.

1-[(*N-tert*-butoxycarbonyl)aminopropyl]-3-(2,4,6-trimethylbenzyl)imidazolium chloride (**11**)

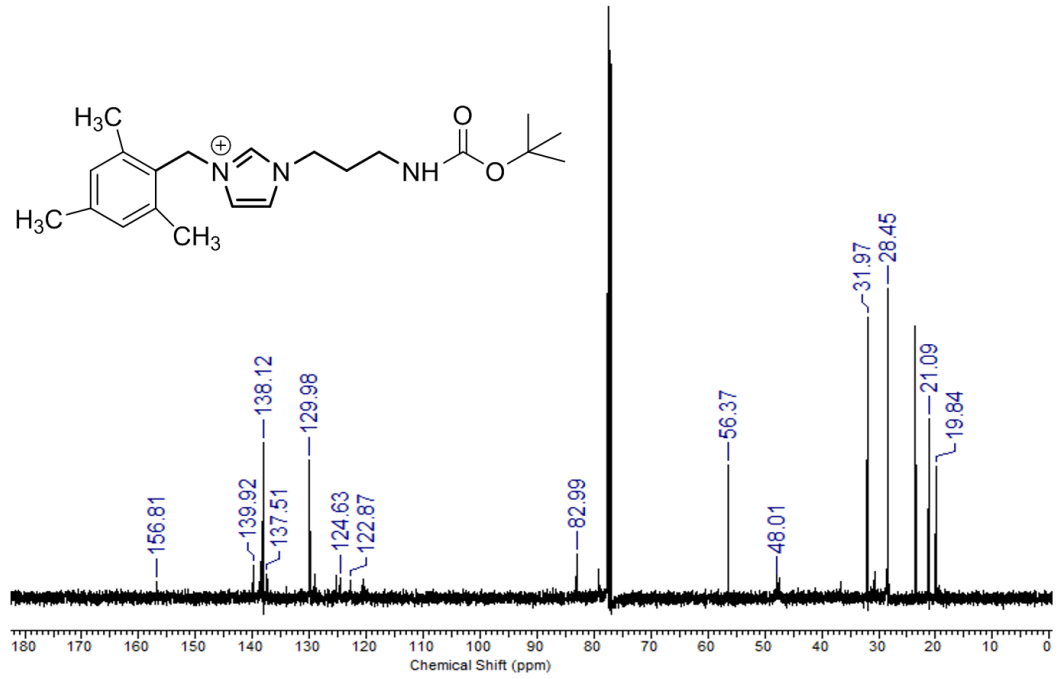

Figure F4. ^{13}C NMR spectrum of the BOC-protected mesityl-imidazole (**11**) $CDCl_3$.

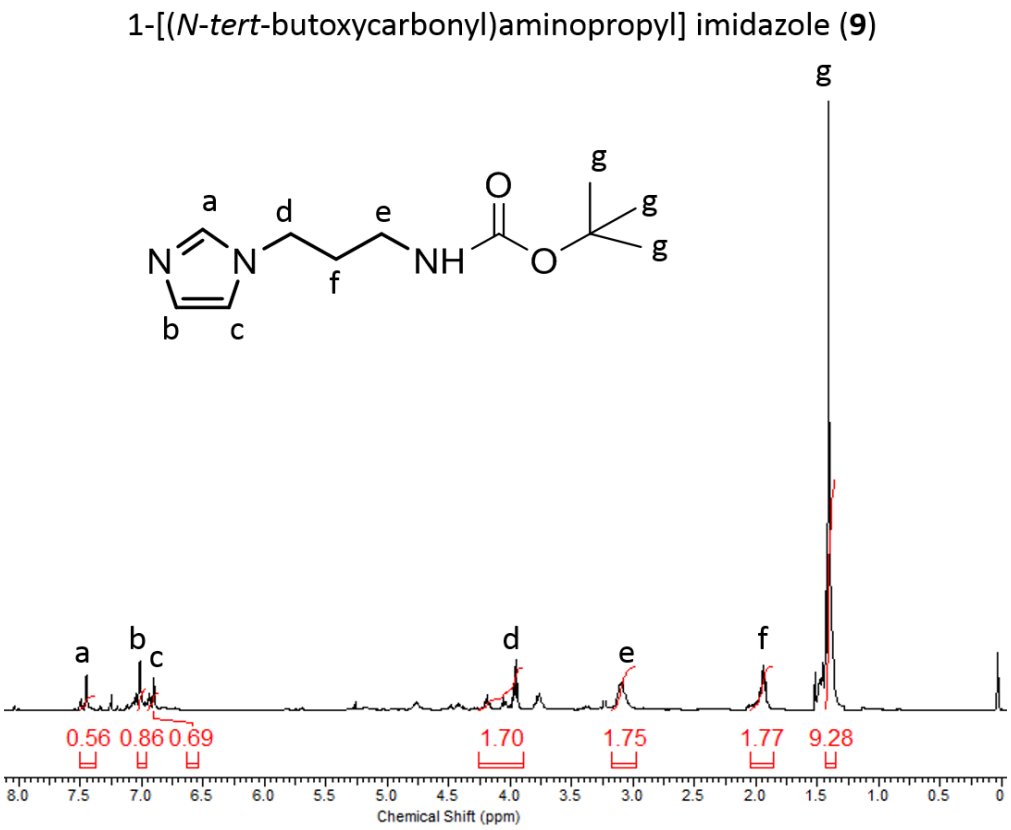

Figure F5. ^{1}H NMR spectrum of the BOC-protected imidazole (**9**) $CDCl_3$.

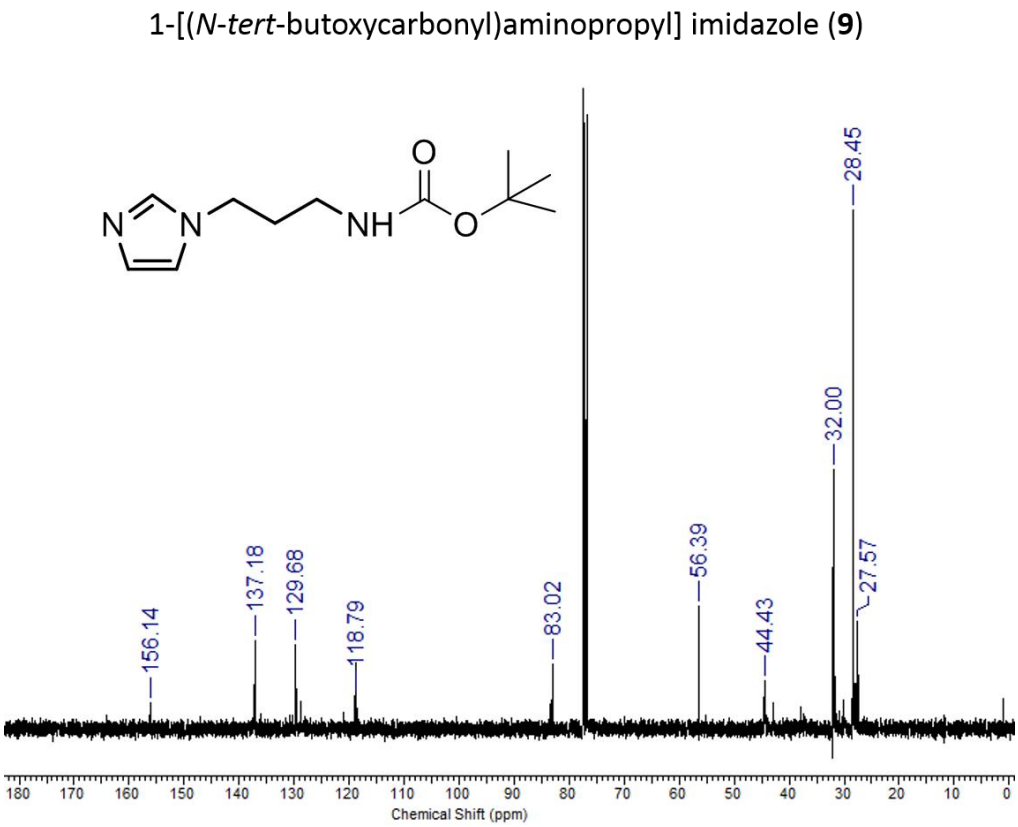

Figure F6. ^{13}C NMR spectrum of the BOC-protected imidazole (**9**) $CDCl_3$.

Appendix G S350 thermogravimetry in air

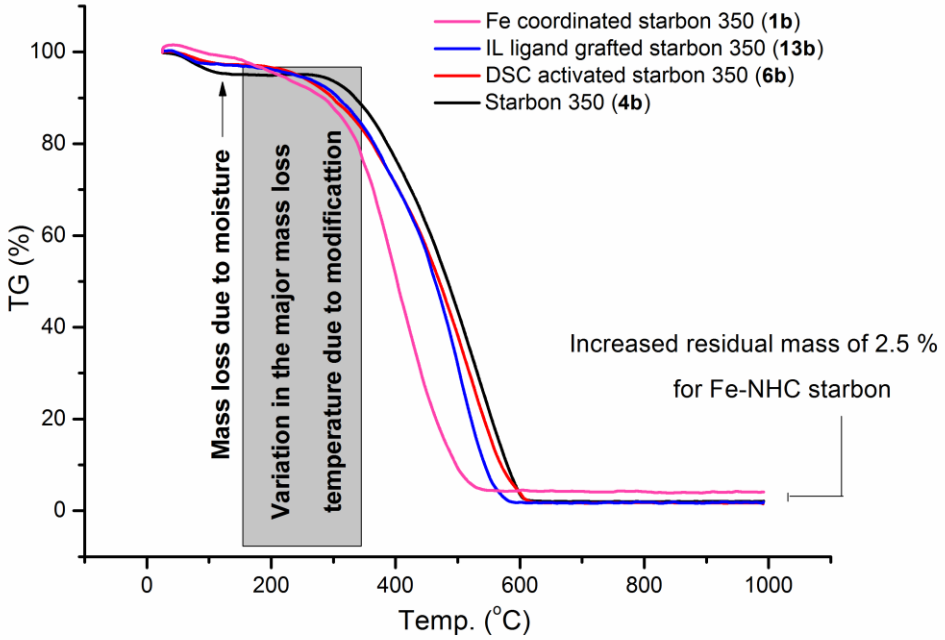

Figure G1. Thermal analysis data (TG) of Starbon™ 350

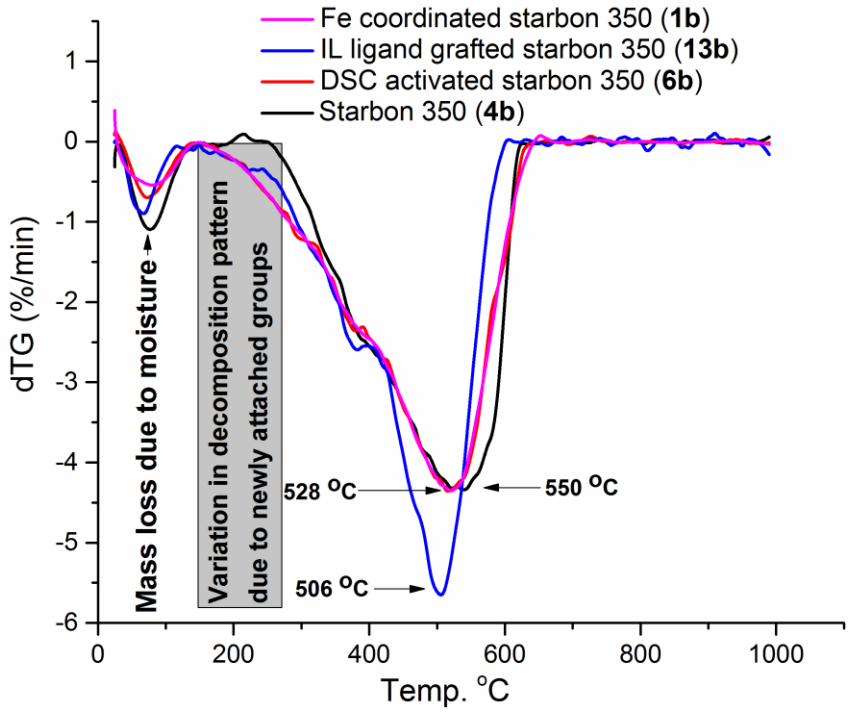

Figure G2. Thermal analysis data (dTG) of Starbon™ 350

References

1. Fitzpatrick, M. J. & Edelsparre, A. H. The genomics of climate change. *Science (80-.).* **359,** 29–30 (2018).

2. Breitburg, D., Levin, L. A., Oschlies, A., Grégoire, M., et al. Declining oxygen in the global ocean and coastal waters. *Science (80-.).* **359,** (2018).

3. Hausfather Z. Analysis: Why scientist think 100% of global warming is due to humans. *CarbonBrief*, 1-19 (2017).

4. Brundtland Commission. *Our Common Future*. (1987).

5. UK Parliament. Securing the future delivering UK sustainable development strategy. *C. London* **13,** 393–402 (2005).

6. United Nations General Assembly. Transforming our world: The 2030 agenda for sustainable development. *https//sustainabledevelopment.un.org/content/documents/7891Transforming%20Our%20World. pdf* 1–5 (2015). doi:10.1007/s13398-014-0173-7.2

7. Gohain, M., Devi, A. & Deka, D. Musa balbisiana Colla peel as highly effective renewable heterogeneous base catalyst for biodiesel production. *Ind. Crops Prod.* **109,** 8–18 (2017).

8. Min, B. K. & Friend, C. M. Heterogeneous gold-based catalysis for green chemistry: low-temperature CO oxidation and propene oxidation. *Chem. Rev.* **107,** 2709–24 (2007).

9. BioSTEP. Creating networks for the transition to a bio-based and circular economy. 1–16 (2017). Available at: http://www.bio-step.eu/fileadmin/BioSTEP/Bio_documents/BioSTEP_Policy_Paper_final.pdf. (Accessed: 8th January 2018). http://www.bio-step.eu/fileadmin/BioSTEP/Bio_documents/BioSTEP_Policy_Paper_final.pdf

10. Corma, A., García-García, P. & Rojas-Buzo, S. Catalytic transfer hydrogenation of biomass-derived carbonyls over Hafnium-based metal-organic frameworks. *ChemSusChem* 23;**11**(2):432-438 (2017).

11. Henrique, M. A., Silvério, H. A., Flauzino Neto, W. P. & Pasquini, D. Valorization of an agro-industrial waste, mango seed, by the extraction and characterization of its cellulose nanocrystals. *J. Environ. Manage.* **121,** 202–209 (2013).

12. Moud, P. H., Kantarelis, E., Andersson, K. J. & Engvall, K. Biomass pyrolysis gas conditioning over an iron-based catalyst for mild deoxygenation and hydrogen production. *Fuel* **211,** 149–158 (2018).

13. Anastas, P. T. & Warner, J. C. *Green Chemistry: Theory and Practice*. (Oxford University Press, 1998).

14. Paudel, S. R., Banjara, S. P., Choi, O. K., Park, K. Y., Kim, Y. M. & Lee, J. W. Pretreatment of agricultural biomass for anaerobic digestion: Current state

and challenges. *Bioresour. Technol.* **245,** 1194–1205 (2017).

15. Duque, A., Manzanares, P. & Ballesteros, M. Extrusion as a pretreatment for lignocellulosic biomass: Fundamentals and applications. *Renew. Energy* **114,** 1427–1441 (2017).

16. Bhutto, A. W., Qureshi, K., Harijan, K., Abro, R., Abbas, T., Bazmi, A. A., Karim, S. & Yu, G. Insight into progress in pre-treatment of lignocellulosic biomass. *Energy* **122,** 724–745 (2017).

17. Arevalo-Gallegos, A., Ahmad, Z., Asgher, M., Parra-Saldivar, R. & Iqbal, H. M. N. Lignocellulose: A sustainable material to produce value-added products with a zero waste approach—A review. *Int. J. Biol. Macromol.* **99,** 308–318 (2017).

18. Bilal, M., Asgher, M., Iqbal, H. M. N., Hu, H. & Zhang, X. Biotransformation of lignocellulosic materials into value-added products—A review. *Int. J. Biol. Macromol.* **98,** 447–458 (2017).

19. Tibolla, H., Pelissari, F. M., Martins, J. T., Vicente, A. A. & Menegalli, F. C. Cellulose nanofibers produced from banana peel by chemical and mechanical treatments: Characterization and cytotoxicity assessment. *Food Hydrocoll.* **75,** 192–201 (2018).

20. Khatoon, N., Ramezani, O. & Kermanian, H. Production of nanocrystalline cellulose from sugarcane bagasse. in *4th International Conference on Nanostructures* 12–14 (2012).

21. Orozco, R. S., Hernández, P. B., Morales, G. R., Núñez, F. U., Villafuerte, J. O., Lugo, V. L., Ramírez, N. F., Díaz, C. E. B. & Vázquez, P. C. Characterization of lignocellulosic fruit waste as an alternative feedstock for bioethanol production. *BioResources* **9,** 1873–1885 (2014).

22. Research, P. Green Chemistry: Biobased chemicals, renewable feedstocks, green polymers, less-toxic alternative chemical formulations, and the foundations of a sustainable chemical industry. *Ind. Biotechnol.* **7,** 431–433 (2011).

23. Antonetti, C., Melloni, M., Licursi, D., Fulignati, S., Ribechini, E., Rivas, S., Parajó, J. C., Cavani, F. & Galletti, A. M. R. Microwave-assisted dehydration of fructose and inulin to HMF catalyzed by niobium and zirconium phosphate catalysts. *Appl. Catal. B Environ.* **206,** 364–377 (2017).

24. Maldonado, C. S., la Rosa, J. R. De, Lucio-Ortiz, C. J., Valente, J. S. & Castaldi, M. J. Synthesis and characterization of functionalized alumina catalysts with thiol and sulfonic groups and their performance in producing 5-hydroxymethylfurfural from fructose. *Fuel* **198,** 134–144 (2017).

25. Antonetti, C., Galletti, A. M. R., Fulignati, S. & Licursi, D. Amberlyst A-70: A surprisingly active catalyst for the MW-assisted dehydration of fructose and inulin to HMF in water. *Catal. Commun.* **97,** 146–150 (2017).

26. Braun, M. & Antonietti, M. A continuous flow process for the production of 2,5-dimethylfuran from fructose using (non-noble metal based) heterogeneous catalysis. *Green Chem.* **19,** 3813–3819 (2017).

27. Raveendra, G., Surendar, M. & Sai Prasad, P. S. Selective conversion of fructose to 5-hydroxymethylfurfural over WO3/SnO2 catalysts. *New J. Chem.* **41,** 8520–8529 (2017).

28. Vandana, J., Aishvarya, K. R. S., Novi, V., Ramachandran, S., Radhakrishnan, H. & Vinoth Kumar, V. Mesoporous titanium dioxide nanocatalyst: a recyclable approach for one-pot synthesis of 5-hydroxymethylfurfural. *IET Nanobiotechnology* **11,** 690–694 (2017).

29. Najafi Chermahini, A., Hafizi, H., Andisheh, N., Saraji, M. & Shahvar, A. The catalytic effect of Al-KIT-5 and KIT-5-SO3H on the conversion of fructose to 5-hydroxymethylfurfural. *Res. Chem. Intermed.* **43,** 5507–5521 (2017).

30. Noma, R., Nakajima, K., Kamata, K., Kitano, M., Hayashi, S. & Hara, M. Formation of 5-(hydroxymethyl)furfural by stepwise dehydration over TiO_2 with water-tolerant lewis acid sites. *J. Phys. Chem. C* **119**, 17117−17125 (2015).

31. Karimi, B., Mirzaei, H. M., Behzadnia, H. & Vali, H. Novel ordered mesoporous carbon based sulfonic acid as an efficient catalyst in the selective dehydration of fructose into 5-HMF: The role of solvent and surface chemistry. *ACS Appl. Mater. Interfaces*. **7**, 19050−19059 (2015).

32. Neațu, F., Marin, R. S., Florea, M., Petrea, N., Pavel, O. D. & Pârvulescu, V. I. Selective oxidation of 5-hydroxymethyl furfural over non-precious metal heterogeneous catalysts. *Appl. Catal. B Environ.* **180,** 751–757 (2016).

33. Bézier, D., Sortais, J.-B. & Darcel, C. N-Heterocyclic Carbene Ligands and Iron: An Effective Association for Catalysis. *Adv. Synth. Catal.* **355,** 19–33 (2013).

34. Liu, J., Li, H., Liu, Y.-C., Lu, Y.-M., He, J., Liu, X.-F., Wu, Z.-B. & Yang, S. Catalytic conversion of glucose to 5-hydroxymethylfurfural over nano-sized mesoporous Al2O3–B2O3 solid acids. *Catal. Commun.* **62,** 19–23 (2015).

35. De, S., Dutta, S. & Saha, B. Microwave assisted conversion of carbohydrates and biopolymers to 5-hydroxymethylfurfural with aluminium chloride catalyst in water. *Green Chem.* **13,** 2859 (2011).

36. Faria, J., Ruiz, M. P. & Resasco, D. E. Carbon nanotube-zeolite hybrid catalysts for glucose conversion in water/oil emulsions. *ACS Catal.* **5**, 4761−4771 (2015).

37. Zhang, Y., Pan, J., Shen, Y., Shi, W., Liu, C. & Yu, L. Brønsted acidic polymer nanotubes with tunable wettability toward efficient conversion of one-pot cellulose to 5-hydroxymethylfurfural. *ACS Sustain. Chem. Eng.* **3**, 871−879 (2015).

38. Jiménez-Morales, I., Moreno-Recio, M., Santamaría-González, J., Maireles-Torres, P. & Jiménez-López, A. Production of 5-hydroxymethylfurfural from glucose using aluminium doped MCM-41 silica as acid catalyst. *Appl. Catal. B Environ.* **164,** 70–76 (2015).

39. Nguyen, H., Nikolakis, V. & Vlachos, D. G. Mechanistic insights into lewis acid metal salt-catalyzed glucose chemistry in aqueous solution. *ACS Catal.* **6,**

1497–1504 (2016).

40. da Silva Lacerda, V., López-Sotelo, J. B., Correa-Guimarães, A., Hernández-Navarro, S., Sánchez-Bascones, M., Navas-Gracia, L. M., Martín-Ramos, P., Pérez-Lebeña, E. & Martín-Gil, J. A kinetic study on microwave-assisted conversion of cellulose and lignocellulosic waste into hydroxymethylfurfural/furfural. *Bioresour. Technol.* **180,** 88–96 (2015).

41. Qi, L., Mui, Y. F., Lo, S. W., Lui, M. Y., Akien, G. R. & Horváth, I. T. Catalytic conversion of fructose, glucose, and sucrose to 5-(hydroxymethyl)furfural and levulinic and formic acids in γ-valerolactone as a green solvent. *ACS Catal.* **4**, 1470–1477 (2014).

42. Qi, X., Watanabe, M., Aida, T. M. & Smith, R. L. Selective conversion of D-fructose to 5-hydroxymethylfurfural by ion-exchange resin in acetone/dimethyl sulfoxide solvent mixtures. *Ind. Eng. Chem. Res.* **47,** 9234–9239 (2008).

43. Upare, P. P., Hwang, D. W., Hwang, Y. K., Lee, U.-H., Hong, D.-Y. & Chang, J.-S. An integrated process for the production of 2,5-dimethylfuran from fructose. *Green Chem.* 10–13 (2015). doi:10.1039/C5GC00281H

44. Fernanda C. de Melo, A. Roberto F. de Souza *et al*. Synthesis of 5-Hydroxymethylfurfural from dehydration of fructose and glucose using ionic liquids. *Brazilian Chem. Soc.* **25,** 2378–2384 (2014).

45. Qu, Y., Li, L., Wei, Q., Huang, C., Oleskowicz-Popiel, P. & Xu, J. One-pot conversion of disaccharide into 5-hydroxymethylfurfural catalyzed by imidazole ionic liquid. *Sci. Rep.* **6,** 26067 (2016).

46. Guan, J., Cao, Q., Guo, X. & Mu, X. The mechanism of glucose conversion to 5-hydroxymethylfurfural catalyzed by metal chlorides in ionic liquid: A theoretical study. *Comput. Theor. Chem.* **963,** 453–462 (2011).

47. Jing, Y., Gao, J., Liu, C. & Zhang, D. Theoretical insight into the conversion mechanism of glucose to fructose catalyzed by $CrCl_2$ in imidazolium chloride ionic iiquids. *J. Phys. Chem. B* **121,** 2171–2178 (2017).

48. Kim, Y. H., Shin, S., Yoon, H. J., Kim, J. W., Cho, J. K. & Lee, Y. S. Polymer-supported *N*-heterocyclic carbene-iron(III) catalyst and its application to dehydration of fructose into 5-hydroxymethyl-2-furfural. *Catal. Commun.* **40,** 18–22 (2013).

49. Shi, J., Liu, W., Wang, N., Yang, Y. & Wang, H. Production of 5-hydroxymethylfurfural from mono- and disaccharides in the presence of ionic liquids. *Catal. Letters* 1–9 (2013). doi:10.1007/s10562-013-1148-6

50. Wang, Y., Pedersen, C. M., Deng, T., Qiao, Y. & Hou, X. Direct conversion of chitin biomass to 5-hydroxymethylfurfural in concentrated $ZnCl_2$ aqueous solution. *Bioresour. Technol.* **143,** 384–390 (2013).

51. Li, X., Jiang, Y., Wang, L., Meng, L., Wang, W. & Mu, X. Effective low-temperature hydrolysis of cellulose catalyzed by concentrated H3PW12O40 under microwave irradiation. *RSC Adv.* **2,** 6921 (2012).

52. Ranoux, A., Djanashvili, K., Arends, I. W. C. E. & Hanefeld, U. 5-

Hydroxymethylfurfural synthesis from hexoses is autocatalytic. *ACS Catal.* **3,** 760–763 (2013).

53. Kılıç, E. & Yılmaz, S. Fructose dehydration to 5-hydroxymethylfurfural over sulfated TiO_2–SiO_2, Ti-SBA-15, ZrO_2, SiO_2, and activated carbon catalysts. *Ind. Eng. Chem. Res.* **54** (19), 5220-5225 (2015).

54. Ma, H., Wang, F., Yu, Y., Wang, L. & Li, X. Autocatalytic production of 5-hydroxymethylfurfural from fructose-based carbohydrates in a biphasic system and its purification. *Ind. Eng. Chem. Res.* **54** (10), 2657−2666 (2015).

55. Mascal, M. 5-(Chloromethyl)furfural is the new HMF: Functionally equivalent but more practical in terms of its production from biomass. *ChemSusChem* **8,** 3391–3395 (2015).

56. Vicente, A. I., Coelho, J. A. S., Simeonov, S. P., Lazarova, H. I., Popova, M. D. & Afonso, C. A. M. Oxidation of 5-chloromethylfurfural (CMF) to 2,5-diformylfuran (DFF). *Molecules* **22,** 1–14 (2017).

57. Mascal, M. & Nikitin, E. B. High-yield conversion of plant biomass into the key value-added feedstocks 5-(hydroxymethyl)furfural, levulinic acid, and levulinic esters via5-(chloromethyl)furfural. *Green Chem.* **12,** 370–373 (2010).

58. Brasholz, M., von Känel, K., Hornung, C. H., Saubern, S. & Tsanaktsidis, J. Highly efficient dehydration of carbohydrates to 5-(chloromethyl)furfural (CMF), 5-(hydroxymethyl)furfural (HMF) and levulinic acid by biphasic continuous flow processing. *Green Chem.* **13,** 1114 (2011).

59. Gao, W., Li, Y., Xiang, Z., Chen, K., Yang, R. & Argyropoulos, D. S. Efficient one-pot synthesis of 5-chloromethylfurfural (CMF) from carbohydrates in mild biphasic systems. *Molecules* **18,** 7675–7685 (2013).

60. Breeden, S. W., Clark, J. H., Farmer, T. J., Macquarrie, D. J., Meimoun, J. S., Nonne, Y. & Reid, J. E. S. J. Microwave heating for rapid conversion of sugars and polysaccharides to 5-chloromethyl furfural. *Green Chem.* **15,** 72–75 (2013).

61. Mascal, M. & Nikitin, E. B. Direct, high-yield conversion of cellulose into biofuel. *Angew. Chemie Int. Ed.* **47,** 7924–7926 (2008).

62. Ma, B., Wang, Y., Guo, X., Tong, X., Liu, C., Wang, Y. & Guo, X. Photocatalytic synthesis of 2,5-diformylfuran from 5-hydroxymethyfurfural or fructose over bimetallic Au-Ru nanoparticles supported on reduced graphene oxides. *Appl. Catal. A Gen.* **552,** 70–76 (2018).

63. Yang, Z., Qi, W., Su, R. & He, Z. 3D flower-like micro/nano Ce-Mo composite oxides as effective bifunctional catalysts for one-pot conversion of fructose to 2,5-diformylfuran. *ACS Sustain. Chem. Eng.* **5,** 4179–4187 (2017).

64. Fang, R., Luque, R. & Li, Y. Efficient one-pot fructose to DFF conversion using sulfonated magnetically separable MOF-derived Fe_3O_4 (111) catalysts. *Green Chem.* **19,** 647–655 (2017).

65. Wang, Y., Sun, H., Tao, X., Shen, Q. & Zhang, Y. Enolate chelating N-heterocyclic carbene complexes of Fe(II): Synthesis, structure and their

catalytic activity for ring-opening polymerization of ε-caprolactone. *Chinese Sci. Bull.* **52,** 3193–3199 (2007).

66. Wanzlick, H. W. Aspects of nucleophilic carbene chemistry. *Angew. Chemie Int. Ed. English* **1,** 75–80 (1962).

67. Wanzlick, H. -W & Schönherr, H. -J. Direct synthesis of a mercury salt carbene complex. *Angew. Chemie Int. Ed. English* **7,** 141–142 (1968).

68. Arduengo, A. J., Harlow, R. L. & Kline, M. A stable crystalline carbene. *J. Am. Chem. Soc.* **113,** 361–363 (1991).

69. Ingleson, M. J. & Layfield, R. a. N-Heterocyclic carbene chemistry of iron: fundamentals and applications. *Chem. Commun. (Camb).* **48,** 3579–89 (2012).

70. Arduengo, A. J. & Iconaru, L. I. Fused polycyclic nucleophilic carbenes - synthesis, structure, and function. *Dalton Trans.* **35**, 6903–6914 (2009).

71. Adhikary, S. Das, Bose, D., Mitra, P., Saha, K. Das, Bertolasi, V. & Dinda, J. Au(i)- and Pt(ii)-N-heterocyclic carbene complexes with picoline functionalized benzimidazolin-2-ylidene ligands; synthesis, structures, electrochemistry and cytotoxicity studies. *New J. Chem.* **36,** 759 (2012).

72. Ohki, Y. & Seino, H. N-Heterocyclic carbenes as supporting ligands in transition metal complexes of N_2. *Dalt. Trans.* **45,** 874–880 (2016).

73. Kandasamy, E. Synthesis and crystal structure of 1-methyl-3- (2-pyridyl) imidazolium hexafluorophosphate. *J. Crystallogr.* **47,** 3122–3172 (2014).

74. Crabtree, R. H. Recent developments in the organometallic chemistry of N-heterocyclic carbenes. *Coord. Chem. Rev.* **251,** 595 (2007).

75. Crudden, C. M. & Allen, D. P. Stability and reactivity of N-heterocyclic carbene complexes. *Coord. Chem. Rev.* **248,** 2247–2273 (2004).

76. Park, J. H., Raza, F., Jeon, S. J., Kim, H. I., Kang, T. W., Yim, D. & Kim, J. H. Recyclable *N*-heterocyclic carbene/palladium catalyst on graphene oxide for the aqueous-phase Suzuki reaction. *Tetrahedron Lett.* **55,** 3426–3430 (2014).

77. Wang, Y., Zhang, T., Li, B., Jiang, S. & Sheng, L. Synthesis, characterization, electrochemical properties and catalytic reactivity of *N*-heterocyclic carbene-containing diiron complexes. *RSC Adv.* **5,** 29022–29031 (2015).

78. Henrion, M., Ritleng, V. & Chetcuti, M. J. Nickel *N*-heterocyclic carbene-catalyzed C-C bond formation: Reactions and mechanistic aspects. *ACS Catal.* **5,** 1283–1302 (2015).

79. Bates, J. I. & Gates, D. P. 4-Phosphino-substituted *N*-heterocyclic carbenes (NHCs) from the abnormal reaction of NHCs with phosphaalkenes. *Organometallics* **31,** 4529–4536 (2012).

80. Hopkinson, M. N., Richter, C., Schedler, M. & Glorius, F. An overview of *N*-heterocyclic carbenes. *Nature* **510,** 485 (2014).

81. Benhamou, L., Chardon, E., Lavigne, G., Bellemin-Laponnaz, S. & César, V. Synthetic routes to *N*-heterocyclic carbene precursors. *Chem. Rev.* **111,** 2705–

2733 (2011).

82. Eastman, K. J. *N*-Heterocyclic carbenes (NHCs). *Baran Lab* 1–18 (1962). doi:10.1002/asia.200900338

83. Kaufhold, S., Petermann, L., Staehle, R. & Rau, S. Transition metal complexes with *N*-heterocyclic carbene ligands: From organometallic hydrogenation reactions toward water splitting. *Coord. Chem. Rev.* **304–305,** 73–87 (2015).

84. Lei, P., Meng, G. & Szostak, M. General method for the Suzuki–Miyaura cross-coupling of amides using commercially available, air- and moisture-stable palladium/NHC (NHC = *N*-Heterocyclic Carbene) complexes. *ACS Catal.* **7,** 1960–1965 (2017).

85. Flanigan, D. M., Romanov-Michailidis, F., White, N. A. & Rovis, T. Organocatalytic reactions enabled by *N*-heterocyclic carbenes. *Chem. Rev.* **115,** 9307–9387 (2015).

86. Grasa, G. A., Singh, R. & Nolan, S. P. Transesterification/acylation reactions catalyzed by molecular catalysts. *Synthesis (Stuttg).* 971–985 (2004). doi:10.1055/s-2004-822323

87. Marion, N., Díez-González, S. & Nolan, S. P. *N*-Heterocyclic carbenes as organocatalysts. *Angew. Chemie Int. Ed.* **46,** 2988–3000 (2007).

88. Yamashita, M., Goto, K. & Kawashima, T. Fixation of both O_2 and CO_2 from air by a crystalline palladium complex bearing *N*-heterocyclic carbene ligands. *J. Am. Chem. Soc.* **127,** 7294–7295 (2005).

89. Chen, C., Ni, S., Zheng, Q., Yu, M. & Wang, H. Synthesis, structure, biological evaluation, and catalysis of two pyrazole-functionalized NHC-Ru ^{II} complexes. *Eur. J. Inorg. Chem.* **2017,** 616–622 (2017).

90. Monticelli, M., Bellemin-Laponnaz, S., Tubaro, C. & Rancan, M. Synthesis, structure and antitumoural activity of triazole-functionalised NHC–metal complexes. *Eur. J. Inorg. Chem.* **2017,** 2488–2495 (2017).

91. Rieb, J., Dominelli, B., Mayer, D., Jandl, C., Drechsel, J., Heydenreuter, W., Sieber, S. A. & Kuhn, F. E. Influence of wing-tip substituents and reaction conditions on the structure, properties and cytotoxicity of Ag(I)- and Au(I)-bis(NHC) complexes. *Dalt. Trans.* **46,** 2722–2735 (2017).

92. Kamijo, S. & Yamamoto, Y. Recent progress in the catalytic synthesis of imidazoles. *Chem. – An Asian J.* **2,** 568–578 (2007).

93. Herrmann, W. A. *N*-Heterocyclic carbenes: A new concept in organometallic catalysis. *Angew. Chemie Int. Ed.* **41,** 1290–1309 (2002).

94. Hahn, F. E. & Jahnke, M. C. Heterocyclic carbenes: Synthesis and coordination chemistry. *Angew. Chemie - Int. Ed.* **47,** 3122–3172 (2008).

95. Albright, A., Eddings, D., Black, R., Welch, C. J., Gerasimchuk, N. N. & Gawley, R. E. Design and synthesis of C2-symmetric *N*-heterocyclic carbene precursors and metal carbenoids. *J. Org. Chem.* **76,** 7341–7351 (2011).

96. Zhong, R., Lindhorst, A. C., Groche, F. J. & Kühn, F. E. Immobilization of *N*-heterocyclic carbene compounds: A synthetic perspective. *Chem. Rev.* **117,** 1970–2058 (2017).

97. Jokić, N. B., Straubinger, C. S., Li Min Goh, S., Herdtweck, E., Herrmann, W. A. & Kühn, F. E. Symmetrical bis-(NHC) palladium(II) complexes: Synthesis, structure, and application in catalysis. *Inorganica Chim. Acta* **363,** 4181–4188 (2010).

98. Zhong, R., Poethig, A., Haslinger, S., Hofmann, B., Raudaschl-Sieber, G., Herdtweck, E., Herrmann, W. A. & Kuehn, F. E. Toward tunable immobilized molecular catalysts: Functionalizing the methylene bridge of bis(*N*-heterocyclic carbene) ligands. *Chempluschem* **79,** 1294–1303 (2014).

99. Jia, W., Wu, Y., Huang, J., An, Q., Xu, D., Wu, Y., Li, F. & Li, G. Poly(ionic liquid) brush coated electrospun membrane: a useful platform for the development of functionalized membrane systems. *J. Mater. Chem.* **20,** 8617 (2010).

100. Lalaoui, N., Reuillard, B., Philouze, C., Holzinger, M., Cosnier, S. & Le Goff, A. Osmium(II) complexes bearing chelating *N*-heterocyclic carbene and pyrene-modified ligands: Surface electrochemistry and electron transfer mediation of oxygen reduction by multicopper enzymes. *Organometallics* **35,** 2987–2992 (2016).

101. Feldman, R. A. & Fraile, J. M. Improved methodology for non-covalent immobilization of tert-butyl-azabis(oxazoline)-copper complex on Al-MCM41. *Appl. Catal. A Gen.* **502,** 166–173 (2015).

102. Rosario Torviso, M., Blanco, M. N., Cáceres, C. V., Fraile, J. M. & Mayoral, J. A. Supported heteropolyanions as solid counterions for the electrostatic immobilization of chiral copper complexes. *J. Catal.* **275,** 70–77 (2010).

103. Feldman, R. A. & Fraile, J. M. Electrostatic immobilization of bis(oxazoline)-copper complexes on mesoporous crystalline materials: Cation exchange vs. incipient wetness methods. *Appl. Catal. A Gen.* **485,** 67–73 (2014).

104. Lambert, R., Coupillaud, P., Wirotius, A. L., Vignolle, J. & Taton, D. Imidazolium-based poly(ionic liquid)s featuring acetate counter anions: Thermally latent and recyclable precursors of polymer-supported *N*-heterocyclic carbenes for organocatalysis. *Macromol. Rapid Commun.* **37,** 1143–1149 (2016).

105. Gao, A., Zhang, H., Hu, L., Hou, A. & Xie, K. Fabrication of silica nanoparticle-supported copper quantum dots and the efficient catalytic Ullmann coupling reaction. *Catal. Commun.* **102,** 118–122 (2017).

106. García-Sancho, C., Cecilia, J. A., Mérida-Robles, J. M., González, J. S., Moreno-Tost, R., Infantes-Molina, A. & Maireles-Torres, P. Effect of the treatment with H_3PO_4 on the catalytic activity of Nb_2O_5 supported on Zr-doped mesoporous silica catalyst. Case study: Glycerol dehydration. *Appl. Catal. B Environ.* **221,** 158–168 (2018).

107. Munoz, M., Kolb, V., Lamolda, A., de Pedro, Z. M., Modrow, A., Etzold, B. J. M., Rodriguez, J. J. & Casas, J. A. Polymer-based spherical activated carbon

as catalytic support for hydrodechlorination reactions. *Appl. Catal. B Environ.* **218,** 498–505 (2017).

108. Wang, H., Liu, Y., Yao, S. & Zhu, P. Selective recognization of dicyandiamide in bovine milk by mesoporous silica SBA-15 supported dicyandiamide imprinted polymer based on surface molecularly imprinting technique. *Food Chem.* **240,** 1262–1267 (2018).

109. Kaboudin, B., Khanmohammadi, H. & Kazemi, F. Polymer supported gold nanoparticles: Synthesis and characterization of functionalized polystyrene-supported gold nanoparticles and their application in catalytic oxidation of alcohols in water. *Appl. Surf. Sci.* **425,** 400–406 (2017).

110. Kim, E., Jang, J. & Chung, J. S. Synthesis and characteristics of silica-supported N-heterocyclic carbene catalyst for ring-opening polymerization of D-lactide to produce polylactide. *Macromol. Res.* **22,** 864–869 (2014).

111. Wang, L. & Chen, E. Y.-X. Recyclable supported carbene catalysts for high-yielding self-condensation of furaldehydes into C10 and C12 furoins. *ACS Catal.* **5,** 6907–6917 (2015).

112. Bahadori, M., Tangestaninejad, S., Moghadam, M., Mirkhani, V., Mechler, A., Mohammadpoor-Baltork, I. & Zadehahmadi, F. Metal organic framework-supported *N*-heterocyclic carbene palladium complex: A highly efficient and reusable heterogeneous catalyst for Suzuki-Miyaura C-C coupling reaction. *Microporous Mesoporous Mater.* **253,** 102–111 (2017).

113. Byun, J. W. & Lee, Y. S. Preparation of polymer-supported palladium/N-heterocyclic carbene complex for Suzuki cross-coupling reactions. *Tetrahedron Lett.* **45,** 1837–1840 (2004).

114. Grohmann, C., Hashimoto, T., Fröhlich, R., Ohki, Y., Tatsumi, K. & Glorius, F. An iron(II) complex of a diamine-bridged bis-*N*-heterocyclic carbene. *Organometallics* **31,** 8047–8050 (2012).

115. Pugh, T. & Layfield, R. A. Reactivity of three-coordinate iron-NHC complexes towards phenylselenol and lithium phenylselenide. *Dalton Trans.* **43,** 4251–4254 (2014).

116. Higman, C. S., Rufh, S. A., McDonald, R. & Fogg, D. E. Synthesis and dynamic behaviour of a dimeric ruthenium benzylidene complex bearing a truncated N-heterocyclic carbene ligand. *J. Organomet. Chem.* **847,** 162–166 (2017).

117. Benaissa, I., Taakili, R., Lugan, N. & Canac, Y. A convenient access to N-phosphonio-substituted NHC metal complexes [M = Ag(i){,} Rh(i){,} Pd(ii)]. *Dalt. Trans.* **46,** 12293–12305 (2017).

118. Andrade, G. A., DiMeglio, J. L., Guardino, E. T., Yap, G. P. A. & Rosenthal, J. Synthesis and structure of palladium(II) complexes supported by bis-NHC pincer ligands for the electrochemical activation of {CO2}. *Polyhedron* **135,** 134–143 (2017).

119. Filonenko, G. a., Cosimi, E., Lefort, L., Conley, M. P., Copéret, C., Lutz, M., Hensen, E. J. M. & Pidko, E. a. Lutidine-derived Ru-CNC hydrogenation

pincer catalysts with versatile coordination properties. *ACS Catal.* **4,** 2667–2671 (2014).

120. Bitzer, M. J., Pöthig, A., Jandl, C., Kühn, F. E. & Baratta, W. Ru–Ag and Ru–Au dicarbene complexes from an abnormal carbene ruthenium system. *Dalt. Trans.* **44,** 11686–11689 (2015).

121. Lee, D. H., Kim, J. H., Jun, B. H., Kang, H., Park, J. & Lee, Y. S. Macroporous polystyrene-supported palladium catalyst containing a bulky N-heterocyclic carbene ligand for Suzuki reaction of aryl chlorides. *Org. Lett.* **10,** 1609–1612 (2008).

122. Schneider, H., Schmidt, D., Eichhöfer, A., Radius, M., Weigend, F. & Radius, U. Synthesis and reactivity of NHC-stabilized iron(II)-mesityl complexes. *Eur. J. Inorg. Chem.* 2600–2616 (2017). doi:10.1002/ejic.201700143

123. Mahatthananchai, J. & Bode, J. W. The effect of the N-mesityl group in NHC-catalyzed reactions. *Chem. Sci.* **3,** 192–197 (2012).

124. Hintermann, L. Expedient syntheses of the *N*-heterocyclic carbene precursor imidazolium salts IPr??HCl, IMes??HCl and IXy??HCl. *Beilstein J. Org. Chem.* **3,** 2–6 (2007).

125. Paradiso, V., Bertolasi, V., Costabile, C., Caruso, T., Dąbrowski, M., Grela, K. & Grisi, F. Expanding the family of Hoveyda–Grubbs catalysts containing unsymmetrical NHC ligands. *Organometallics* **36,** 3692–3708 (2017).

126. Liu, Y., Persson, P., Sundström, V. & Wärnmark, K. Fe *N*-heterocyclic carbene complexes as promising photosensitizers. *Acc. Chem. Res.* **49,** 1477–1485 (2016).

127. Riener, K., Haslinger, S., Raba, A., Ho, M. P., Cokoja, M., Herrmann, W. A. & Ku, F. E. Chemistry of iron *N*−heterocyclic carbene complexes : Syntheses , structures , reactivities , and catalytic applications. *Chem. Rev.* **114,** 5215–5272 (2014).

128. Cardoso, J. M. S. & Royo, B. Unprecedented synthesis of iron–NHC complexes by C–H activation of imidazolium salts. Mild catalysts for reduction of sulfoxides. *Chem. Commun.* **48,** 4944 (2012).

129. Warratz, S., Postigo, L. & Royo, B. Direct synthesis of iron(0) N-heterocyclic carbene complexes by using $Fe_3(CO)_{12}$ and their application in reduction of carbonyl groups. *Organometallics* **32,** 893–897 (2013).

130. Kernbach, U., Ramm, M., Luger, P. & Fehlhammer, W. P. A Chelating Triscarbene ligand and its hexacarbene iron complex. *Angew. Chemie Int. Ed. English* **35,** 310–312 (1996).

131. Jang, G., Wong, J., Huang, Y. & Li, C. Synthesis of HMF in ionic liquids: Biomass-derived products. in synthesis of HMF in ionic liquids: *Biomass-Derived Products* 202–226 (The Royal Society of Chemistry, 2015). doi:10.1039/9781849739764-00202

132. Zhao, H., Holladay, J.E., Brown, H., Zhang, Z. C. Metal chlorides in ionic liquid solvents convert sugar to 5-hydroxymethyfurfural. *Science (80).* **316,**

1597–600 (2007).

133. Lindhorst, A. C., Drees, M., Bonrath, W., Schütz, J., Netscher, T. & Kühn, F. E. Mechanistic insights into the biomimetic catalytic hydroxylation of arenes by a molecular Fe(NHC) complex. *J. Catal.* **352,** 599–605 (2017).

134. Legros, J. & Figadère, B. Iron-promoted C–C bond formation in the total synthesis of natural products and drugs. *Nat. Prod. Rep.* **32,** 1541–1555 (2015).

135. Mako, T. L. & Byers, J. A. Recent advances in iron-catalysed cross coupling reactions and their mechanistic underpinning. *Inorg. Chem. Front.* **3,** 766–790 (2016).

136. Guisán-Ceinos, M., Tato, F., Buñuel, E., Calle, P. & Cárdenas, D. J. Fe-catalysed Kumada-type alkyl–alkyl cross-coupling. Evidence for the intermediacy of Fe(i) complexes. *Chem. Sci.* **4,** 1098 (2013).

137. Arduengo, III, A. J. & Iconaru, L. I. Fused polycyclic nucleophilic carbenes – synthesis, structure, and function. *Dalt. Trans.* **35**, 6903-6914 (2009). doi:10.1039/b907211j

138. Louie, J. & Grubbs, R. H. Highly active iron imidazolylidene catalysts for atom transfer radical polymerization. *Chem. Commun.* **16**, 1479–1480 (2000). doi:10.1039/B003957H

139. Chen, M. Z., Sun, H. M., Li, W. F., Wang, Z. G., Shen, Q. & Zhang, Y. Synthesis, structure of functionalized *N*-heterocyclic carbene complexes of Fe(II) and their catalytic activity for ring-opening polymerization of ??-caprolactone. *J. Organomet. Chem.* **691,** 2489–2494 (2006).

140. Riener, K., Haslinger, S., Raba, A., Högerl, M. P., Cokoja, M., Herrmann, W. A. & Kühn, F. E. Chemistry of Iron *N*-heterocyclic carbene complexes: Syntheses, structures, reactivities, and catalytic applications. *Chem. Rev.* **114,** 5215–5272 (2014).

141. Xiong, J., Zhu, W., Ding, W., Yang, L., Zhang, M., Jiang, W., Zhao, Z. & Li, H. Hydrophobic mesoporous silica-supported heteropolyacid induced by ionic liquid as a high efficiency catalyst for the oxidative desulfurization of fuel. *RSC Adv.* **5,** 16847–16855 (2015).

142. Luque, R. & Garcia Martinez, J. Editorial: From mesoporous supports to mesoporous catalysts: Introducing functionality to mesoporous materials. *ChemCatChem* **5,** 827–829 (2013).

143. Jin, H., Ansari, M. B. & Park, S.-E. Sulfonic acid functionalized mesoporous ZSM-5: Synthesis, characterization and catalytic activity in acidic catalysis. *Catal. Today* **245,** 116–121 (2014).

144. White, R. J., Luque, R., Budarin, V. L., Clark, J. H. & Macquarrie, D. J. Supported metal nanoparticles on porous materials. Methods and applications. *Chem. Soc. Rev.* **38,** 481–94 (2009).

145. Ji, Y. In vitro digestion and physicochemical characteristics of corn starch mixed with amino acid modified by low pressure treatment. *Food Chem.* **242,** 421–426 (2018).

146. Park, E. Y., Kim, M.-J., Cho, M., Lee, J. H. & Kim, J.-Y. Production of starch nanoparticles using normal maize starch via heat-moisture treatment under mildly acidic conditions and homogenization. *Carbohydr. Polym.* **151,** 274–282 (2016).

147. Chandran, A., Kuriakose, S. & Mathew, T. Thermal and photoresponsive studies of starch modified with 2-(5-(4-dimethylamino-benzylidine)-4-oxo-2-thioxo-thiazolidin-3-yl)acetic Acid. *Int. J. Carbohydr. Chem.* **2012,** 1–8 (2012).

148. Wang, S., Kowalski, R. J., Kang, Y., Kiszonas, A. M., Zhu, M.-J. & Ganjyal, G. M. Impacts of the particle sizes and levels of inclusions of cherry pomace on the physical and structural properties of direct expanded corn starch. *Food Bioprocess Technol.* **10,** 394–406 (2017).

149. Long, J., Zhang, B., Li, X., Zhan, X., Xu, X., Xie, Z. & Jin, Z. Effective production of resistant starch using pullulanase immobilized onto magnetic chitosan/Fe3O4 nanoparticles. *Food Chem.* **239,** 276–286 (2018).

150. Park, E. Y., Ma, J.-G., Kim, J., Lee, D. H., Kim, S. Y., Kwon, D.-J. & Kim, J.-Y. Effect of dual modification of HMT and crosslinking on physicochemical properties and digestibility of waxy maize starch. *Food Hydrocoll.* **75,** 33–40 (2018).

151. Sjoqvist, M., Boldizar, a. & Rigdahl, M. Processing and properties of expanded starch materials. *J. Cell. Plast.* **45,** 51–66 (2009).

152. Zia-ud-Din, Xiong, H. & Fei, P. Physical and chemical modification of starches: A review. *Crit. Rev. Food Sci. Nutr.* **57,** 2691–2705 (2017).

153. Budarin, V., Clark, J. H., Hardy, J. J. E., Luque, R., Milkowski, K., Tavener, S. J. & Wilson, A. J. Starbons: New starch-derived mesoporous carbonaceous materials with tunable properties. *Angew. Chemie - Int. Ed.***45**, 3782–3786 (2006).

154. OECD/Food and Agriculture Organization of the United Nations (2015), O.-F. A. O. 2015. *OECD-FAO Agricultural Outlook 2015-2024: HIGHLIGHTS. Oecd/Fao* (2015). doi:10.1787/agr_outlook-2016-en

155. C. Chen, A. R. L. P. and F. G. Pigments in Fruits and Vegetables*: Genomics and Dietetics*. (Springer US, 2015). doi:10.1007/978-1-4939-2356-4

156. Mamma, D. & Christakopoulos, P. Waste Biomass Valor. *Springer* **5,** 529–549 (2014).

157. Mitra, S. K. Mango production in the world -present situation and future prospect. in *Acta Horticulturae* 287–296 (International Society for Horticultural Science (ISHS), Leuven, Belgium, 2016). doi:10.17660/ActaHortic.2016.1111.41

158. Prospectiva 2020. *World Mango Market Supply, Demand and Forecast*. GBD Network. (2015).

159. Matharu, A. S., Houghton, J. A., Lucas-Torres, C. & Moreno, A. Acid-free microwave-assisted hydrothermal extraction of pectin and porous cellulose from mango peel waste – towards a zero waste mango biorefinery. *Green*

Chem. **18,** 5280–5287 (2016).

160. de Melo, E. M., Clark, J. H. & Matharu, A. S. The Hy-MASS concept: hydrothermal microwave assisted selective scissoring of cellulose for in situ production of (meso)porous nanocellulose fibrils and crystals. *Green Chem.* **19,** 3408–3417 (2017).

161. Qi, H., Schulz, B., Vad, T., Liu, J., Mäder, E., Seide, G. & Gries, T. Novel carbon nanotube/cellulose composite fibers as multifunctional materials. *ACS Appl. Mater. Interfaces.* **7**, 22404−22412 (2015).

162. Li, W. Y., Jin, a. X., Liu, C. F., Sun, R. C., Zhang, a. P. & Kennedy, J. F. Homogeneous modification of cellulose with succinic anhydride in ionic liquid using 4-dimethylaminopyridine as a catalyst. *Carbohydr. Polym.* **78,** 389–395 (2009).

163. Ciolacu, D., Ciolacu, F. & Popa, V. Amorphous cellulose—structure and characterization. *Cellul. Chem.* **45,** 13–21 (2011).

164. Srinivas, G., Cheng, X. & Smith, J. C. A solvent-free coarse grain model for crystalline and amorphous cellulose fibrils. *J. Chem. Theory Comput.* **7,** 2539–2548 (2011).

165. Du, Y., Cheng, H., Li, Y., Wang, B., Mao, Z., Xu, H., Zhang, L., Zhong, Y., Yan, X. & Sui, X. Temperature-responsive cellulose sponge with switchable pore size: Application as a water flow manipulator. *Mater. Lett.* **210,** 337–340 (2018).

166. Yue, C., Li, G., Pidko, E. A., Wiesfeld, J. J., Rigutto, M. & Hensen, E. J. M. Dehydration of glucose to 5-hydroxymethylfurfural using Nb-doped tungstite. *ChemSusChem* **9,** 2421–2429 (2016).

167. Yu, I. K. M. & Tsang, D. C. W. Conversion of biomass to hydroxymethylfurfural: A review of catalytic systems and underlying mechanisms. *Bioresour. Technol.* **238,** 716–732 (2017).

168. Shin, J. Y., Lee, B. S., Jung, Y., Kim, S. J. & Lee, S. Palladium nanoparticles captured onto spherical silica particles using a urea cross-linked imidazolium molecular band. *Chem. Commun.* 5238–5240 (2007). doi:10.1039/B711237H

169. Simon, M., Csunderlik, C., Jones, P. G., Neda, I. & Tarta-Micle, A. Disuccinimidyl carbonate. *Acta Crystallogr. Sect. E* **59,** 683–685 (2003).

170. Diamanti, S., Arifuzzaman, S., Elsen, A., Genzer, J. & Vaia, R. a. Reactive patterning via post-functionalization of polymer brushes utilizing disuccinimidyl carbonate activation to couple primary amines. *Polymer (Guildf).* **49,** 3770–3779 (2008).

171. Zuo, Y., Liu, W., Xiao, J., Zhao, X., Zhu, Y. & Wu, Y. Preparation and characterization of dialdehyde starch by one-step acid hydrolysis and oxidation. *Int. J. Biol. Macromol.* **103,** 1257–1264 (2017).

172. Boukhelkhal, M. & Moulai-Mostefa, N. Physicochemical characterization of starch isolated from soft acorns of holm oak (Quercus ilex subsp. ballota (Desf.) Samp.) grown in Algeria. *J. Food Meas. Charact.* **11,** 1995–2005 (2017).

173. Sun, F., Liu, J., Liu, X., Wang, Y., Li, K., Chang, J., Yang, G. & He, G. Effect of the phytate and hydrogen peroxide chemical modifications on the physicochemical and functional properties of wheat starch. *Food Res. Int.* **100,** 180–192 (2017).

174. Warren, F. J., Gidley, M. J. & Flanagan, B. M. Infrared spectroscopy as a tool to characterise starch ordered structure - A joint FTIR-ATR, NMR, XRD and DSC study. *Carbohydr. Polym.* **139,** 35–42 (2016).

175. Hammaecher, C., Joris, B., Goormaghtigh, E. & Marchand-Brynaert, J. Photoactivable nonsymmetrical bifunctional linkers for protein immobilization on attenuated total reflectance FTIR optical devices. *European J. Org. Chem.* **35**, 7952–7959 (2013).

176. Nakayama, H., Nakanishi, J., Shimizu, T., Yoshino, Y., Iwai, H., Kaneko, S., Horiike, Y. & Yamaguchi, K. Silane coupling agent bearing a photoremovable succinimidyl carbonate for patterning amines on glass and silicon surfaces with controlled surface densities. *Colloids Surfaces B Biointerfaces* **76,** 88–97 (2010).

177. Beltran, T. F., Zaragoza, G. & Delaude, L. Mono- and bimetallic manganese-carbonyl complexes and clusters bearing imidazol(in)ium-2-dithiocarboxylate ligands. *Dalt. Trans.* **46,** 1779–1788 (2017).

178. Jones, E. W., Holliman, P. J., Connell, A., Davies, M. L., Baker, J., Hobbs, R. J., Ghosh, S., Furnell, L., Anthony, R. & Pleydell-Pearce, C. A novel dimethylformamide (DMF) free bar-cast method to deposit organolead perovskite thin films with improved stability. *Chem. Commun.* **52,** 4301–4304 (2016).

179. Schuh, C. & Rühe, J. Penetration of polymer brushes by chemical nonidentical free polymers. *Macromolecules* **44,** 3502–3510 (2011).

180. Zumbühl, S., Brändle, A., Hochuli, A., Scherrer, N. C. & Caseri, W. Derivatization technique to identify specifically carbonyl groups by infrared spectroscopy: Characterization of photooxidative aging products in terpenes and terpeneous resins. *Anal. Chem.* **89,** 1742–1748 (2017).

181. Lindenmaier, R., Williams, S. D., Sams, R. L. & Johnson, T. J. Quantitative infrared absorption spectra and vibrational assignments of crotonaldehyde and methyl vinyl ketone using gas-phase mid-infrared, far-infrared, and liquid raman spectra: s-cis vs s-trans Composition Confirmed via Temperature Studies and ab Init. *J. Phys. Chem. A* **121,** 1195–1212 (2017).

182. Yamada, T., Tominari, Y., Tanaka, S. & Mizuno, M. Terahertz and infrared spectroscopy of room-temperature imidazolium-based ionic liquids. *J. Phys. Chem. B* **119,** 15696–15705 (2015).

183. Kiefer, J., Fries, J. & Leipertz, A. Experimental vibrational study of imidazolium-based ionic liquids: Raman and infrared spectra of 1-ethyl-3-methylimidazolium bis(trifluoromethylsulfonyl)imide and 1-ethyl-3-methylimidazolium ethylsulfate. *Appl. Spectrosc.* **61,** 1306–1311 (2007).

184. Yamada, T., Tominari, Y., Tanaka, S. & Mizuno, M. Infrared spectroscopy of ionic liquids consisting of imidazolium cations with different alkyl chain

lengths and various halogen or molecular anions with and without a small amount of water. *J. Phys. Chem. B* **121,** 3121–3129 (2017).

185. Guo, Z., Zeng, S., Zhang, Y., Lu, X., Tian, Y. & Zheng, B. The effects of ultra-high pressure on the structural, rheological and retrogradation properties of lotus seed starch. *Food Hydrocoll.* **44,** 285–291 (2015).

186. Tan, I., Flanagan, B. M., Halley, P. J., Whittaker, A. K. & Gidley, M. J. A method for estimating the nature and relative proportions of amorphous, single, and doubled-helical components in starch granules by ^{13}C CP/MAS NMR. *Biomacromolecules* **8,** 885–891 (2007).

187. Tang, H. & Hills, B. P. Use of MAS NMR to study domain structure and dynamics of polysaccharides in the native starch granules ^{13}C. *Biomacromolecules* **4,** 1269–1276 (2003).

188. Planellas, M., Pleixats, R. & Shafir, A. Palladium nanoparticles in Suzuki cross-couplings: Tapping into the potential of tris-imidazolium salts for nanoparticle stabilization. *Adv. Synth. Catal.* **354,** 651–662 (2012).

189. Bouchmella, K., Dutremez, S. G., Alonso, B., Mauri, F. & Gervais, C. ^{1}H, ^{13}C, and ^{15}N solid-state NMR studies of imidazole- and morpholine-based model compounds possessing halogen and hydrogen bonding capabilities. *Cryst. Growth Des.* **8,** 3941–3950 (2008).

190. Sofia, L. T. A., Krishnan, A., Sankar, M., Raj, N. K. K., Manikandan, P., Rajamohanan, P. R. & Ajithkumar, T. G. Immobilization of phosphotungstic acid (PTA) on imidazole functionalized silica: Evidence for the nature of PTA binding by solid state NMR and reaction studies. *J. Phys. Chem. C* **113,** 21114–21122 (2009).

191. Mao, J. D. & Schmidt-Rohr, K. Separation of aromatic-carbon 13C NMR signals from di-oxygenated alkyl bands by a chemical-shift-anisotropy filter. *Solid State Nucl. Magn. Reson.* **26,** 36–45 (2004).

192. Kaal, J., Brodowski, S., Baldock, J. A., Nierop, K. G. J. & Cortizas, A. M. Characterisation of aged black carbon using pyrolysis-GC/MS, thermally assisted hydrolysis and methylation (THM), direct and cross-polarisation 13C nuclear magnetic resonance (DP/CP NMR) and the benzenepolycarboxylic acid (BPCA) method. *Org. Geochem.* **39,** 1415–1426 (2008).

193. Kaith, B. S., Jindal, R., Jana, A. K. & Maiti, M. Development of corn starch based green composites reinforced with Saccharum spontaneum L fiber and graft copolymers - Evaluation of thermal, physico-chemical and mechanical properties. *Bioresour. Technol.* **101,** 6843–6851 (2010).

194. Bernard, F. L., Duczinski, R. B., Rojas, M. F., Fialho, M. C. C., Carreño, L. Á., Chaban, V. V., Vecchia, F. D. & Einloft, S. Cellulose based poly(ionic liquids): Tuning cation-anion interaction to improve carbon dioxide sorption. *Fuel* **211,** 76–86 (2018).

195. Moreira, G. F., Peçanha, E. R., Monte, M. B. M., Filho, L. S. L. & Stavale, F. XPS study on the mechanism of starch-hematite surface chemical complexation. *Miner. Eng.* **110,** 96–103 (2017).

196. Zhou, J. H., Sui, Z. J., Zhu, J., Li, P., Chen, D., Dai, Y. C. & Yuan, W. K. Characterization of surface oxygen complexes on carbon nanofibers by TPD, XPS and FT-IR. *Carbon N. Y.* **45,** 785–796 (2007).

197. Gurgul, J., ŁąTka, K., Hnat, I., Rynkowski, J. & Dzwigaj, S. Identification of iron species in FeSiBEA by DR UV-vis, XPS and Mössbauer spectroscopy: Influence of Fe content. *Microporous Mesoporous Mater.* **168,** 1–6 (2013).

198. Yan, Z., Zhuxia, Z., Tianbao, L., Xuguang, L. & Bingshe, X. XPS and XRD study of $FeCl_3$-graphite intercalation compounds prepared by arc discharge in aqueous solution. *Spectrochim. Acta - Part A Mol. Biomol. Spectrosc.* **70,** 1060–1064 (2008).

199. Grosvenor, A. P., Kobe, B. A., Biesinger, M. C. & McIntyre, N. S. Investigation of multiplet splitting of Fe 2p XPS spectra and bonding in iron compounds. *Surf. Interface Anal.* **36,** 1564–1574 (2004).

200. Mishra, A., Sharma, R. & Shrivastava, B. D. Spectroscopic studies on transition metal iron complexes of 2- (N-Aryl ethanimidoyl) phenol as ligands. **49,** 740–747 (2011).

201. Groen, J. C., Peffer, L. A. A. & Pérez-Ramírez, J. Pore size determination in modified micro- and mesoporous materials. Pitfalls and limitations in gas adsorption data analysis. *Microporous Mesoporous Mater.* **60,** 1–17 (2003).

202. Li, H., Chen, C. & Balsells Padros, J. Highly Efficient Carbamate Formation from Alcohols and Hindered Amino Acids or Esters Using N,N′-Disuccinimidyl Carbonate (DSC). *Synlett* **2011,** 1454–1458 (2011).

203. Poletto, M., Ornaghi Júnior, H. L. & Zattera, A. J. Native cellulose: Structure, characterization and thermal properties. *Materials (Basel).* **7,** 6105–6119 (2014).

204. Kontturi, E. J. *Surface chemistry of cellulose from natural fibres to model surfaces*. (Universiteitsdrukkerij, Eindhoven University of Technology, 2005). doi:10.6100/IR583690

205. Zhang, J., Zhang, J., Lin, L., Chen, T., Zhang, J., Liu, S., Li, Z. & Ouyang, P. Dissolution of microcrystalline cellulose in phosphoric acid-molecular changes and kinetics. *Molecules* **14,** 5027–5041 (2009).

206. Ishizawa, C. I., Parilla, *Æ*. P. A. & Davis, M. F. Measuring the crystallinity index of cellulose by solid state 13C nuclear magnetic resonance . Cellulose C nuclear magnetic resonance. *Springer.* **16**, 641–647 (2009).

207. Lepetit, A., Drolet, R., Tolnai, B., Montplaisir, D. & Zerrouki, R. Alkylation of microfibrillated cellulose - A green and efficient method for use in fiber-reinforced composites. *Polymer (Guildf).* **126,** 48–55 (2017).

208. Antonetti, C., Licursi, D., Fulignati, S., Valentini, G. & Raspolli Galletti, A. New frontiers in the catalytic synthesis of levulinic acid: From sugars to raw and waste biomass as starting feedstock. *Catalysts* **6,** 196 (2016).

209. Qi, X., Watanabe, M., Aida, T. M., and Smith, R. L., J. Catalytic dehydration of fructose into 5-hydroxymethylfurfural by ion-exchange resin in mixed-aqueous system by microwave heating. *Green Chem.* **10,** 799–805 (2008).

210. Babij, N. R., McCusker, E. O., Whiteker, G. T., Canturk, B., Choy, N., Creemer, L. C., Amicis, C. V. De, Hewlett, N. M., Johnson, P. L., Knobelsdorf, J. A., Li, F., Lorsbach, B. A., Nugent, B. M., Ryan, S. J., Smith, M. R. & Yang, Q. NMR chemical shifts of trace impurities: Industrially preferred solvents used in process and green chemistry. *Org. Process Res. Dev.* **20,** 661–667 (2016).

211. Ngee, E. L. S., Gao, Y., Chen, X., Lee, T. M., Hu, Z., Zhao, D. & Yan, N. Sulfated mesoporous niobium oxide catalyzed 5-hydroxymethylfurfural formation from sugars. *Ind. Eng. Chem. Res.* **53,** 14225–14233 (2014).

212. Gottlieb, H. E., Kotlyar, V. & Nudelman, A. NMR chemical shifts of common solvents as trace impurities. *J. Org. Chem.* **62,** 7512–7515 (1997).

213. Thomas, B., Ginic-Markovic, M., Johnston R, M., Cooper, P. & Petrovsky, N. Observation of the keto tautomer of D-fructose in D2 O using 1 H NMR spectroscopy. *Carbohydr. Res.* **347,** 136–141 (2012).

214. Guan, J., Cao, Q., Guo, X. & Mu, X. The mechanism of glucose conversion to 5-hydroxymethylfurfural catalyzed by metal chlorides in ionic liquid: A theoretical study. *Comput. Theor. Chem.* **963,** 453–462 (2011).

215. Chen, J., Li, K., Chen, L., Liu, R., Huang, X. & Ye, D. Conversion of fructose into 5-hydroxymethylfurfural catalyzed by recyclable sulfonic acid-functionalized metal–organic frameworks. *Green Chem.* **16,** 2490 (2014).

216. Comerford, J. W., Clark, J. H., Macquarrie, D. J. & Breeden, S. W. Clean, reusable and low cost heterogeneous catalyst for amide synthesis. *Chem. Commun. (Camb).* **18**, 2562–2564 (2009).

217. MacMillan, D. S., Murray, J., Sneddon, H. F., Jamieson, C. & Watson, A. J. B. Evaluation of alternative solvents in common amide coupling reactions: replacement of dichloromethane and *N*,*N*-dimethylformamide. *Green Chem.* **15,** 596 (2013).

218. Goodreid, J. D., Duspara, P. a., Bosch, C. & Batey, R. a. Amidation reactions from the direct coupling of metal carboxylate salts with amines. *J. Org. Chem.* **79,** 943–954 (2014).

219. Roughley, S. D. & Jordan, A. M. The medicinal chemist's toolbox: An analysis of reactions used in the pursuit of drug candidates. *J. Med. Chem.* **54,** 3451–3479 (2011).

220. Bai, C., Yao, X. & Li, Y. Easy access to amides through aldehydic C-H bond functionalization catalyzed by heterogeneous Co-based catalysts. *ACS Catal.* **5,** 884–891 (2015).

221. Pattabiraman, V. R. & Bode, J. W. Rethinking amide bond synthesis. *Nature* **480,** 471–9 (2011).